https://doi.org/10.15388/vu.thesis.135
https://orcid.org/0000-0002-6885-1587

VILNIUS UNIVERSITY
CENTER FOR PHYSICAL SCIENCES AND TECHNOLOGY

Vidmantas
TOMKUS

Excitation of secondary radiation with high-intensity laser fields and its application in materials science

DOCTORAL DISSERTATION

Technological Sciences,
Materials Engineering (T 008)

VILNIUS 2021

The dissertation was written between 2015 and 2019 in the Department of Laser Technologies of the Center for Physical Sciences and Technology.

Academic supervisor:
Dr. Kęstutis Regelskis (Center for Physical Sciences Technological Sciences, Material Engineering – T008).

This doctoral dissertation will be defended in a public meeting of the Dissertation Defence Panel:
Chairman - Prof. Dr. habil. Valdas Sirutkaitis (Vilnius University, technological sciences, material engineering – T008);

Members:
Prof. Dr. Diana Adlienė, (Kaunas University of Technology, Technological sciences, Material engineering - T008),
Assoc. prof. Dr. habil. Karoly Osvay (Institute for Applications of High-Intensity Lasers in Nuclear Physics, University of Szeged, Technological sciences, Material engineering – T008),
Assoc. prof. Dr. Artūras Plukis (Center for Physical Sciences and Technology Technological sciences, Material engineering – T008),
Assoc. prof. Dr. Virgilijus Vaičaitis (Vilnius University, Technological sciences, Material engineering – T008).

The dissertation shall be defended at a public meeting of the Dissertation Defence Panel at consideration at 2:00 p. m. on the 4th of February, 2021, in the hall of FTMC Institute of Physics.
Address: Savanoriu Ave. 231, LT-02300 Vilnius, Lithuania
Tel. +370 5 2661 640; e-mail: office@ftmc.lt

The doctoral thesis is available at libraries of FTMC and Vilnius University and VU web page:
www.vu.lt/naujienos/ivykiu-kalendorius

https://doi.org/10.15388/vu.thesis.135
https://orcid.org/0000-0002-6885-1587

VILNIAUS UNIVERSITETAS
FIZINIŲ IR TECHNOLOGIJOS MOKSLŲ CENTRAS

VIDMANTAS
TOMKUS

Antrinės spinduliuotės žadinimas aukšto intensyvumo lazeriniais laukais ir jos taikymas medžiagotyroje

DAKTARO DISERTACIJA

Technologijos mokslai,
Medžiagų inžinerija (T 008)

VILNIUS 2021

Disertacija rengta 2015–2019 metais Valstybinio mokslinių tyrimų instituto Fizinių ir technologijos mokslų centro Lazerinių technologijų skyriuje.

Mokslinis vadovas:
dr. Kęstutis Regelskis (Fizinių ir technologijos mokslų centras, technologijos mokslai, medžiagų inžinerija – T008).

Gynimo taryba:
Pirmininkas:
prof. habil. dr. Valdas Sirutkaitis (Vilniaus universitetas, technologijos mokslai, medžiagų inžinerija – T008);

Nariai:
prof. dr. Diana Adlienė (Kauno technologijos universitetas, technologijos mokslai, medžiagų inžinerija – T008),
asoc. prof. habil. dr. Karoly Osvay (Taikomųjų didelio intensyvumo lazerių branduolinės fizikos institutas, Segedo universitetas (Vengrija), technologijos mokslai, medžiagų inžinerija – T008),
doc. dr. Artūras Plukis (Fizinių ir technologijos mokslų centras, technologijos mokslai, medžiagų inžinerija – T008),
doc. dr. Virgilijus Vaičaitis (Vilniaus universitetas, technologijos mokslai, medžiagų inžinerija – T008).

Disertacija ginama viešame Gynimo tarybos posėdyje 2021 m. vasario 4 d. 14 val. FTMC Fizikos instituto salėje.
Adresas: Savanorių pr. 231, LT-02300 Vilnius, Lietuva
tel. +370 5 266 1640
el. paštas: office@ftmc.lt

Disertaciją galima peržiūrėti Vilniaus universiteto ir FTMC bibliotekose ir VU interneto svetainėje adresu:
https://www.vu.lt/naujienos/ivykiu-kalendorius

TABLE OF CONTENTS

ACKNOWLEDGEMENTS

I am very grateful to my academic supervisor Dr. Kęstutis Regelskis and the Chief of the Department of Laser Technologies of FTMC Dr. Gediminas Račiukaitis for the great support, motivation and useful advice.

Thanks to Dr. Isabel Gallardo González, Dr. Diego Guénot, Jonas Björklund Svensson, Anders Persson, Dr. Olle Lundh, the Department of Physics, Lund University for the collaboration on experimental work Laser wakefield acceleration and X-ray generation as well as a valuable discussion of results.

My sincere gratitude to Lucas Rovige, Dr. Igor Andriyash, Dr. Julius Huijts, Dr. Aline Vernier, Marie Ouillé, Zhao Cheng, Rodrigo Lopez-Martens, Prof. Dr. Jérôme Faure, LOA, CNRS, Ecole Polytechnique, ENSTA Paris, Institute Polytechnique de Paris for the proposal of One-Sided Shock nozzles and the collaboration on experimental work on testing the manufactured structures using near-single-cycle 1 kHz laser system.

Many thanks and appreciation to Dr. Valdas Girdauskas, Juozas Dudutis, Dr. Valdemar Stankevič, Dr. Paulius Gečys and other colleagues from the Department of Laser Technologies of FTMC for the collaborative work on 3D laser processing and characterization of micronozzles and the friendly atmosphere in the laboratory.

The research leading to these results was funded by the Research Council of Lithuania under the grant agreement S- MIP-17-79, European Union's Horizon 2020 Research and Innovation program under ARIES Grant Agreement 730871, and by Laserlab-Europe, H2020 EC-GA 654148. The experimental work at Lund Laser Center was funded by the Knut and Alice Wallenberg Foundation, the Swedish Research Council, and the Crafoord Foundation. The work at Laboratoire d'Optique Appliqué (LOA) of CNRS - Ecole Polytechnique (EP) and ENSTA-Paristech was funded by the European Research Council (ERC Starting Grant FEMTOELEC) under Contract No. 306708, financial support from the Region Ile-de-France (under contract SESAME-2012-ATTOLITE) and the Extreme Light Infrastructure-Hungary Non-Profit Ltd. (under contract NLO3.6LOA).

LIST OF ABBREVIATIONS

BOA	- Break-Out-Afterburner
BW	- Bandwidth
CCD	- Charge-Coupled-Device
CEP	- Carrier envelope phase
CE	- Coulomb Explosion
CFD	- Computational Fluid Dynamics
CMOS	- Complementary Metal-Oxide-Semiconductor
CNC	- Computer Numerical Control
CNRS	- Centre National de la Recherche Scientifique
CPA	- Chirped Pulse Amplification
CNF	- Carbon Nanotube Foam
CT	- Computer tomography
DLC	- Diamond-like Carbon
DPSS	- Diode-Pumped Solid-State
ELI	- Extreme Light Infrastructure
EXAFS	- Extended X-ray Absorption Fine Structure
FWHM	- Full Width at Half Maximum
HCF	- Hollow Core Fiber
GVD	- Group Velocity Dispersion
HHG	- High-Order Harmonics Generation
FBPIC	- Fourier Bessel Particle-in-Cell
FEL	- Free Electron Laser
FLSE	- Femtosecond Laser-Assisted Selective Etching
ICS	- Inverse Compton Scattering
KOH	- Potassium Hydroxide
LLC	- Lund Laser Center
LOA	- Laboratoire d'Optique Appliqué
LWFA	- Laser Wakefield Acceleration
μCT	- Micro-Computed Tomography
MVA	- Magnetic Vortex Acceleration
IDEA	- Interferometric Data Evaluation Algorithm
OPCPA	- Optical Parametric Chirped Pulse Amplifier
PB-PCI	- Propagation Based Phase-Contrast Imaging
PIC	- Particle-in-Cell
PSF	- Point-Spread Function
PWFA	- Plasma Wakefield Acceleration
QED	- Quantum Electrodynamics
OSS	- One-Sided Shock

RANS - Reynolds-Averaged Navier-Stokes
RF - Radio Frequency
RPA - Radiation Pressure Acceleration
RR - Radiation Reaction
RT - Relativistic Transparency
SEM - Scanning Electron Microscope
SPM - Self-Phase Modulation
STII - Self-Truncated Ionization Injection
SWA - Shock Wave Acceleration
TNSA - Target Normal Sheath Acceleration
XANES - X-ray Absorption Near Edge Structure
XAS - X-ray Absorption Spectroscopy
XUV - Extreme Ultraviolet Radiation
WDM - Warm Dense Matter

1. INTRODUCTION

A fast-paced development of high-intensity lasers paves a way to disruptive innovations in particle acceleration, development of table-top X-ray and γ-sources. High-energy physics research pushes the frontiers of fundamental understanding of matter and fosters the advances of knowledge at subatomic and attosecond scale. X-ray and γ-sources based on large accelerator facilities are widely used for material science, biochemistry research and offer new opportunities in the emerging field of nuclear photonics. Construction costs of a conventional radio accelerator reach several hundreds of millions of euros and are hardly affordable for modest research labs and industrial applications. Laser Wakefield Accelerators (LWFA) allow to achieve much higher values of the accelerating electric field and shorten the acceleration distance by hundreds of times. The formation of the electric field in LWFA, parameters of accelerated particles, and secondary radiation are defined by the interaction of propagating laser beam with plasma medium. The control of plasma is challenging, as the fluence of accelerating laser exceeds the limits of laser damage threshold of solid-state materials by several orders of magnitude. The laser-plasma interaction can be controlled by focusing and shaping of the laser beam and changing the properties of plasma targets.

In this work, the structured plasma concentration profiles are used for the acceleration of electron beams and X-ray generation. Tailored profiles are defined by the arrays of supersonic gas jets and intersecting shock waves. The gas jets are formed by the micronozzle arrays manufactured from a single fused silica block using 3D laser microfabrication. The secondary betatron X-ray radiation is generated by the transversal oscillation of electrons in the ion channel of the laser wake.

The thesis is divided into seven chapters. The first three chapters comprise the introduction, statements to defend, approbation, literature review and methods. In chapter 4, the results of Particle-in-Cell simulation of LWFA using structured plasma concentration profiles are presented. In chapter 5, the fluid dynamics of supersonic jets is modelled. In chapter 6, the results of laser microfabrication and nozzle characterization are described. In chapter 7, the experimental results of LWFA and secondary radiation excitation are discussed. At the end of the thesis, the summary of principal findings, references and list of used symbols are presented.

1.1. The Aim of the Research

The aim of the research was to investigate the properties of secondary X-ray radiation using high-intensity laser fields and its implementation for imaging applications in material science. Two tasks were set to achieve the goal:

1. Research of dependence of injection of number of electrons into the LWFA and secondary X-ray radiation on structured plasma concentration profiles.
2. Investigation of new manufacturing methods of micronozzle structures enabling the formation of required plasma concentration profiles.

1.2. Practical Value and Novelty

1.2.1. The Novelty of Research Results

1. The novel method of the control of electron injection in Laser wakefield accelerators (LWFA) and secondary X-ray radiation using structured plasma concentration profiles in injector and wiggler geometry was experimentally demonstrated. Electron acceleration and excitation of secondary radiation were numerically simulated.
2. For the formation of tailored plasma concentration profiles, the new approach of intersecting supersonic gas jets built by micronozzle arrays was proposed. The gas jets were numerically simulated and experimentally characterized.
3. For the manufacturing of micronozzle arrays, the new hybrid method of fused silica processing was introduced, enabling the fast material removal and precise handling of micrometric structures and ensuring the required quality of surface roughness.

1.2.2. Practical Value of Thesis

1. The proposed injection method increases the charge and lowers the energy dispersion of LWFA accelerated electrons. It can be used for the control of parameters of the electron beam in the secondary sources of betatron, Bremsstrahlung and Inversed Compton Scattering of X-ray and γ - radiation.
2. Structured plasma concentration profiles in wiggler geometry increase the transversal oscillation of electrons and brightness of secondary betatron X-ray radiation. The secondary X-ray sources can be implemented

for the imaging of micrometric objects in biomedicine, material science and investigation of femtosecond transient phenomena.

3. The proposed approach of formation of plasma concentration profiles can be implemented for electron acceleration using various lasers of Terawatt and Petawatt peak power and is of particular interest for the few-cycle lasers with kHz repetition rate. Micrometric plasma targets of subcritical density can be implemented for the ion acceleration using high-repetition-rate lasers systems.

1.3. Statements to Defend

1) The charge of accelerated electrons can be increased and the energy dispersion of the electrons can be lowered using combined ionization and density down-ramp triggered injection of structured plasma concentration profiles in injector geometry.
2) The number of photons and brightness of betatron X-ray radiation can be raised by structured plasma concentration profiles in wiggler geometry increasing the transversal oscillations of electrons.
3) Structured plasma concentration profiles in injector and wiggler geometry can be formed by intersecting shock waves of supersonic gas jets of arrays of converging-diverging micronozzles and micronozzles of fixed diameter.
4) Micronozzle arrays of micrometric dimensions resistant to optical damage can be manufactured from transparent materials, such as fused silica, combining fast high-volume removal laser nanosecond rear side processing and high-precision Femtosecond laser-assisted selective etching (FLSE) technique.

1.4. Approbation

The thesis is based on results published in 4 scientific peer-reviewed papers and presented in 7 contributions to conferences as well as in 2 national patent applications.

1.4.1. Scientific Papers

Related to the topic of this thesis (Peer-reviewed and indexed in Clarivate Analytics WoS):

A1. L. Rovige, I. Andriyash, J. Huijts, A. Vernier, V. Tomkus, V. Girdauskas, G. Raciukaitis, J. Dudutis, V. Stankevic, P. Gecys, M. Ouill, Z. Cheng, R. Lopez-Martens, and J. Faure, **Demonstration of stable long-term operation of a kilohertz laser-plasma accelerator**, Phys.Rev.Accel.Beams., 23, 093401(9), (2020), https://doi.org/10.1103/PhysRevAccelBeams.23.093401

A2. V. Tomkus, V. Girdauskas, J. Dudutis, V. Stankevic, P. Gecys, G. Raciukaitis, I. Gallardo González, D. Guénot, J. B. Svensson, A. Persson, O. Lundh, **Radiation from laser wakefield accelerated electron beams and betatron radiation using multijet gas targets**, Sci. Rep. 10, 16807, (2020), https://doi.org/10.1038/s41598-020-73805-7

A3. V. Tomkus, V. Girdauskas, J. Dudutis, P. Gečys, V. Stankevič, G. Račiukaitis, Impact of the wall roughness on the quality of micrometric nozzles manufactured from fused silica by hybrid different laser processing techniques, Appl. Surf. Sc., 483, 205-211, (2019), https://doi.org/10.1016/j.apsusc.2019.03.007

A4. V. Tomkus, V. Girdauskas, J. Dudutis, P. Gečys, V. Stankevič, G. Račiukaitis, **High-density gas capillary nozzles manufactured by hybrid 3D laser machining technique from fused silica**, Opt. Express. 26, 27965, (2018), https://doi.org/10.1364/OE.26.027965

Related to the topic of this thesis (Conference proceedings):

A5. V. Tomkus, L. Rimgaila, V. Stankevič G. Račiukaitis, **Three-dimensional Supersonic Sapphire Micronozzles for Laser-Plasma Wakefield Accelerators**, Chapter in Kawachi T., Bulanov S., Daido H., Kato Y. (eds) X-Ray Lasers 2016. ICXRL 2016. Springer Proceedings in Physics, 202, 167-171, (2018), https://doi.org/10.1007/978-3-319-73025-7_26

A6. V. Tomkus, L. Rimgaila, V. Stankevič, G. Račiukaitis, **Characterisation of Tuneable Gas Target Profiles for Laser Wakefield Acceleration**, High-brightness Sources and Light-driven Interactions Congress 2018 High-Brightness Sources and Light-driven Interactions, OSA Technical Digest, EM3B.4, (2018), https://doi.org/10.1364/EUVXRAY.2018.EM3B.4

A7. V. Tomkus, L. Rimgaila, V. Stankevič, G. Račiukaitis, **Real-time characterization of profiles of laser wakefield and electrons accelerated by few-cycle 1 kHz OCPA system**, 2017 Conference on Lasers and Electro-Optics Europe & European Quantum Electronics Conference (CLEO/Europe-EQEC), CG_P_2, (2017), https://doi.org/10.1109/CLEOE-EQEC.2017.8086823

Not directly related to the topic of this thesis (Conference proceedings):

A8. V. Tomkus, L. Rimgaila, V. Stankevič, G. Račiukaitis, **Plasma Guiding and Scattering Microstructures for Laser-Driven Thomson Sources**, First International Conference on Nuclear Photonics, Proc. SPIE, 10419, 1041901, 198, (2017), https://doi.org/10.1117/12.2280421

1.4.2. National Patents

P1. V. Tomkus, V. Girdauskas, J. Dudutis, V. Stankevič, G. Račiukaitis, **Method and device for generation of coherent radiation**, patent No. 6785, patent date 10.12.2020, patent application No. LT2019513, application date: 03.05.2019.

P2. V. Tomkus, V. Girdauskas, J. Dudutis, V. Stankevič, G. Raciukaitis, **Laser-driven high-dose-rate generating device of ionizing radiation**, patent application No. LT2019075, application date: 03.10.2019.

1.4.3. Conference Presentations

Directly related to the topic of the thesis:

Cl. V. Tomkus, V. Girdauskas, J. Dudutis, V. Stankevic, G. Raciukaitis, I. Gallardo González, D. Guénot, J. B. Svensson, A. Persson, O. Lundh, **Enhanced betatron radiation from multistage gas targets**, ELI User Workshop on Laser-Driven X-ray Sources and Applications, Prague, 24-25.10.2019

C2. V. Tomkus, V. Girdauskas, J. Dudutis, V. Stankevic, G. Raciukaitis, I. Gallardo González, D. Guénot, J. B. Svensson, A. Persson, O. Lundh, **Multistage gas targets from fused silica**, 4th Targetry for High Repetition Rate Laser-Driven Sources Workshop, Milan, Italy, 10-12.06.2019

C3. V. Tomkus, V. Girdauskas, J. Dudutis, V. Stankevic, G. Raciukaitis, I. Gallardo González, D. Guénot, J. B. Svensson, A. Persson, O. Lundh, **The**

control of laser wakefield accelerated electron beams and betatron X-ray radiation using arrays of multiple gas jets, Laser-Plasma Accelerator Workshop, (LPAW2019), Split, Croatia, 05-10.05.2019

C4. V. Tomkus, V. Girdauskas, J. Dudutis, V. Stankevic, P. Gecys, G. Raciukaitis, **Impact of the Wall Roughness on the Quality of Micrometric Nozzles Manufactured from Fused Silica by Hybrid Laser Processing**, The International Conference on Photo-Excited Processes and Applications ICPEPA-2018, Vilnius, Lithuania, 10-11.09.2018

C5. V. Tomkus, V. Girdauskas, J. Dudutis, V. Stankevic, G. Raciukaitis, **High Density Gas Capillaries for Betatron X-ray Sources of Laser Accelerated Electrons**, Nuclear Photonics NP-2018, Brașov, Romania, 24-29.06.2018

C6. V. Tomkus, V. Girdauskas, J. Dudutis, V. Stankevic, G. Raciukaitis, **Characterisation of Tuneable Gas Target Profiles for Laser Wakefield Acceleration**, High- brightness Congress HB-2018, Strasbourg, France, 25-29.03.2018

C7. V. Tomkus, L. Rimgaila, V. Stankevič, G. Račiukaitis, **Real-time Characterization of Profiles of Laser Wakefield and Electrons Accelerated by Few-Cycle 1 kHz OCPA system**, CLEO/Europe-EQEC, Munich, Germany, 25-27.06.2017

C8. V. Tomkus, L. Rimgaila, V. Stankevič, G. Račiukaitis. **Three-dimensional Supersonic Sapphire Micronozzles for Laser-Plasma Wakefield Accelerators**, 15th International Conference on X-Ray Lasers (ICXRL2016), Kansai, Japan, 22-27.05.2016

Not directly related to the topic of the thesis:

C9. V. Tomkus, L. Rimgaila, V. Stankevič, G. Račiukaitis, **Plasma Guiding and Scattering Microstructures for Laser Driven Thomson Sources**, Nuclear Photonics 2016 Conference, Monterey, USA, 16-21.10.2016

1.5. Authors and Co-Authors Contribution

1.5.1. Authors Contribution

The author of the thesis made the main theoretical and experimental work of the study, listed as follows:

- Development of the research methods, planning of the experiment, technical and organizational leadership of the activities to the topic;
- Design of structured plasma targets and numerical simulation of LWFA accelerated electrons and secondary X-ray radiation;
- Definition of micronozzle parameters and numerical simulation of fluid dynamics of supersonic jets;
- Development of micronozzle structures for 3D laser manufacturing from fused silica and participation in the characterization of nozzle jets using interferometric methods;
- Participation in the experimental work of the LWFA of electrons using manufactured micronozzle arrays and measurement of secondary X-ray radiation;
- Implementation of secondary X-ray radiation for the imaging of biological object and polymeric foils and definition of the imaging parameters;
- Analysis, interpretation and visualization of results, preparation of research articles, and presentation at the conferences.

1.5.2. Co-Authors Contribution

- Juozas Dudutis, Dr. Valdemar Stankevič, and Dr. Paulius Gečys - have manufactured the micronozzle arrays from fused silica using 3D laser microfabrication technique.
- Dr. Valdas Girdauskas has advised on the numerical simulation Computational Fluid Dynamics of supersonic jets and developed the experimental set-up of interferometric nozzle characterization.
- Dr. Isabel Gallardo González, Dr. Diego Guénot, Jonas Björklund Svensson, Anders Persson, Dr. Olle Lundh supported the LWFA experiments and X-ray measurement at Lund Laser Center.
- Lucas Rovige, Dr. Igor Andriyash have designed the One-Sided Shock nozzles and together with Dr. Julius Huijts, Dr. Aline Vernier, Marie Ouillé, Zhao Cheng, Rodrigo Lopez-Martens, Prof. Dr. Jérôme Faure supported the LWFA experimental work at LOA, Ecole Polytechnique ENSTA Paris.
- Dr. Kęstutis Regelskis and Dr. Gediminas Račiukaitis have supported in the discussions and preparation of the manuscript of the thesis.

2. LITERATURE REVIEW

2.1. High-Intensity Lasers

The laser intensity has grown revolutionary by more than 14 orders of magnitude over the past 50 years since the discovery of laser in 1960 (Fig. 1). The growth rate exceeded even the predictions of Moore's law stating that the number of transistors in dense integrated circuit doubles about every two years [1-3]. The peak power of lasers increased rapidly with the introduction of Q-switching and mode-locking allowing to shorten the pulse durations from the microsecond domain to the few-femtosecond regime. It enabled to reach maximum obtainable power around 1 GW and intensity of about 10^{14} W/cm^2. Further, the intensity was raised by 8 orders magnitude by the implementation of Chirped Pulse Amplification (CPA) technique and Optical Parametric Chirped Pulse Amplifiers (OPCPA) [4]. Starting from an intensity exceeding 10^{18} W/cm^2, the electromagnetic field produced by a laser allowed to accelerate electrons to relativistic energies.

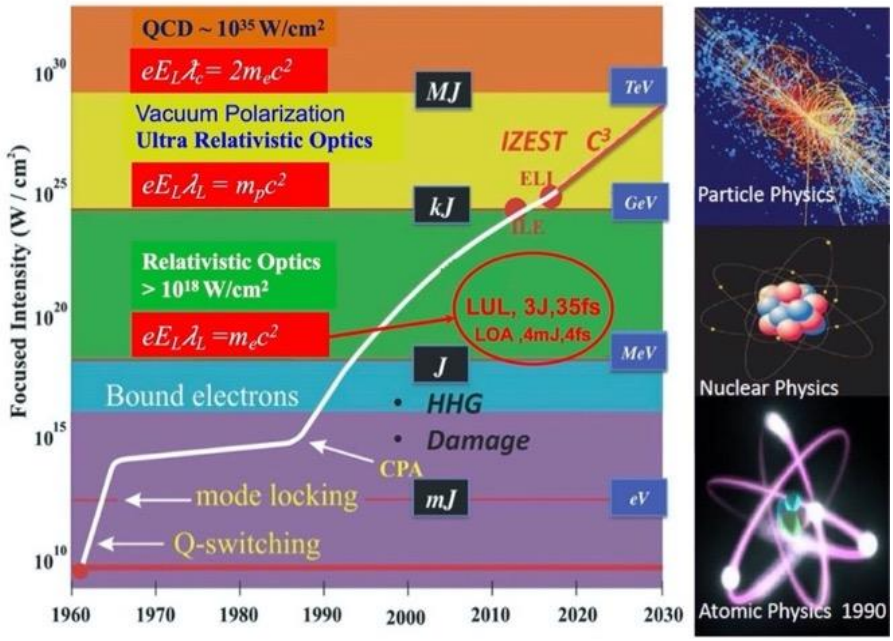

Figure 1. Moore's law of light [1,6]

The high-intensity laser can accelerate electrons and ions, generate coherent and incoherent X-ray or γ - radiation and produce ultra-short pulses at the attosecond scale. Laser-driven sources of ionizing radiation are used in medical imaging, ultrafast radiation biology, material science, and time-

resolved studies of high-resolution atomic physics [5]. New therapies implementing high-energy energy electrons, protons and heavier ions are developed. Laser-driven γ- and neutron sources are used for radiography, non-destructive detection and assay of nuclear materials as well as production and transmutation of radioisotopes.

Present systems deliver Petawatt peak power and focused intensity in the range of 10^{22} - 10^{23} W/cm^2. The lasers with intensities around 10^{25} W/cm^2 are planned to be launched at Extreme Light Infrastructure (ELI) in the near future [7]. At such extreme fields, the exotic physics such as radiation reaction (RR) effects, strong-field vacuum polarization and nonlinear Quantum Electrodynamics (QED) can be investigated. When an external electric field at the Schwinger limit is applied to the vacuum, the real electron-positron pairs can be produced. The electric field at Schwinger limit is $E_S = 1.3 \times 10^{18}$ V/m and requires laser intensities $I_S = 2.3 \times 10^{29}$ W/cm^2 hardly reachable with the help of nowadays technology. However, by using two counterpropagating circularly polarized laser beams, the QED effects are predicted to play a role already at the laser intensities of the order of 10^{24} W/cm^2 [3].

2.2. Sources of Ionizing Radiation

Depending on the available intensity, high-intensity lasers can drive a variety of secondary sources of ionizing radiation. At laser intensities of the order of 10^{14} W/cm^2, coherent XUV radiation in the energy range of tens and hundreds of electronvolt (eV), can be produced using High-Order Harmonics Generation (HHG) from gas targets [8]. At laser intensities on the order of 10^{16} W/cm^2, a short pulses of Kα-line subnanometer wavelength radiation from laser-solid target interaction can be generated [9,10]. It is not collimated, however, and the radiation has isotropic angular distribution. At the intensities above 10^{18} W/cm^2, LWFA can accelerate electrons to relativistic energies. Accelerated electrons enable the development of femtosecond X-ray and γ-sources [5].

X-ray radiation, discovered more than a century ago, traditionally was generated by an X-ray tube. It uses a high voltage to accelerate the electrons released by cathode to a high velocity, and hit a metal target, creating the X-rays. The maximum energy of the produced X-ray photons is limited by the energy of the incident electrons in the hundred keV range depending on the anode voltage of approximately 20-150 kV. The photons of higher energy were produced using γ- sources based on the emission of radioactive nuclei.

X-ray tube radiation consists from characteristic X-ray emission of electron transitions from the upper shells to the K-shell (called K_α, K_β lines),

and from Bremsstrahlung of electrons scattered by the strong electric field near the high-Z nuclei. The highest brightness of X-ray tube radiation is produced using Liquid-Metal-Jet-Anode X-ray tube Sources [11].

Medical linear accelerators accelerate monoenergetic electron beams to the energies between 5 and 30 MeV. The electrons can be used directly or collided at a target such as tungsten to produce γ-ray beam in 9-15 MeV range [12]. Modern X-rays sources are based on synchrotron radiation from electrons accelerated radially using bending magnets, undulators or wigglers. The highest brightness of X-ray radiation is achieved using Free Electron Lasers (FEL) [13]. The electron radiation in the field of bending magnet is continuous with characteristic critical wavelength λ_{cbend} defined as:

$$\lambda_{cbend} = \frac{4\pi m_e c}{3eB_{bend}\gamma^2}, \tag{1}$$

where γ is the Lorentz factor of the electron, e is the electron charge, c is the speed of light in vacuum, B_{bend} is the magnetic field of bending magnet. In practical units, the corresponding critical photon energy of synchrotron radiation in keV can be calculated using the relation:

$$W_{bend}\left[keV\right] \simeq \frac{3hB_{bend}\gamma^2}{4\pi m_e} \simeq 0.665 W_e^2\left[GeV\right]B\left[T\right], \tag{2}$$

where W_e is the electron energy in GeV.

The fundamental harmonics of undulator radiation is described by the relation:

$$\lambda_{ru} = \frac{\lambda_u}{2\gamma^2}\left(1+\frac{K_u^2}{2}+\gamma^2\theta_u^2\right) \simeq \frac{\lambda_u}{2\gamma^2}, \tag{3}$$

where λ_u is the spatial period of the undulator magnets, θ_u is the angle of undulator radiation relative to the electron beam axis, and K_u is the undulator strength parameter defined as:

$$K_u = \frac{eB_u\lambda_u}{2\pi m_e c} = 0.934 B_u[T]\lambda_u[cm], \tag{4}$$

where B_u is the magnetic field, and λ_u is the spatial period of the undulator magnets in cm. The photon energy of the fundamental harmonics of undulator radiation in keV W_{ru} can be estimated as:

$$W_{ru}\left[keV\right] \simeq \frac{2\gamma^2 hc}{e\lambda_u} \simeq \frac{0.95 W_e^2\left[GeV\right]}{\lambda_u\left[cm\right]}, \tag{5}$$

where W_e is the electron energy in GeV. For K~1, the oscillation amplitude of the motion is small, and the radiation is generated at specific undulator harmonics being multiple of λ_{ru}. If K>>1, the oscillation amplitude is bigger, and it leads to broad-spectrum wiggler radiation. Synchrotron X-ray sources have an average brightness of 10^{22}, and the peak brightness of FEL is around 10^{33} photons/s/mm^2/mrad^2/0.1%BW (0.1%BW means - 10^{-3} of bandwidth centred around the corresponding frequency). It exceeds many orders of magnitude the brightness of X-ray tubes being approximately of 10^7 ph/s/mm^2/mrad^2/0.1%BW. A synchrotron producing X-rays requires particle energies of a few GeV. X-ray FEL operates at the energy level of 8-17.5 GeV and produces X-rays up to 20 keV. Each GeV of energy requires approximately 100 m of acceleration length. It leads to the construction of large facilities with the cost of hundreds of millions of euros.

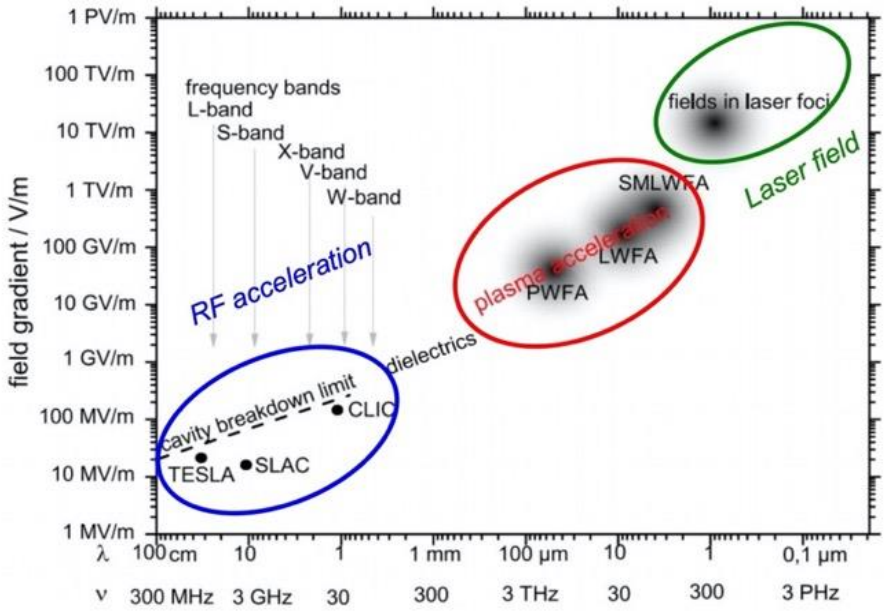

Figure 2. Moore's law of particle accelerators [14-16]

With the decreasing of the wavelength of accelerating electromagnetic waves, the electric field increases within the distance of one wave period (Fig. 2). However, the limiting factor of Radio Frequency (RF) accelerators is the ionization of the cavity material, causing the breakdown of resonators. A plasma can support arbitrarily high electric fields limited only by the critical plasma concentration allowing the propagation of a laser beam. The central wavelength of current high-power laser systems is typically in the range of 0.8-1.0 µm. Therefore, the maximal electric field is limited to E_{pmax} ~ 1 TV/m.

It exceeds by more than 3 orders of magnitude the highest field of RF-based cavities in the range of 200 - 400 MV. At the relativistic intensity of approximately 10^{18} W/cm^2, the laser electric field exceeds the electric field reached in plasma accelerators by one or two orders of magnitude. However, the electron interacting with homogenous electromagnetic laser field in a vacuum with no boundaries in the infinite region does not gain the energy [17]. To enable the Direct Laser Acceleration (DLA) of electrons, additional measures, such as the implementation of tight focusing, radially-polarized pulses [18] or use of magnetic $\vec{v}_e \times \vec{B}_L$ forces is required, where $\vec{v}_e$ is the electron velocity and $\vec{B}_L$ is the magnetic field of the laser [19-21]. The laser wakefield acceleration in electron plasma wave is a predominant mechanism currently used for the laser acceleration of charged particles like electrons, positrons and ions. Laser plasma accelerators driven by 100 TW to PW scale laser systems can produce electron beams in the energy range of 100 MeV - 1 GeV. The accelerated electrons are implemented for the generation of femtosecond X-ray beams via betatron, Inverse Compton Scattering (ICS), undulator or Bremsstrahlung radiation. Despite of remarkable progress in X-ray generation using RF methods, there is a need for compact light sources delivering femtosecond pulses of bright, high-energy X-ray and γ-ray radiation, emitted from a source size of the order of microns. LWFA allows substantial miniaturization of accelerators, reduced installation costs, and facilitates the access of universities, research institutions and industry to the advanced photon sources as well.

2.3. Laser Wakefield Acceleration

2.3.1. Definition of LWFA Parameters

The plasma waves are formed by propagating of high-intensity laser or energetic particle beam matched to the plasma parameters [22]. In the Gaussian electric field of the laser, electrons, undergoing oscillatory motion, experience non-linear ponderomotive force. It causes the particle to move towards the area of a weaker field strength of the inhomogeneous electric field. The net force during the period of electron motion in the weaker area does not offset the net force of the oscillation in the stronger field area. So, over a complete cycle, the particle moves towards the area of a lesser force. The sign of the charge of a particle does not change the direction of the force. The complex behaviour of the electron accelerated in the plasma field cannot be fully described analytically, and approximate models are based on the data

of numerical particle-in-cell (PIC) simulation and experimental results. Nevertheless, analytical relations can be successfully used to predict the experimental conditions of laser acceleration.

The motion of an electron in a light field can be described as [23,24]:

$$\frac{d\vec{p}_e}{dt} = m_e \frac{d\vec{v}_e}{dt} = -e\left[\vec{E}_L + \vec{v}_e \times \vec{B}_L\right], \tag{6}$$

where $\vec{p}_e$ is the electron momentum, *t - is* the time, m_e is the electron mass, and $\vec{E}_L$ is the electric field of the laser. In the non-relativistic case ($\vec{v}_e \ll c$, $B_{0L}=E_{0L}/c$, where E_{0L} and B_{0L} are the amplitudes of the laser electric and magnetic field), the $\vec{v}_e \times \vec{B}_L$ term can be neglected, and the relation reduces to $m_e\, d\vec{v}_e/dt = -e\vec{E}_L$. Assuming the electric field can be expressed as $\vec{E}_L = E_{0L}(\vec{r}_{0e})\cos(\omega_L t)$ and integrating $d\vec{v}_e/dt$ over time, the first order linear part of the electron velocity function of time will be: $\vec{v}_e = -\frac{e}{m_e\omega_L} E_{0L}(\vec{r}_0)\sin(\omega_L t)$, where ω_L is the cyclic frequency of the laser electric field, and r_0 is the radius vector of the electron. The first order linear part of the electron radius function of time will be $\vec{r}_e = -\frac{e}{m_e\omega_L^2} E_{0L}(\vec{r}_{0e})\cos(\omega_L t)$. The ponderomotive force of the electrons perceived in the laser electric field is proportional to the gradient of intensity I_L being proportional to the square of electric field $F_p \sim \nabla I_L \sim \nabla E_{L0}^2$. The linear and non-linear components of the electric field can be expressed as $\vec{E}_L = \vec{E}_L\big|_{\vec{r}_0} + \vec{r}_e \nabla \vec{E}_L\big|_{\vec{r}_0}$. The ponderomotive force can be described by the non-linear part of the electric field by averaging the electric field amplitude over the oscillation period $T_L = 2\pi/\omega_L$ and assuming $\left\langle \sin^2(\omega t)\right\rangle = 1/2$ as:

$$\vec{F}_p = -e\vec{r}_e \nabla \left\langle \vec{E}_L \right\rangle_{T_L} = -\frac{e^2}{4m_e\omega_L^2} \nabla \vec{E}_L^2 \tag{7}$$

The ponderomotive force can also be expressed by the gradient of ponderomotive potential ψ_p as $F_p = -\nabla_\perp \psi_p$. The ponderomotive force in the axial direction F_{pz} will be the partial derivative of ψ_p with the respect of normalized z coordinate ζ along the propagation axis $\zeta = z - v_g t$ as

$F_{pz} = -\partial_\zeta \psi_p$, where v_g is the laser group velocity. The ponderomotive potential ψ_p is actually equal to the mean kinetic energy of electrons W_{ekin}:

$$\psi_p = \frac{e^2}{4m_e\omega_L^2}\vec{E}_L^2 = \frac{1}{2}m_e\left\langle v_e\right\rangle_{T_L}^2 = \frac{1}{2}m\frac{1}{2}\left(\frac{eE_0}{m_e\omega_L}\right)^2 = W_{ekin}\,, \qquad (8)$$

where $\left\langle v_e\right\rangle_{T_L}^2$ is the electron velocity averaged over the oscillation period T_L. Every electron receives two pushes from the ponderomotive force in opposite directions, corresponding to the rising and falling edge of the laser pulse (Fig. 3a-c). The ponderomotive force leads to a longitudinal separation of charges in the z-direction, and the plasma wave structure travelling with the velocity v_φ can constantly accelerate the co-moving electrons.

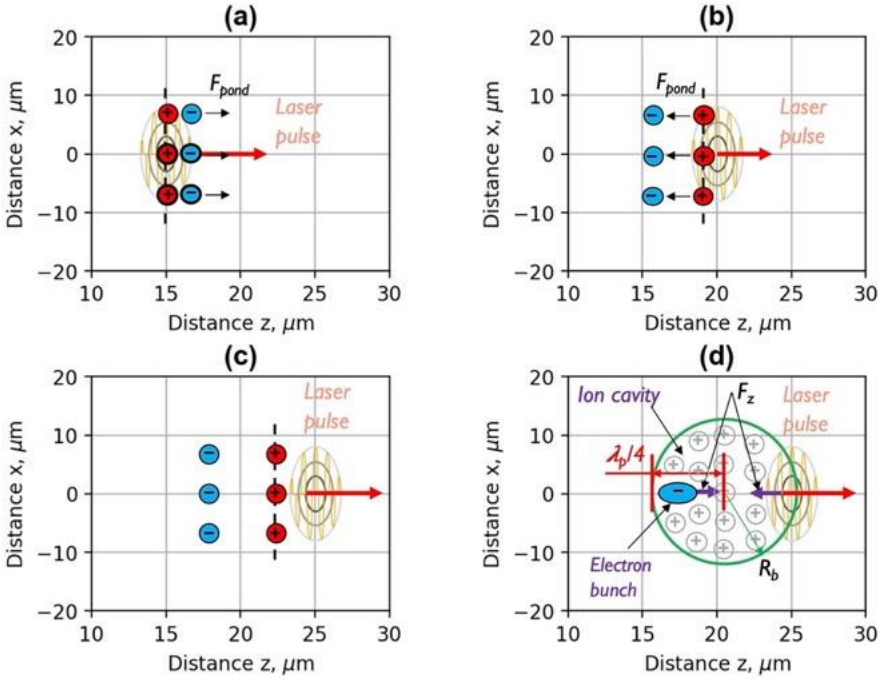

Figure 3. The images of ponderomotive force acting on oscillating electrons in Gaussian electric field of the laser **(a-c)**, electron acceleration in the plasma bubble **(d)** [23,25].

When the electron velocity v_e around the laser intensity of 10^{18} W/cm^2 becomes close to the light velocity in a vacuum $\vec{v}_e = e\vec{E}_L / m_e\omega_L \simeq c$, it is convenient to introduce the normalized laser vector potential or laser strength parameter a_0:

$$a_0 = \frac{eE_{0L}}{m_e c\omega_L} = \frac{\lambda_L eE_{0L}}{2\pi m_e c^2} \simeq 0.857\lambda_L[\mu m]\sqrt{I_{L18}\left[W/cm^2\right]}, \tag{9}$$

where λ_L is the laser wavelength in μm, and I_{L18} is the laser intensity in W/cm^2 relative to the 10^{18} W/cm^2.

Then, the Lorentz factor of the electron will be $\gamma = (1 + a_0^2)^{1/2}$, and the ponderomotive potential can be written as:

$$\psi_p = \frac{m_e c^2}{4} a_0^2 \quad , \tag{10}$$

In the relativistic case, the ponderomotive force in the axial direction can be expressed as:

$$F_{pz} \simeq \frac{\partial \psi_p}{\partial \zeta} = \frac{m_e c^2}{4\langle \gamma_\perp \rangle} \frac{\partial a_0^2}{\partial \zeta}, \tag{11}$$

where $\langle \gamma_\perp \rangle = \sqrt{1 + a_0^2/2}$ is a cycle averaged Lorentz factor of an electron in perpendicular direction. Assuming transverse ponderomotive force of the laser is roughly balanced by the force of the ion channel in the scale of the plasma wavelength λ_p, and the results of 3D particle-in-cell (PIC) simulations [26,27], the derivative of a_0^2 will be $\partial a_0^2 / \partial \zeta \simeq 2a_0^2 / k_p = 2a_0^2\, \omega_p / c$, where k_p is the wavenumber of the plasma wave. The maximal axial ponderomotive field can be calculated as:

$$E_{p\max} = \frac{m_e c^2}{4e\langle \gamma \rangle} \frac{\partial a_0^2}{\partial \zeta} \simeq \frac{m_e c\omega_p}{2e\langle \gamma \rangle} a_0^2 \simeq \frac{m_e c\omega_p \sqrt{a_0}}{e} \tag{12}$$

The plasma electric field can be written as $E_{p\max} = E_p \sqrt{a_0}$, where $E_p = m_e c\omega_p / e$ is the plasma electric field in the non-relativistic limit. E_p and plasma wavelength λ_{pe} in practical units can be calculated as:

$$E_p[V/m] = \frac{m_e c\omega_p}{e} = \frac{m_e c^2 2\pi}{e\lambda_p} \simeq 96\sqrt{n_{p18}[cm^{-3}]} \tag{13}$$

$$\lambda_p[\mu m] = 2\pi c\sqrt{\frac{m_e \varepsilon_0}{n_e e^2}} \simeq 3.34 / \sqrt{n_{p20}[cm^{-3}]}, \tag{14}$$

where λ_p is the plasma wavelength in μm, and n_{p18} and n_{p20} are the plasma concentrations in cm^{-3} relative to the 10^{18} cm^{-3} and 10^{20} cm^{-3}.

In a vacuum, a laser pulse undergoes Rayleigh diffraction, i.e., the laser spot size ω_s evolves according to $\omega_s = \omega_0 (1 + z^2/Z_R^2)^{1/2}$, where ω_0 is the laser

waist at the focal point $z = 0$ and $Z_R = \pi\omega_0^2/\lambda_L$ is the Rayleigh length. Without an additional guiding, the laser-plasma interaction distance is limited to a few Z_R. A laser pulse can be guided with a nearly constant spot size by a plasma channel that has a parabolic refraction index or plasma concentration profile. In such a profile, the maximum of refraction index and a minimum of the plasma concentration are on the axis of laser beam propagation. The index of refraction in plasma $n_r < 1$ and it can be expanded as [28,29]:

$$n_r \simeq 1 - \frac{\omega_p^2}{2\omega_L^2}\left(1 + \frac{\partial n_r}{n_{r0}} - \frac{a_0^2}{4} - 2\frac{\partial\omega_L}{\omega_L}\right), \tag{15}$$

where $n_{r0} = c/v_{ph} \simeq c(1-\omega_p^2/2\omega_L^2)$, v_{ph} is the laser phase velocity, $\partial n_r/n_{r0}$ is the refraction index change due to the plasma density depletion from the transverse ponderomotive force, and the term $a_0^2/4$ is due to relativistic mass corrections. The third term represents the modulation of the index of refraction due to the spectral bandwidth $\partial\omega_L/\omega_L$, and it is responsible for the group velocity dispersion (GVD). The change of the index of refraction from relativistic mass corrections can self-guide a laser beam. It this case, all electrons on the laser path are expelled by the ponderomotive force, leaving a three-dimensional bubble-shaped cavity behind. For the self-guided propagation of the laser beam, its spot size and intensity must be appropriately chosen. The requirements for a matched profile can be estimated from 3D PIC simulations assuming that the transverse ponderomotive force of the laser is roughly balanced by the force of the ion channel, which pulls back the ponderomotively expelled electrons $4a_0^2/k_p < \gamma_{\perp} > R_b \approx k_p R_b$ and substituting $< \gamma_{\perp} > \approx a_0$ [30]. Equating these two expressions yields to $k_p R_b = 2\sqrt{a_0}$, the optimal waist of the laser beam can be calculated as:

$$\omega_0 \simeq R_b = \lambda_p \sqrt{a_0}/\pi, \tag{16}$$

where R_b is the blowout radius [28]. The blowout radius has to be matched with the laser spot size ω_0, and for the pulse duration, the condition $c\tau_L < \omega_0$ has to be satisfied. Considering 3D PIC simulations, the laser power P_L required to guide the channel has to satisfy the condition $k_p R_b \approx 4$, and $P_L = a_0^2 P_{Lc}/8$. It yields to $a_0 \geq 4$. P_L and P_{Lc} can be calculated as [30] :

$$P_L[GW] = 21.5\left(a_0 R_B/\lambda_L\right)^2 \tag{17}$$

$$P_{Lc}[GW] = 17\left(\lambda_p/\lambda_L\right)^2 \tag{18}$$

Nonlinear terms of $\gamma = (1 + a_0^2)^{1/2}$ prevent catastrophic self-focusing when $P_L > P_{Lc}$. Based on the experimental observations, a_0 has to be greater than $a_{0c} \approx (\lambda_L/\lambda_p)^{2/5}$.

For designing of LWFA in the blowout regime, first, the value of $a_0 > a_{0c}$ for a given laser energy E_L and wavelength λ_L is defined. Knowing the value of a_0, the pulse duration τ_L and the pulse waist ω_0 are calculated. Then, using the equations (14) and (16), the optimal plasma wavelength and plasma concentration are defined [29].

The n_r expression (15) comprises only the linear terms and it is valid in the weakly relativistic regime, in tenuous plasmas $\omega_p/\omega_L << 1$, and for long enough pulses with the envelope $\omega_L \tau_L >> 1$. It helps, however, to understand relativistic self-focusing [31], self-modulation [32], or self-compression [33] occurring during the LWFA process using ultra-short few-cycle pulses [29]. The term $\partial n_r/n_{r0}$ is responsible for the frequency decrease in the regions where the refractive index gradient is negative. This results in the asymmetric broadening of the spectrum. The term $a_0^2/4$ is responsible for relativistic self-phase modulation (SPM), which causes the front of the pulse to be red-shifted and rear of the pulse - blue-shifted. This effect causes a symmetric broadening of the spectrum. Spectral broadening originates from the changes of the index of refraction: $\partial\omega_L/\omega_L \sim \partial n_r/\partial\zeta$. The varying group velocity along the plasma wave cause the self-compression of the pulse, which can reach durations shorter than the initial transform limit [34]. For pulse durations longer than 30 fs, $\delta\omega_L/\omega_L < 0.1$, and dispersion can be neglected. For the few-cycle laser pulses ~5 fs, the $\delta\omega_L/\omega_L \sim 0.25$, and the local n_r change, SPM, and dispersion have a considerable impact on the laser propagation.

In relativistic cases, in the motion of an electron in a light field (6) also the term $\vec{v}_e \times \vec{B}$ contributing to the axial direct laser acceleration has to be taken into account.

2.3.2. Injection Mechanisms

The plasma environment used for acceleration of electrons is created by the ionizing of the gas in gas jets, gas cells or discharge capillaries. Except of the discharge capillaries, where the plasma channel is formed by the high-voltage discharge current, the gas is ionized by the electric field of high-intensity laser pulse itself suppressing the atomic Coulomb field of the atoms. Before the electric field reaches the ionization threshold, the electrons can also be ionized by tunnelling ionization [35]. The laser wake creates an electrical field structure trailing the laser pulse almost at the same speed. The electrons

oscillating in the laser field are not accelerated, they are only moving around the rest positions. The plasma wakefield has to trap the electrons from the plasma background, or external electrons have to be injected into the bubble cavity. There are several schemes used for the injection of electrons.

In the wave-breaking self-injection scheme [36], an initial momentum is required for the electron to be trapped by a plasma wave. The threshold momentum required for the trapping decreases for larger plasma wave amplitude and lower plasma wave phase velocity. As the driver propagates into the plasma, more charge will be trapped until the amplitude of the plasma wave is substantially reduced due to beam loading. Wave-breaking injection is possible when the axial electric field E_{pmax} exceeds the wave-breaking limit E_{WB}, and the oscillation amplitude of electrons exceeds the plasma wavelength. The wave-breaking limit of the laser electric field E_{WB} for the phase velocity of the plasma wave v_ϕ close to the laser group velocity v_g ($v_\phi \approx v_g \approx c$), can be calculated as follows:

$$E_{WB} = \sqrt{2\left(\gamma_p - 1\right)} E_p \ , \tag{19}$$

where $\gamma_p = 1/\sqrt{1 - v_\phi^2 / c^2} \simeq \lambda_p / \lambda_L$ is the relativistic correction factor of the plasma wave. Comparing the relations of E_p and E_{WB}, the injection will start at a_0>2.1 For 30 fs laser pulses and laser wavelength of 1 μm, the relativistic plasma wave correction factor γ_p increases the E_{WB} relative to E_p approximately by a factor of 7. The control the charge of self-injected electrons is difficult, and the energy dispersion of accelerated electrons is high.

To increase the injection stability and to achieve more mono-energetic electron beams, different approaches of injection as density down-ramp triggered [37-44] injection, injection by colliding beams [45-47], ionization-assisted [48-51] or self-truncated electron injection (STII) [52-57] are developed.

In the down-ramp density triggered injection case, the formation of tailored plasma profiles by using two or more stages of nozzles [58-60], insertion of wire [43], razor blade [61] or capillary jet [39] into the nozzle jet causing shock waves is implemented. In the down-ramp density gradient scheme (Fig. 4a) [43], a negative plasma concentration gradient along the laser propagation direction $dn_p/dz < 0$ leads to an elongation of the plasma period. It increases due to the elongation of the plasma period $\lambda_p \sim \sqrt{1/n_p}$, and the increase of the laser group velocity satisfying the relation $v_{ph} v_g = c^2$:

$$v_g = c\sqrt{1-\omega_p^2/\omega_L^2} \simeq c(1-\omega_p^2/2\omega_L^2) \tag{20}$$

Both effects facilitate the injection of electrons. A particular case of the down-ramp density injection is a downward shock front in a supersonic jet providing a sudden step in the plasma density. The injected electron is trapped by the wake wave if its momentum $\vec{p}_e$, exceeds the threshold momentum of the electron inside of the plasma bubble. In the down-ramp density gradient scheme, the electrons are injected when the maximum momentum of electrons in the plasma region with higher concentration becomes larger than the minimum momentum of the electron inside of the plasma bubble in the second part of the plasma region with lower concentration.

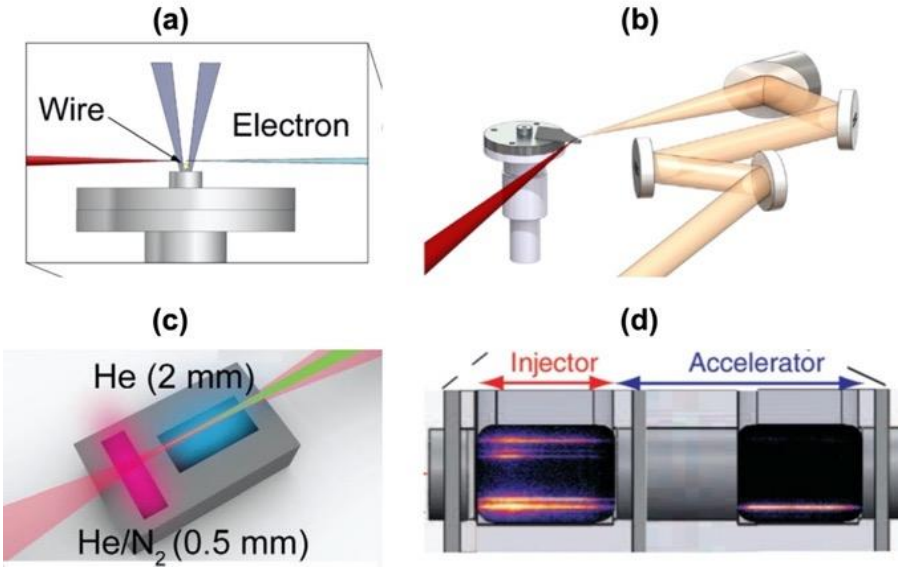

Figure 4. Images of electron injection using a shock wave by insertion of wire [43] **(a)**, colliding beam injection [47] **(b)**, and images of ionization injection using two nozzles [51] **(c)**, and double gas cell [50] **(d)**.

The phase velocity of wake wave $v_\phi = \omega_p/k_p$ decreases in accordance with the relationship $k_p = k_{p0} - t\partial\omega_p/\partial z$. When plasma wave number k_p becomes large enough to satisfy the condition when electron velocity $v_e = v_\phi$, the wave breaks. The wave-breaking condition for Lorentz factor of an electron can be described as [44]:

$$\gamma \geq \frac{\beta_\phi \tau_\phi + 1}{\sqrt{\left(\beta_\phi \tau_\phi + 1\right)^2 - \beta_\phi^2}} \ , \tag{21}$$

where $\beta_\phi = c/v_\phi$ is the dimensionless phase velocity of the plasma wake wave, $\tau_\phi = ct\Delta\omega_p/(\omega_p L_{dr})$ is the dimensionless plasma inhomogeneity parameter, L_{dr} is the length of plasma concentration down-ramp, and $\Delta\omega_p$ is the absolute change of the local plasma frequency in the region of plasma concentration down-ramp.

In the colliding beam injection scheme (Fig. 4b) [47], a second, counter-propagating injection pulse with the smaller laser strength parameter a_0 collides with the drive laser pulse at a certain position determined by the relative timing. When two pulses collide, they form a standing wave with the spatial scale of $\lambda_L/2$. The resulting ponderomotive force is governed by the laser wavelength instead of the pulse length as in a propagating pulse. It facilitates the pre-acceleration of electrons from the background plasma leading to trapping and injection. The collision point inside a plasma stretch defines the injection position and allows to tune the electron beam energy.

In the ionization injection scheme (Fig. 4cd), a small amount of heavier gas atoms, for example N_2, is mixed into the light gases, such as H_2 and He using two nozzles [51,62] or double gas cell [50]. Typically, the light gases and electrons from nitrogen L-shell (N^{1+} - N^{5+}) are ionized already by the pedestal of the laser pulse. The laser propagates through a fully ionized plasma, the electrons of which are all expelled by the ponderomotive potential. No trapping from the background plasma is possible. An additional ionization of N_2 of K- shell electrons takes place close to the peak of the laser pulse, within the trapping zone of accelerating field. In a homogeneous mixed-gas plasma, the ionization injection occurs over a long injection distance, thus resulting in large energy spread.

In the Self-Truncated ionization injection scheme, the ionization method is modified [57]. It helps to solve the problem of the large energy spread. The duration of electron injection into the wakefield is restricted by a small mismatch between the laser spot size and the plasma cavity radius. Electrons available for injection can be easily tuned with the concentration of high-Z gas doping. It allows loading a reasonably high charge of ~ 100 pC with low energy spread into a wakefield. Additionally, a combination of geometric and relativistic self-focusing can increase the load up to the nanocoulomb range [54].

Nevertheless, additional work is required to research novel injection methods of electrons in to the LWFA aiming to increase the energy and charge of accelerated electrons, as well as lower energy dispersion of the electron beams.

2.3.3. Acceleration Scaling Laws

Laser plasma wake acceleration in the blowout regime requires laser intensity of a_0>2-4, the laser waist ω_0 and longitudinal pulse length $c\tau_L$ dimensions have to be close to the half of the plasma wavelength $\lambda_p/2$. In this regime, the laser-plasma interaction distance exceeds the range of laser defocusing limited to a few Rayleigh distances Z_R. However, as the laser propagates through the plasma, the energy of the laser field is transferred to the wakefield. The acceleration distance and maximal energy of electrons are limited by the energy depletion and dephasing effects of the laser pulse.

The energy from the front of the laser pulse is transferred to the plasma wave. It etches the front of the pulse and creates a red shifting of the laser light. This pulse erosion occurs at velocity v_{etch} and causes the pulse to be fully etched after a distance $L_{etch} = v_{etch}\, c\tau_L$. v_{etch} can be calculated as [34]:

$$v_{etch} = c\omega_p^2 / \omega_L^2 \tag{22}$$

The etching of the pulse front causes an effective decrease of the laser pulse group velocity v_g, and decrease of the wakefield phase velocity v_ϕ. The effective electron acceleration is limited by the dephasing of the phase velocity of laser wakefield defined as the difference between the laser group and front etching velocity. The wakefield phase velocity v_ϕ and the dephasing length L_d over the bubble radius can be calculated as:

$$v_\phi = v_g - v_{etch} \simeq c(1 - 3\omega_p^2 / 2\omega_L^2) \tag{23}$$

$$L_d = \frac{c}{c - v_\phi} R_b = \frac{2\omega_L^2}{3\omega_p^2} R_b \simeq \frac{2\sqrt{a_0}}{3\pi} \frac{\lambda_p^3}{\lambda_L^2} \tag{24}$$

The pump depletion length L_{pd} can be estimated by equating the laser pulse energy to the energy left behind in the wakefield, $E_{pz}^2 L_{pd} = E_L^2 \lambda_p/2$ [63].

$$L_{pd} = \frac{\lambda_p^2}{\lambda_L^2} c\tau_L \tag{25}$$

The wakefield excitation and electron acceleration are optimal when longitudinal pulse length is:

$$c\tau_L \simeq 2R_b/3 = 2\sqrt{a_0}\lambda_p / 3\pi \tag{26}$$

It corresponds to the situation where the dephasing length L_d equals to the pump depletion length L_{pd}. When both transverse and longitudinal boundary conditions are met, the wakefield maximum amplitude is $E_{p\max} = E_p\sqrt{a_0}$. The maximum reachable energy is achieved when electrons are accelerated

within the dephasing length L_d. Assuming the wakefield is linear, and the average accelerating field is half of the E_{pmax}., the maximum energy of accelerated electrons can be estimated as:

$$W_e \simeq e\frac{E_{p\max}}{2}L_d = \frac{2m_e c^2 a_0}{3}\frac{\lambda_p^2}{\lambda_L^2} \tag{27}$$

$$W_e\left[GeV\right] = 1.7\left(\frac{P_L\left[TW\right]}{100}\right)^{1/3}\left(\frac{10^{18}}{n_p\left[cm^{-3}\right]}\right)^{2/3}\left(\frac{0.8}{\lambda_L\left[\mu m\right]}\right)^{4/3} \tag{28}$$

The maximal acceleration distance and maximal energy of electrons can be increased by using external guiding of the laser by creating a parabolic plasma concentration profile in the discharge capillary (Fig. 5a) [64-67], laser pulse front tilting [68,69], the formation of the flying focus [70,71] or by the longer focal depth and spatio-temporal shaping of the laser beam [72-74] (Fig. 5b). The acceleration distance can be tuned by changing of the chirp of accelerating laser beam [59], focusing of the electron beam [75,76], combining LWFA and Plasma Wakefield Acceleration (PBWA) [77-79] as well as complex adaptive control [80,81]. Using Petawatt laser guiding in laser-heated capillary allowed to reach the electron energies up to 8 GeV [82].

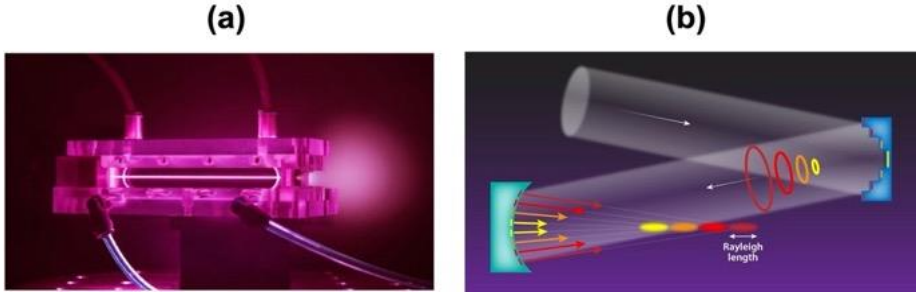

Figure 5. Images of external guiding of the laser beam by discharge capillary [83] **(a)**, and spatio-temporal shaping [74] **(b)**.

For the lasers with extremely short pulses available at kHz repetition rate, additional acceleration limits have to be considered. The few-cycle laser pulses use an ultra-broad spectral bandwidth, spanning over an entire octave, starting at 500 nm and reaching 1 μm wavelengths. Therefore, the negative dispersion introduced by the plasma cannot be neglected during propagation [34]. In the linear limit, the pulse duration τ_{Lz} in the plasma evolves as:

$$\tau_{Lz}(z) = \tau_L\sqrt{1 + z^2/L_{disp}^2}\ , \tag{29}$$

where τ_L is the Fourier transform-limited duration, and L_{disp} is the dispersion length scale in the plasma. The dispersion length approximately can be calculated as:

$$L_{disp} = 4\pi c^2 \tau_L^2 \frac{\lambda_p^2}{\lambda_L^3} \tag{30}$$

This is not strictly valid for few-cycle laser pulses. The dispersion length of a 5-fs transform-limited pulse for λ_L=0.8 μm in a homogeneous plasma electronic density 9×10^{19} cm^{-3} is 110 μm and for 3.8 fs and 2×10^{20} cm^{-3} drops to 20 μm [29,34]. The GVD increases and the dispersion length is shorter for shorter laser pulse duration, lower plasma density, and for longer laser wavelengths: $L_{disp} \sim \lambda_L^{-3}$. This causes a rapid stretching of the single-cycle laser pulse. Therefore, in experiments, the compensation of plasma dispersion by adding a small positive chirp to the laser pulse is introduced.

As the laser pulse is nearly composed of a single light cycle, the Carrier envelope phase (CEP) is expected to have an effect on injection and acceleration. Most of the trapped electrons have been ionized by the most intense cycle. The absolute CEP is no longer conserved because the laser group velocity v_g is different from the phase velocity v_{ph}. The phase slippage length $L_{2\pi}$ defined as the propagation length needed to dephase the CEP by 2π can be calculated as [34]:

$$L_{2\pi} = \lambda_L \frac{c}{v_{ph} - v_g} \simeq \frac{\lambda_p^2}{\lambda_L} \tag{31}$$

The phase slippage length $L_{2\pi}$ for the plasma concentration 1.5×10^{20} cm^{-3} and λ_L=0.8 μm is 100 μm.

In Table 1, the scaling parameters for different laser classes with powers from multi-Joule, Petawatt lasers to millijoule, Terawatt systems are presented. It shows that mJ-lasers are sufficient to reach the blowout regime if extremely short laser pulses for LWFA (~ 5 fs) are used.

Table 1. Scaling laws for laser-plasma accelerators in the blowout regime for the laser wavelength λ_L=0.8 μm [29].

P_L	a_0	W_L,J	τ_L,fs	ω_0,μm	Z_R,mm	n_p,cm^{-3}	L_d,mm	W_e,MeV
0.5PW	4.8	30	60	26	2.6	10^{17}	45	4200
30TW	3.5	1	25	10	0.4	10^{18}	2.8	500
1TW	2	0.004	5	2.1	0.018	10^{20}	0.025	10

The laser energy W_L required for the LWFA in the blowout regime scales as $W_L \sim \tau_L^3 \sim \lambda_p^3$, and the gained energy of accelerated electrons as $W_e \sim \tau_L^2 \sim \lambda_p^2$.

2.4. Laser Ion Acceleration

The recent development of laser technology with the energy of ten of joules enabled the generation of Petawatt pulses with intensities exceeding 10^{21} W/cm^2. New facilities that will produce femtosecond pulses of ultra-relativistic intensities ~ 10^{23}-10^{24} W/cm^2 [84] are being built in Europe. The interaction of such intense laser pulses with a dense target can accelerate protons and heavier ions. Ion beams are of great interest in nuclear fusion, medicine and high-energy-density physics. Proton and ion beam therapy for cancer has proven to be successful because of a localized dose deposition in the region of Bragg peak and protection of healthy tissues [85]. Due to the particle mass, proton velocity could reach relativistic energies at the laser intensities of the order of 10^{24} W/cm^2.

Even if such lasers will be available, the electron shielding would prohibit ions from the direct laser acceleration. The laser energy first has to be coupled with electrons and then, transferred to the ions.

The basic mechanisms of ion acceleration are Target Normal Sheath Acceleration (TNSA) [86], Coulomb Explosion (CE) [87], Radiation Pressure Acceleration (RPA) [88], and Magnetic Vortex Acceleration (MVA) [89]. In the experiments, also combinations of basic mechanisms, such as Shock Wave Acceleration (SWA) [90], Break-Out-Afterburner (BOA) [91], Relativistic Transparency (RT) [92,93] are used. All these mechanisms can be parametrized in terms of two dimensionless parameters: $\alpha_0 = a_0 / \varepsilon_p$ relativistic transparency parameter and $\delta_a = d_p \sqrt{a_0} / \lambda\!\!\!^{-}_L$ - target thickness parameter, approximately equal to the collisionless skin-depth divided over the reduced laser wavelength. ε_p and δ_a are described as [94]:

$$\varepsilon_p = \pi \frac{n_p l_t}{n_{cL} \lambda_L} = \pi \frac{\lambda_L l_t}{\lambda_p^2} \tag{32}$$

$$\delta_a = \frac{d_p}{\lambda\!\!\!^{-}_L} \sqrt{a_0} \simeq \frac{\lambda_p}{\lambda_L} \sqrt{a_0} \ , \tag{33}$$

where l_t is the target thickness, n_c is the critical plasma concentration for the laser wavelength, $\lambda\!\!\!^{-}_L = c/\omega_L$ and $d_p = c/\omega_p$. At $a_0 = \varepsilon_p$, defined as normalized surface density, the plasma becomes transparent.

In Fig. 6, the region (I) corresponds to overdense opaque and the region (II) - to the transparent plasma. In region (I), the ions are accelerated in the TNSA regime. The laser radiation is absorbed by electrons in the skin depth of the target. If the target is relatively thin (less than tens of microns), hot electrons can leave the rear side of the target, forming a sheath with electric charge separation. Electric field pulls and accelerates ions in the direction normal to the rear surface.

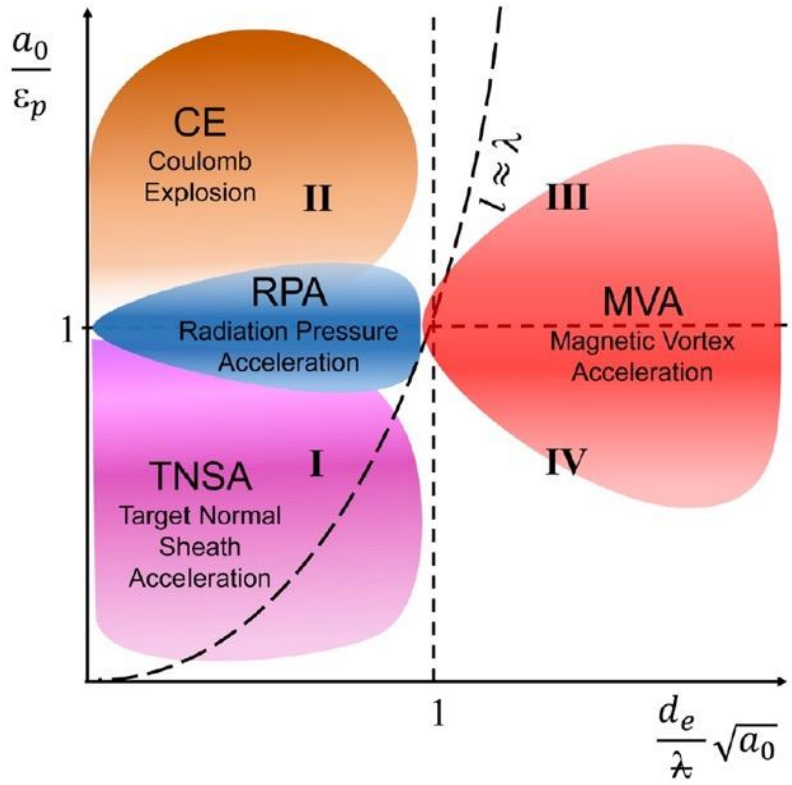

Figure 6. Different regions of Laser ion acceleration regimes: TNSA (Target Normal Sheath Acceleration), Coulomb explosion, Radiation Pressure Acceleration (RPA), and Magnetic Vortex Acceleration (MVA) [94].

The electron spectrum is broadly spread, however, some fraction of these electrons run away from ions and the rest of them are pulled back toward ions. In the Breakout Afterburner (BOA) phase, the plasma turns to classically underdense because of the increase of relativistic mass of electrons, and the

laser can propagate through the plasma. This results in an enhanced longitudinal electric field compared to the earlier stages of the interaction, that co-propagate with the ions. The ions are accelerated as a bunch to high energies.

Most of the laser ion acceleration experimental results were obtained in the TNSA regime. The TNSA mechanism is effective in accelerating of light ions, primarily protons. In the TNSA regime, protons with the maximum energy around 70 MeV were achieved [94]. The maximum proton energy is proportional to the normalized laser vector potential $\sim a_0 \sim \lambda_L I_L^{1/2}$ [95]. In region (II), the laser radiation is so intense that it blows out almost all electrons from the target and the Coulomb explosion occurs.

At laser intensities above 10^{21} W/cm^2, RPA starts to dominate over TNSA. Scaling laws of RPA predict a much more favourable gain of the ion energy $W_i \sim I_L^2$ relative to the TNSA regime. TNSA contribution to ion acceleration can be reduced by using circular light polarization of a beam. In the absence of an oscillating component in the $\vec{v}_e \times \vec{B}$ force, electron heating is strongly suppressed. All particle species are accelerated to the same velocity, which results in a monochromatic spectrum. At the transparency threshold, in the vicinity of $a_0 = \varepsilon_p$, line, the conditions for ion acceleration in the RPA regime are realized. The RPA mechanism can be divided into two regimes. In case of thicker targets of the order of micrometers, the light pressure accelerates ions in Hole-Boring or SWA regime. When the target becomes sufficiently thin, and the hole boring front reaches the target rear, the so-called Light Sailing phase begins. In this case, the thickness becomes comparable to or less than the skin depth. The target is accelerated as a whole by the incoming radiation pressure. The ion acceleration mechanisms in Fig. 6, are most efficient when $\delta_a < 1$ and below 10^{23}W/cm^2 when the radiation reaction is insignificant. The energy of ions W_{LS} gained in Light Sailing regime can be estimated as [96]:

$$W_{LS} = \frac{m_i V_i^2}{2} = 2 m_e c^2 \left(\frac{m_e}{m_p} \right) \left(\frac{Z}{A} \frac{\lambda_L^2}{\lambda_p^2} \frac{c\tau_L}{l_t} a_0^2 \right)^2 \sim I_L^2 \quad , \tag{34}$$

where m_i is ion mass, V_i ion velocity, m_p proton mass, Z ion charge number, and A is atomic mass number. For the optimal Light Sailing, thickness condition requires $a_0 = 1$, and $a_0 = \varepsilon_p$. Substituting l_t from (12), the energy of ions W_{LSopt} can be estimated as:

$$W_{LSopt} = 2\pi^2 m_e c^2 \left(\frac{m_e}{m_p} \right) \left(\frac{Z}{A} \frac{c\tau_L}{\lambda_L} a_0 \right)^2 \tag{35}$$

For solid densities, the target thickness for Light Sailing regime has to be equal to $l_t \sim \lambda_L/100$ or ~ 10 nm. Such ultrathin foils can be produced by diamond-like carbon foil technology [97]. Alternatively, more diluted target, such as dense gas at 500-1000 bar of pressure or Carbon Nanotube Foam (CNF) can be used. Using a 9.2 J laser with circular polarization at 6×10^{20} W/cm^2 intensity and $a_0 \approx 16$, RPA mechanism allowed to reach 93 MeV energy of protons from 15 nm DLC targets [98] and 48 MeV/u energy of C^{6+} ions per nucleon from double 80 μm CNF and 20 nm Diamond-like carbon (DLC) targets [99].

In regions (III) and (IV), in Fig. 6, where $\delta_a > 1$, the plasma is underdense. For an ultrashort laser pulse at the border, between domains (III) and (IV), the plasma target thickness l_t is approximately equal to the energy depletion length, corresponding to the $a_0 = \varepsilon_p$. In this region, the laser pulse deposits almost all its energy in the plasma producing a large number of fast electrons in the vicinity of the target rear surface. This results in quasi-static magnetic field generation of MVA regime.

In the dissertation work, the laser with the intensities of 2×10^{18} - 3×10^{19} W/cm^2 corresponding to a_0 between 2 and 4 were used. The target thickness l_t was ~ 10^2- $10^3\times\lambda_L$ and $\lambda_p >> \lambda_L$ corresponding to $\alpha_0 << 1$. At these conditions, ions can be considered motionless, and further, the acceleration of ions will not be discussed. However, the technology of structured plasma targets, presented in the work, can be of great interest for the formation of high-density gas jets for ion acceleration by laser systems with kHz repetition rate [100]. All solid and foam targets are destroyed at the interaction with a laser pulse and mechanical change of the targets at kHz rate is challenging. For such systems, a permanent supply of cryogenic fluids or high-density gases is necessary.

2.5. LWFA-Driven Sources of Secondary Radiation

In this work, the LWFA sources of betatron X-ray radiation of electrons oscillating in an ion channel are investigated. The other main types of LWFA-driven X-ray and γ-ray sources are the undulator radiation, Inverse Compton Scattering (ICS), and Bremsstrahlung radiation. These sources are compact and deliver collimated femtosecond coherent and incoherent radiation [5,25]. The main radiation mechanism is based on the emission from accelerated relativistic electrons. The type of moving charge synchrotron radiation depends on the electron trajectories and timing. The intensity of synchrotron radiation scales as $\sim N_e$ for bending magnet, $\sim N_e \times N_{poles}$ for wiggler, $\sim N_e \times$

N_{poles}^2 for undulator, and ~ $N_e^2 \times N_{poles}^2$ for FEL, where N_e is the number of electrons and N_{poles} is the number of magnetic poles accelerating electron [5].

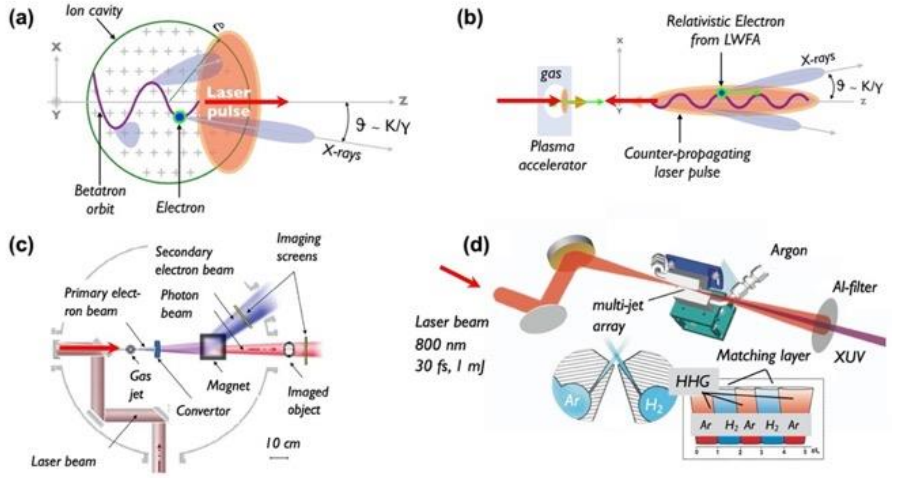

Figure 7. Images of betatron X-ray radiation of electrons oscillating in an ion channel **(a)**, secondary X-ray radiation of Inverse Compton scattering **(b)** [25]**,** γ-ray radiation of Bremsstrahlung using high-Z converter [101] **(c)**, and High Harmonic Generation using a quasi-phase-matching gas array [102] **(d)**.

In the case of betatron radiation, electrons simultaneous to the laser wakefield acceleration undergo transverse oscillations in the ion channel along the longitudinal axis of the plasma wave (Fig.7a). This motion of relativistic electrons, called betatron oscillations, produces a synchrotron, collimated radiation of broadband X-rays. In the blowout regime, the equation of motion for an electron can be described by simplified expressions assuming a spherical ion cavity. The cyclic frequency of the electron oscillation is expressed as $\omega_\beta = \omega_p / \sqrt{2\gamma}$, where ω_p is the cyclic frequency of the plasma, and γ is the Lorentz factor of accelerated electrons. The ion cavity acts as a wiggler with a period ω_p and betatron undulator strength parameter K_β, which depends on the initial conditions of an electrons upon injection into the cavity, electron energy and betatron oscillation radius r_β. The wavelength of the betatron oscillation λ_β in microns can be estimated as [103]:

$$\lambda_\beta[\mu m] = \lambda_p \sqrt{2\gamma} = 4.72\sqrt{\gamma / n_{p20}\left[cm^{-3}\right]} \ , \qquad (36)$$

where n_{p20} is plasma concentration in cm^{-3} relative to the 10^{20} cm^{-3}. The fundamental wavelength of the betatron radiation $\lambda_{r\beta}$ in nanometers can be calculated as:

$$\lambda_{r\beta}[nm] = \lambda_\beta / 2\gamma^2 = \lambda_p \Big/ \sqrt{2\gamma^3} = 2.36\times10^3 \Big/ \sqrt{\gamma^3 n_{p20}\left[cm^{-3}\right]} \quad (37)$$

The betatron undulator strength parameter K_β can be estimated using the relation:

$$K_\beta = \gamma k_\beta r_\beta = 1.33\sqrt{\gamma n_{p20}[\mathrm{cm}^{-3}]}\, r_\beta[\mu\mathrm{m}], \quad (38)$$

where $k_\beta = 2\pi/\lambda_\beta$ is the electron oscillation wave vector, r_β is the radius of electron oscillations in μm. The K_β is typically in the range of 10-20, meaning the electrons are oscillating in the wiggler regime. For $K_\beta >> 1$, the critical energy of betatron radiation $W_{c\beta}$ in practical units can be defined using the relation:

$$W_{c\beta}[\mathrm{keV}] = \frac{\hbar\omega_{c\beta}}{e} = \frac{3\gamma^3\hbar c k_\beta^2 r_\beta}{2e} = 5.24\times10^{-4}\gamma^2 n_{p20}[\mathrm{cm}^{-3}] r_\beta[\mu\mathrm{m}], \quad (39)$$

where $\omega_{c\beta}$ is the cyclic critical frequency of betatron oscillations. The total energy of synchrotron radiation $W_{r\beta tot}$ emitted by electron per unit of the photon energy $dW_{r\beta}$ and unit of solid angle $d\Omega$ in the direction of the laser radiation at $\theta = 0$ at the critical energy $W_{c\beta}$, can be calculated using the following expression [103]:

$$\left.\frac{d^2 W_{r\beta tot}}{dW_{r\beta} d\Omega}\right|_{\theta=0} = N_\beta \frac{3e^2}{2\pi^3\hbar\varepsilon_0 c}\gamma^2 \left(\frac{W_{r\beta}}{W_{c\beta}}\right)^2 K_{2/3}^2\left(\frac{W_{r\beta}}{W_{c\beta}}\right), \quad (40)$$

where $W_{r\beta}$ is the photon energy of synchrotron radiation, N_β is the total number of oscillations of one electron in the betatron ion channel, $\hbar$ is the reduced Planck constant, and $K_{2/3}$ is the modified Bessel function of the second kind.

In the experimental works, for laser energies 1-10 J and pulse durations less than 100 fs, betatron spectra peaked between 1 and 150 keV from 20 MeV to 2 GeV electron beams have been reported [104-106]. The oscillation radii were in the range of 0.5-5 μm. There have been demonstrations of the production of synchrotron radiation from laser-accelerated electrons in conventional undulators. Laser-produced electron bunches between 55 and 75 MeV were injected into a 1 m-long undulator having a period λ_u = 2 cm and an undulator strength parameter K=0.6. The obtained synchrotron radiation was in the visible and infrared part of the spectrum (700-1000 nm) and estimated a peak spectral brightness of photons was 2.8×10^5 [107]. The photon energy of radiation was limited by the size of the undulator period and energy of electrons available. The concept of operation is of significant

interest for the development of a compact free-electron laser based on a laser-plasma accelerator.

In the Inverse Compton Scattering (ICS) process, the relativistic electron is scattered by a laser photon whereby the energy of an electron is upshifted (Fig. 7b) [25]. In the rest frame, electron sees the Doppler upshifted electromagnetic field from the laser and scatters the light in a classic dipole radiation pattern. A second upshift occurs while returning to the lab frame. If the scattering laser vector potential is such that $a_0 \ll 1$, Compton scattering emission is mostly at the fundamental λ_{ICS} and in the case of a head-on collision (φ=180°), can be calculated as:

$$\lambda_{ICS} = \frac{1+\gamma^2\theta^2 + a_0^2/2}{2\gamma^2(1-\cos\phi)}\lambda_L \simeq \frac{\lambda_L}{4\gamma^2} \tag{41}$$

It corresponds to the undulator radiation with the undulator period $\lambda_u = \lambda_L/2$ and strength parameter $K_{ICS} \simeq a_0 = 0.855\sqrt{I_L\left[10^{18}\,W/cm^2\right]\lambda_L^2\left[\mu m\right]}$. The ICS photon energy in keV in practical units can be expressed as [25]:

$$W_{ICS}\left[keV\right] \simeq \frac{4\gamma^2 hc}{e\lambda_L} \simeq \frac{0.019 W_e^2\left[MeV\right]}{\lambda_L\left[\mu m\right]} \tag{42}$$

The Compton scattering cross-section is very small ($\sigma_{compt} = 6.65 \times 10^{-25}$ cm^{-2}). Therefore, a high density of electrons and photons and high-quality beams at the interaction point are required. In the ICS experiments, tuneable (5-42 keV), quasi-monochromatic X-ray beam from a modest laser system 60 TW with low divergence was reported. 300 MeV electrons accelerated by a 1.9 J 35 fs laser, produced X-ray radiation between 100 keV and 1 MeV [108], as well as 9-15 MeV gamma-rays (3×10^5 photons/shot) using a scattering laser, doubled in frequency by a KDP crystal [109]. The efficiency of laser energy conversion into γ-ray were approximately 2%. In this scheme, nonlinear spectral broadening of the scattered X-ray can be reduced by chirping the scattering laser pulse, which yields a significant increase in the ICS source brightness [110].

In the case of Bremsstrahlung, LWFA electrons propagate through a high-Z material converter and are deflected by the background ions (Fig. 7c) [101]. During the deflection time, a flat spectrum of Bremsstrahlung radiation is generated with the frequencies comparable to the inverse collision time and exponentially falling off for higher frequencies. Femtosecond Bremsstrahlung produced by LWFA electrons is more collimated (5°) than γ -rays from direct irradiation of solid targets (>45°) and exceeds the yield of γ -rays by two orders of magnitude [101,111]. Electron beams with the energy around

40 MeV, interacting with a tantalum converter, have been used to produce γ-rays with a small source size (320 μm) and low divergence (a few degrees). The source duration was of the order of the laser pulse duration (30 fs), and the photon dose was on the order of 1 Gy a few centimetres from the source. Approximately 10^8 photons per shot were generated in the 8-17 MeV γ -ray region by 10-45 MeV LWFA electron beams produced with a 10 TW laser system and crossing a 2 mm tantalum slab [112]. The estimated source brightness was 10^{17}- 10^{21} in photons/s/mrad^2/mm^2/0.1% BW. The main parameters of laser and non-laser X-ray sources are presented in Table 2.

The development of table-top X-ray and γ-sources requires further research and optimization of plasma targets. Tailored plasma channels are of interest for optimization of betatron radiation aiming to increase the critical energy, the number of photons per shot and brightness of X-ray and γ-ray sources. Tuning of betatron radiation is implemented using two-stage nozzles. The first nozzle with lower plasma concentration can be optimized for the acceleration of electrons, and the second one - with higher concentration - can be used for focusing (Fig. 8a) [113] or act as a plasma radiator (Fig. 8b) [114,115].

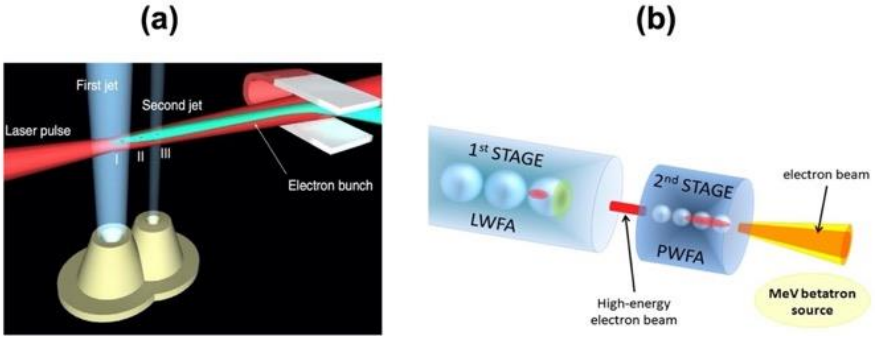

Figure 8. Images of tailored plasma profiles used for the control of secondary radiation: plasma lens of the electron beam [113] **(a)** and plasma radiator [115] **(b)**.

Additionally, plasma concentration can be increased by cryogenically cooling [116] and cluster formation in gas jets [117]. The efficiency of betatron radiation can be raised by increasing of betatron radius using an off-axis injection of electron beam [118] or a second laser pulse [119]. The betatron X-ray radiation increases by direct-laser-acceleration of electrons in the plasma wake [105], by applying of the electrical field of optical lattice [120], nanostructures [121,122], magnetic fields of plasma [123].

Table 2. Summary of X-ray and γ-ray source performance [5,25].

	X-ray tube, liquid	Medical LINAC	HHG	Laser K_α	Betatron	ICS	Brems-strah-lung	Undu-lator	FEL
Energy range, eV	10^3-10^5	10^3-10^7	10-10^3	10^3-10^5	10^3-10^5	10^3-10^7	10^3-10^8	170	150
Bandwidth, %	100	100	100	100	100	50	100	22	20
Photons per shot	-	10^7	10^5-10^9	10^6	10^8-10^9	10^7-10^8	10^8	7×10^4	10^5
Peak Brightness	10^7- 10^8	10^8- 10^{11}	10^{14}	10^{14}-10^{17}	10^{18}-10^{24}	10^{17}-10^{21}	10^{17}- 10^{21}	10^{18}-10^{25}	10^{28}-10^{33}
Source size, μm	5	5×10^3	2	300	1.8	1.5	320	270	270
Duration, fs	-	5×10^9	<30	<30	<30	<30	<30	<30	<30
Collimation, mrad	50	50	2.5	50	2.5	10	50	0.18	0.18
Repetition rate, Hz	150	50-200	10-10^3	10-10^3	10	10	10	10	10

The resonant timing and phase of injection [124] and axially modulated plasma field matched to the half of the betatron period [125] increase the brightness of X-ray radiation.

The structured plasma concentration profiles in the injector and wiggler geometry discussed in this work can be used for the enhancement of betatron oscillation, formation of electron beams of ICS and Bremsstrahlung sources, as well for increasing the HHG yield using a quasi-phase-matching gas array (Fig. 7d) [25,102]. LWFA X-ray sources have the potential for diagnostic applications. LWFA betatron X-rays generated from a small source inside the plasma wakefield are suitable for lens-less phase-contrast imaging of biomedical objects. The costs of lab-based and medical X-ray generators typically ranges from tens to hundreds of thousand euros. Large-scale facilities usually need an investment of several hundred million euros, and it is mostly limited to research purposes [5]. The sources with a brightness of 3-4 orders above medical X-ray generators, i.e., in the range of 10^{11} to 10^{13} ph/s/mm^2/mrad^2/0.1% BW would be sufficient for most X-ray imaging methods. Laser-driven X-ray sources can deliver the required quality of X-ray radiation at prices significantly below the large-scale synchrotron research facilities.

γ-ray of LWFA ICS and Bremsstrahlung sources can be used for radiography and non-destructive inspection of cargo containers or welded structures (pipes, vessels, tanks). γ-rays and neutrons from LWFA can be implemented for the transmutation of nuclear waste and active interrogation. LWFA-driven secondary radiation presents several advantages such as a micrometric source size for good spatial resolution and femtosecond pulse duration for time-resolved studies. Ultrashort LWFA sources are especially suitable pump-probe techniques for investigation of transient phenomena in biochemistry, material science, and states of extreme matter [5].

2.6. Micronozzle Manufacturing Techniques

Implementation of separate plasma stages for injection and acceleration of electron as well as X-ray generation increases mechanical complexity of LWFA system. The structured plasma targets are hard to realize in the case of ultra-shot laser pulse duration (<10 fs), where dephasing length could be less than 100 μm [29,34]. The structured plasma targets can be formed using supersonic micronozzle arrays producing longitudinal gas profiles of varying concentration. The manufacturing and operation of nozzle arrays are simpler compared to the installation of gas capillaries or gas cells.

Jet nozzles for gas injection into the laser interaction area can be fabricated from different materials using various mechanical machining, etching, and stereolithography-based technologies (Fig. 9) [126-129]. The nozzle materials should be resistant to harsh operational conditions. Independently of the design, the most challenging is the manufacturing of the nozzle inner surface defining the gas flow. The metal CNC machining is time-consuming and is not suitable for fabricating complex structures with a high aspect ratio of channels (Fig. 9de). Stereolithography-based methods allow rapid manufacturing from plastics and metals of custom-shaped nozzles down to 100 μm size at a low cost (Fig. 9ab) [128]. However, additional post-processing, polishing of surfaces, the opening of blocked apertures are required. The available materials are of moderate resistance. In the sub-millimetre scale, the printed holes fail in maintaining the circular shape, and the achievable aspect ratio is close to one [129].

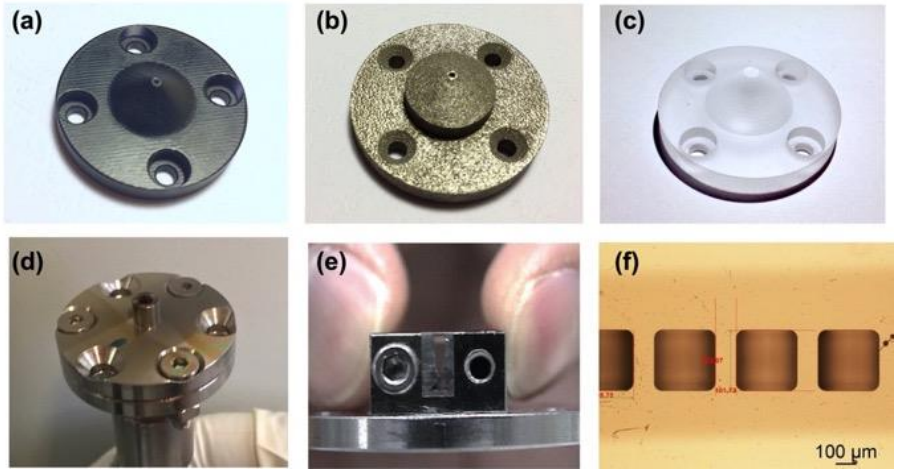

Figure 9. Images of micronozzles fabricated using 3D printing **(a)**, laser sintering **(b)**, electro-erosion **(d,e)** [137,138], and 3D laser microfabrication from fused silica **(c, f)** [139,140].

Implementation of fused silica for the manufacturing of micronozzles is an attractive and cost-effective alternative (Fig. 9cf). Fused silica nozzles have by an order of magnitude higher optical damage threshold [130] comparing to polymeric structures [131]. The ablation threshold of fused silica [132] is several times larger than for metals [133]. The softening temperature of fused silica is larger than that of plastics and the melting point of metals, such as aluminium, copper or iron [134]. Stainless-steel nozzles used for plasma targets in laser systems operating at kHz repetition rate start to show

turbulence after less than 10^4 shots [135]. The fused silica nozzles ensure reliable operation after 3-5 × 10^7 shots [136].

The fused silica nozzles are fragile however, and at backing pressures exceeding 100 bar have to be handled with care. In the range of modest pressures of 20-60 bar the operation time of fused silica nozzles is much longer compared to metallic or polymeric nozzles. Nevertheless, the processing precision and the speed of glassy materials raise issues. The performance of direct laser ablation is limited in the case of thick samples. Plasma shielding, scattering from the sidewalls, debris accumulation create serious challenges, preventing fabrication of deep and taper-less structures [141]. One of the solutions is to remove the material from the rear side of a sample, which is usually referred to as the rear-side processing, back-side ablation or bottom-up technique [142-147]. The overview and comparison of various micro-hole drilling techniques in glass could be found in [148]. Liquid-assisted femtosecond laser drilling allows manufacturing of high aspect ratio holes (50:1) at the speed of several μm/s [143]. The drilling depth is limited by the accumulation and redeposition of the processing debris [149]. The redeposition and accumulation effects can be reduced by tightly focusing nanosecond laser pulses, which induce micro-cracks in the glass. Using this method, the material can be removed as large particles with the size up to hundreds of microns [144,146]. This technique can be applied for the removal of large-scale volume. However, it is not suitable for the manufacturing of channels with diameter less than 100 μm and the surface quality is moderate. The performance of a gas jet nozzle depends on its dimensions and the wall roughness. The surface roughness and waviness reduce the performance of these nozzles [126,150,151]. The femtosecond laser-assisted selective chemical etching technique (FLSE) improves the average surface roughness of the microchannel more than 10 times compared to nanosecond rear-side processing [152-155]. However, due to the long fabrication time, it is less competitive in the processing of high-volume parts.

In this work, the micronozzles using laser-assisted hybrid microfabrication technique were manufactured. The large volume of glass was removed by nanosecond pulses, and the final micro-holes were manufactured by the FLSE technique. Laser-assisted hybrid microfabrication technique [139,156] of fused silica allowed the formation of centimetre-size frame and channels of the diameter less than 40 μm with the surface roughness < 1 μm from a single block. The formation quality exceeds the precision of 3D printing (Fig. 9ab) [129] and electro-erosion technique (Fig. 9de) [137,138].

3. EXPERIMENTAL SETUP AND METHODS

3.1. Experimental Setup

The experimental work of the thesis was done at Lund Laser Center (LLC) and Laboratoire d'Optique Appliqué (LOA) of CNRS - Ecole Polytechnique (EP) and ENSTA-Paristech. The access to the laser facilities was supported by European Union's Horizon 2020 Research and Innovation program under ARIES Grant Agreement 730871, and by Laserlab-Europe, H2020 project EC-GA 654148. The main work related to the research of secondary X-ray radiation was done at 40 TW 35 fs laser in Lund Laser Center. Afterwards, the nozzle microfabrication technology proposed in the thesis was implemented for the manufacturing of novel nozzles designed by LOA. The plasma targets created by these nozzles were used for the LWFA of electrons by few-cycle 0.8 TW 4 fs 1 kHz laser. The energy and spatial distribution of accelerated electrons using structured plasma targets at LLC experiment were numerically simulated using the FBPIC PIC (Particle in Cell) algorithm [157]. The obtained results were post-processed to evaluate the number of X-ray photons per shot and the brightness of electron-generated betatron radiation using the analytical expressions [103]. The concentrations, velocities, pressures and temperatures of the gas jets were calculated using the OpenFOAM software [158].

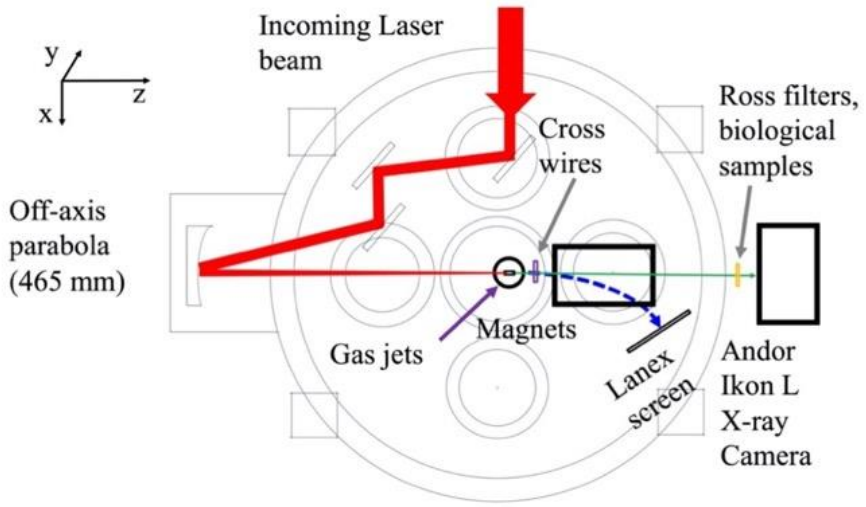

Figure 10. Experimental setup of the laser wakefield acceleration of electrons and measurement of betatron radiation of 40 TW 35 fs Lund Laser Centre facilities [140].

The experimental setup of the LLC experiment is shown in Fig. 10. For the laser wakefield acceleration and measurement of secondary X-ray radiation,

the 800 nm 1.8 J Ti:Sa laser at the repetition rate <1 Hz with a pulse duration of 35 fs and pulse energy on the target of 700-880 mJ was used. The laser beam was focused on the gas jet in a vacuum using a 4-inch offset parabola with the focal length of 465 mm leading correspondingly to a focal spot of 8 μm FWHM. The aberration correction of the laser beam has been controlled by a deformable mirror, which ensured the high quality of the focused beam. The laser polarization was horizontal along the x-axis. These laser parameters correspond to the peak intensity of 3.6×10^{19} W cm^{-2} and laser strength parameter $a_0 \simeq 4.0$. The laser strength parameter a_0 was defined, assuming the peak power of a sech^2 laser pulse is $\approx$ 0.88 times the pulse energy divided by the FWHM pulse duration. LWFA parameters used in the LLC experiment are presented in Table 3.

Table 3. LWFA parameters of LLC experiment [140].

	Geometry	Laser strength parameter a_0	Gas concentration, cm^{-3}	Laser spot FWHM, μm	Gas
1.	Injector	4.0	$3x10^{18}$	8	He
2.	Injector	4.0	$2x10^{18}$	8	He+1%N_2
3.	Wiggler	4.0	$1x10^{19}$	8	He+1%N_2

The experimental setup of the laser wakefield acceleration of electrons at LOA is presented in Fig. 11.

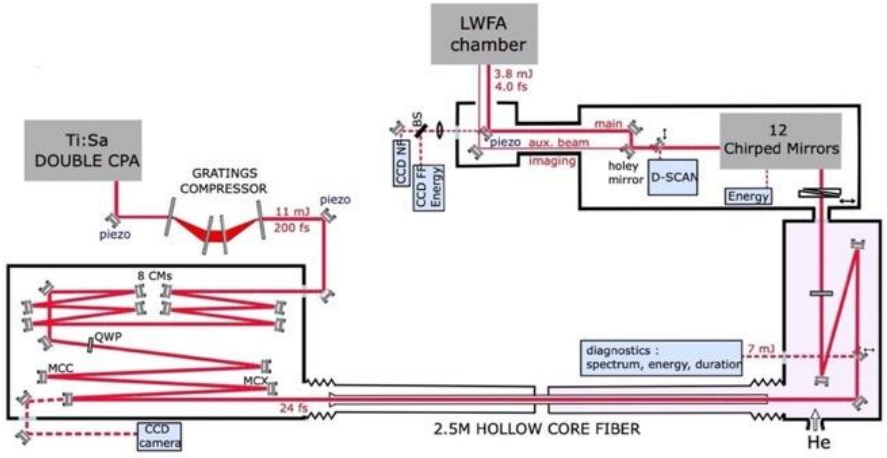

Figure 11. Experimental setup of the laser wakefield acceleration of electrons of 0.8 TW 4 fs 1 kHz LOA Salle noir laser system [136].

The experiment was conducted using the Salle Noire laser system at LOA, which provides 10 mJ, 25 fs FWHM laser pulses at kilohertz repetition rate, with a central wavelength λ_0 = 800 nm. The pulse was post-compressed in a helium-filled Hollow Core Fiber (HCF) [159]. Through a pair of motorized fused silica wedges, the amount of dispersion to fine-tune pulse compression or add chirp to the pulse was controlled. The pulse temporal intensity profile using the D-scan technique [160] was measured. The energy on target was 3.8 mJ, and the pulses were focused by an f/4 off-axis parabola, resulting in a 6.2 μm × 5.5 μm FWHM focal spot. These laser parameters correspond to the measured peak intensity of 2.0×10^{18} W cm^{-2} and a strength parameter $a_0 \simeq 1.0$. The laser-plasma accelerator was run at a repetition rate of 1 kHz. The gas jet flowed continuously while the pumping system was able to maintain a vacuum of a few 10^{-3} mbar. The data were collected by accumulating measurements over ten shots.

The geometries and dimensions of the nozzle arrays used in the experiments are presented in Fig. 12-13.

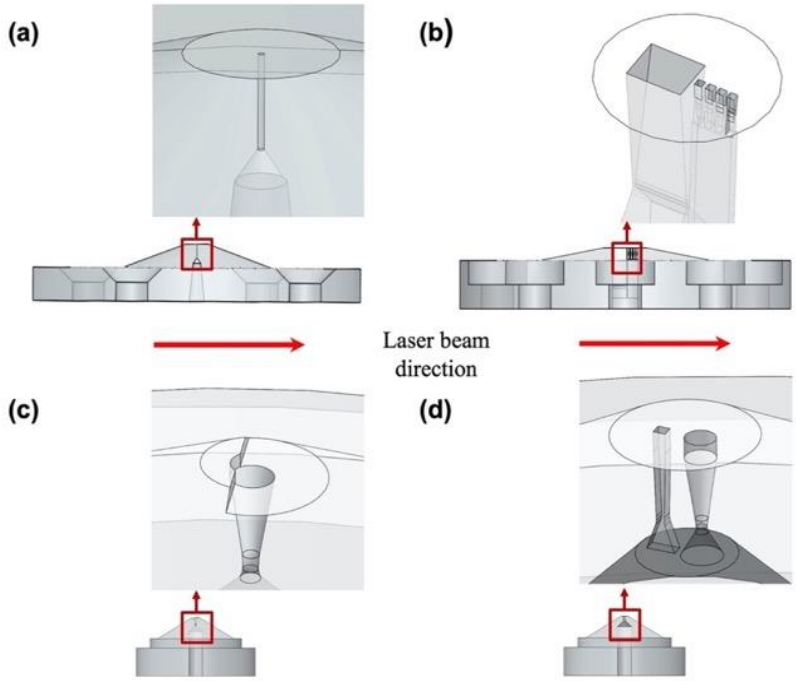

Figure 12. Nozzles used in the experiments: high-density cylindrical nozzle of fixed diameter **(a)**, nozzle array of LLC experiment **(b)**, One-Sided Shock nozzle **(c)**, and double nozzle **(d)** used in LOA experiment.

In Table 4, the dimensions and notation of nozzle arrays used in Lund Laser center experiments are shown. The nozzle arrays in LLC experiment (Fig. 12b and 13) were made from two sections. The first section comprises a main supersonic converging-diverging nozzle of 1.5 mm (S1) or 2.25 mm (Arr3) length commonly used for laser-plasma acceleration. The second section consists of an array of 1 or 4 smaller nozzles of 200-300 μm length located 100 μm away from the main nozzle (Arr2, Arr3, Arr4). The nozzle arrays are oriented in wiggler or injector geometry. In wiggler geometry, the array is placed after the main nozzle, and in injector geometry, the injector nozzle is placed before the main nozzle relative to the incoming laser beam. The notation LxW and L1xW1 means the length and width of the outlet of the first and second array section, correspondingly. The notation L2xW2 means the length and width of the throat of the first array section, while L3xW3 means the length and width of the throat of the second array section.

Table 4. The dimensions of nozzle arrays used in LLC experiment [140].

No.	First section			Second section		
	Description	Outlet dimen-sions, mm, (LxW)	Throat dimen--sions, mm, (L2xW2)	Descrip-tion	Outlet dimen-sions, mm, (L1xW1)	Throat dimen-sions, mm, (L3xW3)
#1	Single slit converging-diverging nozzle S1	1.5 x 1.2	1.5 x 0.12	-	-	-
#2	Single slit converging-diverging nozzle Arr2	1.5 x 1.2	1.5 x 0.12	Slit array of 4 nozzles	0.2 x 0.2	0.2 x 0.2
#3	Single cylindrical converging-diverging nozzle Arr3	∅ 2.25	∅ 0.5	Slit array of 4 nozzles	0.2 x 0.2	0.2 x 0.2
#4	Single slit converging-diverging nozzle Arr4	1.5 x 1.2	1.5 x 0.12	Single slit conver-ging-diver-ging nozzle	0.3 x 0.3	0.3 x 0.2

In Fig. 13ab, the examples of the arrays Arr2 and Arr4 in wiggler and injector geometries are shown. In the array Arr3, for the acceleration of electrons a cylindrical de Laval nozzle with the outlet diameter of 2.25 mm instead of a converging-diverging 1.5 mm slit nozzle was used. The SEM images of a cross-section of a nozzle array Arr2 cut in half are shown in Fig. 13cd. The red arrows indicate the orientation of the nozzle arrays relative to the incoming laser beam.

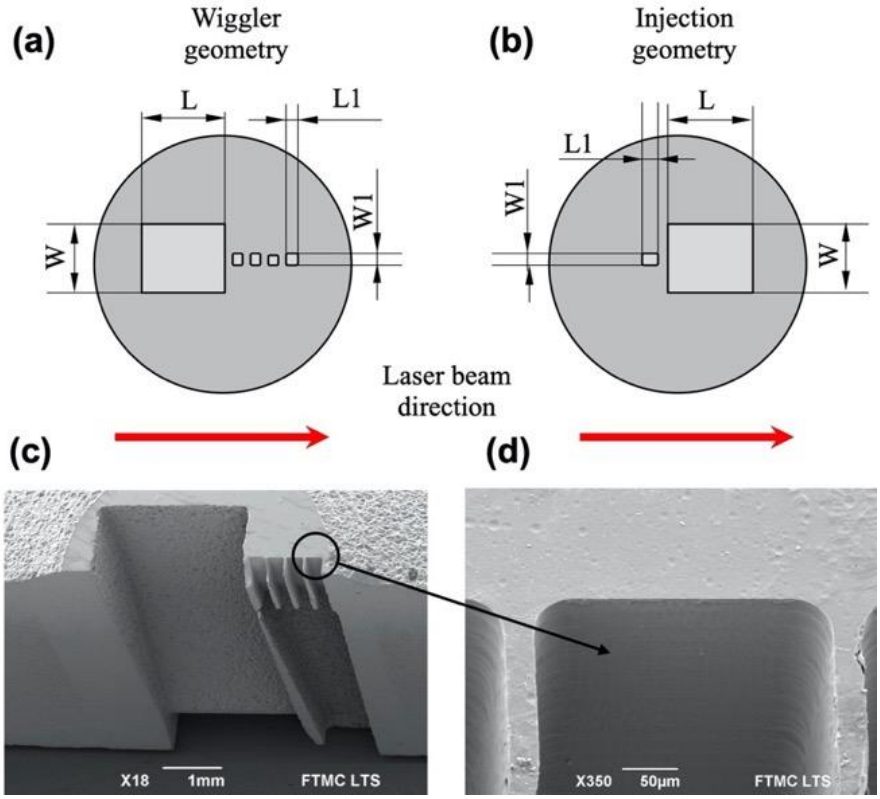

Figure 13. Geometries of the nozzle arrays **Arr2 (a)**, **Arr4 (b)**, used in LLC experiments, and SEM image of a half-cut nozzle **Arr2 (c,d)** [140].

3.2. Measurement of Gas Density Profiles

The gas density profiles of high-density cylindrical nozzles (Fig. 12a) were measured using nitrogen, Mach-Zehnder interferometer and continuous-wave 632.8 nm He-Ne laser. The interferograms were subsequently filtered using Fourier transformation (Fig. 14) [161-163]. The gas nozzles were tested in a vacuum chamber at the vacuum level of 10^{-5} mbar. The laser was operated,

and the interferometer was installed outside of the vacuum chamber with one of the interferometer arms crossing the vacuum chamber through the windows of the optical quality of λ/10. Nitrogen was used for the determination of the gas density profiles because of the sufficiently higher refractive index relative to the helium. The Abel transformation was performed to get the 3D map of the nozzle gas density. The phase was retrieved, and the density profiles were reconstructed using the interferometric data evaluation algorithms (IDEA) [162]. The diagram of the Mach-Zehnder interferometer is presented in Fig. 14a. The images of measured phase interferograms of the gas jet at the backing pressure of 60 bar of 300 μm cylindrical nozzle for helium are given in Fig. 14b, and for nitrogen - in Fig. 14c.

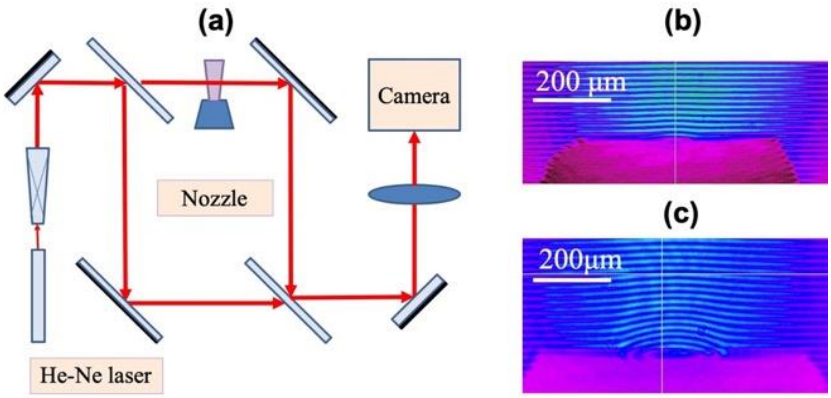

Figure 14. Diagram of Mach-Zehnder interferometer **(a)**, and measured phase interferogram of helium **(b)** and nitrogen **(c)** gas jet at the backing pressure of 60 bar of the cylindrical nozzle with the outlet diameter of 300 μm [139].

The nozzles were driven by the Parker 9 series microvalve with the 0.8 mm orifice, actuated by a specialised pulse driver enabling millisecond operation. The operation of the microvalves and CCD cameras were synchronised and triggered by the master oscillator. Using the integral phase distribution $\varphi_{int}(x,y,z)$, the gas concentration n_g was calculated by the relation $n_g = \varepsilon_0\lambda_L\varphi_{int}/\pi\alpha_p d_v$, where $\lambda_L = 632$ nm is the laser wavelength, $\alpha_p = 18.52\times10^{-41}$ Fm^2 is the polarizability of the argon gas atoms, and $d_v = 17$ μm is the reconstruction length of cubic voxels. The tomographic reconstruction of the phase volume profile was calculated using Simultaneous Iterative Reconstruction Technique (SIRT) algorithm [163].

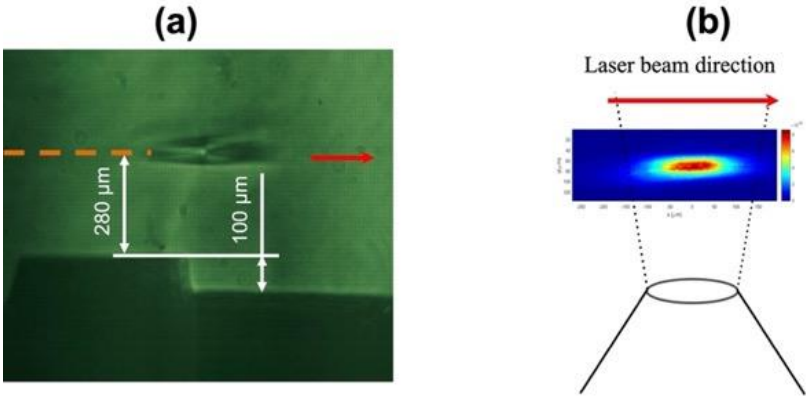

Figure 15. The shadowgram **(a)** and the principle of measurement of nitrogen plasma profile using One-Sided Shock nozzle at backing pressure 20 bar **(b)** [136].

The gas density profiles of nozzle arrays used in the LLC experiment (Fig. 12b) and nozzles used in the LOA lab (Fig. 12cd) were measured using a quadriwave lateral shearing interferometer (SID4-HR, Phasics) [164,165]. Argon was implemented for the measurements in the LLC case, and nitrogen in the LOA experiment. Additionally, in the LOA lab, the plasma density profile was characterized experimentally by sending the laser pulse into a nitrogen gas jet produced by One-Sided Shock (OSS) nozzle (Fig 15). The plasma column ionized by the main beam was illuminated from the side by a probe beam and imaged on the interferometer SID4-HR [164,165]. The plasma density profiles were derived from the phase maps via Abel inversion, assuming radial symmetry around the horizontal axis.

3.3. Characterization of Electron Beams

The energy and spatial distribution of the accelerated electrons at LLC experiment were measured using a Kodak Lanex Regular scintillation screen with a dipolar 0.8 T magnet of a total length of 20 cm located at the distance of 50 mm from the source. The width of the magnetic spectrometer was 5 cm, and the spacing of the dipole gap was 15 mm. The measuring range of the spectrometer was 20-300 MeV. Scintillation screen images were captured using Andor Zyla 4.2 Plus CMOS 16-bit camera. The camera CCD was of 2048 x 2048 pixels of the size of 6.5 µm. The transverse and longitudinal distribution of the magnetic field of the dipole magnet was mapped using a Hall probe. The energy and divergence of the electron beam were calculated using images of Lanex scintillation screen and previously published

calibration factors of 6.95×10^{-8} pC/count for the scintillating screens measured at linear accelerator [166]. The energy deposition per electron exceeding few MeV is almost constant, and the number of emitted fluorescence photons was proportional to the beam charge [167]. The spectral distribution of the electrons was estimated from the number of counts of Lanex screen and the position of electrons bent in the magnetic field. The relation between electron energy and position on the scintillating screen was simulated using Comsol Multiphysics. The measurement uncertainty introduced by the ±10 mrad divergence of the 125 MeV electron beam was 7.5 MeV. It corresponded to the accuracy of ±6%.

The charge and spatial distribution of the accelerated electrons at LOA experiment were measured with a calibrated CsI (Tl) phosphor screen imaged onto a CCD camera of high dynamic range. The laser beam and electrons with energies below 100 keV were blocked by a thin aluminium foil in front of the phosphor screen. The energy of the electrons was measured with a retractable spectrometer made of a 500 μm pinhole and two permanent cylindrical magnets.

3.4. Characterization of X-Ray Radiation

The betatron radiation at LLC experiment was registered using the Andor iKon-L SO X-ray camera, sensitive to X-rays from 100 eV to 20 keV. The X-ray CCD was of 2048 × 2048 square pixels with a pixel size of 13.5 μm. The camera window was made of 250 μm-thick beryllium. A 50 μm Kapton window with an additional shield of 3 μm aluminium foil was installed at the outlet of the vacuum chamber to block the remaining 800 nm laser beam and extreme ultraviolet (XUV) radiation of electrons from bending magnet of the spectrometer. The X-ray camera was installed at a distance of 73 cm from the source, and the betatron radiation passed through the air gap of 12 cm.

3.5. Definition of Critical Energy and Size of X-Ray Source

The synchrotron-like spectrum of the betatron radiation was defined using the Ross filters [168]. The Ross-filter array was inserted into the X-ray beam at the distance of 6 cm from the exit of the experimental chamber. The filter array was composed of intersecting strips with different *K* or *L* absorption edges energies of the elements Ni, Cu, Zn, Al, Ti, Zr, Cu within the range of expected energy range of the betatron radiation. The thicknesses and K/L_1 edge absorption energies of the Ross filter materials are shown in Table 5.

Table 5. The thickness and K/L_1 edge absorption energies of Ross filters [140,169]

Material	Ni	Cu	Zn	Al	Ti	Zr	Cu
Thickness (μm)	5.0	25.0	5.0	6.0	6.0	3.0	3.0
K/L_1 absorption energy, keV	8.33 K	8.98 K	9.66 K	1.56 K	4.97 K	2.54 L_1	8.98 K

The thicknesses of filter materials were adjusted in such a way that the transmitted spectra are identical to all wavelengths except those lying within the narrow pass band between the two *K* (or L_1 in case of zirconium) absorption limits. Combining the different sets of Ross filter pairs, it was possible to evaluate the photon flux within a particular spectral range. The region covered with the copper filter of 25 μm thickness was used for the measurement of background radiation at X-ray camera. The background radiation was estimated as 300 counts per pixel on average and was deducted from the measured counts per pixel of betatron radiation. The critical energy of betatron radiation was evaluated by calculating the squared difference between the measured transmission and the theoretical one for each critical energy of synchrotron radiation [170]. The number of photons per count N_{photC} at the critical betatron radiation energy $W_{c\beta}$ measured by Ross filters was estimated as:

$$N_{photC} = \alpha_c S_n(W_{r\beta}, W_{c\beta}) \ , \tag{43}$$

where α_c = 11.9 eV/counts - the X-ray detector sensitivity calibration constant, and $W_{c\beta}$ is the critical energy of synchrotron radiation. $S_n(W_{r\beta}, W_{c\beta}) = S_1 / S_{eff}$ is the normalized synchrotron-like spectrum calculated in the energy range from W_{min}= *100 eV* to W_{max}=*30 keV* as:

$$S_1(W_{r\beta}, W_{c\beta}) = \int_{W_{\min}}^{W_{\max}} \left(\frac{W_{r\beta}}{W_{c\beta}}\right)^2 K_{2/3}^2\left(\frac{W_{r\beta}}{2W_{c\beta}}\right) dW_{r\beta} \tag{44}$$

$$S_{eff}(W_{r\beta}, W_{c\beta}) = \int_{E_{\min}}^{E_{\max}} \left(\frac{W_{r\beta}}{W_{c\beta}}\right)^2 K_{2/3}^2\left(\frac{W_{r\beta}}{2W_{c\beta}}\right) Tr_{tot}(W_{r\beta}) \cdot Q_e(W_{r\beta}) W_{r\beta} dW_{r\beta} \ , \tag{45}$$

where $Tr_{tot}(W_{r\beta})$ is the pass factor of all materials placed between the X-ray source and X-ray camera, and $Q_e(W_{r\beta})$ is the quantum yield of the Andor iKon-L SO BR-DD camera. In the calculations, the attenuation of 3 μm aluminium, 250 μm Kapton, 250 μm Beryllium and 120 mm of air were taken into the account.

The radius of the betatron source was determined by measuring of the Fresnel diffraction from the 50 μm tungsten cross-wires, placed 28 mm from the source, magnifying the image 26 times and comparing the intensities of X-ray signals in the horizontal and vertical directions. The intensity distribution of the Fresnel diffraction was calculated using the relations given in [170-172]:

$$I_{sfr}(x_d) = \int S_s(x_s)\overline{I}_{sfr}(x_d + x_s\frac{r_{2wd}}{r_{1sw}})dx_s \ , \tag{46}$$

where $I_{sfr}(x_d)$ is the total radiation intensity reaching the detector from all source points, x_s and x_d are the coordinates of the source and detector planes respectively, r_{1sw} is the distance between the source and the cross wires, r_{2wd} is the distance between the cross wires and the detector, $S_s(x_s)$ is the radiation distribution, and $\overline{I}_{sfr}(x_d, x_s)$ - the spectrum averaged intensity. The normalized radiation intensity of the point source in the detector plane was calculated using the relation:

$$I_{sfr}(x_d) = \left|\sqrt{\frac{r_{sd}}{i\lambda_{c\beta}r_{1sw}r_{2wd}}}\exp\left(\frac{-i\pi}{\lambda_{c\beta}r_{2wd}}(2xx_d - \frac{r_{sd}}{r_{1sw}}x_d^2 - \frac{r_{1sw}}{r_{sd}}x_d^2)\right)Tr_{c\beta}(x,\lambda_{c\beta})dx\right|^2 , \tag{47}$$

where x is the coordinates of the wire plane and the distance between the source and detector $r_{sd} = r_{1sw} + r_{2wd}$. The wavelength transmission coefficient was calculated using the relation:

$$Tr_{c\beta}(x,\lambda_{c\beta}) = e^{-\mu_{c\beta}(\lambda_{c\beta})\cdot 2\sqrt{R_w^2 - x^2}} \ , \tag{48}$$

where R_w is the radius of the wire and $\mu_{c\beta}(\lambda_{c\beta})$ is the attenuation coefficient. The intensity distribution of the Fresnel diffraction was calculated for the spectrum of a synchrotron with the average critical energy $W_{c\beta}$ = 2.4 keV, considering the quantum efficiency of the X-ray camera and the attenuation of the filters used.

3.6. Definition of the Number of Photons per Shot and Brightness

The number of photons per shot N_{phot} and brightness Br of the betatron X-ray source at FWHM level were defined by post-processing of the data of X-ray images. The number of photons per shot N_{phot} was calculated as:

$$N_{phot} = N_{photC}N_c \ , \tag{49}$$

where N_{photC} is the number of photons per count, and N_c is the number of counts. The number of counts N_c was estimated by integrating the function of the spatial distribution of counts per pixel $C(x_{px}, y_{px})$ over the coordinates x_{px} and y_{px} expressed in pixel number:

$$N_c = \int_{-\infty}^{+\infty} C(x_{px}, y_{px}) dx_{px} dy_{px} \tag{50}$$

The function $C(x_{px}, y_{px})$ was assumed to consist of two parts: Gaussian distribution of X-ray radiation and background part C_{bg}:

$$C(x_{px}, y_{px}) = C_{gd} e^{-\frac{(x_{pxr}-x_{pxc})^2}{2\sigma_x^2}+\frac{(y_{pxr}-y_{pxc})^2}{2\sigma_y^2}} + C_{bg}\ , \tag{51}$$

where C_{gd} is the amplitude of Gaussian part of counts per pixel, x_{rpx} and y_{rpx} are coordinates of in pixels tilted by the angle θ_{gd}: $x_{pxr} = x_{px}\cos(\theta_{gd}) - y_{px}\sin(\theta_{gd})$ and $y_{pxr} = x_{px}\sin(\theta_{gd}) + y_{px}\cos(\theta_{gd})$, x_{pxc} and y_{pxc} are the center coordinates of Gaussian distribution, and σ_x and σ_y are the standard deviations of Gaussian distribution of X-ray counts per pixel in x and y - direction (Fig. 16).

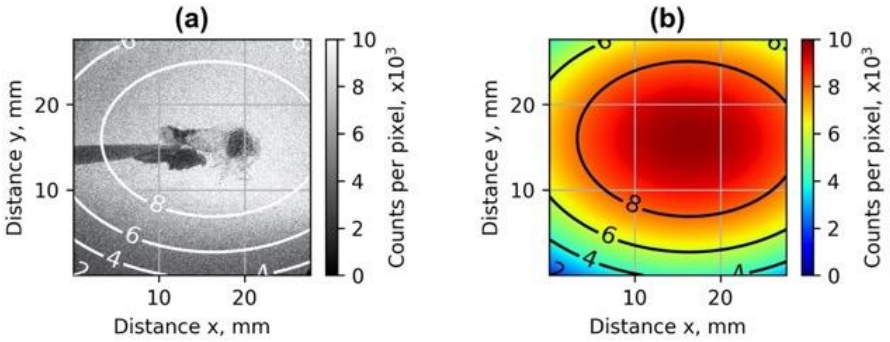

Figure 16. An example of X-ray image **(a)** and defined contours of normal Gaussian distribution of X-ray radiation **(b)** [140].

C_{bg} was estimated by averaging of counts per pixel of the first and last column as well as an upper and lower row of the X-ray image. The initial parameters of Gaussian distribution $x_{pxc}^0, y_{pxc}^0, \sigma_x^0, \sigma_y^0, \theta_{gd}^0, C_{bg}^0$ were calculated using the following relations:

$$x^0_{pxc}, y^0_{pxc} = \frac{\sum_i^n X, Y_{pxi}(C_i - C_{bg})}{\sum_i^n (C_i - C_{bg})} \quad , \tag{52}$$

$$\sigma^0_{x,y} = \sqrt{\frac{\sum_i^n (C_{x,yci} - C_{bg})(x, y_{pxi} - x, y_{pxc})^2}{\sum_i^n (C_{x,yci} - C_{bg})}} \, , \tag{53}$$

$$M_{xx,yy} == \frac{\sum_i^n (X, Y_{pxi} - x, y_{pxc})^2 (C_i - C_{bg})}{\sum_i^n (C_i - C_{bg})} \quad , \tag{54}$$

$$M_{xy} = \frac{\sum_i^n (X_{pxi} - x_{pxc})(Y_{pxi} - y_{pxc})(C_i - C_{bg})}{\sum_i^n (C_i - C_{bg})} \, , \tag{55}$$

$$\theta^0_{gd} = 0.5 arctg\left(\frac{2M_{xy}}{M_{xx} - M_{yy}}\right) , \tag{56}$$

where X_{pxi} and Y_{pxi} are the coordinate grids of rows and columns of the X-ray image, C_i - counts per pixel of the i-th pixel, C_{xci} and C_{yci} are correspondingly the row and column of counts per pixel at central coordinates of Gaussian distribution of x_{pxc} and y_{pxc}, and M_{xx}, M_{yy} and M_{xy} are the momenta of Gaussian distribution used for calculation of tilting angle θ_{gd}. The initial parameters of Gaussian distribution $x^0_{pxc}, y^0_{pxc}, \sigma^0_x, \sigma^0_y, \theta^0_{gd}, C^0_{bg}$ were optimized by calculating the minimum of the squared difference between the measured X-ray image data and the best fit of Gaussian distribution function:

$$f(C_{gd}, x_{pxc}, y_{pxc}, \sigma_x, \sigma_y, \theta_{gd}, C_{bg}) = C_{gd} e^{-\frac{(x_{pxr} - x_{pxc})^2}{2\sigma_x^2} + \frac{(y_{pxr} - y_{pxc})^2}{2\sigma_y^2}} + C_{bg} \tag{57}$$

The spatial distribution of illumination exceeded the size of X-ray sensors, therefore, afterwards, only the Gaussian part of the X-ray radiation was considered, and the total number of counts N_c was estimated assuming:

$$N_c = \int_{-\infty}^{+\infty} C_{gd} e^{-\frac{(x_{rpx} - x_{cpx})^2}{2\sigma_x^2} + \frac{(y_{rpx} - y_{cpx})^2}{2\sigma_y^2}} dx_{px} dy_{py} = C_{gd} 2\pi\sigma_x\sigma_y \tag{58}$$

The number of counts at FWHM level was calculated as:

$$N_{cFWHM} = C_{gd}\, 2\ln 2\, \frac{\pi \sigma_x \sigma_y}{2} \tag{59}$$

The halves of the divergence in mrad in x and y direction of radiation $\theta_{0.5x}$, $\theta_{0.5y}$ were defined estimating the standard deviation σ_x and σ_y of normal Gaussian distribution of X-ray counts per pixel in x and y-direction as:

$$\theta_{0.5x,y} = 1000 arctg\left(\sqrt{2\ln 2}\, \frac{\sigma_{x,y} l_{px}}{l_{sd}} \right), \tag{60}$$

where l_{px} = 13.5 μm is the pixel size and l_{sd} = 730 mm is the distance between the source X-ray camera detector. The averaged divergence of betatron radiation was calculated as $\theta_{\perp\beta} = \theta_{0.5y\beta} + \theta_{0.5x\beta}$. The brightness of the source in units of photons/s/mm^2/mrad^2/0.1%BW was calculated as:

$$Br = \frac{N_{phot}}{1000\pi\theta_{0.5x\phi}\theta_{0.5y\beta}\pi r_\beta^2 \tau_L} \quad , \tag{61}$$

where r_β is a measured radius of betatron source of 5 μm in mm, and τ_L is the duration of the laser pulse. The figures were visualized using Matplotlib plotting library for the Python programming language [173].

4. NUMERICAL LWFA SIMULATIONS

The material related to this chapter was published [A2] and in [C1, C2, C3].

4.1. Simulation of Electron Beam Profiles

The LWFA electron acceleration and betatron X-ray radiation were numerically simulated using the FBPIC PIC (Particle in Cell) algorithm [157]. The quasi-cylindrical FBPIC algorithm enables much faster simulation of laser and electron beams than full 3D PIC algorithms. For the modelling of structured plasma targets, simplified plasma concentration profiles comprising injector (Fig. 17 ab) and wiggler geometries (Fig. 17 cd) were used. The injector geometry had a short 200 μm plasma section, 100 μm gap and 1.5 mm accelerating section. Wiggler geometry had 1.5 mm long acceleration section and a wiggler comprising four 200 μm plasma regions and gaps of 100 μm length. The injector geometry was used for the design of the array Arr4, and the wiggler geometry - for the design of the array Arr2. The 1.5 mm long plasma profile corresponds to the single nozzle S1 implemented in the experiments.

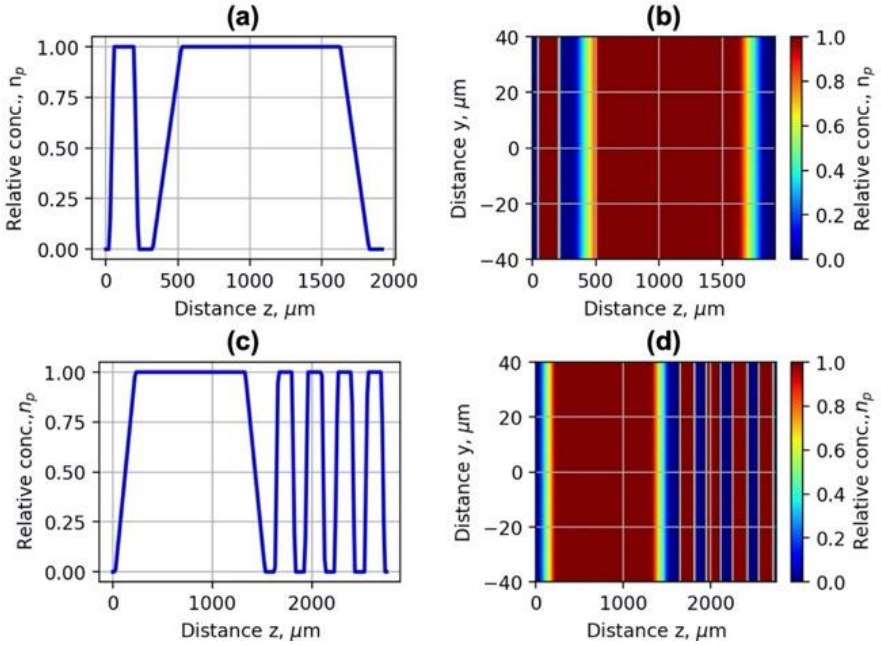

Figure 17. Simplified plasma concentration profiles of the injector **(a,b)** and wiggler **(c,d)** geometries used in the simulation [140].

This notation of the nozzles will be used further in the discussion on simulation and experimental results. The simulation parameters were chosen according to the experimental setup of Lund Ti:Sa laser. The laser strength parameter a_0 was calculated considering the focal length of the focusing mirror of 465 mm and the laser beam diameter at the FWHM level of 8 μm. It corresponded to the $a_0 = 4.0$.

To evaluate different LWFA scenarios, the simulation for $a_0 = 2.3$ and the laser beam diameter at the FWHM level of 10.9 μm was run as well. The perpendicular radius of the simulation zone was 20 μm. The resolution of the mesh grid was 0.05 μm, and the time step was 0.17 fs. The simulation was performed for various acceleration distances of 0.5-2.5 mm based on the geometry of nozzles implemented in the experiment. The initial plasma concentration of 3×10^{18} cm^{-3} corresponding to the LWFA bubble regime was estimated using analytical relations (14-18).

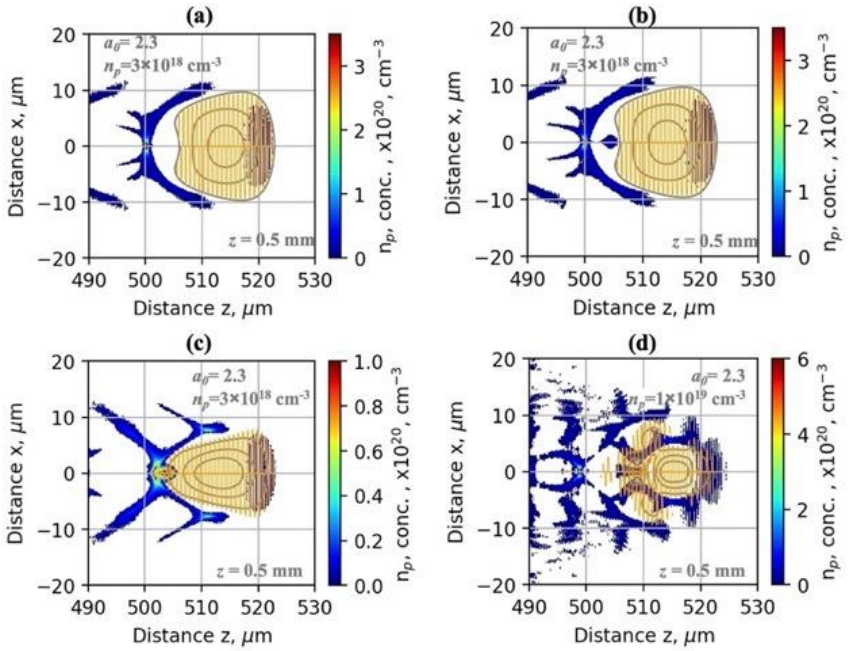

Figure 18. Simulated profiles of the spatial distribution of concentration of electrons injected by density down-ramp triggered injection for the array **Arr4** in injector geometry for $a_0 = 2.3$, $n_p = 3\times10^{18}$ cm^{-3} pure He **(a)**, by combined density down-ramp triggered and ionization injection for mixture He+1%N_2 **(b)**, and by ionization injection for single nozzle **S1** $n_p = 3\times10^{18}$ cm^{-3} **(c)** and $n_p = 1\times10^{19}$ cm^{-3} **(d)** for mixture He+1%N_2. The acceleration distance z = 0.5 mm. The grey contour lines indicate the envelope of the electric field of the laser pulse.

In the numerical simulations, the plasma concentration was changed in the range of 1×10^{18} - 1.0×10^{19} cm^{-3} to define the optimal acceleration conditions and estimate the efficiency of secondary betatron X-ray radiation. Calculations were made for pure helium and the gas mixture of He + 1%N_2. In Fig. 18-20, the simulation results of different injection schemes using density-triggered, ionization, and combined density down-ramp triggered and ionization injection are presented. With the intention to increase the contrast of the images, the plasma concentration data below 3% from the maximum in the Fig. 18-19 are not shown and lighted by white areas.

In Fig. 18ab, the simulation results of the spatial distribution of LWFA electrons using density down-ramp injection for the array Arr4 in injector geometry and $a_0 = 2.3$, $n_p = 3\times10^{18}$ cm^{-3} are presented. The plasma wavelength $\lambda_p = 19.3$ μm corresponds to the LWFA bubble regime, and match the laser beam diameter FHWM of 10.9 μm and $\tau_L = 32$ fs.

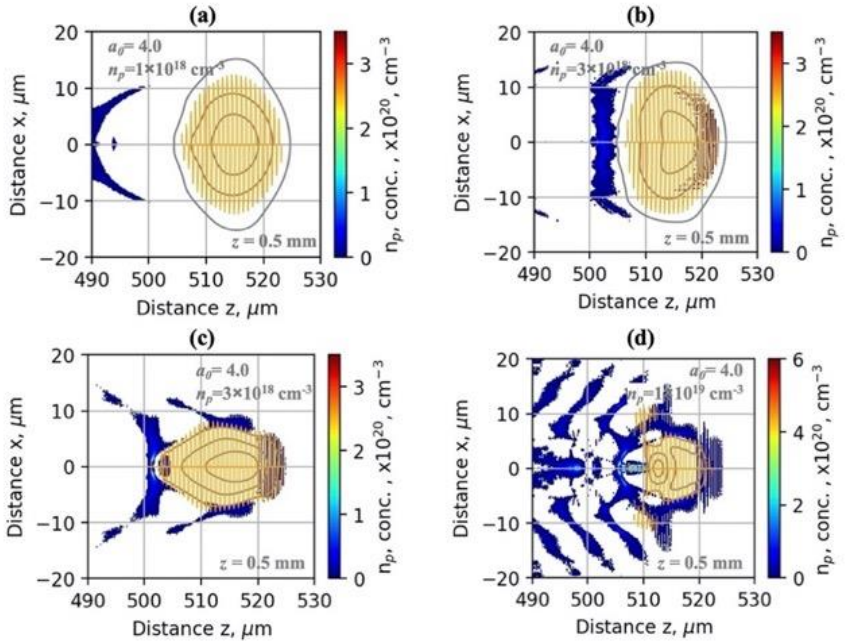

Figure 19. Simulated profiles of the spatial distribution of concentration of electrons injected by combined density down-ramp triggered and ionization injection for the array **Arr4** in injector geometry for mixture He+1%N_2 $a_0 = 4.0$, $n_p = 1\times10^{18}$ cm^{-3} **(a)** and $n_p = 3\times10^{18}$ cm^{-3} **(b)**. Simulated profiles of the spatial distribution of ionization injection for single nozzle **S1** $n_p = 3\times10^{18}$ cm^{-3} **(c)** and $n_p = 1\times10^{19}$ cm^{-3} **(d)**. The acceleration distance z = 0.5 mm.

In the Fig. 18a, the injection of electrons of pure helium, and in Fig. 18b, an additional injection of nitrogen ionized electrons inside of the plasma

bubble is shown. Both of these regimes lead to the formation of quasi-monoenergetic bunch of accelerated electrons; however, the injected charge is low. In Fig. 18c and 18d, the ionization injection of nitrogen electrons for the single nozzle and $n_p = 3\times10^{18}$ cm^{-3} is presented. The accelerated electrons achieve the highest energy, and the divergence of the electron beam is the lowest (Fig. 20 ac). The continuous injection causes a broad energy spectrum of accelerated electrons however. In the case of Fig. 18d and 19d, the simulation results for $n_p = 1\times10^{19}$ cm^{-3} and laser strength parameter $a_0 = 2.3$ and $a_0 = 4.0$ are shown correspondingly.

For the higher plasma concentration and shorter plasma wavelength, the optimal beam diameter *FHWM* is 7.9 μm. The optimal laser pulse duration $\tau_L = 18$ fs is shorter than $\tau_L = 35$ fs used in the experiment, and several plasma waves are excited. The accelerated electrons are spread in the broad lateral plasma wake (Fig. 18d,19d, and 21 ac).

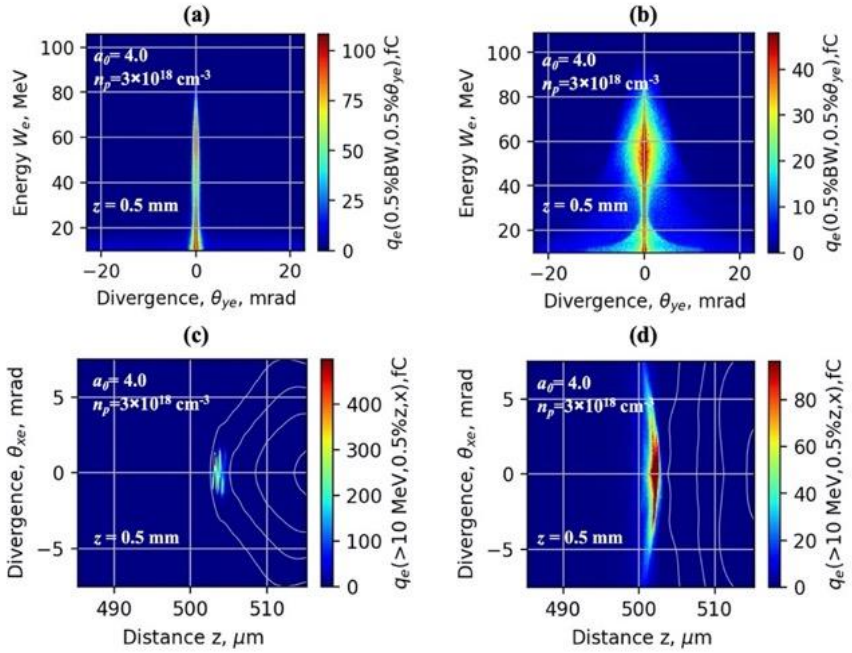

Figure 20. Simulated profiles of the spatial charge distribution in y- **(a, b)** and xz **(c,d)** directions of electrons injected by ionization injection for a single nozzle **S1** for mixture He+1%N_2 $a_0 = 4.0$, $n_p = 3\times10^{18}$ cm^{-3} **(a,c)**. Simulated profiles of the spatial charge distribution of electrons injected by combined density down-ramp triggered and ionization injection for the array **Arr4** in injector geometry **(b,d)** [140]. The acceleration distance z = 0.5 mm.

In Fig. 18b, 19 ab, and 20bd, the simulation results of injection schemes using combined ionization and density-triggered injection are presented. In the case of $a_0 = 2.3$ and $n_p = 3\times10^{18}$ cm^{-3} (Fig. 18b), the relatively low laser intensity and plasma concentration result in a small number of injected electrons. In the case of $a_0 = 4.0$ and $n_p = 1\times10^{18}$ cm^{-3} (Fig. 19a), the laser intensity is higher, however, the charge of injected electrons is still low because of low plasma concentration. The plasma wavelength and the radius of the plasma bubble of is too large for the efficient acceleration of electrons. In Fig. 19b and 20 bd, the higher laser strength parameter $a_0 = 4.0$ and matched plasma wavelength of $n_p = 3\times10^{18}$ cm^{-3} result in the injection of higher charge into the wake and formation of the quasi-monoenergetic bunch (Fig. 20b).

For this regime, several conditions have to be met. The plasma concentration, laser beam focusing and pulse duration have to correspond to the LWFA bubble regime. The length of the plasma density down-ramp region has to be close to the plasma wavelength, and the laser beam has to be focused into the beginning region of the down-ramp. The laser intensity has to be sufficient to accelerate the higher number of injected electrons and not to exceed the threshold of continuous ionisation injection inside of the plasma bubble.

The energy of accelerated electron for the single 1.5 mm nozzle S1, $a_0 = 2.3$ and the plasma concentration $n_p = 3\times10^{18}$ cm^{-3} reaches 150-200 MeV. The divergence is 2-3 mrad. With the increase of plasma concentration from $n_p = 3\times10^{18}$ cm^{-3} to $n_p = 1.0\times10^{19}$ cm^{-3}, the energy of the accelerated electrons decreases to 30-80 MeV. In Fig. 21, the energy and divergence of accelerated electrons for $n_p = 1\times10^{19}$ cm^{-3} at the acceleration distance $z = 2.5$ mm are shown. The divergence of the electron beam for $a_0 = 2.3$ increases to 10 - 15 mrad (Fig. 21a). In the case of the higher laser strength parameter of $a_0 = 4.0$, the energy of the accelerated electrons for the single 1.5 mm nozzle S1 reaches 30-100 MeV. The divergence of the electron beam increases further to 20-40 mrad (Fig. 21c).

In Fig. 21bd, the charge profiles of electrons accelerated using a nozzle array Arr2 are presented. For $a_0 = 2.3$, the slit nozzle array increases the divergence of the electron beam to 30-60 mrad (Fig. 21b), being 2-3 times larger compared to the divergence of the electron beam of the single nozzle shown in Fig. 21a. The energy of electrons remains similar. In the case of Fig. 21d, the divergence of the electron beam increases to 30-50 mrad being 30-50% larger compared to the divergence of the electron beam of the single nozzle shown in the Fig. 21c. The implementation of the slit array for $a_0 = 4.0$ (Fig. 21d) is less efficient relative to the case of $a_0 = 2.3$ (Fig. 21b) because the electron beam has larger divergence due to the shorter Rayleigh length. In

the case of $a_0 = 4.0$, the laser beam focused to the diameter of 8 μm, and in the case of $a_0 = 2.3$ - to 10.9 μm FWHM.

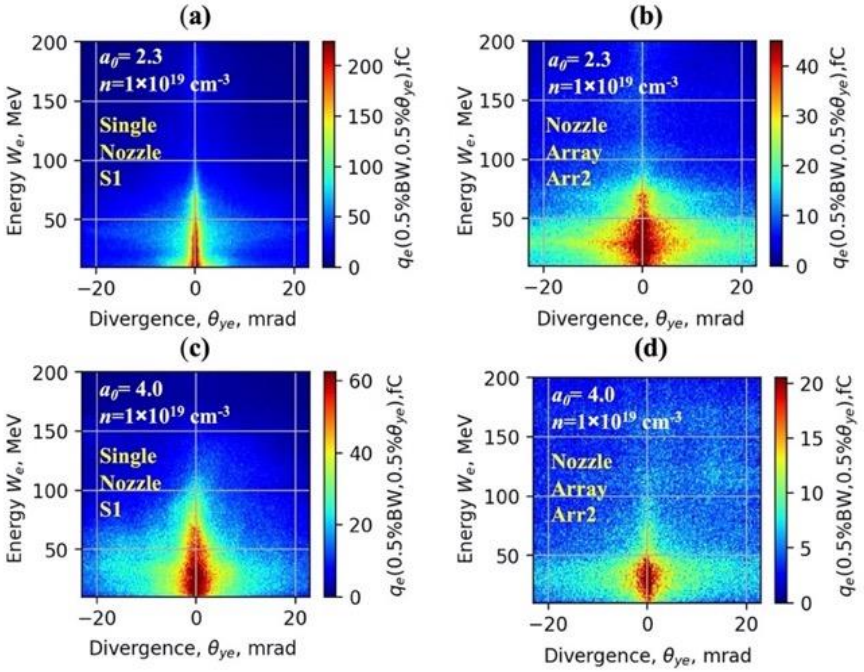

Figure 21. Simulated profiles of the distribution of the energy and divergence of electron charge for the single Laval nozzle **S1** (**a**), array **Arr2** (**b**) for $a_0 = 2.3$, and the single Laval nozzle **S1** (**c**), and array **Arr2** (**d**) for $a_0 = 4.0$ and $n_p = 1\times10^{19}$ cm^{-3} at the acceleration distance z = 2.5 mm [140].

4.2. Estimation of Secondary X-Ray Radiation

The number of X-ray photons per shot and the brightness of electron - generated betatron radiation were evaluated by postprocessing of data of spatial distribution electron momenta of FBPIC PIC simulation [103]. The energy of synchrotron radiation into the unit of photon energy and unit of space angle in the direction of the laser radiation at $\theta = 0$, generated by one electron at the corresponding critical energy $W_{c\beta}$was calculated using relations (39,40). The wavelength and the cyclic frequency of the electron betatron oscillation were calculated using relations (14,36). The total number of electron oscillations in the betatron ion channel was estimated by the relation:

$$N_\beta = 4.7\times10^{10}\frac{1}{\lambda_L[\mu\text{m}]\sqrt{\gamma n_e[\text{cm}^{-3}]}}\frac{L_\beta}{\lambda_L}, \qquad (62)$$

where $L_\beta=2r_\beta$ and τ_L is the laser wavelength. If $r_\beta^2/2\gamma_z \ll 1$, the ratio of the radius of the electron oscillation to the $\sqrt{2\gamma_z}$ is approximately equal to the ratio of the components of the electron momentum in the transverse and longitudinal directions $r_\beta^2/2\gamma_z \simeq p_{e\perp}^2/p_{ez}^2 \simeq p_{e\perp}^2/\gamma_z^2$, or the ratio of the Lorenz factors in the transverse and longitudinal direction [103]. Based on the relations above, the betatron radius of electron oscillations was calculated as $r_\beta = p_{e\perp}\sqrt{2/\gamma_z}$. The transversal divergence (FWHM) of electrons $\theta_{e\perp}$ was calculated as the average of the divergences in the *x*- and *y*-directions. The angle of the betatron radiation in the oscillation plane was calculated as $\theta_{0.5\perp\beta} = K_\beta/\gamma$, and the divergence $\theta_{\perp\beta} = 2\ \theta_{0.5\perp\beta}$. The angle of radiation in the perpendicular plane was calculated as $\theta_{0.5s\beta} = 1/\gamma$ and $\theta_{s\beta} = 2\theta_{0.5s\beta}$, correspondingly. The number of photons N_{phot1} radiated by one electron was calculated by dividing the spectral density over the photon energy $W_{r\beta} = \hbar\omega_{r\beta}$, integrating over the range of energies from $W_{min}=100\ eV$ to $W_{max}=30\ keV$ of the sensitivity of X-ray camera and multiplying by a stereo angle of $\pi\theta_{\perp\beta}\theta_{s\beta}/8$:

$$N_{phot1} = \int_{\theta_{\min}}^{\theta_{\max}} \int_{W_{\min}}^{W_{\max}} \frac{1}{W_{r\beta}} \frac{d^2 W_{r\beta tot}}{\partial W_{r\beta} \partial\Omega}\bigg|_{\theta=0} dW_{r\beta} d\Omega = \frac{\pi\theta_{\perp\beta}\theta_{s\beta}}{8} \int_{E_{\min}}^{E_{\max}} \frac{1}{W_{r\beta}} \frac{dW_{r\beta tot}}{dW_{r\beta}}\bigg|_{\theta=0} dW_{r\beta} = \int_{E_{\min}}^{E_{\max}} \frac{dN_{phot1}}{dW_{r\beta}} dW_{r\beta} \quad (63)$$

The total number of photons per shot N_{phot} was estimated by summing the spectra of the number of photons generated by electrons with a critical energy of $W_{c\beta i}$ and integrating over the range of energies from $W_{min}=100\ eV$ to $W_{max}=30\ keV$:

$$N_{phot} = \int_{W_{\min}}^{W_{\max}} \sum_i \frac{dN_{phot1}(W_{c\beta i})}{dW_{r\beta}} dW_{r\beta} \quad (64)$$

The total brightness *Br* of all electrons in 0.1% bandwidth/mrad^2/mm^2 units was calculated as:

$$Br = \int_{W_{\min}}^{W_{\max}} \sum_i \frac{1}{2000\pi r_{\beta i}^2 \tau_L} \frac{dN_{phot1}(W_{c\beta i})}{dW_{r\beta}} dW_{r\beta}\ , \quad (65)$$

where $r_{\beta i}$ is expressed in mm, and τ_L is the duration of the laser pulse.

In Fig. 22a-c, the simulated charge of accelerated electrons having transversal divergence (FWHM) $\theta_{e\perp}$, betatron radius $r_{c\beta}$, and critical synchrotron energy $W_{c\beta}$ of betatron radiation are presented.

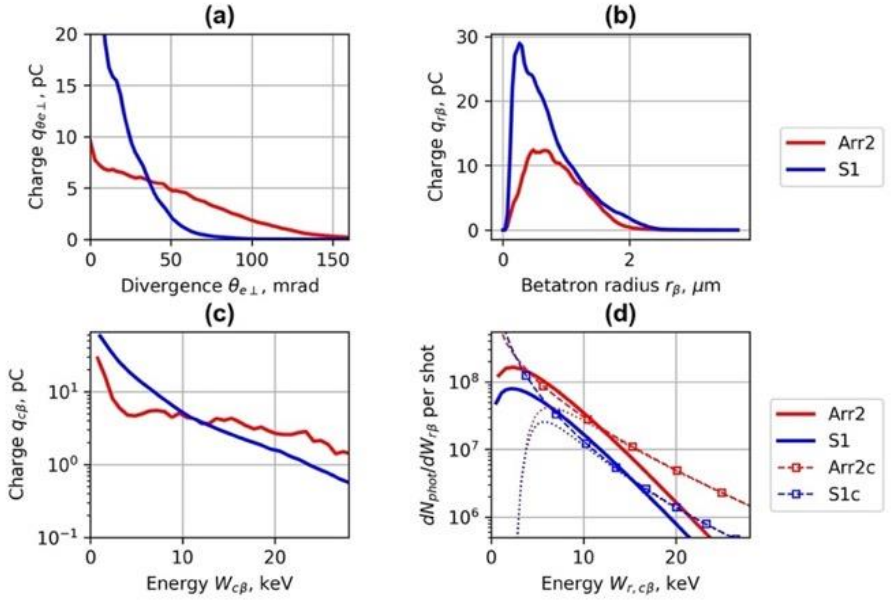

Figure 22. The simulated charge of electrons accelerated by the array **Arr2** and single nozzle **S1** having divergence (FWHM) $\theta_{e\perp}$ **(a)**, betatron radius $r_{c\beta}$ **(b)**, and critical synchrotron energy $W_{c\beta}$ **(c)**. Calculated spectral density $dN_{phot}/dW_{r\beta}$ of photon number per shot for the array **Arr2** and single nozzle **S1 (d)** for $a_0 = 4.0$ and $n_p = 1\times10^{19}$ cm^{-3}. The dashed lines **Arr2c** and **S1c** show the calculated density of $dN_{phot}/dW_{r\beta}$, the dotted lines - the $dN_{phot}/dW_{r\beta}$ attenuated by the materials placed between the X-ray source and camera, and the solid lines **Arr2** and **S1** show the synchrotron-like spectra with the mean critical energy $W_{c\beta}$ measured using Ross filters [140].

The calculations have shown that the implementation of the nozzle array Arr2 increased the number of electrons having a higher transversal divergence (Fig. 22a) and extended the average of betatron radius (Fig. 22b) and critical energy by 15 - 20% (Fig. 22c). Although the increase of betatron radius was relatively small, the increase of electron divergence for the array Arr2 relative to single nozzle S1 was 30-50% (Fig. 21). At the acceleration distance of 2.5 mm, the calculated divergence corresponded to the distribution of electrons in the transversal radius of 50 μm on average.

The resulting X-ray radiation is defined by the superposition of radiation of electrons at different spatial positions. In Fig. 22d, the calculated spectral density $dN_{phot}/\,dW_{r\beta}$ of photon number per shot for the array Arr2 and single nozzle S1 is presented. The calculation demonstrated the increase of the number of photon number per shot caused by the plasma density profile in wiggler geometry 2-3 times, and the total number of photon number reached 5×10^8. The betatron synchrotron parameter K_β increased from 5 to 10, while

changing the plasma concentration from 3×10^{18} cm^{-3} to 1×10^{19} cm^{-3}. With the implementation of the plasma density profile in wiggler geometry, the betatron synchrotron parameter K_β increased from 10 to 14-20. The betatron synchrotron strength parameter K_β was estimated using the relation (38). In these ranges of K_β values, the betatron source operates in the wiggler mode and has a broadband synchrotron-like radiation spectrum.

4.3. Discussion on LWFA Simulation and X-Ray Radiation Parameters

The FBPIC simulation of LWFA has shown that the structured plasma targets can be implemented for the control of injection and acceleration of electrons and enhance the efficiency of secondary betatron X-ray radiation. Varying the density down-ramp gradient, the number of injected electrons, the position of the injected electron bunch, and final electron energy can be changed. According to the relation (21) and 3D PIC simulations [41,42,44], there is an optimal gradient length of the order of the plasma wake wavelength enabling the formation of a quasi-monoenergetic bunch of accelerated electrons. The short length of the plasma down-ramp region leads to the broadening of the energy spectrum because of the large number of injected electrons. The injected space charge modifies the electric field inside the wake and reduces the energy of accelerated electrons. When the density down-ramp length is larger than the plasma wavelength, the electrons are trapped in several wakefield periods. It results in the energy spectrum broadening, and the drop of accelerated electron energy as in the case of sharp transition. When the length of the plasma concentration down-ramp is close to the plasma wavelength, the number of injected electrons is smaller, and the electric field inside the wake is less affected [44]. The slower electrons are injected in the region with higher wakefield and, vice versa, the faster electrons reach the wake wave region where the field is weaker. In such a way, a quasi-monoenergetic bunch a finite length and energy dispersion in pure He is formed (Fig. 18a). Changing the gradient scale and plasma concentration, it is possible to ensure the stable injection and decrease the energy dispersion of accelerated electrons. The charge of accelerated electrons is relatively low, however.

In the case of a single nozzle (Fig. 18cd, 19cd, and 20 a), the ionization injection scheme led to a stable, though continuous injection and broad energy dispersion of accelerated electrons. The charge of injected electrons increased with the increasing of the plasma concentration. The energy of accelerated

electrons reduced, and the energy dispersion was higher (Fig. 21bd). It raised the efficiency of secondary X-ray betatron radiation.

The density triggered injection can be combined with ionization injection using the mixture He+1%N_2. By maintaining the length of plasma concentration gradient close to the plasma wavelength and focusing the laser beam into the beginning region of down-ramp, the injection of higher charge into the plasma wake was achieved (Fig. 18b, 19b, and 20b). The load of the electric field of the wake has to be optimal, however. The laser intensity has to be sufficient to accelerate the bigger number of injected electrons, however not to exceed the threshold of a continuous ionisation injection inside of the plasma bubble. Increasing the laser strength parameter from a_0 = 2.3 to a_0 = 4.0, and using combined ionization and density down-ramp triggered injection resulted in the formation of electron bunch of average energy of 50 MeV (Fig. 19b and 20b). Acceleration of quasi-monoenergetic electron bunches can be achieved using self-truncated ionization injection scheme by focusing of laser beam 1.5 mm behind the gas-jet exit [57]. However, a careful adjustment of the laser profile and spectral-phase correction in the intermediate field before the laser focus is required. Ionization-assisted together with density-down-ramp injection was investigated using two jets of different gases. The first jet with He+N_2 mixture, and the second with pure helium resulted in the generation of quasi-monoenergetic electron bunches [51]. In this work, a more simple and efficient method of combined density triggered and optical ionisation injection using nozzle array in injector geometry and He+N_2 mixture for the formation of stable quasi-monoenergetic electron bunches was proposed.

Implementation of nozzle arrays in the wiggler geometry increased the divergence of the electron beam by a factor 1.5-2 for $n_p = 3\times10^{18}$ cm^{-3} and by 30 - 50% for $n_p = 1\times10^{19}$ cm^{-3} (Fig. 21). The plasma density grid extended the transversal motion of electrons and increased the number of photons per shot and brightness of X-ray radiation 2-3 times (Fig. 22d). More electrons had higher critical energy of synchrotron radiation, and their contribution to the total X-ray emission was larger (Fig. 22c). The resulting spectrum and source size of X-ray radiation was defined by the superposition of radiation of electrons with diverse momenta radiating at different spatial positions in the radius of approximately 50 μm. The prevailing radiation of electrons corresponded to the critical synchrotron energy $W_{c\beta}$ of 2-3 keV.

4.4. Conclusions

The charge, energy, and divergence of accelerated electrons can be controlled by structured plasma targets comprising tailored injector, acceleration, and wiggler sections.

- The charge of accelerated electrons can be increased and the energy dispersion of the electrons can be lowered using combined ionization and density down-ramp triggered injection of the structured plasma concentration profiles in injector geometry.
- The plasma concentration, the diameter of the focused laser beam and pulse duration have to correspond to the LWFA bubble regime, and the length of the plasma concentration gradient has to be close to the plasma wavelength.
- The intensity of the laser beam has to be sufficient to accelerate the higher number of injected electrons and not to exceed the threshold of continuous ionisation injection inside of the plasma bubble.
- With increasing the plasma concentration by a factor of 2-3, the amount of accelerated charge and the divergence of electron beam increase 2-2.5 times. It increases the efficiency of betatron oscillation.
- Introducing the plasma target in wiggler geometry increases the betatron radius and the critical energy of betatron radiation by 15-20%. The betatron radius defined by numerical simulation is 1-2 μm. The radiating electrons at a distance of 2.5 mm are distributed within the radius of 50 μm on average.
- Implementation of plasma target in wiggler geometry for $a_0 = 4.0$ and $n_p = 1 \times 10^{19}$ cm^{-3} increases the divergence by 30-50%, and number of photons per shot of betatron X-ray radiation 2-3 times relative to a single nozzle.

5. NUMERICAL SIMULATION OF GAS TARGETS

The material related to this chapter was published [A1, A2, A3, A4] and in [C1, C2, C3, C4].

To estimate the gas density distribution of structured gas targets, the velocity, pressure, and temperature of gas jets and corresponding shock waves of converging-diverging, and high-density cylindrical capillaries micronozzle arrays were simulated. The numerical simulation was performed using OpenFOAM [139] compressible steady-flow solver rhoSimpleFoam. The Reynolds-averaged Navier-Stokes (RANS) k_t - ω_t Shear Stress Transport (SST) turbulence model was applied. The turbulence was described using two transport equations and two variables k_t and ω_t, where k_t is the turbulent kinetic energy and ω_t - the specific rate of dissipation of the turbulence kinetic energy k_t into internal thermal energy. A general thermo-physical model of calculation was based on internal energy and compressibility parameter $\psi=1/R_{spec}T$, where R_{spec} is the specific gas constant and T is the temperature. For the estimation of the dependence of gas concentration n_g on backing pressure, the approach of ideal gases was used. The molecular concentration of ideal gases n_g was calculated as $n_g = N_A \rho/M_m$, where N_A is the Avogadro constant and M_m is the molar mass of the gas [174]. At the standard temperature and pressure of T=273.15 K, and P=101.325 kPa, n_g corresponds to 2.687×10^{25} m^{-3}. For the calculation of the molecular gas concentration of the same gas under two different conditions of the pressure $P_{1,2}$, volume $V_{1,2}$ and temperature $T_{1,2}$, the relation $p_1V_1/T_1= p_2V_2/T_2$ was used. The molecular gas concentration increases proportionally to the ratio of actual pressure and temperature. Material properties used in the simulation are given in Table 6.

Table 6. Material properties used in simulation [174]

Properties	Units	Nitrogen	Helium
Molecular mass	g/mol	28.02	4.02
Density at 1 bar and 273.15 K	kg/m^3	1.256	0.185
Specific heat capacity C_p	J/kg K	1004	5193
C_p/C_v	-	1.4	1.67
Speed of sound at 273.15 K	m/s	331.2	973
Sutherland constant A_s	-	1.458×10^{-6}	1.633×10^{-6}
Sutherland temperature T_s	K	110.8	147.0
Refractive index n at 632 nm, 1 bar and 273.15 K	-	1.000298	1.0000349

The actual values of the density, the speed of sound and refraction index were recalculated in the simulation based on the local values of pressure and temperature. Nitrogen gas was implemented as the main modelling media to define optimal geometries of the nozzles during their manufacturing. The results are applicable also to helium frequently used as a laser wakefield acceleration media. The concentration differences at the nozzle outlet for nitrogen and helium are in the range of 7-10% only.

The dynamic viscosity of the fluid μ_s was calculated according to the Sutherland viscosity model as a function of the temperature T from the Sutherland coefficient A_s and Sutherland temperature T_s, according to:

$$\mu_s = \frac{A_s\sqrt{T}}{\left(1+T_s/T\right)}. \tag{66}$$

Inlet and outlet boundary conditions were defined as the total pressure P_0 calculated by the static gas pressure P, velocity vector U and density ρ:

$$P_0 = P + \frac{1}{2}\rho\vec{U}^2, \tag{67}$$

Fixed velocity and temperature were set at the inlet boundary and the static pressure was defined at the outlet boundary. For the wall type boundaries, the no-slip condition was used, and the two-dimensional geometry of wedge symmetry was implemented.

For the formation of high-concentration plasma profiles, the gas jet expansion in to the vacuum of capillary-micronozzles was investigated. The capillaries of fixed diameter have lower gas expansion rate of 1.2-1.4 at the outlet of the nozzle compared to the typical converging-diverging de Laval nozzles. The sonic line, where the gas velocity equals the speed of sound (the Mach number M = 1), is located inside of the capillary [175]. The flow in the major part of the channel is subsonic. Starting with the pressure difference of approximately 700 mbar, the gas velocity reaches the speed of sound and M = 1.2-1.4 in the vicinity of the exit cross-section [176]. Because of the strong pressure gradient, the streamlines overcome the viscous shear forces of the walls and form a converging-diverging boundary layer of varying thickness close to the capillary exit [177]. In such a way, an effective de Laval nozzle is formed and the gas is accelerated to supersonic velocities.

5.1. Numerical Simulation of High-Density Capillaries

The simulated images of gas concentration and Mach number of nitrogen and helium at the backing pressure of 60 bar of a cylindrical nozzle with a fixed diameter of 300 μm are presented in Fig. 23. The simulation area comprises the length of microcapillary of 2.8 mm and 6 × 4 mm simulation area of the expansion of the gases. Because of the high aspect ratio 1:18 (150 μm and 2.8 mm) only the part of the simulation - 600 × 600 μm close to the outlet of the nozzle - is shown.

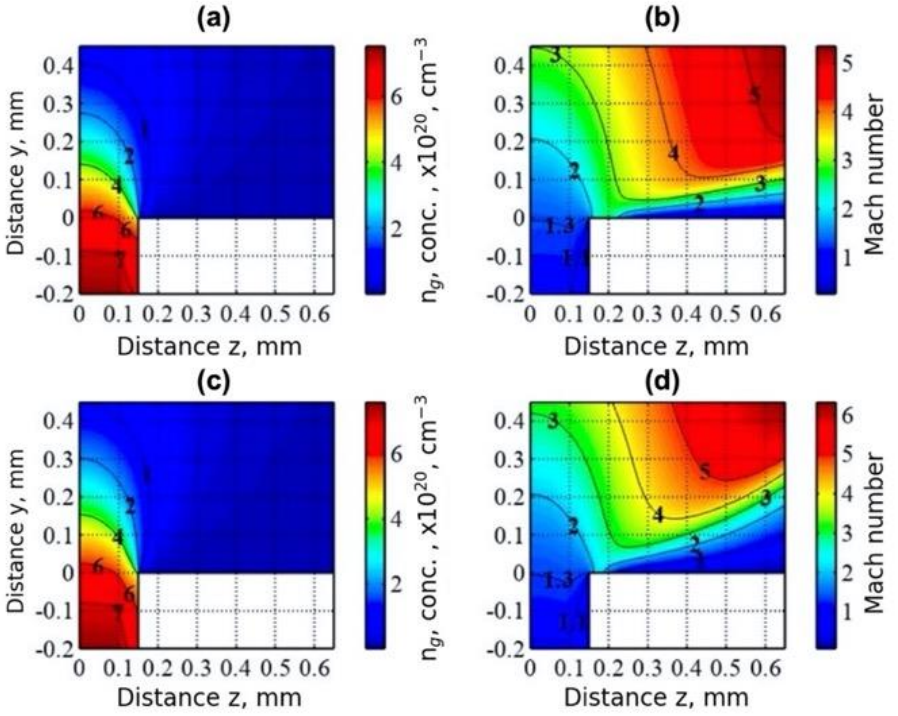

Figure 23. Simulated gas concentration **(a)**, Mach number **(b)** of nitrogen and concentration **(c)** and Mach number **(d)** of helium at the backing pressure of 60 bar of a cylindrical nozzle with the fixed diameter of 300 μm [139].

The concentrations at the outlet of the nozzle for nitrogen and helium are similar, as the gas density ρ depends on the Mach number M being close to critical to both of gases [139]:

$$\frac{\rho}{\rho_0} = \left(1 + \frac{k_a - 1}{2} M^2\right)^{\left(\frac{1}{k_a - 1}\right)}, \tag{68}$$

where ρ_0 is the critical density at the point where gas flow turns from subsonic to supersonic. Slight differences of concentration are caused mainly by the difference of the adiabatic index k_a of monoatomic gas of helium (5/3 = 1.67) and adiabatic index of diatomic nitrogen gas (7/5 = 1.4). Higher deviations of Mach number between nitrogen and helium at larger distances depend on the gas temperature and speed of sound being inversely proportional to the square root of the molecular mass of gases. Helium having lower molecular mass expands quicker, and the local temperature drops to the lower values compared to nitrogen. It results in higher Mach numbers of helium defined as a ratio of gas flow velocity and local speed of sound.

5.2. Impact of the Wall Roughness on the Quality of Nozzles

To evaluate different microfabrication techniques, the impact of the wall roughness on the quality and jet concentration of cylindrical micronozzles, manufactured from fused silica, with fixed diameters of 50 μm, 100 μm and 200 μm, was investigated. The simulation of the impact of the wall roughness on the gas flow in Laval nozzles of the diameter of millimeter dimensions can be performed using analytical methods of isentropic gas flow. However, the simulation results of the isentropic gas flow of the nozzles of the size of tens and hundreds of micrometers differ significantly from the experimental results [178]. The methods of computational fluid dynamics were used for the analysis of the impact of the wall roughness on the supersonic gas flow inside of the cylindrical nozzle. Triangle mesh was created in the simulation area except for the region close to the wall. For the modelling of the boundary layer, a quadrilateral cell mesh with increasing thickness was implemented. Subsonic and supersonic gas flow was simulated using Reynolds-averaged Navier-Stokes (RANS) formulation and the two-equation k_t-ε_t turbulence model, where ε_t is the rate of dissipation of turbulent kinetic energy. Gas flow and heat exchange in the boundary layer were evaluated using a wall functions method. Boundary conditions at the input were defined by the total pressure P_0 (comprising static and dynamic pressure), uniform input velocity and fluid temperature T_0. On the wall, the no-slip boundary condition, and at the outlet, a boundary condition of fixed static pressure 0.1 mbar was applied. Nitrogen gas was implemented as a modelling media. The dynamic viscosity of the fluid μ_s was calculated according to the three coefficient Sutherland viscosity model as a function of the temperature T, reference value of viscosity μ_0 = 1.7894×10^{-5} Pa/s, a reference ambient temperature T_0 = 273.11 K and Sutherland temperature T_s = 110.56 K:

$$\mu_s = \mu_{s0}\left(\frac{T}{T_0}\right)^{\frac{3}{2}}\frac{(T_0+T_s)}{(T+T_s)}. \tag{69}$$

Wall roughness was modelled using two parameters: k_{rf}, which is equivalent to the sand roughness height, defined as roughness on turbulent flows by measuring the pressure drop in pipes coated with uniform sand grain and non-dimensional roughness parameter C_{ra}, which can allow for other types of roughness [156]. Experimentally, a number of different parameters was defined to characterise the surface roughness. The estimation of sand-grain roughness parameter k_{rf} based on the relations with measured surface roughness values is presented in Table 7.

An arithmetic average of absolute values R_a was calculated as:

$$R_a = \frac{1}{n}\sum_{i=1}^{n}|y_i|, \tag{70}$$

where y_i is the distance from the average height of a profile for measurement i, and n is the number of measurements. R_{RMS} and R_{zd} roughness parameters were calculated correspondingly as a mean squared and the peak-to-valley values of from the average height of a profile using relations (71, 72).

Table 7. Estimated sand-grain roughness based on measured surface roughness parameters [178]

Measured surface roughness parameter	Estimated sand-grain roughness, k_{rf}
R_a	$k_{rf} = 5.863R_a$
R_{RMS}	$k_{rf} = 3.100R_{RMS}$
R_{zd}	$k_{rf} = 0.978R_{zd}$

The peak-to-valley parameters R_{pi} and R_{vi} refer to the largest distances above and below the mean line for one of five measurements with equal scanning length in the longitudinal direction.

$$R_{RMS} = \sqrt{\frac{1}{n}\sum_{i=1}^{n}y_i^2} \tag{71}$$

$$R_{zd} = \frac{1}{5}\sum_{i=1}^{n}\left(R_{pi} - R_{vi}\right) \tag{72}$$

The fluid entering a pipe develops a velocity profile due to viscous forces propagating from the interior wall of a pipe. The viscous drag on the wall

decreases the velocity of the gas flow and leads to the formation of the boundary layer. In the case of laminar flow, the velocity profile becomes parabolic in the fully developed region. In the case of turbulent flow, the velocity profile is more flattened because of mixing in a radial direction [179]. The length of the entry region along the pipe is a function of Reynolds number Re of the flow. In the case of laminar flow, the hydrodynamic entry length L_{lam} can be estimated by $L_{lam} = 0.06\ Re\ D_h$, where D_h is the hydraulic diameter or inside pipe diameter in the case of circular pipe [179]. L_{lam} can exceed the pipe diameter by 2 orders or magnitude. For turbulent flow, the entry length L_{turb} is much shorter. The entrance effect becomes insignificant beyond a pipe length of approximately 10 times - $L_{turb} \sim 10D_h$. The Reynolds number can be calculated as $Re = \rho U D_h/\mu_s = Q_p D_h/A/\nu$, where $\nu = \mu_s/\rho$ is the kinematic viscosity, Q_p is the volumetric flow rate, and A_p is the pipe's cross-sectional area [150,179].

For the nitrogen with $\mu_s = 1.663 \times 10^{-5}$ kg/m/s and M=1.4 at the capillary outlet for the micronozzles with the diameter of 50-200 μm, the Reynolds number vary in the range of 4.0×10^4 - 1.6×10^5. In this range of Reynolds numbers, the flow is turbulent. The surface-to-volume ratio of the flow increases with the reduction of pipe diameter and increasing of wall roughness. The contact area between the gas and wall becomes larger. It results in increased friction and loss of the energy between the flowing gas and the wall. The velocity and total pressure of the gas flow drop [150].

The simulation results, presented in Fig. 24a, indicate that wall roughness with sand-grain roughness parameter k_{rf} = 2.5 μm (second line) has a considerable impact on the gas concentration values at the outlet of the 50 μm-diameter cylindrical nozzle. In the case of roughness parameter k_{rf} = 0 μm, the flow at the distance of 2.8 mm is not developed and the velocity profile is more flattened (Fig. 24b). With the increase of roughness parameter k_{rf} to 2.5-15, the turbulence and thickness of the boundary layer become larger. The velocity profile gets more developed. However, both the total and static pressure as well as gas concentration at the outlet of the nozzle drop. For the roughness parameter k_{rf} of 10-15 μm, the friction energy losses raise the temperature in the vicinity of the wall. It results in an increase of pressure and gas concentration in the boundary layer (Fig. 24cd). The gas concentration at the axis of the 50 μm - diameter nozzle with sand-grain roughness parameter k_{rf} = 2.5-10 μm drops by 23% relative to the smooth wall with k_{rf} = 0 μm (Fig. 24a). The impact of wall roughness on the nozzle with a diameter of 100 μm is relatively smaller. The gas concentration on the axis of the nozzle with sand-grain roughness parameter k_{rf} = 10 μm (second line) concentration drops by 17% relative to the smooth wall (Fig. 24c). The simulation results of

the nozzle with a 200 µm diameter, presented in Fig. 24 d, show that the impact on the concentration at the outlet of the nozzle does not exceed 7% for sand-grain roughness parameter k_{rf} up to 15 µm.

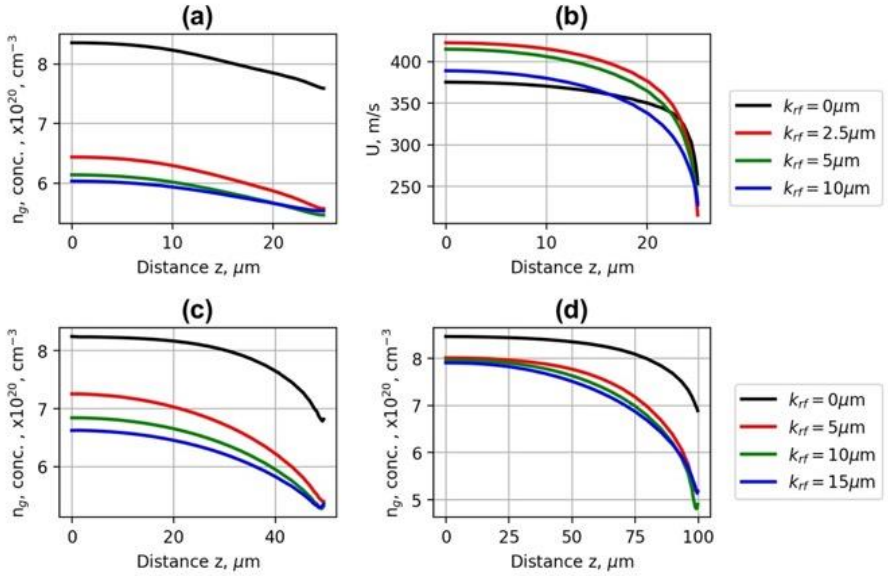

Figure 24. Simulated transversal N_2 concentration **(a, c-d)** and velocity **(b)** profiles at 60 bar backing pressure at the valve of the nozzles with the fixed diameter of 50 µm **(a, b)**, 100 µm **(c)** and 200 µm **(d)** and different values of the sand-grain roughness parameter k_{rf} [156].

Additionally, the chipping of the channel edges was modelled by approximation of the outlet section of the capillary by a cone with the angle of 30°. The modelling has shown that the chipping of the channel edges results in the more stochastic behaviour of the concentration of the gas jet and deviations of the concentration can not be described by the symmetrical model of cylindrical nozzles. The chipping of the edges reduced gas concentration of cylindrical nozzles by additional 15-17%.

5.3. Implementation of Shock-Waves in Structured Plasma Profiles

In Fig. 25, the simulation results of the velocity, temperature, gas pressure, and concentration of the micronozzle array Arr3 are presented. The interference of shock waves of colliding jets resulted in the formation of diamond-shaped pressure (Fig. 25c) and density (Fig. 25d) grid. The shock waves also affected the region of the nozzle array used for LWFA. Thus, the region was compressed, and a shock wavefront between the first and second part of the array was built.

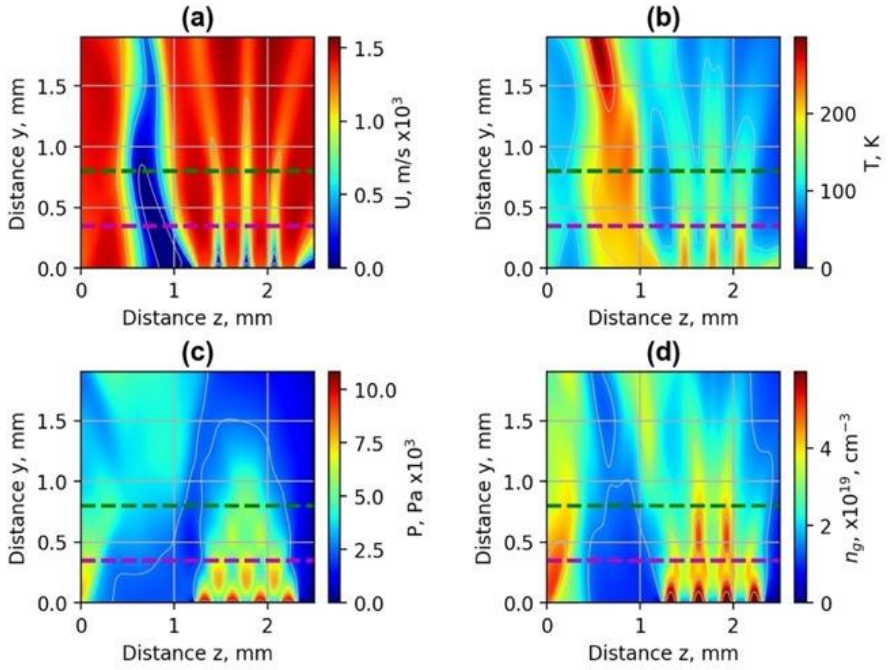

Figure 25. Simulated spatial distribution of a velocity (**a**), temperature (**b**), pressure (**c**) and concentration (**d**) of the gas jet of **Arr3** at the backing pressure of 30 bar. The green dashed line indicates the distance of the laser beam of 800 μm, and the magenta dashed line shows the distance of 400 μm above the nozzle [140].

The shock waves increased the gas density of the middle jets by a factor of 2 relatively to the edge jets not having the neighbouring jet streams. The middle jets reached the height of 0.9-1.2 mm while the height of outside jets was 0.5-0.6 mm. The laser beam propagating at different distances above the nozzle can cross different profiles of plasma concentration. In Fig. 25 cd, the green and magenta dashed lines indicate the laser-nozzle distance of 800 μm and 400 μm, correspondingly.

In Fig. 26, the simulated profiles of molecular nitrogen concentration of One-Sided Shock (OSS) nozzle proposed by LOA are presented. The formation of the shock-front was designed in the construction of the nozzle, consisting of a 100μm throat and 300μm exit diameter “De Laval” nozzle having a one-side straight section of 100μm at the outlet of the nozzle.

3D CFD simulation was realized at LOA using the software ANSYS Fluent at the backing pressure of 20bar. The simulation clearly shows the down-ramp gradient originating from the shock-front at the upper straight section of the nozzle wall.

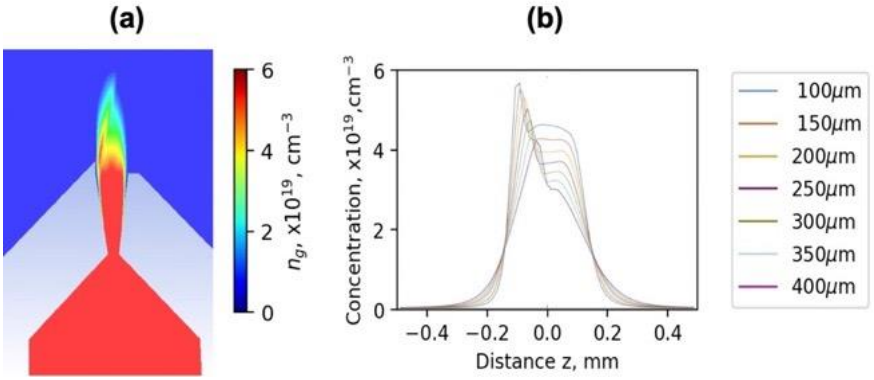

Figure 26. 2D gas concentration of molecular nitrogen One-Sided Shock jet of the diameter of 300 mm simulated using Fluent 3D at a backing pressure of 50 Bar **(a)**, and 1D gas concentration profiles at different heights above the nozzle outlet **(b)** [136].

5.4. Discussion on Simulation of Computational Fluid Dynamics

The simulation results of Computational Fluid Dynamics (CFD) have shown that the structured plasma targets can be formed using gas jets of converging-diverging and high-density cylindrical nozzles of fixed diameter. The density profiles can be shaped by implementing the interference of intersecting shock waves. Depending on the nozzle expansion rate and backing pressure of 20 to 60 bar, the gas concentrations of converging-diverging nozzles of 1×10^{18} - 8×10^{19} cm^{-3} at the distance of 400-800 μm from the outlet of the nozzle can be achieved. The gas concentration of converging-diverging nozzles drops slowly by a factor of 1.5-2 at the distance of a diameter from the outlet. The gas concentration at the exit of cylindrical micronozzles of fixed diameter at the 20-60 bar of backing pressure was in the range of 2-6×10^{20} cm^{-3}. This value is higher relative to converging-diverging nozzles with the throat of the same size as the cylindrical nozzle. The outlet area of converging-diverging nozzles is typically several times greater than the critical area of the throat. The gas concentration of cylindrical nozzles dropped by orders of magnitude at the distance of 4-5 diameters from the outlet. At these distances, the gas concentration depends linearly on the backing pressure of the valve. The density at the outlet of the cylindrical nozzle is close to the critical density of subsonic flow inside of the capillary, and the Mach number of the gas jet is in the range of 1.2-1.4. Leaving the capillary, the gas expands quickly, and at the distance of the diameter of the nozzle, reaches the velocity of 2-3 Mach. At a distance, being equal to 0.5-0.7 diameters of the nozzles from the outlet, the concentration profile is relatively

flat, and the concentration changes 20-30% within the focused beam of 10-20 μm at FWHM of accelerating laser. The concentration can be raised by increasing the backing pressure several times. The maximal pressure is limited by the mechanical characteristics of the valve and strength of the material. The supersonic converging-diverging nozzles have advantages where more extended flat profiles with modest gas concentration and long focusing length of the laser beam are implemented. Cylindrical nozzles of fixed diameter have advantages where high-density, short-length gas targets are required, and the laser beam is focused close to the nozzle outlet area.

The simulation results of the cylindrical nozzle with the roughness parameter of 5-10 % from the diameter of the nozzle have shown that the thickness and turbulence of the boundary layer in the vicinity of the wall increases. Because of the friction losses, the pressure and gas concentration at the outlet of the nozzle drops. At the roughness parameter of 10 % from the diameter of the nozzle, the concentration drops by 17% relative to the smooth wall.

The CFD simulation demonstrated the formation of pressure and density grid above the nozzle array caused by the intersecting shock waves in gas. The interference of shock waves is defined by the period of nozzle array as well as by the pressure, temperature, and expansion rate of colliding jets. Alternatively, it was demonstrated that the density down-ramp gradient could be formed by a shock wave reflected from the side of the nozzle wall (Fig. 26).

5.5. Conclusions

Structured plasma targets can be built by combining the jets of converging-diverging micronozzles and micronozzles of fixed diameter and shaping the density profiles by intersecting shock waves of supersonic jets:

- Depending on the longitudinal and transversal density profile requirements, the gas jets building structured plasma targets can be formed using converging-diverging cylindrical, slit nozzles as well as cylindrical nozzles of fixed-diameter.
- The gas density down-ramp regions required for injector and wiggler geometry can be built by superposition of intersecting shock waves of supersonic jets or jets reflected from the nozzle wall.
- The position of the shock-wave front defines the position of the density down-ramp in the nozzle arrays in injector and wiggler geometry.

- The surface roughness has an impact on the quality of the jet when the sand-grain roughness exceeds 1-2% of the diameter of the nozzle diameter or the diameter of the throat of the converging-diverging nozzle.
- The chipping of the nozzle edge at the angle of 30° of the cylindrical nozzles of fixed diameter decreases the gas concentration at the outlet of the nozzle by 15-17%.

6. MANUFACTURING AND CHARACTERIZATION OF MICRO-NOZZLES

The material related to this chapter was published [A2, A3, A4, A5, A6, A7] and in [C1, C2, C3, C4, C5, C6, C7].

6.1. Hybrid Method of 3D Laser Manufacturing

A novel method of hybrid 3D laser machining technique for the manufacturing of nozzle arrays was developed [139]. Fast removal nanosecond rear-side processing was used for the frame manufacturing, and Femtosecond Laser-assisted Selective Chemical Etching (FLSE) technique was implemented for the high-precision channel formation. The nozzle consisted of the 12-35 mm-diameter holder with a frustum of a cone and micronozzles, fabricated along the element axis. The commercially-available 150 x 150 mm^2 and 76 mm-diameter fused silica plates with the thicknesses of 6.3 mm and 12.7 mm, respectively, were used as raw material. The flowchart of different laser processing techniques tested in manufacturing is presented in Fig. 27.

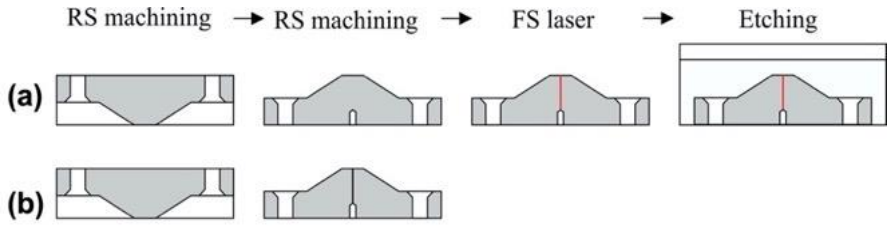

Figure 27. The flowchart of nozzle fabrication by hybrid laser machining technique **(a)**, and nanosecond rear-side machining **(b)**. In the processing steps, the laser beam propagates from top to bottom [156].

In the case of hybrid laser machining technique (Fig. 27a), in the first step, the large volume of the material was removed by nanosecond laser pulses via highly-efficient rear-side machining technique and the preform for a nozzle was fabricated. Gas jet nozzles were fabricated using the second harmonics (532 nm) of a diode-pumped solid-state (DPSS) laser (from Ekspla). The pulse duration, measured at full-width at half-maximum, was 4.5 ns. The laser system provided the maximum average laser power of 18 W at the 200 kHz pulse repetition rate. The galvanometer scanner intelli*SCAN* 14 (from SCANLAB) was used to guide the laser beam in the XY plane, focused by the

telecentric f-theta lens with the focal length of 80 mm. The diameter of the focused beam at the $1/e^2$ level equalled to 10.5 µm. Typical pulse energy and laser fluence was 90 µJ and 210 J/cm^2, respectively. The material removal rate was over 2 mm^3/s. In the second step, the sample was turned upside down, and the adapter was fabricated via rear-side machining to connect the micronozzle to the valve and to reduce the thickness of glass to 2 mm for processing using FLSE.

In the third step, the material was modified using a femtosecond laser and then etched in a KOH solution of 10M concentration to form a microchannel for 22 hours. This technique allowed to fabricate 40-50 µm-diameter channels, while for the nanosecond rear-side machining alone (Fig. 27b), the minimum diameter was 100 µm. The wavelength, pulse duration FWHM, and pulse energy of the femtosecond laser system (Yb:"KGW Pharos" laser from Light Conversion) were 515 nm, 300 fs, <1 µJ, correspondingly. The repetition rate was set to 500 kHz, and the processing speed was 0.5 mm/s to ensure the 1000 pulses/µm density. The laser beam was focused with a 100x microscope objective (from Mitutoyo, NA=0.5) to achieve ~2 µm spot size.

The vertical channel was formed according to the fabrication geometry, demonstrated in Fig. 28a. The whole channel length was divided into nine sections with a single section length of ~230 µm. The section was composed of the layers consisting of a set of concentric circles, which increased the etched cavity size.

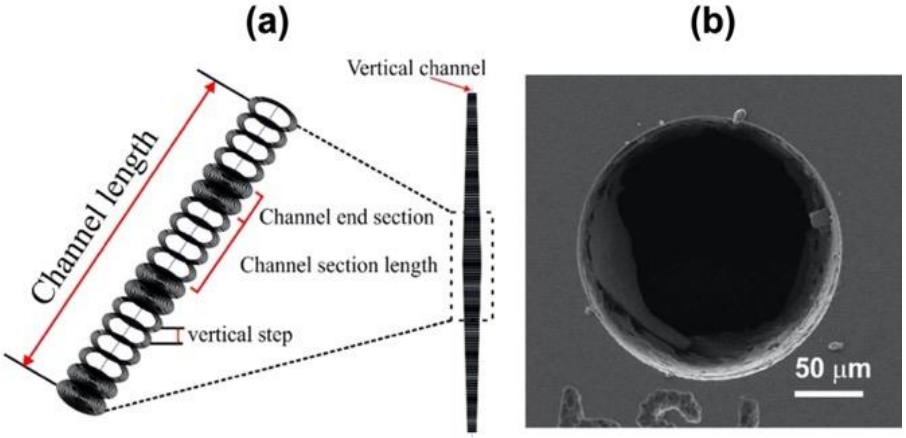

Figure 28. Fabrication geometry of the modifications of the nozzle channel prepared for the chemical etching **(a)** and the SEM picture of the channel entrance after 22 h etching in 10M KOH **(b)** [139].

The concentric circles were manufactured by translating the sample relative to the laser focus with the XY positioning system that allows the accuracy of ~300 nm (Aerotech ANT150). The single-layer was not entirely filled by the circles to minimise the fabrication time. The z step between the layers in the single section was defined experimentally and was 4-5 μm. The circle's radius in the layer was changed by the 1.5 μm step.

This sectional fabrication facilitated the access of KOH to the modified structure. During the etching process, the etched section was separated and fall out. Therefore the clear etchant could achieve the deeper sections. Due to the aberrations [139], for the deeper focusing the pulse energy dissipated, and higher energy was needed to induce the required modifications. In this way, ~300 nJ pulse energy was used for the first section, and ~800 nJ pulse energy - for the last section. The vertical channel shape was precompensated by changing the maximum section radius to achieve the taper-less microchannel. The total laser fabrication time of 100 μm diameter channel was ~21 min. In such way, the manufacturing showed no chipping on the microchannel entrance surface, shown in Fig. 28b, and the diameter accuracy control has been improved up to +/- 2 μm, depending on the channel size precompensation. The images of a nozzle with cylindrical microcapillary manufactured by a hybrid technique are presented in Fig. 29.

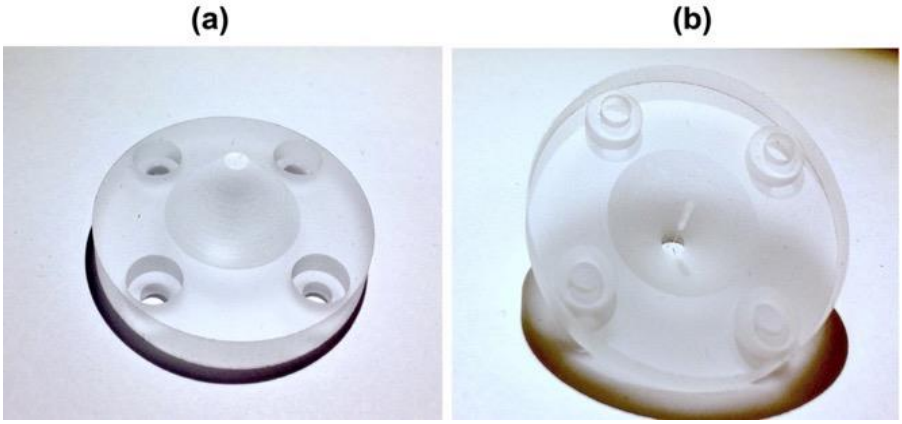

Figure 29. The frame of the nozzle structure (diameter 35 mm, height 12.7 mm) **(a)** of 2 mm-length capillaries with the outlet diameter of 100 μm **(b)** , laser-machined in fused silica with the subsequent etching in KOH [139].

The optical microscope images of fabricated Laval micronozzle arrays and One-Sided Shock nozzle (OSS) [136,140] using the FLSE technique are presented respectively in Fig. 30 and 31a.

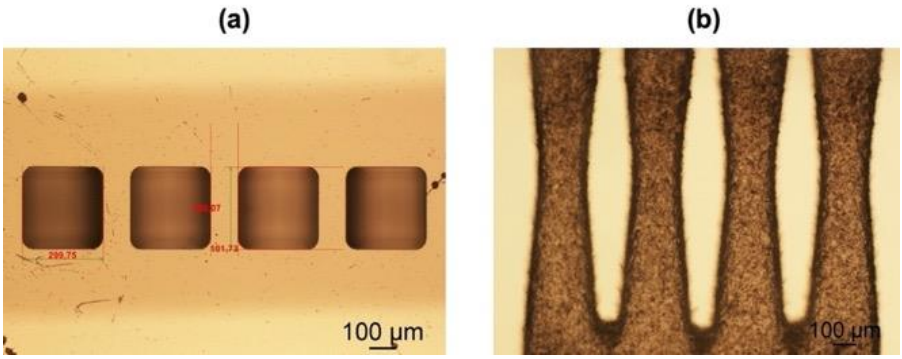

Figure 30. The top **(a)** and cross-section **(b)** images of Laval micronozzle array of the diameter of 200 µm, manufactured using the FLSE technique.

The frame of the OSS nozzle was manufactured using ns-rear side processing, and the inner channel was produced by FLSE technique. The upper surface was finished using femtosecond and picosecond ablation, enabling more precise processing than the ns-rear side technique.

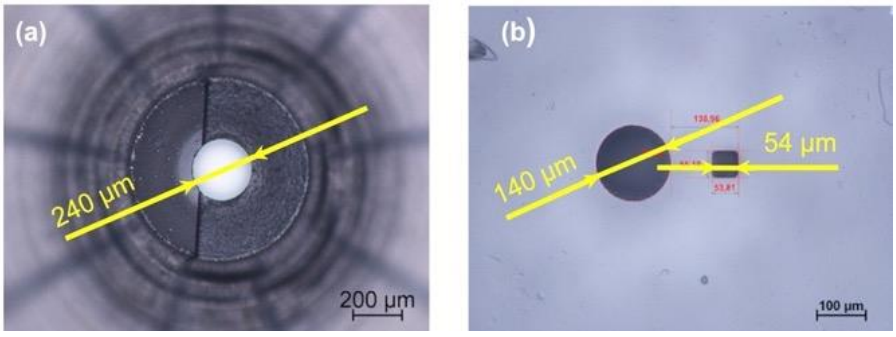

Figure 31. Optical microscope images of One-Sided Shock nozzle **(a)**, and double nozzle of the diameter of 140 µm and 54 µm **(b)** manufactured by FLSE technique used in LOA experiments.

6.2. Dependence of the Nozzle Quality on Surface Roughness

The quality and wall roughness of nozzles, manufactured from fused silica using three different laser processing techniques: the hybrid nanosecond rear-side processing and femtosecond laser-assisted selective etching (FLSE) technique [139,156], the nanosecond laser rear-side (RS) processing

alone [146], and nanosecond laser rear-side processing technique with the subsequent etching in KOH solution for 4 hours was investigated (Fig. 32).

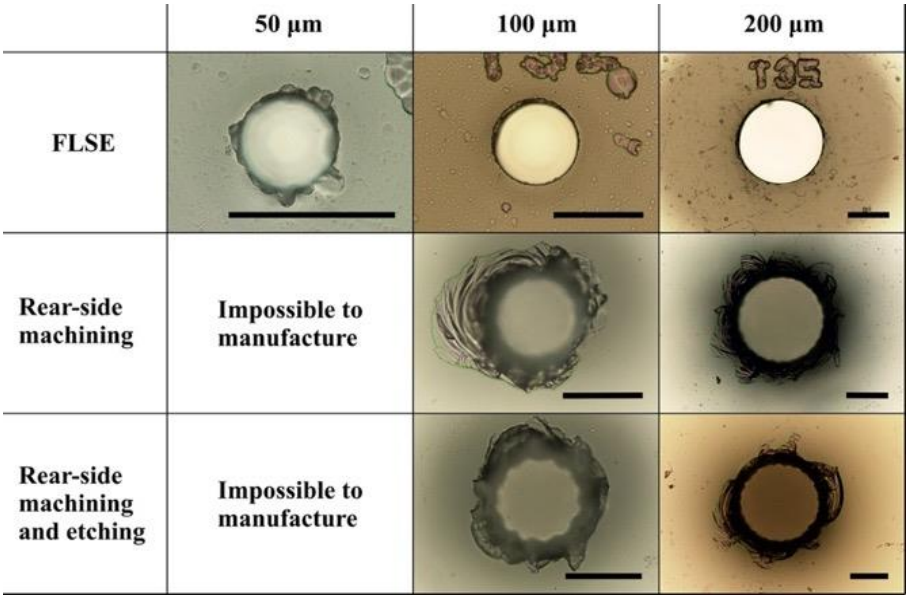

Figure 32. Optical microscope images of cylindrical nozzles, manufactured via different techniques. Scale bar is 100 µm-length [156].

The cylindrical nozzles with a diameter of 50 µm, 100 µm and 200 µm were fabricated and characterised using Mach-Zehnder interferometer and gas jet concentration reconstruction. FLSE allowed the manufacturing of 100 µm and 200 µm-diameter nozzles with excellent geometry and chip-free edges. However, slight chipping (~10 µm) appeared in 50 µm-diameter holes. It should be noted that the real diameter of 50 µm nozzle was 56 µm. In the case of nanosecond laser rear-side machining technique, the surface chipping was about 100 µm. The actual diameters of nozzles, discussed below, were 92 µm, manufactured using FLSE technique, 105 µm, drilled using nanosecond laser rear-side processing and 108 µm, produced by nanosecond laser rear-side processing technique and etched additionally in KOH solution for 4 hours. For simplicity, these are referred to 100 µm-diameter nozzles. The real diameters of 200 µm nozzles were 204 µm, 204 µm and 210 µm, respectively. The blurred grey and black area around the holes, which were fabricated using nanosecond laser, indicates that the outlet edge of nozzles is chamfered. Therefore, the profiles of microchannels were investigated using stylus profiler Dektak 150 (from Veeco).

The typical profiles at the outlet of nozzles with the diameter of 100 µm and 200 µm fabricated by nanosecond rear-side machining technique alone are presented in Fig. 33ac, and with the subsequent etching in KOH solution - in Fig. 33bd. A grey area represents the ideal cylindrical nozzle, while the distance x = 0 µm is the axis of a nozzle. Red dotted contours show the geometry of the chamfered edge, used for the simulations of a conical outlet with the angle of 30^0.

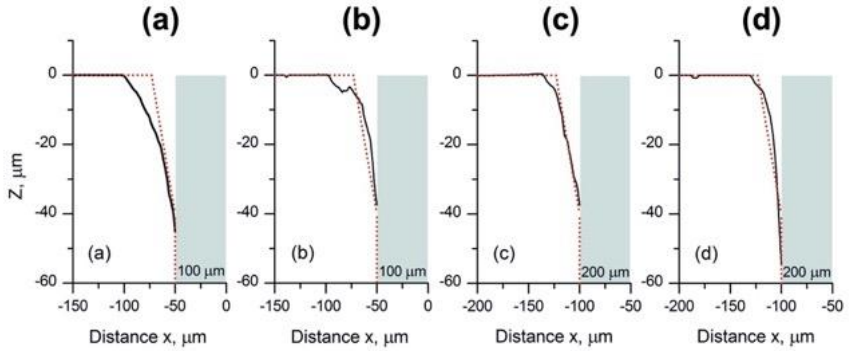

Figure 33. Measured profiles (solid black lines) at the outlet of cylindrical nozzles with the diameter of 100 µm **(a, b)** and 200 µm **(c, d)**, fabricated by nanosecond rear-side machining technique alone **(a, c)** and by nanosecond rear-side machining technique with the subsequent etching in KOH **(b, d)**. A grey area represents the ideal cylindrical nozzle, while the distance x = 0 µm is the axis of a nozzle. Red dashed contours show the geometry of the chamfered edge, used for simulations [156].

After the initial interferometric measurements, the surface of the nozzles, drilled using nanosecond laser rear-side processing and produced by nanosecond laser rear-side processing technique and etched additionally in KOH solution, were polished. The upper layer, containing the chamfered edge, was removed. The right angle of the outlet edge was nearly restored, and the concentration profiles were measured again. The scanning electron microscope (SEM) images of the opened microchannels are presented in Fig. 34a-c. The topologies of surfaces, fabricated by nanosecond laser rear-side machining alone and with the subsequent etching in KOH for 4 hours are presented in Fig. 34d and 34e, respectively. The measured surface roughness and estimated sand-grain roughness parameter k_{rf}, according to the relations, are presented in Table 8. The average roughness and average peak-to-valley distance of a nozzle, fabricated by rear-side machining technique, were R_a = 1.4 µm and R_{zd} = 8 µm. The subsequent etching in KOH for 4 hours

resulted in a rougher surface with the average roughness of 1.7 µm (R_{zd} = 10.4 µm).

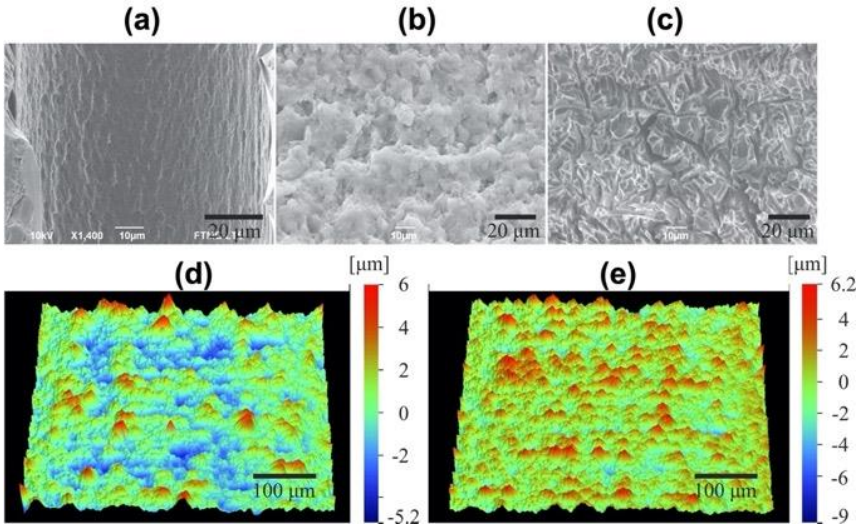

Figure 34. SEM images of the opened microchannels, fabricated by FLSE technique **(a)**, nanosecond rear-side machining **(b)** and rear-side machining with the subsequent etching in KOH **(c)**. 0.5 x 0.4 mm^2 topographies of the flat surface, fabricated by rear-side machining **(d)** and rear-side machining with the subsequent etching in KOH **(e)** [156].

Using femtosecond and picosecond ablation, the surface roughness R_{zd} of 3-5 µm, correspondingly, was achieved. In comparison, the FLSE technique allowed to reach the significantly smoother surface. In this case, the average roughness and average peak-to-valley distance were R_a = 0.12 µm and R_{zd} = 0.57 µm.

Table 8. The measured surface roughness of the fabricated channels and estimated sand-grain roughness parameter, according to the relations, given in Table 7 [156].

	FLSE	RS machining	RS machining and etching
R_a [µm]	0.12	1.4	1.7
R_{RMS} [µm]		1.7	2.1
R_{zd} [µm]	0.57	8	10.4
k_{rf} @ R_a [µm]	0.70	8.2	10.0
k_{rf} @ R_{RMS} [µm]		5.3	6.5
k_{rf} @ R_{zd} [µm]	0.56	7.8	10.2

The estimated sand-grain roughness parameter k_{rf}, based on the average roughness and average peak-to-valley distance, was in the submicron range for FLSE technique, while for the rear-side machining alone and with subsequent etching in KOH it was equal to ~8 μm and ~10 μm, respectively. The values of sand-grain roughness, estimated according to the root-mean-square roughness R_{RMS}, were slightly lower.

6.3. Characterization of Gas Jet Profiles

The results of simulated (left side) and reconstructed (right side) transversal nitrogen concentration profiles from measured interferograms of cylindrical nozzles with the diameter of 50 μm, 100 μm, and 200 μm using IDEA software package [162] and Abel transformation [180] are given in Fig. 35. The concentration profiles of nozzles, manufactured by FLSE technology, are presented in Fig. 35abe, and the concentration profiles of nozzles, fabricated by nanosecond rear-side machining technique, are given in Fig. 35cf. The concentration profile of a 100 μm-diameter nozzle, made by the nanosecond rear-side machining technique with the subsequent etching in KOH, is shown in Fig. 35d. Additionally, the impact of edge chipping at the outlet of the nozzle channel, fabricated by the nanosecond rear-side machining technique, was estimated. Chipping resulted in the formation of the conical chamfered edge with the angle of 30 degrees at 40 μm depth below the outlet of the nozzle. The chipping decreased the gas concentration at the outlet of the nozzle by 15-17%. The total reduction of the concentration, comprising the impact of wall roughness with the parameter k_{rf} = 10 μm and edge section with the angle of 30 degrees, was 30% for the nozzle with the diameter of 100 μm, and 20% for the nozzle with the diameter of 200 μm. The subsequent etching of channels, fabricated with nanosecond rear-side machining technique, in KOH solution for 4 hours resulted in the quite different surface morphology, as seen in Fig. 34ce, and higher sand-grain roughness parameter equalled to 10 μm. The gas concentration, measured at 60 bar backing pressure at the outlet of 50 μm cylindrical channel, manufactured by FLSE technique, at the distance of 40-60 μm from the outlet of the nozzle was $1\text{-}2\times10^{20}$ cm^{-3}. The gas concentration, measured at the outlet of 100 μm cylindrical channel, fabricated by nanosecond rear-side processing technique, at the distance of 50-80 μm from the outlet of the nozzle was 25-30% lower relative to the channel with the sand roughness of the wall k_{rf} = 0.56 μm, achieved by FLSE technique. The measured gas concentrations were $1.4 - 2.2\times10^{20}$ and $1.8 - 3\times10^{20}$ cm^{-3}, correspondingly.

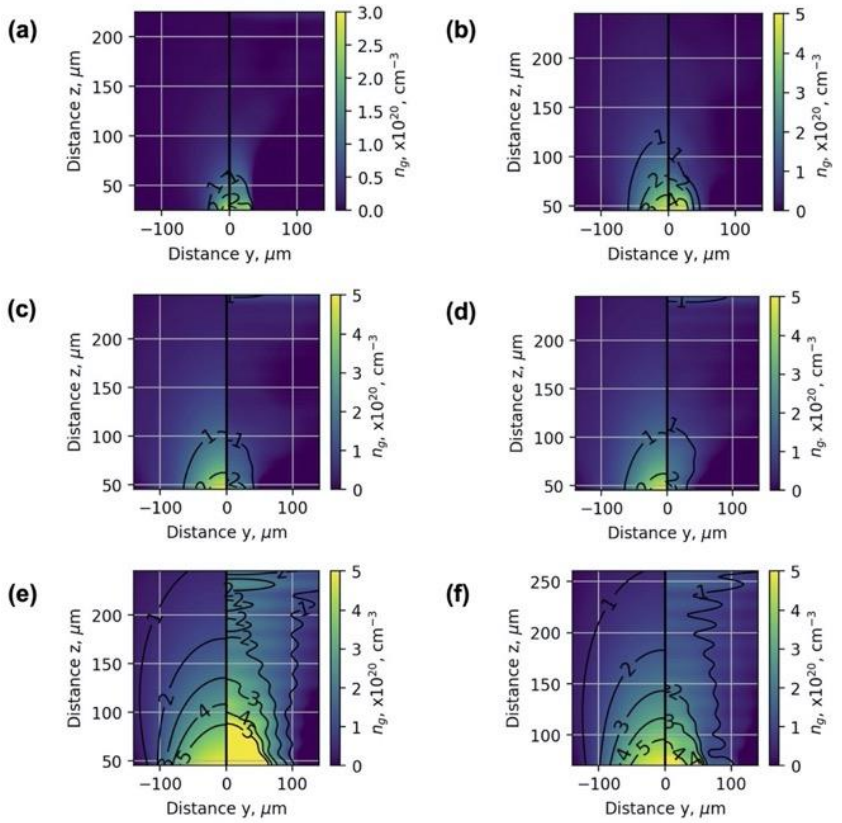

Figure 35. Simulated (left side) and reconstructed (right side) transversal N_2 concentration profiles of cylindrical nozzles with the diameter of 50 μm **(a)**, 100 μm **(b)**, 200 μm **(e)**, manufactured by FLSE technology, 100 μm **(c)** and 200 μm **(f)**, fabricated by the nanosecond rear-side machining technique, and 100 μm **(d)**, fabricated by the nanosecond rear-side machining technique with the subsequent etching in KOH, at 60 bar of backing pressure at the valve [156].

The gas concentration, measured at the outlet of 200 μm cylindrical channel at the distance of 80-140 μm from the outlet of the nozzle, was 15-25% lower in the channel, fabricated by nanosecond rear-side processing technique relative to the channel, made by FLSE technique. The measured gas concentrations were 2.3 - 4.5×10^{20} and 2.9 - 5.1×10^{20} cm^{-3}, correspondingly.

The reconstructed concentration profiles of the 2.25 mm cylindrical converging-diverging nozzle and 1.5 mm slit nozzle S1 at the backing pressure of 30 bar argon used in Lund Laser Center are presented in Fig. 36a and Fig. 36b, respectively. The nozzle characterization has shown that the gas target of the single cylindrical Laval nozzle with the diameter of 2.25 mm has the 1.5 mm-long gas concentration plateau and the ramps with the length of

0.6 mm at each side of the nozzle. The single slit Laval nozzle with a length of 1.5 mm S1 has the 0.9 mm-long gas concentration plateau and the ramps with the length of 0.8 mm at each side of the nozzle.

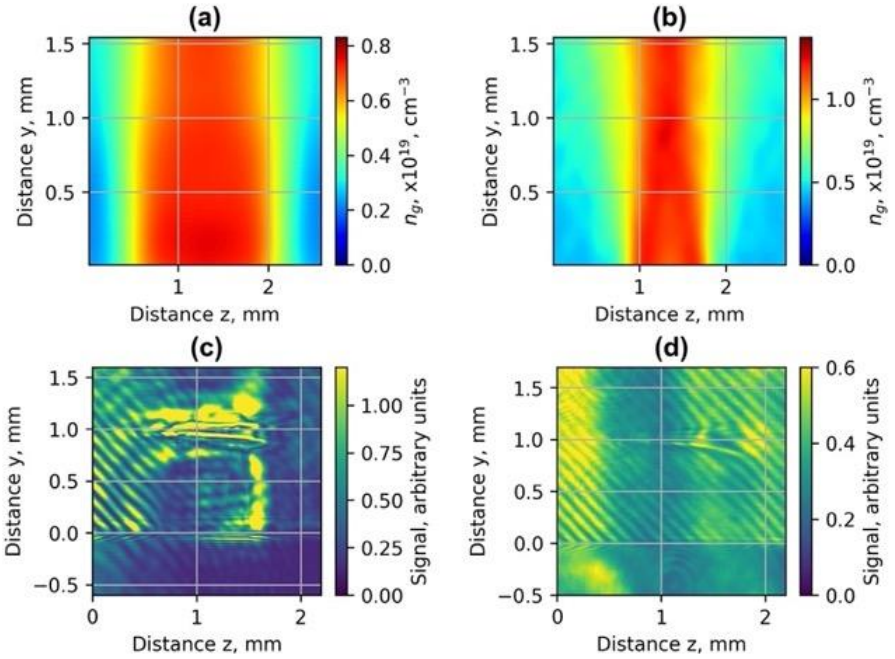

Figure 36. Gas concentration profiles reconstructed using measured wavefront sensor phase diagrams for the cylindrical converging-diverging nozzle with the diameter of 2.25 mm **(a)**, slit converging-diverging nozzle with the length of 1.5 mm **S1 (b)** at the backing pressure of 30 bar. Shadowgrams of the nozzle **S1** for $n_p = 1 \times 10^{19}$ cm^{-3} **(c)**, and array **Arr4** for $n_p = 2 \times 10^{18}$ cm^{-3} in injector geometry **(d)** [140].

Estimating the dependence of plasma concentration n_p on backing pressure, it was assumed that the plasma concentration n_p is proportional to the gas concentration n_g and depends on the ionisation level. The molecular concentration in the central part of the Arr2 cylindrical nozzle at the backing pressure of 26 bar and n_g was estimated as $5{\times}10^{18}$ cm^{-3}. The same concentration for the S1 nozzle was reached at the backing pressure of 18 bar. Calculating the plasma concentration n_p, it was assumed that helium is fully ionized to He^{+2} and helium plasma concentration n_p corresponding to $n_g = 5{\times}10^{18}$ cm^{-3} is equal to $n_p = 1{\times}10^{19}$ cm^{-3}.

The propagation of the laser beam and the formation of the plasma channel was monitored using Wollaston prism and a probe beam split from the driving

laser and crossing the gas jet perpendicularly. The interferograms of Wollaston prism was used for shadowgraphy diagnostics. The shadowgrams of the single nozzle S1 for $n_p = 1 \times 10^{19}$ cm^{-3}, and the array Arr4 for $n_p = 2 \times 10^{18}$ cm^{-3}in injector geometry are shown in Fig. 36c and Fig. 36d, respectively. In Fig. 37, the shadowgrams of Arr2 and Arr3 showing the formation of the grid of shock waves are shown.

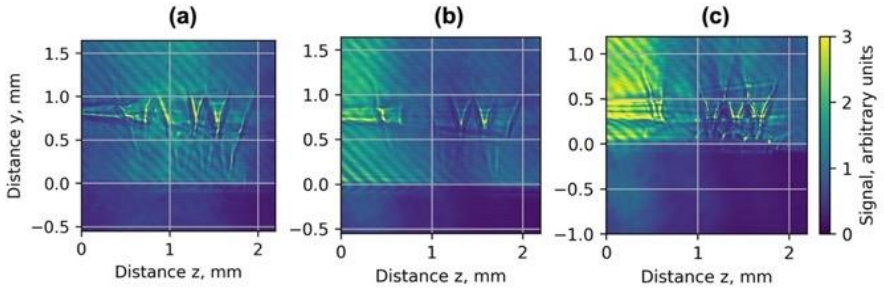

Figure 37. The interferograms of the array **Arr2** (**a**) and the array **Arr3** for the laser beam at the distance of 800 μm (**b**) and 400 μm (**c**) above the nozzle outlet for the $n_p = 1{\times}10^{19}$cm^{-3} [140].

The shock waves of the array Arr2 were observed at the laser-nozzle distance of 800 μm (Fig. 37a). The interferogram images of the array Arr3 (Fig. 37bc) showed a substantial difference in the distribution of plasma density depending on the distance of the laser beam above the nozzle. At the distance of 800 μm (Fig. 37b), the 150-200 μm width of the laser wakefield of the ionized region was narrower, and the shock waves were seen only in the center part of the array Arr2. At the distance of 400 μm (Fig. 37c), the width of the ionized region increased to 200-250 μm and the intersecting shock-wave fronts of all array nozzles were clearly visible.

In Fig. 38a, the reconstructed nitrogen plasma concentration profiles of One-Sided Shock (OSS) 300 μm nozzle using Abel inversion from the interferogram of the propagating laser beam are shown. The OSS nozzle was used in LOA experiments. The reconstructed profiles show the formation of negative plasma density gradient. The nitrogen concentration profiles presented in Fig. 38a, correspond to the actual plasma concentration used in the experiments, where L-shell of nitrogen is fully ionised to N^{+5}. The nitrogen plasma concentration exceeds the molecular gas concentration approximately by a factor of 10. In Fig. 38b, the integral phase profile of double 54/140 μm nozzle is presented.

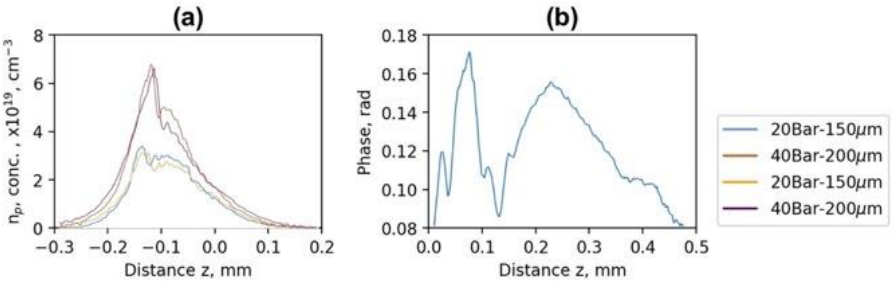

Figure 38. Reconstructed N_2 plasma concentration profiles of One-Sided Shock 300 μm nozzle **(a)** at the backing pressure of 20 and 40 Bar used in the LOA experiments, and measured N_2 integral phase of double 54/140 μm nozzle at the backing pressure of 30 Bar **(b)** [136].

6.4. Discussion on Micronozzle Manufacturing

The FLSE technique allowed to fabricate nozzles with the smallest sand-grain roughness $k_{rf} = 0.56$ of the wall, estimated according to the measured peak-to-valley distance. In the case of nanosecond rear-side processing technique, the sand-grain roughness of the wall equalled to 8 μm, which was by order of magnitude larger compared to the FLSE technique. The nanosecond rear-side processing technique caused the significant chipping of glass edges at the outlet of a nozzle, which occurs when a thin layer of glass fractures breaks in the final stage of drilling. Chipping resulted in the conical chamfered nozzle outlet with the angle of 30 degrees at 40 μm depth below the outlet of the nozzle. The wet etching revealed the randomly-distributed intra-volume cracks close to the microchannel, which were induced due to nanosecond laser processing.

The simulation results of the cylindrical nozzles with the roughness parameter $k_{rf} = 0$ μm, presented in Fig. 24acd, are in good correspondence with experimental results of the nozzles with diameters of 50 μm, 100 μm and 200 μm, manufactured by FLSE technique (Fig. 35abe). The simulation results of the channels with $k_{rf} = 10$ μm and outlet conus with the angle of 30 degrees, presented in the Fig. 24acd, correspond with the experimental results of gas concentration of the nozzles fabricated by nanosecond rear-side processing technique within 10-15% (Fig. 35cf). After the polishing of the front surface with chamfered edges, the quality of nozzles, fabricated by a nanosecond laser, was improved by 10%. The gas concentration reduction decreased below 15% for 100 μm-diameter nozzles (Fig. 35d).

The measured gas concentrations of converging-diverging 2.25 mm cylindrical nozzle and 1.5 mm slit nozzle S1 at the backing pressure of 30 bar were $4 - 8\times10^{18}$ and $0.6 - 1.5\times10^{19}$ cm^{-3}, correspondingly. Within the accuracy of 10%, the measured gas concentration corresponds to the CFD simulations, presented in section 5. During the experiment, helium was ionized up to He^{+2}, and the plasma concentration exceeded twice the gas concentration. The nitrogen profiles, shown in Fig. 38, correspond to the actual plasma concentration used in the experiments when nitrogen L-shell is fully ionized up to N^{+5}. The plasma concentration exceeds the molecular gas concentration of nitrogen approximately by a factor of 10.

6.5. Conclusions

Micronozzle arrays of micrometric dimensions resistant to optical damage can be manufactured from transparent materials, such as fused silica, combining several laser microfabrication techniques:

- Nanosecond rear-side processing allows fast material removal of high-volume parts ~2-2.5 mm^3/s with the 18 W average laser power.
- The peak-to-peak surface roughness R_{zd} of 5-8 μm of the walls of nanosecond rear-side processing and edge chipping of the nozzle outlet limits the application of this technique to the manufacturing of nozzles with the diameter more than 200-300 μm.
- The gas concentration at the outlet of the nozzle manufactured by nanosecond rear-side technique decreases by 20-30% for the nozzle with the diameter of 100 μm and by 15-25% for the nozzle with the diameter of 200 μm relative to the nozzles processed by FLSE technique.
- The wall roughness has an effect on the gas flow when the height of the roughness structure R_{zd} exceeds 1-2% of the diameter of the nozzle.
- The femtosecond and picosecond surface ablation improve the surface roughness R_{zd} to 3-5 μm.
- The formation of nozzles using the FLSE technique enables the formation of channels with dimensions of less than 40 μm and surface roughness $R_{zd} < 0.7$ μm. However, due to the long fabrication time, it is less competitive for processing of high-volume parts than rear-side material removal.

7. EXPERIMENTAL LWFA OF ELECTRON BEAMS AND EXCITATION OF SECONDARY RADIATION X-RAY RADIATION

The material related to this chapter was published [A1, A2] and [C1, C2, C3].

7.1. Laser Wakefield Acceleration of Electron Beams

The experimental work on laser wakefield electron acceleration and excitation of betatron X-ray radiation was done in Lund Laser Center. The results of the energy and spatial distribution of accelerated electrons are presented in Fig. 39. The laser intensity on target corresponded to the laser strength parameter $a_0 \simeq 4.0$. The parameters of accelerated electrons were measured using a magnetic spectrometer and Lanex scintillation screen.

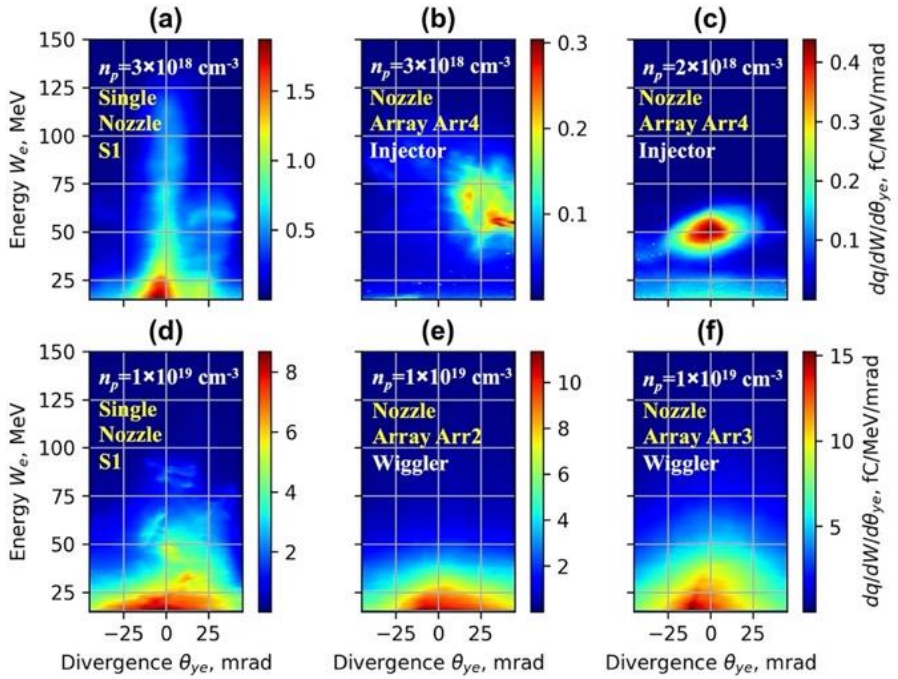

Figure 39. Experimental profiles of energy and spatial distribution of electrons for $n_p = 3\times10^{18}$ cm^{-3} for the single **S1** nozzle for the mixture He+1% **(a)** , for the array **Arr4** in injector geometry for pure He **(b)** and for $n_p = 2\times10^{18}$ cm^{-3} for the mixture He+1%N_2 **(c)**. Experimental profiles of energy and spatial distribution of the charge of electrons for $n_p = 1\times10^{19}$ cm^{-3} for the single **S1** nozzle **(d)** and for the array **Arr2 (e)** and **Arr3 (f)** for the mixture He+1%N_2 in wiggler geometry [140].

The energy spectrum data and spatial distribution of charge of electrons for a single S1 nozzle and the arrays Arr2-Arr4 were averaged over 10 shots. At a lower backing pressure of 5-12 bar of He+1%N_2 gas, the electrons accelerated using single nozzle S1 had the highest energy and lowest divergence (FWHM) (Fig. 39a). The implementation of the array Arr4 in injector geometry enabled density-triggered injection of electrons. Electron bunches of 50-80 MeV were observed at a low backing pressure of 5-7 bar of pure He (Fig. 39b). The corresponding plasma concentration was approximately $n_p = 3\times10^{18}$ cm^{-3}. The separate electron bunches had low energy dispersion of 5-10 MeV. However, the fluctuations of the accelerated charge and spatial distribution from shot-to-shot were observed. It resulted in the increased energy dispersion of electron bunches averaged over 10 shots. For the mixture of He+1%N_2 at backing pressure of 4-5 bar, more stable injection of the electrons, and quasi-monoenergetic electron bunches of 4-5 pC and 50±10 MeV were measured (Fig. 39c). For all other cases presented in Fig. 39, no considerable fluctuations of the spatial distribution of charge and divergence from shot to shot were observed. Increasing of the backing pressure up to 18-21 bar for the single nozzle S1, the array Arr2, and up to 21-26 bar for the array Arr3 in wiggler geometry, resulted in the substantial growth of the injected electrons and the enlarged divergence of the electron beam (Fig. 39d-f). Higher divergence increased the efficiency of betatron radiation. In the experiments, the 18-bar backing pressure of He+1%N_2 mixture for S1, Arr2, Arr4 and 26 bar for Arr3 corresponded to the plasma concentration of approximately $n_p=1\times10^{19}$ cm^{-3}.

In Fig. 40-42, the dependence of mean energy, charge and divergence of accelerated electrons on gas backing pressure are presented. The highlighted regions indicate the pressure when X-ray generation was most efficient. Interpolated solid lines providing a guide to the eye were calculated using a cubic spline. The maximum of X-ray radiation for the 1.5 mm single nozzle S1, was reached at the backing pressure of 16-18 bar (Fig. 40ab). The number of X-ray photons per shot increased along with the growth of mean energy, the charge of accelerated electrons, and divergence of the electron beam. The injected charge of electrons modifies the electric field inside of the plasma bubble, and the mean energy of electrons starts to drop. At the low backing pressure of 9-11 bar, the mean energy was the highest, and reached 46 MeV. However, the injected charge low, in the range of 30 pC, and the divergence was approximately 30 mrad. The X-ray yield was low. The most efficient X-ray generation was observed at the backing pressure when the charge of accelerated electrons was near the maximum of 60-80 pC, the divergence of

the electron beam increased to 75-85 mrad, and the mean electron energy of 35- 40 MeV was close to the maximum for this amount of injected charge.

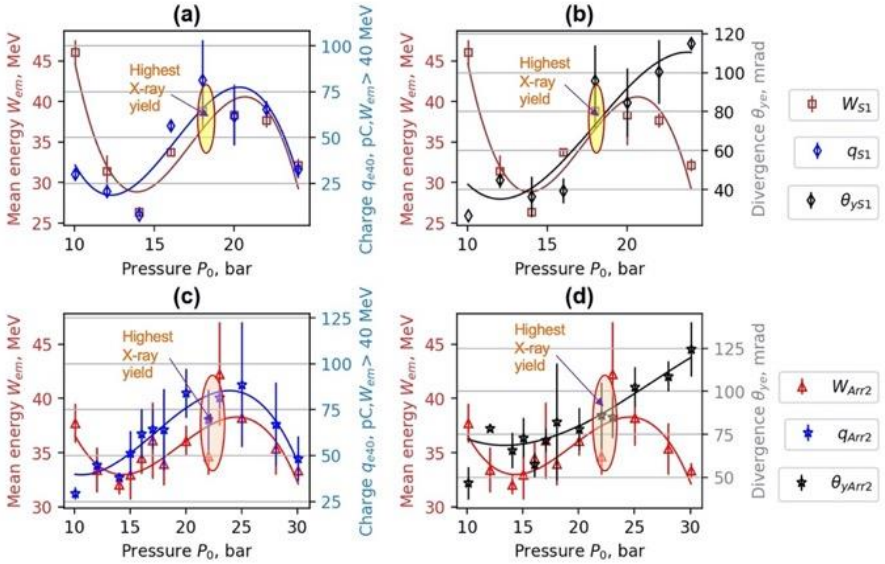

Figure 40. Experimental dependence of mean energy W_{em}, charge q_{e40} for $W_e > 40$ MeV (**a, c**) and mean divergence θ_{ye} (FWHM) (**b, d**) of accelerated electrons on gas backing pressure. $\boldsymbol{W_{S1}}$**,** $\boldsymbol{q_{S1}}$**,** $\boldsymbol{\theta_{S1}}$ correspond to the nozzle **S1** and $\boldsymbol{W_{Arr2}}$, $\boldsymbol{q_{Arr2}}$, $\boldsymbol{\theta_{Arr2}}$ - to **Arr2** in wiggler geometry. Interpolated solid lines provide a guide to the eye [140].

Further increase of the backing pressure led to an additional growth of divergence. Dropping the mean energy and a smaller amount of the accelerated electrons resulted in the reduction of X-ray radiation.

At the lower backing pressure of 15 bar, the implementation of the array Arr2 in the wiggler geometry, increased the divergence of accelerated electrons by 40% from 40 to 60 mrad. At the backing pressure of 20 bar, the average divergence of accelerated electrons for S1 and Arr2 was similar, in the range of 80 mrad. However, for Arr2 the increase of the charge of accelerated electrons (W_e>40 MeV) and a drop of mean energy by 20% relative to S1 nozzle were observed. The maximum of X-ray radiation for the array Arr2 was reached at a backing pressure of 19-22 bar, and was higher by a factor of 2-3 relative to the single nozzle S1.

The same trend of the increase of X-ray yield with an increase of divergence and charge was also observed for the array Arr3 (Fig.41). The 2.25 mm acceleration part of the array Arr3 was by a factor of 1.5 times longer than acceleration distance of the nozzle S1 and the array Arr2. Therefore, the energy of accelerated electrons was higher. The maximum of X-ray radiation was reached at the higher backing pressure of 24-26 bar because of the higher

expansion ratio of 2.25 mm nozzle relative to S1 and Arr2 nozzles. The higher expansion ratio of the 2.25 mm nozzle resulted in different distribution of gas concentration defined by the intersecting shock waves of jets of the first and second part of the array Arr3. High gas concentration regions of the wiggler array were formed at a lower distance from the nozzle outlet relative to S1 and Arr2 nozzles. At the distance of 800 μm of laser beam above the array Arr3 (Fig. 41ab), the injected charge grew along with the increasing of backing pressure from 15 until 28 bar. However, it remained low, in the range of 25-30 pC. The divergence of the electron beam increased from 20 to 80 mrad, and the mean energy dropped from 50 MeV to 32 MeV. The yield of X-ray was low. At the distance of 400 μm of laser beam above the array Arr3 (Fig. 41cd), the substantial increase of charge (W_e>40 MeV) up to 100 pC and mean energy up to 43 MeV was observed. The divergence of the electron beam remained at the same level of 80 mrad. The charge of accelerated electrons increased by a factor of 4, and X-ray radiation - by a factor of 5 relative to the case when the laser beam propagated 800 μm of above the outlet of the nozzle.

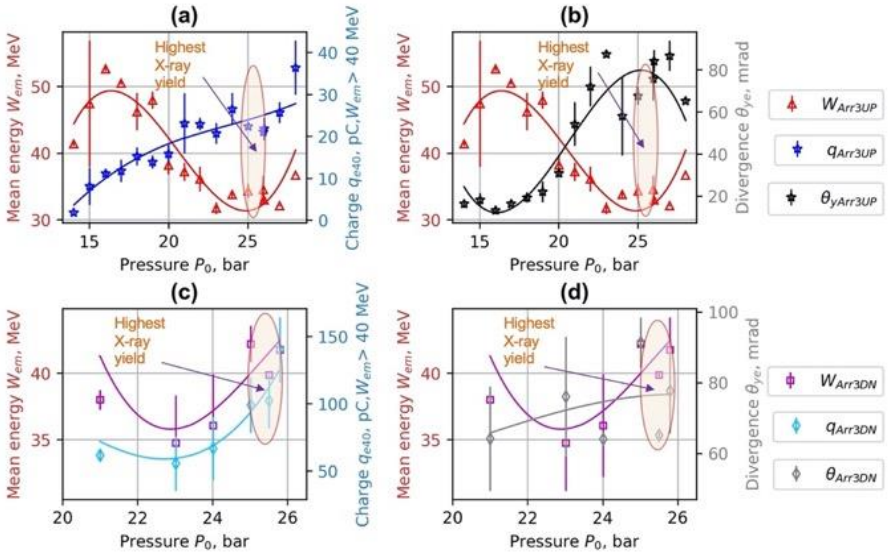

Figure 41. Experimental dependence of mean energy W_{mean}, charge q_{e40} for W_e > 40 MeV (**a, c**) and mean divergence θ_{ye} (FWHM) (**b, d**) of accelerated electrons on gas backing pressure for the array **Arr3** in wiggler geometry. $\boldsymbol{W_{Arr3UP}}$, $\boldsymbol{q_{Arr3UP}}$, $\boldsymbol{\theta_{Arr3UP}}$ were measured at the distance of 800 μm, and - $\boldsymbol{W_{Arr3DN}}$, $\boldsymbol{q_{Arr3DN}}$, $\boldsymbol{\theta_{Arr3DN}}$ - at the distance of laser beam above the nozzle of 400 μm [140].

In Fig. 42, the dependence of the mean energy and charge of accelerated electrons, and divergence of the electron beam on the laser energy for the array

Arr3 are presented. The laser beam was propagating 400 μm above the nozzle outlet. The accelerated charge grew by a factor 2-2.5 and the mean energy and divergence by 10 % by increasing the laser pulse energy from 0.6 to 0.9 J. It resulted in the increase of number of photons per shot and brightness of X-ray radiation by a factor of 2.7, and growth of the synchrotron critical energy by 12%. In the range of 0.9-1.2 J, the parameters depended weakly on laser pulse energy and did not change more than 20%.

In Fig. 43, the spectral intensity and spatial distribution of charge of accelerated electrons for One-Side-Shock (OSS) nozzle using LOA ENSTA 0.8 TW 4 fs 1 kHz laser are presented [136]. The measured electron spectra were averaged over 100 shots. The blue line shows the mean spectrum measured over the period of 0-150 min, and the yellow line - over the period of 250-300 min. The shaded areas show the standard deviation. The black error bar indicates the spectrometer resolution at 2.4MeV. The statistics the beam charge was collected from 20 acquisitions, each consisting of an accumulation over 10 shots.

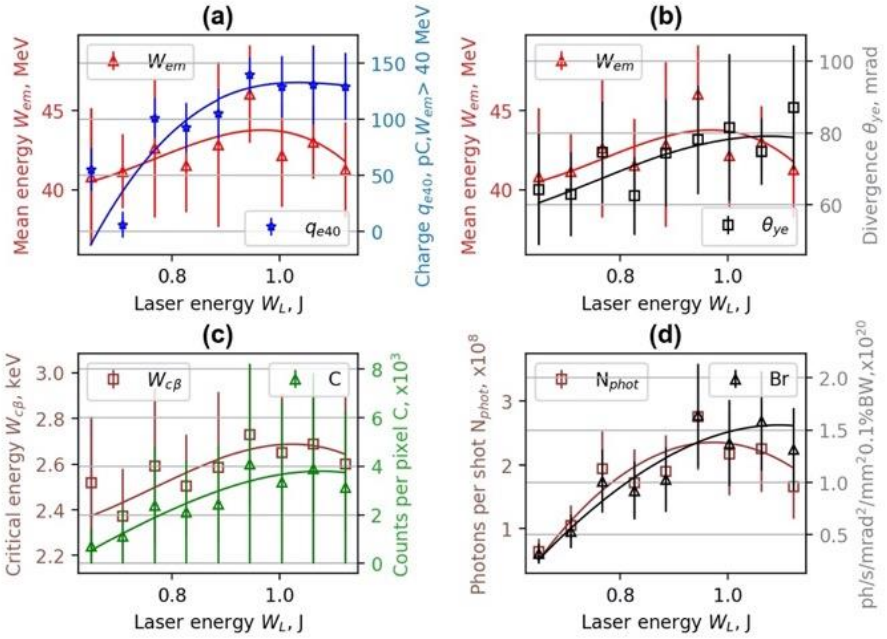

Figure 42. Experimental dependence of mean energy W_{em}, charge q_{e40} for W_e > 40 MeV **(a)** and mean divergence θ_{ye} **(b)** of accelerated electrons, and betatron critical energy, counts per pixel **(c)**, photons per shot and brightness **(d)** of X-ray radiation for the array **Arr3** laser-nozzle distance of 400 μm and $n_p = 1x10^{19}cm^{-3}$ on the laser energy on target.

The total charge per shot was 2.6 pC ± 0.6 pC, and the beam divergence is approximately 80 mrad FWHM. Density down-ramp triggered injection of OSS nozzle resulted in a stable injection and acceleration of electrons within 5 hours of a long-term stability test. The fused-silica nozzles showed high resilience to damage, and ensured continuous LWFA operation for about 3 - 5 × 10^7 shots.

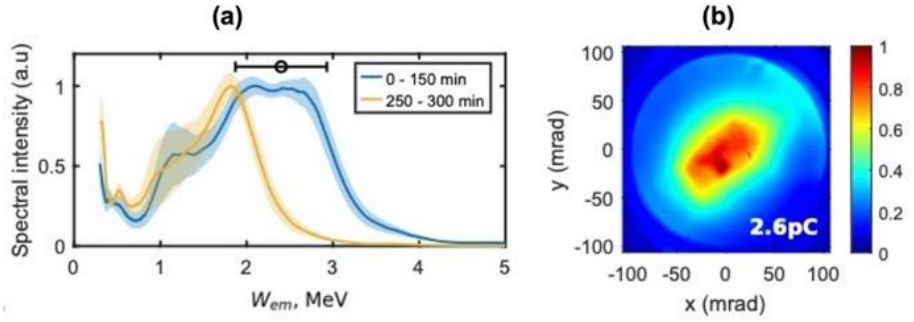

Figure 43. Experimental profiles of spectral intensity **(a)** and spatial distribution of charge of accelerated electrons **(b)** using 300 μm One-Sided Shock nozzle using 3.8 mJ 4 fs 1 kHz LOA laser [136]. The shaded areas show the standard deviation.

7.2. Excitation of Secondary X-Ray Radiation

The experimental data of betatron X-ray radiation measured in the Lund Laser Center are presented in Fig.44-47 and in Table 9. In Fig. 44-45, the dependence of characteristics of X-ray betatron radiation corresponding to the parameters of electron beams presented in Fig. 40-41 are shown.

As discussed in the previous section, the number of X-ray photons per shot and brightness increased proportionally to the mean energy, number of radiating electrons and the divergence of the electron beam enhancing the oscillations of betatron. All these three parameters were not reached at the same time. At 16-18 bar of backing pressure, for the single nozzle S1 the highest number of X-ray photons per shot of 1.0×10^8 and the brightness of 0.3×10^{20} ph/s/mrad^2/mm^2/0.1%BW were observed (Fig. 44 ab). With further increase of backing pressure > 20 bar, the divergence of the electron beam increased further. Despite declining energy of electrons, the efficiency of X-ray radiation was compensated by the growing divergence of electron beam and dropped insignificantly. In the whole backing pressure range of 10-26 bar, the divergence of X-ray radiation increased with the raise of backing pressure from 60 to 65 mrad.

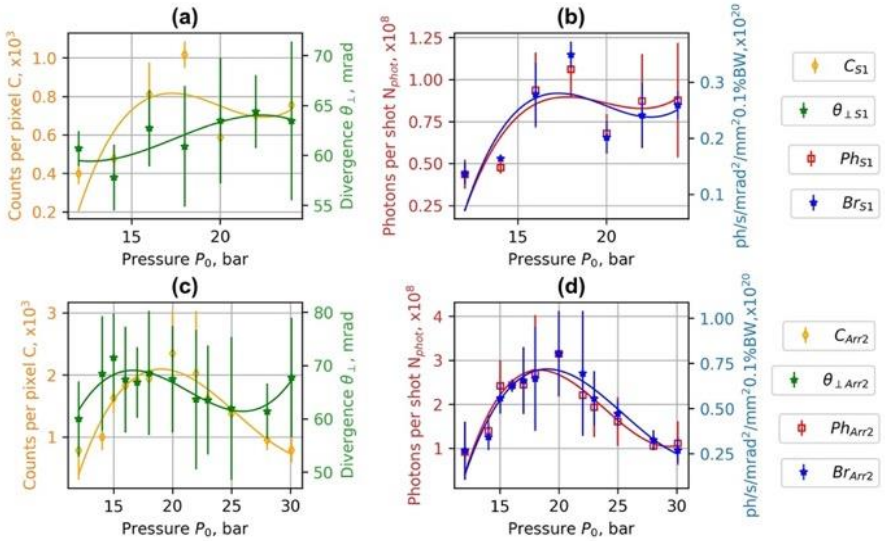

Figure 44. Experimental dependence of counts per pixel C, divergence $\theta_{\perp}$ (FHWM) (**a, c**), photons per shot N_{phot} and brightness Br (**b, d**) of X- ray radiation on gas backing pressure. ***C*$_{S1}$, *θ*$_{⊥S1}$, *Ph*$_{S1}$, *Br*$_{S1}$** correspond to the nozzle **S1** and ***C*$_{Arr2}$, *θ*$_{⊥Arr2}$, *Ph*$_{Arr2}$, *Br*$_{Arr2}$** - to the array **Arr2** in wiggler geometry. Interpolated solid lines provide a guide to the eye [140].

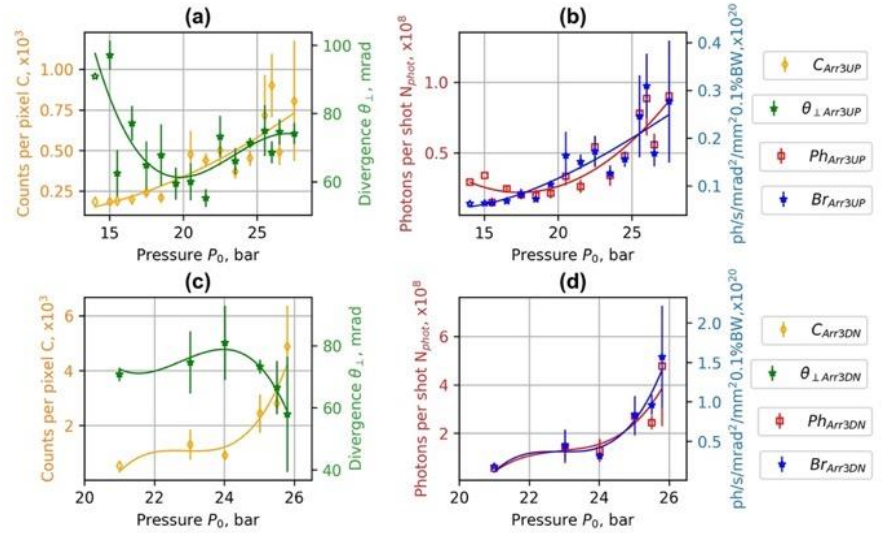

Figure 45. Experimental dependence of counts per pixel C, divergence $\theta_{\perp}$ (FHWM) (**a, c**), photons per shot N_{phot} and brightness Br (**b, d**) of X-ray radiation on gas backing pressure for the array **Arr3** in wiggler geometry. ***C*$_{Arr3UP}$, *θ*$_{⊥Arr3UP}$, *Ph*$_{Arr3UP}$, *Br*$_{Arr3UP}$** were measured at the laser - nozzle distance of 800 μm, and - ***C*$_{Arr3DN}$, *θ*$_{⊥Arr3DN}$, *Ph*$_{Arr3DN}$, *Br*$_{Arr3DN}$** at the distance of 400 μm [140].

At 18-22 bar of backing pressure, for the array Arr2 the number of X-ray photons per shot of 3.0×10^8 and the brightness of 0.7×10^{20} ph/s/mrad^2/mm^2/0.1%BW were reached (Fig. 44 cd). These values were by a factor of 2-3 higher than X-ray radiation observed for a single nozzle S1. With further increasing of backing pressure up to 25 bar, the number of X-ray photons for shot dropped by a factor of 1.5, similarly as in the case of single nozzle S1. With further increasing of backing pressure up to 30 bar the number of X-ray photons for shot decreased by a factor of 3, and the divergence of X-ray radiation increased from 60 to 70 mrad.

At the backing pressure of 25- 26 bar for the array Arr3, the number of X-ray photons for shot of $3.0\text{-}5.5\times10^8$ and the brightness of $1.1\text{-}1.6\times10^{20}$ ph/s/mrad^2/mm^2/0.1%BW at the laser-nozzle distance of 400 μm above the nozzle were observed (Fig. 45cd).

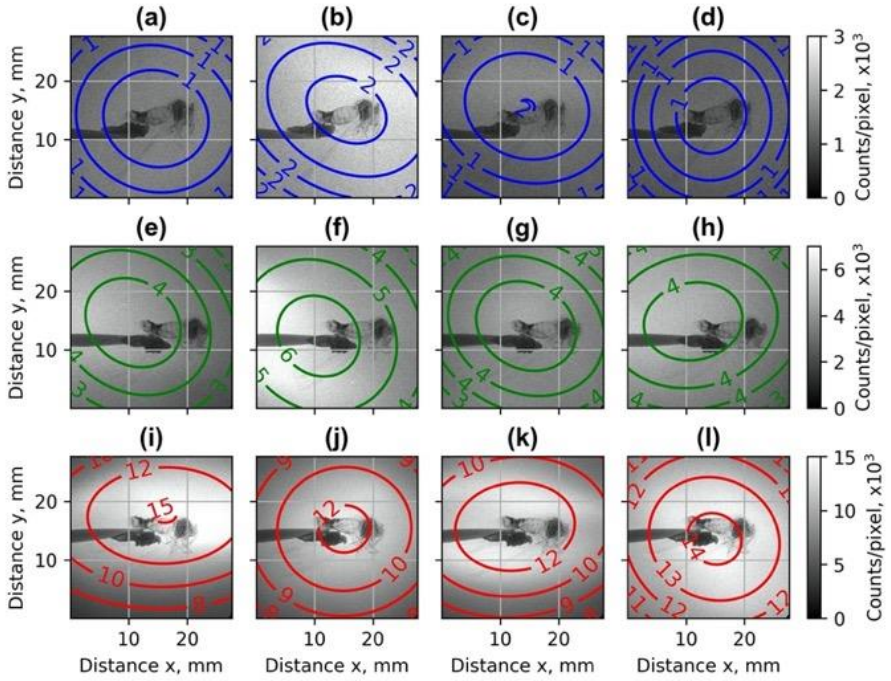

Figure 46. Estimation of Gaussian distribution of counts per pixel per shot of typical examples of X-rays images using the single nozzle **S1** (**a - d**), the array **Arr2** (**e- h**), and the array **Arr3** (**i-l**) at the distance of laser beam above the nozzle of 400 μm [140].

These values were by a factor of 4-5 higher than the maximum of X-ray radiation reached for the array Arr3 at the laser-nozzle distance of 800 μm (Fig. 45 ab). The limitations of the gas supply system prevented further

increase of the backing pressure. Therefore, no data about the possible decrease of X-ray radiation at higher backing pressure were obtained. For the array Arr2 and Arr3 at the laser-nozzle distance of 400 μm, the drop of the divergence of X-ray radiation (FHWM) by 15-30% in the region of the backing pressure corresponding to the highest X-ray yield was observed (Fig. 44c and 45c).

Typical examples of the spatial distribution of X-rays radiation for the single nozzle S1 and the arrays Arr2, Arr3 are shown in Fig. 46. The measurement of the divergence $\theta_{\perp}$ (FHWM) of X-ray radiation has shown that the intensity distribution in the x-y direction changes from circular to elliptical from shot to shot. In average, the X-ray distribution for Arr3 was more elongated in x-direction parallel to the laser polarisation relative to S1 and Arr2 nozzles.

In Fig. 47a, the X-ray image and Fig. 47b, the transmission diagrams of Ross filters and camera window used for the measurement of synchrotron critical energy of the betatron source are shown.

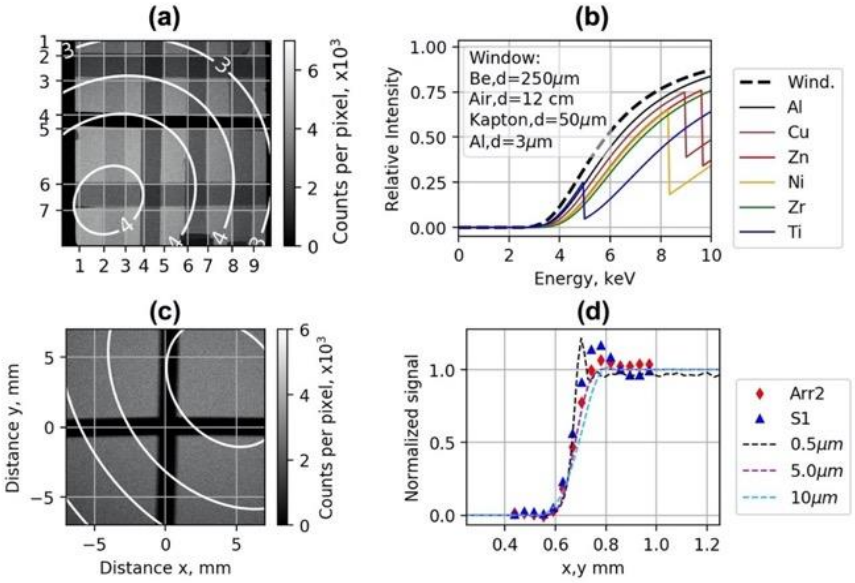

Fig. 47. X-ray image **(a)**, and transmission diagrams of Ross filters and camera window **(b)** used for the meausurement of critical energy of synchrotron radiation of betatron source. X-ray image of 50 μm tungsten cross wires **(c)**, and the results of measurement of X-ray source size **(d)**.

The critical energy of betatron radiation was evaluated by calculating the squared difference between the measured X-ray radiation passing through the Ross filters, and the theoretical one for each critical energy of synchrotron

radiation. For the single nozzle S1 and the array Arr2, the betatron radiation corresponded to the synchrotron radiation with the critical energy of 2.3 - 2.5±0.1 keV. The radiation spectrum of the array Arr3 for the laser-nozzle distance 800 μm and 400 μm had the best match to the synchrotron radiation with the critical energy of 2.2 keV±0.2 keV and 2.6 keV±0.1 keV, correspondingly.

In Fig. 47c, the X-ray image of 50 μm tungsten cross wires and the Fig. 47d, the results of measurement of the oscillation radius of a betatron source are shown. The radius of betatron source was measured by a comparison of the diffraction signal from the wire edge with the calculated intensities of the Fresnel diffraction integral signals for different source sizes between 0.5 and 10 μm (Fig. 47d) [170-172]. The radius of betatron source changed from 3.5±1 μm for single slit nozzle S1 and 11 bar of gas backing pressure to 7.5±1 μm for the array Arr2 and 29 bar of gas backing pressure. For the calculation of the brightness of X-ray radiation in the range of 15-26 bar of backing pressure, the fixed average radius of 5 μm was used.

This maximal values of number of photons per shot and brightness for nozzles implemented in the experiment as well as corresponding divergence and charge of the accelerated electron are summarised in Table 9. The number of photons per shot and spatial distribution of X-ray radiation were measured using the Andor iKon-L SO X-ray camera described in Section 3. The spatial profiles of the betatron radiation were calculated using the relations of Gaussian approximation of intensity of X-ray radiation (49-61). The number of photons per shot was estimated by postprocessing of counts per pixel of X-ray images at FWHM level at the corresponding critical energy $W_{c\beta}$. In Table 9, the divergence of X-ray radiation $\theta_{\perp}$ is given first, and the numbers in parentheses indicate the mean divergence θ_{ye} of electrons in the y-direction. The divergence values $\theta_{\perp}$ were calculated by measuring separately and averaging of the ellipse radii afterwards.

The implementation of the nozzle array Arr2 in wiggler geometry increased the critical energy of betatron radiation by 8-10% relative to the single nozzle S1. For the Arr2, the number of X-ray photons per shot and the brightness of the source increased by a factor 2-3 relative to the single nozzle S1. For the array Arr3, the changing of the laser - nozzle distance of laser beam from 800 μm to 400 μm increased the number of X- ray photons per shot and the brightness of the source by a factor of 4-5. For the array Arr2, the charge of accelerated electrons with the energy >40 MeV was 85±20 pC, and for the array Arr3 - 130±25 pC. The field of view of the camera was only 35 mrad; therefore, the divergence values of X-ray radiation in Table 9 were

extrapolated from X-ray images assuming Gaussian distribution of the betatron radiation (Fig. 46).

Table 9. The data of accelerated electrons and betatron radiation of single nozzles and arrays in wiggler geometry for $n_p = 1\times10^{19}$cm^{-3} and $a_0 = 4.0$. In the case of #1-3, the laser-nozzle distance was 800 μm, and in the case of #4, - 400 μm [140].

No	Description	Char-ge>40 MeV, pC	Counts per pi-xel, FHWM	Critical energy, keV	Diver-gence $\theta_\perp$ (θ_{ey}), mrad, FHWM	Photons per shot, FHWM	Bright-ness, 0.1% BW/s mrad^2/ mm^2, FHWM
#1	1.5 mm single slit converging-diverging nozzle **S1**	70±10	900± 300	2.3±0.2	75±10 (80±20)	1.1±0.5 $\times10^8$	0.3±0.1 $\times10^{20}$
#2	1.5 mm slit converging-diverging nozzle with an array of 4 nozzles **Arr2**	85±20	1800± 500	2.5±0.2	80±10 (80±20)	2.9±0.7 $\times10^8$	0.7±0.1 $\times10^{20}$
#3	2.25 mm de Laval nozzle with an array of 4 nozzles **Arr3** (distance 800 μm)	30±10	900± 200	2.2±0.2	50±15 (80±10)	1.0±0.2 $\times10^8$	0.3±0.1 $\times10^{20}$
#4	2.25 mm de Laval nozzle with an array of 4 nozzles **Arr3** (distance 400 μm)	130± 25	4900± 1500	2.6±0.1	70±30 (90±20)	5.5±4.8 $\times10^8$	1.6±0.5 $\times10^{20}$

7.3. Application of LWFA X-Ray Radiation

The LWFA-driven betatron source was used for the transmission imaging of biological objects and polymer foil. In Fig. 48b-d, examples of X-ray transmission images of a bee using the single nozzle S1 are shown.

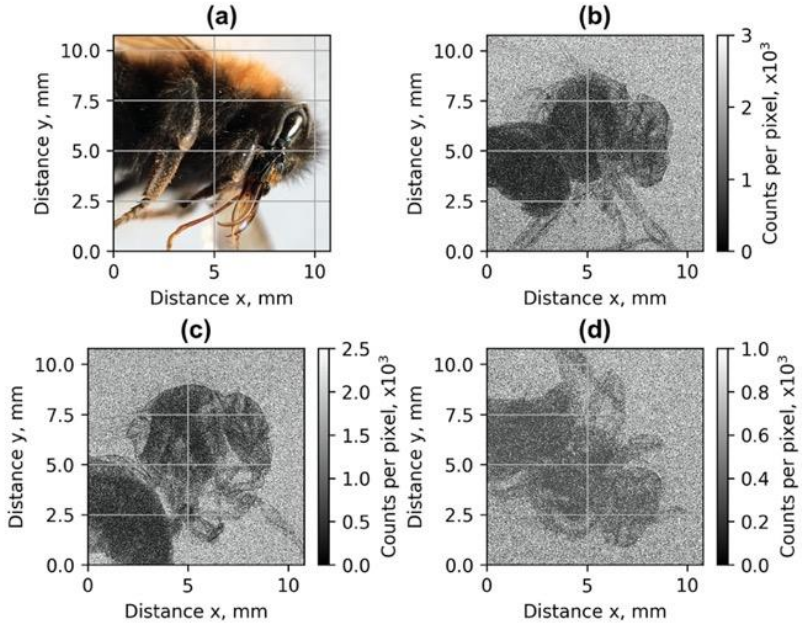

Figure 48. An optical **(a)** and examples of X-ray transmission images of a bee (**b-d**) for $a_0 = 4.0$ and plasma concentration $n_p = 1\times10^{19}$ cm^{-3} using X-ray source of single nozzle **S1**.

In Fig. 49b, an example of a X-ray transmission image of a polymer foil using the array Arr2 is shown. In Fig. 50b-d, the X-ray transmission images averaged over 10 shots of a moth using the single nozzle S1 (Fig. 50b), the array Arr2 (Fig. 50c), and the array Arr3 at the laser-nozzle distance of 400 μm (Fig. 50d) are presented. Increasing the number of photons per shot and brightness of the source resulted in the reduction of noise and better image quality (Table 9, Fig. 48 and 50).

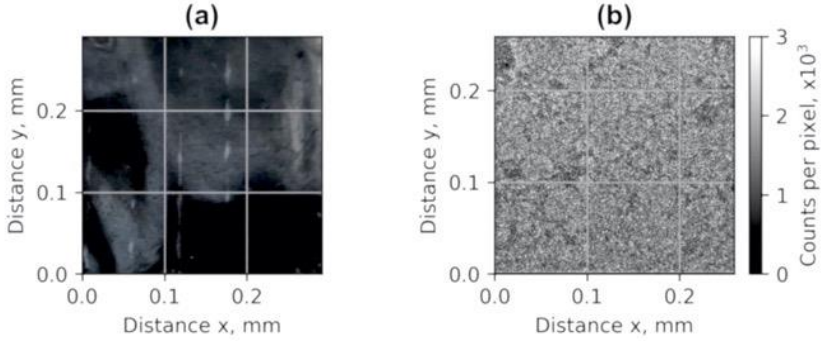

Figure 49. An optical and X-ray transmission image of 40 mm thick polymer foil for $a_0 = 4.0$ and plasma concentration $n_p = 1\times10^{19}$ cm^{-3} using X-ray source of the array **Arr2**.

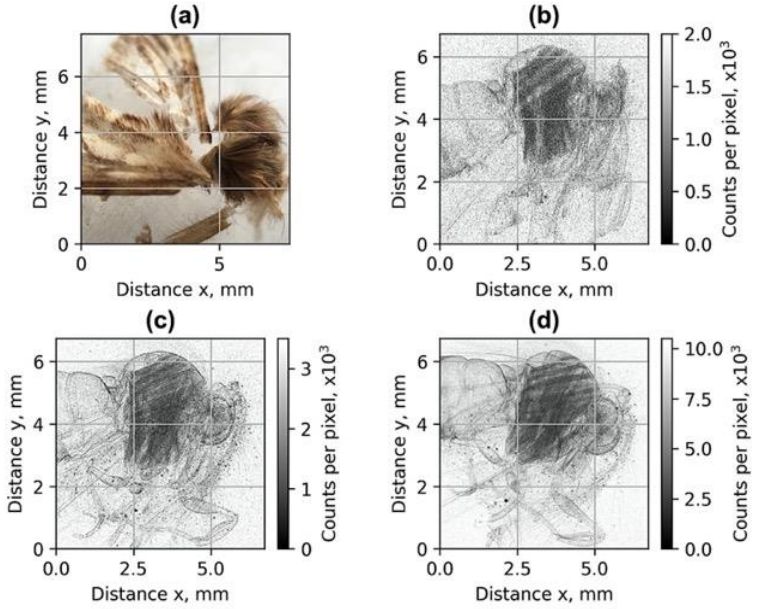

Figure 50. An optical **(a)** and X-ray transmission image (**b-d**) of a moth averaged over 10 shots for $a_0 = 4.0$ and plasma concentration $n_p = 1\times10^{19}\,\mathrm{cm}^{-3}$ using X-ray source of single nozzle **S1**, the array **Arr2,** and the array **Arr3** at the laser-nozzle distance of 400 μm.

Both arrays in wiggler geometries - Arr2 and Arr3 - produced more X-ray radiation than the single nozzle S1. The best image quality was obtained using the array Arr3 at the laser-nozzle distance of 400 μm. The highest X-ray flux generated by electrons accelerated at a longer distance using array Arrr3 relative to Arr2 ensured the minimal image noise of the image.

In Fig. 51, the X-ray images used for the estimation of imaging resolution are presented. In the Fig. 51bc, small details - leg outlines and hair of the moth image (Fig. 51a) - of the size of approximately 20 μm, can be observed. The moth imaging resolution was limited by the pixel size of 13.5 μm of the detector. The moth was placed outside of the vacuum chamber at the distance of 6 cm before the X-ray detector and it resulted in low magnification of 1.08.

In the case of Fig. 51d, the cross wires were located at 70 cm from the detector, and the magnification was 26. Further, the resolution X-ray source for the phase-contrast imaging (PCI) and tomography [170] was estimated. PCI allows non-invasive analysis in low-absorbing materials, such as soft tissue. The phase-contrast imaging of phase gradients of the interfaces between tissues is much more sensitive than transmission imaging. It helps to identify tumours within a tissue with similar absorption properties at an early stage. In-line, or propagation-based phase-contrast imaging (PB-PCI) requires

no optical components and can be implemented with broadband X-rays having spatial coherence.

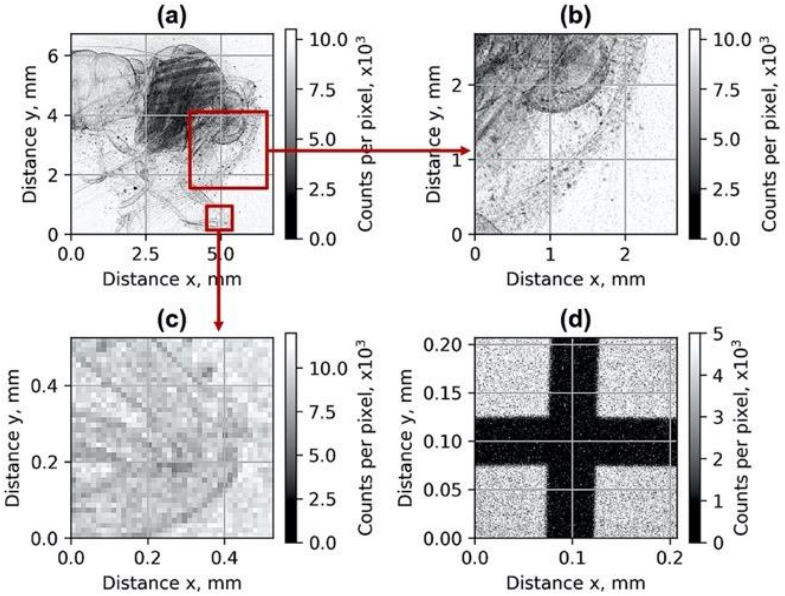

Figure 51. The images of X-ray transmission of a moth **(a-c)** and 50 μm tungsten cross-wires **(d)** averaged over 10 shots for $a_0 = 4.0$, $n_p = 1\times10^{19}$ cm^{-3} used for the evaluation of imaging resolution of X-ray source for the array **Arr3** at the laser-nozzle distance of 400 μm [140].

The PB-PCI resolution was defined evaluating the Point-spread function $P_s(x,y,M_g)$ (PSF) of the imaging system at the object plane using the relations in references [181,182].

$$P_s(x,y,M_g) = \frac{1}{2\pi\sigma_{sys}^2(M_g)} e^{-\frac{x^2+y^2}{2\sigma_{sys}^2(M_g)}}, \quad (73)$$

where $M_g = (r_{1sw} + r_{2wd})/r_{1sw}$ is the geometric magnification of the imaging system. The variance of the PSF- σ_{sys}^2 was calculated as [182]:

$$\sigma_{sys}^2(M_g) = \frac{M_g^2-1}{M_g^2}\sigma_{src}^2 + \frac{\sigma_{\det}^2}{M_g^2} + \sigma_{\min}^2, \quad (74)$$

where σ_{src} - and σ_{det} are the standard deviations of the source intensity distribution and the detector point distribution, respectively. The diffraction term $\sigma_{min}^2 = \lambda_{c\beta}\, r_{2wd}\, /4M_g$, is calculated if evaluating σ_{sys} beyond the first Fresnel zone. At a long distance from the diffracting object and excluding the influence of the object, the finest achievable spatial resolution of cross-wire

imaging was estimated as $2\sigma_{sys}(M_g)$ [181]. Assuming the Gaussian distribution, 10 μm diameter (FWHM) of the source, and magnification of 26, the imaging resolution was estimated to be of 9 μm (defined as double the standard deviation of the source intensity distribution σ_{src} approximately).

7.4. Discussion on LWFA and X-Ray Generation Efficiency

The analysis of X-ray radiation dependence on backing pressure has shown that the maximum number of photons per shot corresponds to the peak of charge and divergence of the electron beam while maintaining a high energy of accelerated electrons. For the single nozzle S1, the maximum energy of accelerated electrons was reached at the backing pressure of 5-12 bar (Fig. 39a). At this backing pressure, the gas density matches the plasma bubble condition and is optimal for the acceleration of electrons. However, the divergence of the electron beam was small, and the yield of X-ray radiation was low. The implementation of the nozzle array Arr4 in injection geometry and the mixture of He+1%N_2 enabled stable injection of the electrons, and formation of quasi-monoenergetic electron bunches of 4-5 pC and 50±10 MeV (Fig. 39c).

With increasing of the gas density and implementation of nozzle array in wiggler geometry, the accelerated charge grows, and the divergence increases (Fig. 39d-f). It leads to a higher yield of in X-ray radiation even the mean energy starts to drop. The maximal number of X-ray photons per shot was reached at the backing pressure of 18-22 bar for the single nozzle S1 and Arr2 and 25-26 bar for the array Arr3. The nozzle S1, the arrays Arr2 and Arr3 had different gas expansion rates resulting in different gas concentration at the outlet of the nozzle. The plasma concentration of $n_p = 1\times10^{19}$ cm^{-3} for the array Arr3 was reached at higher gas backing pressure. The distance of LWFA acceleration for Arr3 nozzle was longer than for the array Arr2; therefore, the energy of accelerated electrons and X- ray yield using the array Arr3 was higher.

The implementation of nozzle arrays in wiggler geometry resulted in the increase of divergence of the electron beam for $a_0 = 4.0$ and $n_p = 1\times10^{19}$ cm^{-3} by 30-50% (Fig. 21cd, 22a, and 41). The comparison of shadowgrams of plasma diagnostics of S1, Arr2, Arr3 nozzles (Fig. 36c and 37) and the OpenFoam simulation results (Fig. 25cd) confirmed the formation of the plasma density grid in the propagation path of the laser beam. It corresponded approximately to the plasma density profiles simulated using FBPIC algorithm. For the array Arr2, the shock waves were present at the laser-nozzle distance of 800 μm. For the Arr3 having higher gas jet expansion rate, the

plasma density array was formed by intersecting shock waves at the laser-nozzle distance of 400 μm. The modelled plasma profiles in wiggler geometry predicted the growth of X-ray photon number per shot relative to a single plasma section profile. The experimental results confirmed the increase in the efficiency of X-ray radiation. The spatial distribution of X- ray radiation varied from circular to elliptical one as well as the orientation of elliptical distribution altered from shot to shot. It indicated that the divergence and direction of X-ray radiation depend on the spatial distribution of plasma rather than on laser polarization. The interference of shock waves was defined by the period of nozzle array as well as by the pressure, temperature, and expansion rate of colliding jets. The measured critical energy of betatron radiation was in the range of 2.2-2.6 keV and the radius of the betatron source - 5 μm on average. In the numerical simulations, the betatron radius defined as the ratio of transversal and longitudinal electron momenta of electrons was 1-2 μm (Fig. 22b). The difference between the calculated and experimentally measured radius of X-ray source could be explained by the much broader transversal distribution radius >50 μm of electrons at the acceleration distance of 2.5 mm. The resulting spectrum and source size of X-ray radiation was defined by the superposition of radiation of electrons with diverse momenta radiating at different spatial positions. The X-ray radiation with the photon energy of several keV is mainly generated by electrons having higher energy and concentrated in the radius of approximately 5μm. The electrons located in the broad halo of 50μm have lower energy and generate radiation with photon energies < 2 keV (Fig. 22d). More intense X-ray radiation from the central part of electron bunch in the radius of 5 μm can also explain the decrease of X-ray divergence (FWHM) observed at the backing pressure corresponding to the maximum of X-ray yield for Arr3 (Fig 45c).

The small size and short duration of betatron X-ray source provide new opportunities for the diagnostics in material science. The spatial resolution of the clinical computed tomography (CT) scanners is usually in the mm range. X-ray micro-computed tomography (μCT) systems achieve a resolution of less than 100 μm [183]. However, the X-ray flux of μCT is limited by the melting of an anode of a sub-mm scale if the current is too high [184]. The LWFA-driven X-ray sources achieve resolutions of few microns. The pulse duration of the betatron X-ray radiation can be approximated to the duration of electron bunch propagation and is in the range of a few femtosecond [119]. The betatron X-ray radiation allows to study fast dynamic processes in plasma physics, phase transitions and states of Warm Dense Matter (WDM) at femtosecond and picosecond scale [5].

Transient phenomena are investigated with pump-probe techniques, where laser pump radiation excites a sample of interest, and another beam probes the process evolution. The short duration of the LWFA generated X-rays can be implemented in temporally resolved X-ray absorption spectroscopy (XAS). The electronic density of states, electron-ion equilibration processes, the static and local atomic structure can be characterized by X-ray Absorption Near Edge Structure (XANES) and Extended X-ray Absorption Fine Structure (EXAFS) techniques [185]. During the excitation process, K_α absorption lines are shifted due to the electron screening is reduction. The depth of the absorption lines changes during the time when a part of electrons recombines [186]. Excited electrons leave unoccupied states and it allows the absorption below L-edges creating the absorption pre-edge structure during the first hundred femtoseconds that follow the pump laser irradiation [187]. Femtosecond X-ray crystallography allows to study atomic motions of biological and chemical structures with the duration of one vibrational period of approximately 100 fs. Ultrafast time-resolved X-ray diffraction enables the observation of the instantaneous atomic positions, phase transition between amorphous, liquid or crystalline [188]. Using betatron X-ray source, ultrafast transient WDM processes of extreme temperature, pressure, and density present in stars and inertial confinement fusion can be studied.

The LWFA-driven electron beams can be implemented for the excitation of high energy photons at MeV range using Compton scattering and Bremsstrahlung to penetrate dense objects. A small source size of few μm and femtosecond duration of electron bunch ensures good spatial and temporal resolution of the radiography imaging [5]. Micrometric plasma targets of subcritical density can be used for ion acceleration in the lasers systems operating at a high-repetition rate.

Emerging advanced synchrotron and LWFA-driven sources of ionizing radiation facilitate the research and development of new therapy irradiation concepts. The novel modality of FLASH-radiotherapy using synchrotron X-rays [189] and LINAC Very High Energy Electron (VHEE) beams of 50-200 MeV [190] allows the delivery of large single doses of radiation (10-20 Gy) at mean dose-rates of 30-100 Gy/s. Medical linear accelerators generate photon and electron beams with energies in the range between 5 and 20 MeV and deposit a large fraction of their energy on the skin. The electrons of similar energy are mostly used for treatments of superficial cancers. The increased inertia of very high-energy electrons (VHEEs) due to relativistic effects reduces scattering and enables irradiation of deep-seated tumours. The modelling data indicate that focused 200 MeV and 2 GeV beams achieve highly localised dose deposition at the target depth of 15 cm [191]. The

reduction of irradiation exposure to a few milliseconds enhances the tumour control and reduces the radiation side effects on the health tissues. Several pre-clinical models show that VHEE, delivered at ultra-high dose-rates are able to protect normal lung [192] and brain tissues [189]. The basic requirement for a FLASH treatment is a very high dose-rate (exceeding ~ 40 Gy/s) over single unfractionated irradiation compared to the conventional dose-rate irradiation of 0.03-0.05 Gy/s [189,193]. The peak dose-rate of the pulse in the LINAC and synchrotron experiments reach 1.2×10^{3} - 9.0×10^{12} Gy/s. The practical implementation of FLASH treatment is limited by the lack of hospital-scale accelerators, however.

The VHEE beams from laser-plasma accelerators can provide an alternative for FLASH-radiotherapy applications. The LWFA source deliver the ultrafast dose in the time scale of molecular motion. The adaptative responses of cells and tissues to clustered DNA damages-repairs, the behaviour of secondary electrons in the prethermal regime of ionization clusters has still to be investigated yet [194]. Typical doses obtained from 200 TW laser producing ~0.5 nC electron bunches of 50-250 MeV are in the range of few cGy per shot. The peak dose rate per shot reaches $\sim10^{13}$ Gy s^{-1} [193,195]. In recent LWFA experiments, the dose delivered to the target with few hundreds of shots was 1.6 Gy [193]. The LWFA source was optimized to provide a “pencil beam” suitable to irradiate millimetre size volumes at depths up to 10 cm. To reach the necessary FLASH dose-rate of 40 Gy/s, the operation at kHz repetition rate, monoenergetic electron beams and improvement of long-term stability is required. Stable delivery of $3\text{-}5 \times 10^{7}$ shots using LOA 4 TW 1 kHz laser paves the way for the development of compact LWFA-driven X-ray FLASH radiotherapy systems [136].

7.5. Conclusions

In the experimental tests, the control of injection of electrons and the increase of the number of photons per shot, critical energy and brightness of the secondary X-ray betatron radiation using structured plasma targets, was demonstrated.

- The implementation of the nozzle array in the injector geometry and the combined density down-ramp triggered, while ionization-injection of electrons enabled the formation of quasi-monoenergetic bunches of electrons with a charge of 4-5 pC and energy of 50±10 MeV.
- Using 40 TW, 35 fs laser at the Lund Laser Centre energies accelerated electrons of 30-150 MeV and 1.0×10^{8} - 5.5×10^{8} photons per shot of betatron radiation have been measured.
- The implementation of the nozzle array in the wiggler geometry increased the number of photons per shot, and the brightness of X-ray by a factor of 2-3 relative to a single-jet plasma target source.
- The measured betatron source size was of 3-7 μm on average.
- The resolution of X-ray imaging limited by the source size was 9 μm.
- Using near-single-cycle 0.8 TW 4 fs 1 kHz laser, the electron beams with a charge of 1-2.6 pC and 2-3 MeV energy were obtained for the continuous operation of 5 hours.
- The fused-silica nozzles showed high resilience to damage and provided reliable and reproducible results after operation for about 3 - 5×10^{7} shots.

LIST OF MAIN CONCLUSIONS

1) The numerical PIC simulation and experimental results confirmed that the charge of accelerated electrons could be increased and the energy dispersion of the electrons can be lowered using the combined ionization and density down-ramp triggered injection of structured plasma concentration profiles in injector geometry.

2) For $a_0 = 4.0$ and $n_p = 1 \times 10^{19}$ cm^{-3} the implementation of structured plasma concentration profiles in wiggler geometry increased transversal electron divergence by 30-50%, and the number of photons per shot of betatron X-ray radiation 2-3 times relative to the single jet gas target.

3) The simulation of computational fluid dynamics and interferometric measurements confirmed that structured plasma concentration profiles could be built by intersecting shock waves of supersonic jets of arrays of converging-diverging micronozzles and micronozzles of a fixed diameter.

4) Micronozzle arrays of micrometric dimensions resistant to optical damage can be manufactured from transparent materials, such as fused silica, combining fast removal laser nanosecond rear side processing and high-precision FLSE technique.

SUMMARY

In this thesis, the properties of electron beams and secondary X-ray radiation using high-intensity Laser Plasma Wakefield Accelerators (LWFA) and structured plasma concentration profiles in wiggler and injector geometry were studied.

The LWFA electron acceleration using Particle-in-Cell FBPIC code was numerically simulated. The simulation results of electron distribution were post-processed for the estimation of the parameters of secondary X-ray radiation. The formation of gas targets by intersecting supersonic jets was modelled using OpenFOAM software of computational fluid dynamics. Arrays of converging-diverging micronozzles and micronozzles of fixed diameter were designed for the formation of required gas density profiles. The nozzles were manufactured from fused silica using hybrid nanosecond laser rear-side machining and femtosecond laser-assisted selective etching (FLSE) technique. The wall roughness and edge chipping impact on the subsonic and supersonic gas flow was estimated.

The experimental work of LWFA electron acceleration and measurement of secondary betatron X-ray radiation was done using the 40 TW, 35 fs laser at the Lund Laser Centre. Electron energies of 30-150 MeV and 1.0×10^8 - 5.5×10^8 photons per shot of betatron radiation have been measured. Using nozzle arrays in injector geometry and combined density down-ramp and ionization injection, quasi-monoenergetic electron bunches of 4-5 pC and 50±10 MeV were generated. The implementation of the betatron source with structured plasma concentration profiles in wiggler geometry raised the efficiency of X-ray generation and increased the number of photons per shot by a factor of 2-3 compared to a single-jet gas target. The resolution of X- ray transmission imaging limited by the source size was 9 μm.

The micronozzle fabrication technology was implemented for the stable LWFA acceleration of electrons using LOA ENSTA near-single-cycle 0.8 TW 4 fs 1 kHz laser. The electron beams with a charge of several picocoulombs and 2-3 MeV energy were obtained for the continuous operation of 5 hours. The fused-silica nozzles showed high resilience to damage and provided reliable and reproducible results after operation for about 3-5 × 10^7 shots. The formation of tailored plasma profiles with the dimensions of less than 40 μm with nozzle surface roughness < 1 μm was demonstrated.

REFERENCES

1. T. Tajima and G. Mourou, “Zettawatt-exawatt lasers and their applications in ultrastrong-field physics”, Physical Review Special Topics - Accelerators and Beams **5**(3), 44-52, (2002).
2. G. A. Mourou, T. Tajima, and S. V. Bulanov, “Optics in the relativistic regime”, Reviews of Modern Physics **78**(2), (2006).
3. J. F. Ong, W. R. Teo, T. Moritaka, and H. Takabe, “Radiation reaction in the interaction of ultraintense laser with matter and gamma ray source”, Physics of Plasmas **23**(5), (2016).
4. D. Strickland and G. Mourou, “Compression of amplified chirped optical pulses”, Optics Communications **56**(3), 219-221, (1985).
5. F. Albert and A. G. R. Thomas, “Applications of laser wakefield accelerator-based light sources”, Plasma Physics and Controlled Fusion **58**(10), 103001, (2016).
6. J. S. Lee and G. B. Cleaver, “Investigation of the Quantum Vacuum as an Energy Sink for Subcritical and Supercritical Vaporization Lasers”, Heliyon **6**(1), (2018).
7. G. A. Mourou, G. Korn, Wolfgang. Sandner, and J. L. Collier, *ELI - Extreme Light Infrastructure: Science and Technology with Ultra-Intense Lasers, Whitebook* (THOSS Media GmbH, 2011).
8. T. Popmintchev, M. C. Chen, D. Popmintchev, P. Arpin, S. Brown, S. Ališauskas, G. Andriukaitis, T. Balčiunas, O. D. Mücke, A. Pugzlys, A. Baltuška, B. Shim, S. E. Schrauth, A. Gaeta, C. Hernández-García, L. Plaja, A. Becker, A. Jaron-Becker, M. M. Murnane, and H. C. Kapteyn, “Bright coherent ultrahigh harmonics in the kev x-ray regime from mid-infrared femtosecond lasers”, Science **336**(6086), 1287-1291, (2012).
9. M. M. Murnane, H. C. Kapteyn, M. D. Rosen, and R. W. Falcone, “Ultrafast X-ray pulses from laser-produced plasmas”, Science **251**(4993), 531-536, (1991).
10. K. Sokolowski-Tinten, C. Blome, C. Dietrich, A. Tarasevitch, M. Horn von Hoegen, D. von der Linde, A. Cavalleri, J. Squier, and M. Kammler, “Femtosecond x-ray measurement of ultrafast melting and large acoustic transients”, Physical Review Letters **87**(22), 225701-225701-4, (2001).
11. T. Tuohimaa, M. Otendal, and H. M. Hertz “Phase-contrast x-ray imaging with a liquid-metal-jet-anode microfocus source”, Applied Physics Letters **91**(7), (2007).

12. P. Scampoli, C. Carpentieri, M. Giannelli, V. Magaddino, L. Manti, C. Moriello, M. A. Piliero, S. Righi, and F. di Martino, "Radiobiological characterization of the very high dose rate and dose per pulse electron beams produced by an IORT (intra operative radiation therapy) dedicated linac", Translational Cancer Research **6**(S5), S761-S768, (2017).
13. E. J. Jaeschke, S. Khan, J. R. Schneider, and J. B. Hastings, *Synchrotron Light Sources and Free-Electron Lasers: Accelerator Physics, Instrumentation and Science Applications* (Springer International Publishing, 2016).
14. W. D. Kilpatrick, "Criterion for vacuum sparking designed to include both rf and dc", Review of Scientific Instruments **28**(10), 824-826, (1957).
15. A. Grudiev and W. Wuensch, "A new local field quantity describing the high gradient limit of accelerating structures", in *Proceedings of the 24th Linear Accelerator Conference, LINAC 2008* (American Physical Society, 2009), **12**(10), pp. 936-938.
16. B. Hidding, A. Beaton, L. Boulton, S. Corde, A. Doepp, F. A. Habib, T. Heinemann, A. Irman, S. Karsch, G. Kirwan, A. Knetsch, G. G. Manahan, A. M. M. de la Ossa, A. Nutter, P. Scherkl, U. Schramm, and D. Ullmann, "Fundamentals and Applications of Hybrid LWFA-PWFA", in *Springer Proceedings in Physics* (Springer Science and Business Media, LLC, 2019), **231**, pp. 95-120.
17. E. Esarey, P. Sprangle, and J. Krall, "Laser acceleration of electrons in vacuum", Physical Review E **52**(5), 5443-5453, (1995).
18. M. Wen, Y. I. Salamin, and C. H. Keitel, "Electron acceleration by a radially-polarized laser pulse in a plasma micro-channel", Optics Express **27**(2), 557, (2019).
19. L. J. Wong, K. H. Hong, S. Carbajo, A. Fallahi, P. Piot, M. Soljačić, J. D. Joannopoulos, F. X. Kärtner, and I. Kaminer, "Laser-Induced Linear-Field Particle Acceleration in Free Space", Scientific Reports **7**(1), 1-9, (2017).
20. J. L. Shaw, N. Lemos, K. A. Marsh, F. S. Tsung, W. B. Mori, and C. Joshi, "Estimation of direct laser acceleration in laser wakefield accelerators using particle-in-cell simulations", Plasma Physics and Controlled Fusion **58**(3), (2016).
21. C. Gahn, G. D. Tsakiris, A. Pukhov, J. Meyer-Ter-Vehn, G. Pretzler, P. Thirolf, D. Habs, and K. J. Witte, "Multi-MeV electron beam generation by direct laser acceleration in high-density plasma channels", Physical Review Letters **83**(23), 4772-4775, (1999).

22. T. Tajima and J. M. Dawson, “Laser electron accelerator”, Physical Review Letters **43**(4), 267-270, (1979).
23. Paul. Gibbon, *Short Pulse Laser Interactions with Matter: An Introduction* (Imperial College Press, 2005).
24. W. L. Kruer, *The Physics of Laser Plasma Interactions* (CRC Press, 2018).
25. S. Corde, K. Ta Phuoc, G. Lambert, R. Fitour, V. Malka, A. Rousse, A. Beck, and E. Lefebvre, “Femtosecond x rays from laser-plasma accelerators”, Reviews of Modern Physics **85**(1), 1-48, (2013).
26. W. Lu, C. Huang, M. Zhou, W. B. Mori, and T. Katsouleas, “Nonlinear theory for relativistic plasma wakefields in the blowout regime”, Physical Review Letters **96**(16), 165002, (2006).
27. I. Kostyukov, A. Pukhov, and S. Kiselev, “Phenomenological theory of laser-plasma interaction in “bubble” regime”, Physics of Plasmas **11**(11), 5256-5264 (2004).
28. W. Lu, M. Tzoufras, C. Joshi, F. S. Tsung, W. B. Mori, J. Vieira, R. A. Fonseca, and L. O. Silva, “Generating multi-GeV electron bunches using single stage laser wakefield acceleration in a 3D nonlinear regime”, Physical Review Special Topics - Accelerators and Beams **10**(6), 061301, (2007).
29. J. Faure, D. Gustas, D. Guénot, A. Vernier, F. Böhle, M. Ouillé, S. Haessler, R. Lopez-Martens, and A. Lifschitz, “A review of recent progress on laser-plasma acceleration at kHz repetition rate”, Plasma Physics and Controlled Fusion **61**(1), 014012, (2019).
30. W. Lu, C. Huang, M. Zhou, M. Tzoufras, F. S. Tsung, W. B. Mori, and T. Katsouleas, “A nonlinear theory for multidimensional relativistic plasma wave wakefields”, in *Physics of Plasmas* (American Institute of Physics AIP, 2006), **13**(5), p. 056709.
31. A. B. Borisov, A. v. Borovskiy, O. B. Shiryaev, V. v. Korobkin, A. M. Prokhorov, J. C. Solem, T. S. Luk, K. Boyer, and C. K. Rhodes, “Relativistic and charge-displacement self-channeling of intense ultrashort laser pulses in plasmas”, Physical Review A **45**(8), 5830-5845, (1992).
32. P. Sprangle and E. Esarey, “Interaction of ultrahigh laser fields with beams and plasmas”, Physics of Fluids B **4**(7), 2241-2248, (1992).
33. C. Ren, B. J. Duda, R. G. Hemker, W. B. Mori, T. Katsouleas, T. M. Antonsen, and P. Mora, “Compressing and focusing a short laser pulse by a thin plasma lens”, Physical Review E - Statistical Physics, Plasmas, Fluids, and Related Interdisciplinary Topics **63**(2), 8, (2001).

34. B. Beaurepaire, A. Lifschitz, and J. Faure, “Electron acceleration in sub-relativistic wakefields driven by few-cycle laser pulses,” New Journal of Physics **16**, 23023, (2014).
35. L. v. Keldysh, “Ionization in the field of a strong electromagnetic wave”, Soviet Physics JETP **20**(5), 1307-1314, (1965).
36. S. Bulanov, N. Naumova, F. Pegoraro, and J. Sakai, “Particle injection into the wave acceleration phase due to nonlinear wake wave breaking”, Physical Review E - Statistical Physics, Plasmas, Fluids, and Related Interdisciplinary Topics **58**(5), R5257-R5260, (1998).
37. N. H. Matlis, A. J. Gonsalves, S. Steinke, J. van Tilborg, B. Shaw, D. E. Mittelberger, C. G. R. Geddes, and W. P. Leemans, “Transient behavior of a supersonic three-dimensional micronozzle with an intersecting capillary”, Journal of Applied Physics **119**(7), (2016).
38. A. J. Gonsalves, K. Nakamura, C. Lin, D. Panasenko, S. Shiraishi, T. Sokollik, C. Benedetti, C. B. Schroeder, C. G. R. R. Geddes, J. van Tilborg, J. Osterhoff, E. Esarey, C. Toth, and W. P. Leemans, “Tunable laser plasma accelerator based on longitudinal density tailoring”, Nature Physics **7**(11), 862-866, (2011).
39. M. Hansson, B. Aurand, X. Davoine, H. Ekerfelt, K. Svensson, A. Persson, C. G. Wahlström, and O. Lundh, “Down-ramp injection and independently controlled acceleration of electrons in a tailored laser wakefield accelerator”, Physical Review Special Topics - Accelerators and Beams **18**(7), (2015).
40. L. Fan-Chiang, H.-S. Mao, H.-E. Tsai, T. Ostermayr, K. K. Swanson, S. K. Barber, S. Steinke, J. van Tilborg, C. G. R. Geddes, and W. P. Leemans, “Gas density structure of supersonic flows impinged on by thin blades for laser-plasma accelerator targets”, Physics of Fluids **32**(6), 066108, (2020).
41. F. Massimo, A. F. Lifschitz, C. Thaury, and V. Malka, “Numerical studies of density transition injection in laser wakefield acceleration”, Plasma Physics and Controlled Fusion **59**(8), (2017).
42. H. Ekerfelt, M. Hansson, I. Gallardo González, X. Davoine, and O. Lundh, “A tunable electron beam source using trapping of electrons in a density down-ramp in laser wakefield acceleration”, Scientific Reports **7**(1), 12229, (2017).
43. M. Burza, A. Gonoskov, K. Svensson, F. Wojda, A. Persson, M. Hansson, G. Genoud, M. Marklund, C. G. Wahlström, and O. Lundh, “Laser wakefield acceleration using wire produced double density ramps”, Physical Review Special Topics - Accelerators and Beams **16**(1), (2013).

44. A. v. Brantov, T. Z. Esirkepov, M. Kando, H. Kotaki, V. Y. Bychenkov, and S. V. Bulanov, "Controlled electron injection into the wake wave using plasma density inhomogeneity", Physics of Plasmas **15**(7), 073111, (2008).
45. G. Fubiani, E. Esarey, C. B. Schroeder, and W. P. Leemans, "Beat wave injection of electrons into plasma waves using two interfering laser pulses", Physical Review E - Statistical Physics, Plasmas, Fluids, and Related Interdisciplinary Topics **70**(1), 12, (2004).
46. M. Zeng, M. Chen, L. L. Yu, W. B. Mori, Z. M. Sheng, B. Hidding, D. A. Jaroszynski, and J. Zhang, "Multichromatic narrow-energy-spread electron bunches from laser-Wakefield acceleration with dual-color lasers", Physical Review Letters **114**(8), (2015).
47. M. Hansson, B. Aurand, H. Ekerfelt, A. Persson, and O. Lundh, "Injection of electrons by colliding laser pulses in a laser wakefield accelerator", Nuclear Instruments and Methods in Physics Research, Section A: Accelerators, Spectrometers, Detectors and Associated Equipment **829**, 99-103, (2016).
48. Q. Zhao, S. M. Weng, Z. M. Sheng, M. Chen, G. B. Zhang, W. B. Mori, B. Hidding, D. A. Jaroszynski, and J. Zhang, "Ionization injection in a laser wakefield accelerator subject to a transverse magnetic field", New Journal of Physics **20**(6), (2018).
49. M. Hansson, T. L. Audet, H. Ekerfelt, B. Aurand, I. Gallardo González, F. G. Desforges, X. Davoine, A. Maitrallain, S. Reymond, P. Monot, A. Persson, S. Dobosz Dufrénoy, C. G. Wahlström, B. Cros, and O. Lundh, "Localization of ionization-induced trapping in a laser wakefield accelerator using a density down-ramp", Plasma Physics and Controlled Fusion **58**(5), 055009, (2016).
50. B. B. Pollock, C. E. Clayton, J. E. Ralph, F. Albert, A. Davidson, L. Divol, C. Filip, S. H. Glenzer, K. Herpoldt, W. Lu, K. A. Marsh, J. Meinecke, W. B. Mori, A. Pak, T. C. Rensink, J. S. Ross, J. Shaw, G. R. Tynan, C. Joshi, and D. H. Froula, "Demonstration of a narrow energy spread, ~0.5 GeV electron beam from a two-stage laser wakefield accelerator.", Physical review letters **107**(4), 045001, (2011).
51. G. Golovin, S. Banerjee, S. Chen, N. Powers, C. Liu, W. Yan, J. Zhang, P. Zhang, B. Zhao, and D. Umstadter, "Control and optimization of a staged laser-wakefield accelerator", Nuclear Instruments and Methods in Physics Research Section A: Accelerators, Spectrometers, Detectors and Associated Equipment **830**, 375-380, (2016).

52. S. Li, N. A. M. Hafz, M. Mirzaie, T. Sokollik, M. Zeng, M. Chen, Z. Sheng, and J. Zhang, "Enhanced single-stage laser-driven electron acceleration by self-controlled ionization injection", Optics Express **22**(24), 29578, (2014).
53. M. Mirzaie, S. Li, M. Zeng, N. A. M. Hafz, M. Chen, G. Y. Li, Q. J. Zhu, H. Liao, T. Sokollik, F. Liu, Y. Y. Ma, L. M. Chen, Z. M. Sheng, and J. Zhang, "Demonstration of self-truncated ionization injection for GeV electron beams", Scientific Reports **5**, 14659, (2015).
54. A. Irman, J. P. Couperus, A. Debus, A. Köhler, J. M. Krämer, R. Pausch, O. Zarini, and U. Schramm, "Improved performance of laser wakefield acceleration by tailored self-truncated ionization injection", Plasma Phys.Control.Fusion **60**(4), (2018).
55. J. Götzfried, A. Döpp, M. F. Gilljohann, F. M. Foerster, H. Ding, S. Schindler, G. Schilling, A. Buck, L. Veisz, and S. Karsch, "Physics of High-Charge Electron Beams in Laser-Plasma Wakefields", Physical Review X **10**(4), (2020).
56. M. Zeng, M. Chen, Z. M. Sheng, W. B. Mori, and J. Zhang, "Self-truncated ionization injection and consequent monoenergetic electron bunches in laser wakefield acceleration", Physics of Plasmas **21**(3), 030701, (2014).
57. J. P. Couperus, R. Pausch, A. Köhler, O. Zarini, J. M. Krämer, M. Garten, A. Huebl, R. Gebhardt, U. Helbig, S. Bock, K. Zeil, A. Debus, M. Bussmann, U. Schramm, and A. Irman, "Demonstration of a beam loaded nanocoulomb-class laser wakefield accelerator", Nature Communications **8**(1), (2017).
58. M. Vargas, W. Schumaker, Z. H. He, Z. Zhao, K. Behm, V. Chvykov, B. Hou, K. Krushelnick, A. Maksimchuk, V. Yanovsky, and A. G. R. Thomas, "Improvements to laser wakefield accelerated electron beam stability, divergence, and energy spread using three-dimensional printed two-stage gas cell targets", Applied Physics Letters **104**(17), (2014).
59. H. T. Kim, K. H. Pae, H. J. Cha, I. J. Kim, T. J. Yu, J. H. Sung, S. K. Lee, T. M. Jeong, and J. Lee, "Enhancement of electron energy to the multi-GeV regime by a dual-stage laser-wakefield accelerator pumped by petawatt laser pulses", Physical Review Letters **111**(16), (2013).
60. Z. Zhang, J. J. Liu, W. Wang, W. Li, C. Yu, Y. Tian, R. Qi, C. Wang, Z. Qin, M. Fang, J. J. Liu, K. Nakajima, R. Li, and Z. Xu, "Generation of high quality electron beams from a quasi-phase-stable cascaded

laser wakefield accelerator with density-tailored plasma segments", New Journal of Physics **17**(10), (2015).

61. K. K. Swanson, H. E. Tsai, S. K. Barber, R. Lehe, H. S. Mao, S. Steinke, J. van Tilborg, K. Nakamura, C. G. R. Geddes, C. B. Schroeder, E. Esarey, and W. P. Leemans, "Control of tunable, monoenergetic laser-plasma-accelerated electron beams using a shock-induced density downramp injector", Physical Review Accelerators and Beams **20**(5), (2017).
62. G. Golovin, S. Banerjee, J. Zhang, S. Chen, C. Liu, B. Zhao, J. Mills, K. Brown, C. Petersen, and D. Umstadter, "Tomographic imaging of nonsymmetric multicomponent tailored supersonic flows from structured gas nozzles", Applied Optics **54**(11), 3491, (2015).
63. E. Esarey, C. B. Schroeder, and W. P. Leemans, "Physics of laser-driven plasma-based electron accelerators", Reviews of Modern Physics **81**(3), 1229-1285, (2009).
64. W. P. P. Leemans, A. J. J. Gonsalves, H.-S. S. Mao, K. Nakamura, C. Benedetti, C. B. B. Schroeder, Cs. Tóth, J. Daniels, D. E. E. Mittelberger, S. S. S. Bulanov, J.-L. L. Vay, C. G. R. G. R. Geddes, and E. Esarey, "Multi-GeV Electron Beams from Capillary-Discharge-Guided Subpetawatt Laser Pulses in the Self-Trapping Regime", Physical Review Letters **113**(24), 245002, (2014).
65. C. G. R. Geddes, C. Toth, J. van Tilborg, E. Esarey, C. B. Schroeder, D. Bruhwiler, C. Nieter, J. Cary, and W. P. Leemans, "High-quality electron beams from a laser wakefield accelerator using plasma-channel guiding", Nature **431**(7008), 538-541, (2004).
66. S. Karsch, J. Osterhoff, A. Popp, T. P. Rowlands-Rees, Z. Major, M. Fuchs, B. Marx, R. Hörlein, K. Schmid, L. Veisz, S. Becker, U. Schramm, B. Hidding, G. Pretzler, D. Habs, F. Grüner, F. Krausz, and S. M. Hooker, "GeV-scale electron acceleration in a gas-filled capillary discharge waveguide", New Journal of Physics **9**, (2007).
67. J. Luo, M. Chen, W. Y. Wu, S. M. Weng, Z. M. Sheng, C. B. Schroeder, D. A. Jaroszynski, E. Esarey, W. P. Leemans, W. B. Mori, and J. Zhang, "Multistage Coupling of Laser-Wakefield Accelerators with Curved Plasma Channels", Physical Review Letters **120**(15), (2018).
68. A. Popp, J. Vieira, J. Osterhoff, Z. Major, R. Hörlein, M. Fuchs, R. Weingartner, T. P. Rowlands-Rees, M. Marti, R. A. Fonseca, S. F. Martins, L. O. Silva, S. M. Hooker, F. Krausz, F. Grüner, and S. Karsch, "All-optical steering of laser-wakefield-accelerated electron beams", Physical Review Letters **105**(21), (2010).

69. C. Yu, J. Liu, W. Wang, W. Li, R. Qi, Z. Zhang, Z. Qin, J. Liu, M. Fang, K. Feng, Y. Wu, L. Ke, Y. Chen, C. Wang, Y. Xu, Y. Leng, C. Xia, R. Li, and Z. Xu, "Enhanced betatron radiation by steering a laser-driven plasma wakefield with a tilted shock front", Applied Physics Letters **112**(13), (2018).
70. D. H. Froula, J. P. Palastro, D. Turnbull, A. Davies, L. Nguyen, A. Howard, D. Ramsey, P. Franke, S. W. Bahk, I. A. Begishev, R. Boni, J. Bromage, S. Bucht, R. K. Follett, D. Haberberger, G. W. Jenkins, J. Katz, T. J. Kessler, J. L. Shaw, and J. Vieira, "Flying focus: Spatial and temporal control of intensity for laser-based applications", Physics of Plasmas **26**(3), (2019).
71. A. J. Howard, D. Turnbull, A. S. Davies, P. Franke, D. H. Froula, and J. P. Palastro, "Photon Acceleration in a Flying Focus", Physical Review Letters **123**(12), 124801, (2019).
72. S. Smartsev, C. Caizergues, K. Oubrerie, J. Gautier, J.-P. Goddet, A. Tafzi, K. T. Phuoc, V. Malka, and C. Thaury, "Axiparabola: a long-focal-depth, high-resolution mirror for broadband high-intensity lasers", Optics Letters **44**(14), 3414, (2019).
73. J. P. Palastro, J. L. Shaw, P. Franke, D. Ramsey, T. T. Simpson, and D. H. Froula, "Dephasingless Laser Wakefield Acceleration", Physical Review Letters **124**(13), (2020).
74. J. van Tilborg, "Lining Up for Wakefield Acceleration", Physics **13**, 1-2, (2020).
75. D. H. Froula, L. Divol, P. Davis, J. P. Palastro, P. Michel, V. Leurent, S. H. Glenzer, B. B. Pollock, and G. Tynan, "Magnetically controlled plasma waveguide for laser wakefield acceleration", Plasma Physics and Controlled Fusion **51**(2), (2009).
76. R. Lehe, C. Thaury, E. Guillaume, A. Lifschitz, and V. Malka, "Laser-plasma lens for laser-wakefield accelerators", Physical Review Special Topics - Accelerators and Beams **17**(12), (2014).
77. P. E. Masson-Laborde, M. Z. Mo, A. Ali, S. Fourmaux, P. Lassonde, J. C. Kieffer, W. Rozmus, D. Teychenné, R. Fedosejevs, D. Teychenne, R. Fedosejevs, D. Teychenné, and R. Fedosejevs, "Giga-electronvolt electrons due to a transition from laser wakefield acceleration to plasma wakefield acceleration", Physics of Plasmas **21**(12), 1-28, (2014).
78. T. Z. Zhao, K. Behm, C. F. Dong, X. Davoine, S. Y. Kalmykov, V. Petrov, V. Chvykov, P. Cummings, B. Hou, A. Maksimchuk, J. A. Nees, V. Yanovsky, A. G. R. Thomas, and K. Krushelnick, "High-Flux Femtosecond X-Ray Emission from Controlled Generation of

Annular Electron Beams in a Laser Wakefield Accelerator", Physical Review Letters **117**(9), (2016).

79. M. F. Gilljohann, H. Ding, A. Döpp, J. Götzfried, S. Schindler, G. Schilling, S. Corde, A. Debus, T. Heinemann, B. Hidding, S. M. Hooker, A. Irman, O. Kononenko, T. Kurz, A. Martinez De La Ossa, U. Schramm, and S. Karsch, "Direct Observation of Plasma Waves and Dynamics Induced by Laser-Accelerated Electron Beams", Physical Review X **9**(1), (2019).
80. J. Lin, Y. Ma, R. Schwartz, D. Woodbury, J. A. Nees, M. Mathis, A. G. R. Thomas, K. Krushelnick, and H. Milchberg, "Adaptive control of laser-wakefield accelerators driven by mid-IR laser pulses", Optics Express **27**(8), 10912, (2019).
81. S. J. D. Dann, C. D. Baird, N. Bourgeois, O. Chekhlov, S. Eardley, C. D. Gregory, J. N. Gruse, J. Hah, D. Hazra, S. J. Hawkes, C. J. Hooker, K. Krushelnick, S. P. D. Mangles, V. A. Marshall, C. D. Murphy, Z. Najmudin, J. A. Nees, J. Osterhoff, B. Parry, P. Pourmoussavi, S. v. Rahul, P. P. Rajeev, S. Rozario, J. D. E. Scott, R. A. Smith, E. Springate, Y. Tang, S. Tata, A. G. R. Thomas, C. Thornton, D. R. Symes, and M. J. V. Streeter, "Laser wakefield acceleration with active feedback at 5 Hz", Physical Review Accelerators and Beams **22**(4), 041303, (2019).
82. A. J. Gonsalves, K. Nakamura, J. Daniels, C. Benedetti, C. Pieronek, T. C. H. de Raadt, S. Steinke, J. H. Bin, S. S. Bulanov, J. van Tilborg, C. G. R. Geddes, C. B. Schroeder, C. Tóth, E. Esarey, K. Swanson, L. Fan-Chiang, G. Bagdasarov, N. Bobrova, V. Gasilov, G. Korn, P. Sasorov, and W. P. Leemans, "Petawatt Laser Guiding and Electron Beam Acceleration to 8 GeV in a Laser-Heated Capillary Discharge Waveguide", Physical Review Letters **122**(8), 084801 (2019).
83. "Compact free-electron lasers to be developed at LBNL | Laser Focus World", https://www.laserfocusworld.com/lasers-sources/article/16558768/compact-freeelectron-lasers-to-be-developed-at-lbnl.
84. J. Badziak, "Laser-driven ion acceleration: Methods, challenges and prospects", in *Journal of Physics: Conference Series* (2018), **959**(1), p. 12001.
85. T. Tajima, D. Habs, and X. Yan, "Laser Acceleration of Ions for Radiation Therapy", Reviews of Accelerator Science and Technology **02**(01), 201-228, (2009).
86. S. C. Wilks, A. B. Langdon, T. E. Cowan, M. Roth, M. Singh, S. Hatchett, M. H. Key, D. Pennington, A. MacKinnon, and R. A.

Snavely, “Energetic proton generation in ultra-intense laser-solid interactions”, Physics of Plasmas **8**(2), 542-549, (2001).

87. S. V. Bulanov, T. Esirkepov, V. S. Khoroshkov, A. v. Kuznetsov, and F. Pegoraro, “Oncological hadrontherapy with laser ion accelerators”, Physics Letters, Section A: General, Atomic and Solid State Physics **299**(2-3), 240-247, (2002).
88. T. Esirkepov, M. Borghesi, S. V. Bulanov, G. Mourou, and T. Tajima, “Highly efficient relativistic-ion generation in the laser-piston regime”, Physical Review Letters **92**(17), 175003, (2004).
89. Y. J. Gu, Z. Zhu, X. F. Li, Q. Yu, S. Huang, F. Zhang, Q. Kong, and S. Kawata, “Stable long range proton acceleration driven by intense laser pulse with underdense plasmas”, Physics of Plasmas **21**(6), 063104, (2014).
90. D. Haberberger, S. Tochitsky, F. Fiuza, C. Gong, R. A. Fonseca, L. O. Silva, W. B. Mori, and C. Joshi, “Collisionless shocks in laser-produced plasma generate monoenergetic high-energy proton beams”, Nature Physics **8**(1), 95-99, (2012).
91. B. J. Albright, L. Yin, K. J. Bowers, B. M. Hegelich, K. A. Flippo, T. J. T. Kwan, and J. C. Fernández, “Relativistic Buneman instability in the laser breakout afterburner”, Physics of Plasmas **14**(9), 094502, (2007).
92. S. Palaniyappan, B. M. Hegelich, H. C. Wu, D. Jung, D. C. Gautier, L. Yin, B. J. Albright, R. P. Johnson, T. Shimada, S. Letzring, D. T. Offermann, J. Ren, C. Huang, R. Hörlein, B. Dromey, J. C. Fernandez, and R. C. Shah, “Dynamics of relativistic transparency and optical shuttering in expanding overdense plasmas”, Nature Physics **8**(10), 763-769, (2012).
93. B. Gonzalez-Izquierdo, M. King, R. J. Gray, R. Wilson, R. J. Dance, H. Powell, D. A. MacLellan, J. McCreadie, N. M. H. Butler, S. Hawkes, J. S. Green, C. D. Murphy, L. C. Stockhausen, D. C. Carroll, N. Booth, G. G. Scott, M. Borghesi, D. Neely, and P. McKenna, “Towards optical polarization control of laser-driven proton acceleration in foils undergoing relativistic transparency”, Nature Communications **7**(1), 1-10, (2016).
94. S. V. S. Bulanov, E. Esarey, C. B. Schroeder, S. V. S. Bulanov, T. Z. Esirkepov, M. Kando, F. Pegoraro, and W. P. Leemans, “Radiation pressure acceleration: The factors limiting maximum attainable ion energy”, Physics of Plasmas **23**(5), 056703, (2016).
95. L. Robson, P. T. Simpson, R. J. Clarke, K. W. D. Ledingham, F. Lindau, O. Lundh, T. McCanny, P. Mora, D. Neely, C. G. Wahlström,

M. Zepf, and P. McKenna, “Scaling of proton acceleration driven by petawatt-laser-plasma interactions”, Nature Physics **3**(1), 58-62, (2007).

96. A. Macchi, M. Borghesi, and M. Passoni, “Ion acceleration by superintense laser-plasma interaction”, Reviews of Modern Physics **85**(2), 751-793, (2013).

97. W. Ma, V. K. Liechtenstein, J. Szerypo, D. Jung, P. Hilz, B. M. Hegelich, H. J. Maier, J. Schreiber, and D. Habs, “Preparation of self-supporting diamond-like carbon nanofoils with thickness less than 5 nm for laser-driven ion acceleration”, in *Nuclear Instruments and Methods in Physics Research, Section A: Accelerators, Spectrometers, Detectors and Associated Equipment* (North-Holland, 2011), **655**(1), pp. 53-56.

98. I. J. Kim, K. H. Pae, I. W. Choi, C. L. Lee, H. T. Kim, H. Singhal, J. H. Sung, S. K. Lee, H. W. Lee, P. v. Nickles, T. M. Jeong, C. M. Kim, and C. H. Nam, “Radiation pressure acceleration of protons to 93 MeV with circularly polarized petawatt laser pulses”, Physics of Plasmas **23**(7), 070701, (2016).

99. W. J. Ma, I. J. Kim, J. Q. Yu, I. W. Choi, P. K. Singh, H. W. Lee, J. H. Sung, S. K. Lee, C. Lin, Q. Liao, J. G. Zhu, H. Y. Lu, B. Liu, H. Y. Wang, R. F. Xu, X. T. He, J. E. Chen, M. Zepf, J. Schreiber, X. Q. Yan, and C. H. Nam, “Laser Acceleration of Highly Energetic Carbon Ions Using a Double-Layer Target Composed of Slightly Underdense Plasma and Ultrathin Foil”, Physical Review Letters **122**(1), 014803, (2019).

100. A. Sharma and C. Kamperidis, “High energy proton micro-bunches from a laser plasma accelerator”, Scientific Reports **9**(1), 1-10, (2019).

101. A. Ben-Ismaïl, O. Lundh, C. Rechatin, J. K. Lim, J. Faure, S. Corde, and V. Malka, “Compact and high-quality gamma-ray source applied to 10 μm-range resolution radiography”, Applied Physics Letters **98**(26), 264101, (2011).

102. A. Willner, F. Tavella, M. Yeung, T. Dzelzainis, C. Kamperidis, M. Bakarezos, D. Adams, M. Schulz, R. Riedel, M. C. Hoffmann, W. Hu, J. Rossbach, M. Drescher, N. A. Papadogiannis, M. Tatarakis, B. Dromey, and M. Zepf, “Coherent control of high harmonic generation via dual-gas multijet arrays”, Physical Review Letters **107**(17), 175002, (2011).

103. I. Kostyukov, S. Kiselev, and A. Pukhov, “X-ray generation in an ion channel”, Physics of Plasmas **10**(12), 4818-4828, (2003).

104. X. Wang, R. Zgadzaj, N. Fazel, Z. Li, S. A. Yi, X. Zhang, W. Henderson, Y. Y. Chang, R. Korzekwa, H. E. Tsai, C. H. Pai, H. Quevedo, G. Dyer, E. Gaul, M. Martinez, A. C. Bernstein, T. Borger, M. Spinks, M. Donovan, V. Khudik, G. Shvets, T. Ditmire, and M. C. Downer, "Quasi-monoenergetic laser-plasma acceleration of electrons to 2 GeV", Nature Communications **4**(1), 1-9, (2013).

105. S. Cipiccia, M. R. Islam, B. Ersfeld, R. P. Shanks, E. Brunetti, G. Vieux, X. Yang, R. C. Issac, S. M. Wiggins, G. H. Welsh, M. P. Anania, D. Maneuski, R. Montgomery, G. Smith, M. Hoek, D. J. Hamilton, N. R. C. Lemos, D. Symes, P. P. Rajeev, V. O. Shea, J. M. Dias, and D. A. Jaroszynski, "Gamma-rays from harmonically resonant betatron oscillations in a plasma wake", Nature Physics **7**(11), 867-871, (2011).

106. M. Schnell, A. Sävert, I. Uschmann, O. Jansen, M. C. Kaluza, and C. Spielmann, "Characterization and application of hard X-ray betatron radiation generated by relativistic electrons from a laser-wakefield accelerator", Journal of Plasma Physics **81**(4), 1-38, (2015).

107. H. P. Schlenvoigt, K. Haupt, A. Debus, F. Budde, O. Jäckel, S. Pfotenhauer, H. Schwoerer, E. Rohwer, J. G. Gallacher, E. Brunetti, R. P. Shanks, S. M. Wiggins, and D. A. Jaroszynski, "A compact synchrotron radiation source driven by a laser-plasma wakefield accelerator", Nature Physics **4**(2), 130-133, (2008).

108. N. D. Powers, I. Ghebregziabher, G. Golovin, C. Liu, S. Chen, S. Banerjee, J. Zhang, and D. P. Umstadter, "Quasi-monoenergetic and tunable X-rays from a laser-driven Compton light source", Nature Photonics **8**(1), 28-31, (2014).

109. C. Liu, G. Golovin, S. Chen, J. Zhang, B. Zhao, D. Haden, S. Banerjee, J. Silano, H. Karwowski, and D. Umstadter, "Generation of 9 MeV γ-rays by all-laser-driven Compton scattering with second-harmonic laser light", Optics Letters **39**(14), 4132, (2014).

110. E. Esarey, S. K. Ride, and P. Sprangle, "Nonlinear Thomson scattering of intense laser pulses from beams and plasmas", Physical Review E **48**(4), 3003-3021, (1993).

111. Y. Glinec, J. Faure, L. le Dain, S. Darbon, T. Hosokai, J. J. Santos, E. Lefebvre, J. P. Rousseau, F. Burgy, B. Mercier, and V. Malka, "High-resolution γ-ray radiography produced by a laser-plasma driven electron source", Physical Review Letters **94**(2), 025003, (2005).

112. A. Giulietti, N. Bourgeois, T. Ceccotti, X. Davoine, S. Dobosz, P. D'Oliveira, M. Galimberti, J. Galy, A. Gamucci, D. Giulietti, L. A.

Gizzi, D. J. Hamilton, E. Lefebvre, L. Labate, J. R. Marquès, P. Monot, H. Popescu, F. Réau, G. Sarri, P. Tomassini, and P. Martin, "Intense γ-ray source in the giant-dipole-resonance range driven by 10-TW laser pulses", Physical Review Letters **101**(10), 105002, (2008).

113. C. Thaury, E. Guillaume, A. Döpp, R. Lehe, A. Lifschitz, K. Ta Phuoc, J. Gautier, J. P. Goddet, A. Tafzi, A. Flacco, F. Tissandier, S. Sebban, A. Rousse, and V. Malka, "Demonstration of relativistic electron beam focusing by a laser-plasma lens", Nature Communications **6**, 6860, (2015).

114. J. A. Holloway, P. A. Norreys, A. G. R. Thomas, R. Bartolini, R. Bingham, J. Nydell, R. M. G. M. Trines, R. Walker, and M. Wing, "Brilliant X-rays using a Two-Stage Plasma Insertion Device", Scientific Reports **7**(1), 3985, (2017).

115. J. Ferri, S. Corde, A. Döpp, A. Lifschitz, A. Doche, C. Thaury, K. Ta Phuoc, B. Mahieu, I. A. Andriyash, V. Malka, and X. Davoine, "High-Brilliance Betatron γ -Ray Source Powered by Laser-Accelerated Electrons", Physical Review Letters **120**(25), 254802, (2018).

116. A. J. J. Goers, G. A. A. Hine, L. Feder, B. Miao, F. Salehi, J. K. K. Wahlstrand, H. M. M. Milchberg, A. J. J. Goers, L. Feder, B. Miao, F. Salehi, J. K. K. Wahlstrand, and H. M. M. Milchberg, *Multi-MeV Electron Acceleration by Subterawatt Laser Pulses* (American Physical Society, 2015), **115**(19), p. 194802.

117. L. M. Chen, W. C. Yan, D. Z. Li, Z. D. Hu, L. Zhang, W. M. Wang, N. Hafz, J. Y. Mao, K. Huang, Y. Ma, J. R. Zhao, J. L. Ma, Y. T. Li, X. Lu, Z. M. Sheng, Z. Y. Wei, J. Gao, and J. Zhang, "Bright betatron X-ray radiation from a laser-driven-clustering gas target", Scientific Reports **3**(1), 1912, (2013).

118. S. W. Hwang and H. J. Lee, "Betatron radiation of an Off-axis injected electron in a laser wakefield accelerator", Journal of the Optical Society of Korea **13**(1), 86-91, (2009).

119. O. Lundh, J. Lim, C. Rechatin, L. Ammoura, A. Ben-Ismaïl, X. Davoine, G. Gallot, J. P. Goddet, E. Lefebvre, V. Malka, and J. Faure, "Few femtosecond, few kiloampere electron bunch produced by a laser-plasma accelerator", Nature Physics **7**(3), 219-222, (2011).

120. I. A. Andriyash, E. D'Humières, V. T. Tikhonchuk, and P. Balcou, "Betatron emission from relativistic electrons in a high intensity optical lattice", Physical Review Special Topics - Accelerators and Beams **16**(10), (2013).

121. I. A. Andriyash, R. Lehe, A. Lifschitz, C. Thaury, J.-M. Rax, K. Krushelnick, and V. Malka, "An ultracompact X-ray source based on a laser-plasma undulator", Nature Communications **5**(1), 4736, (2014).
122. X. Zhang, T. Tajima, D. Farinella, Y. Shin, G. Mourou, J. Wheeler, P. Taborek, P. Chen, F. Dollar, and B. Shen, "Particle-in-cell simulation of x-ray wakefield acceleration and betatron radiation in nanotubes", Physical Review Accelerators and Beams **19**(10), (2016).
123. J. Tan, Y. Li, B. Zhu, C. Zhu, J. Wang, D. Li, X. Lu, Y. Li, and L. Chen, "Short-period high-strength helical undulator by laser-driven bifilar capacitor coil", Optics Express **27**(21), 29676, (2019).
124. K. Huang, Y. F. Li, D. Z. Li, L. M. Chen, M. Z. Tao, Y. Ma, J. R. Zhao, M. H. Li, M. Chen, M. Mirzaie, N. Hafz, T. Sokollik, Z. M. Sheng, and J. Zhang, "Resonantly Enhanced Betatron Hard X-rays from Ionization Injected Electrons in a Laser Plasma Accelerator", Scientific Reports **6**, 27633, (2016).
125. J. P. Palastro, D. Kaganovich, and D. Gordon, "Enhanced betatron X-rays from axially modulated plasma wakefields", Physics of Plasmas **22**(6), 063111, (2015).
126. Y. Cai, Z. Liu, Z. Shi, Q. Song, and Y. Wan, "Optimization of machining parameters for micro-machining nozzle based on characteristics of surface roughness", International Journal of Advanced Manufacturing Technology **80**(5-8), 1403-1410, (2015).
127. M. C. Louwerse, H. v. Jansen, M. N. W. Groenendijk, and M. C. Elwenspoek, "Nozzle fabrication for micropropulsion of a microsatellite", Journal of Micromechanics and Microengineering **19**(4), 045008, (2009).
128. S. W. Jolly, Z. He, C. McGuffey, W. Schumaker, K. Krushelnick, and A. G. R. Thomas, "Stereolithography based method of creating custom gas density profile targets for high intensity laser-plasma experiments", Review of Scientific Instruments **83**(7), 073503, (2012).
129. A. Döpp, E. Guillaume, C. Thaury, J. Gautier, K. Ta Phuoc, and V. Malka, "3D printing of gas jet nozzles for laser-plasma accelerators", Review of Scientific Instruments **87**(7), 073505, (2016).
130. B. C. Stuart, M. D. Feit, A. M. Rubenchik, B. W. Shore, and M. D. Perry, "Laser-induced damage in dielectrics with nanosecond to subpicosecond pulses", Physical Review Letters **74**(12), 2248-2251, (1995).

131. A. Butkutė, L. Čekanavičius, G. Rimšelis, D. Gailevičius, V. Mizeikis, A. Melninkaitis, T. Baldacchini, L. Jonušauskas, and M. Malinauskas, "Optical damage thresholds of microstructures made by laser three-dimensional nanolithography", Optics Letters **45**(1), 13, (2020).
132. S. Z. Xu, C. Z. Yao, W. Liao, X. D. Yuan, T. Wang, and X. T. Zu, "Experimental study on 800 nm femtosecond laser ablation of fused silica in air and vacuum", Nuclear Instruments and Methods in Physics Research, Section B: Beam Interactions with Materials and Atoms **385**, 46-50, (2016).
133. P. T. Mannion, J. Magee, E. Coyne, G. M. O'Connor, and T. J. Glynn, "The effect of damage accumulation behaviour on ablation thresholds and damage morphology in ultrafast laser micro-machining of common metals in air", Applied Surface Science **233**(1-4), 275-287, (2004).
134. M. J. Weber, *Handbook of Optical Materials* (CRC Press, 2018).
135. I. Prencipe, J. Fuchs, S. Pascarelli, D. W. Schumacher, R. B. Stephens, N. B. Alexander, R. Briggs, M. Büscher, M. O. Cernaianu, A. Choukourov, M. de Marco, A. Erbe, J. Fassbender, G. Fiquet, P. Fitzsimmons, C. Gheorghiu, J. Hund, L. G. Huang, M. Harmand, N. J. Hartley, A. Irman, T. Kluge, Z. Konopkova, S. Kraft, D. Kraus, V. Leca, D. Margarone, J. Metzkes, K. Nagai, W. Nazarov, P. Lutoslawski, D. Papp, M. Passoni, A. Pelka, J. P. Perin, J. Schulz, M. Smid, C. Spindloe, S. Steinke, R. Torchio, C. Vass, T. Wiste, R. Zaffino, K. Zeil, T. Tschentscher, U. Schramm, and T. E. Cowan, "Targets for high repetition rate laser facilities: Needs, challenges and perspectives", High Power Laser Science and Engineering **5**, 17, (2017).
136. L. Rovige, J. Huijts, I. Andriyash, A. Vernier, V. Tomkus, V. Girdauskas, G. Raciukaitis, J. Dudutis, V. Stankevic, P. Gecys, M. Ouille, Z. Cheng, R. Lopez-Martens, and J. Faure, "Demonstration of stable long-term operation of a kilohertz laser-plasma accelerator", Physical Review Accelerators and Beams **23**(9), 093401, (2020).
137. J. P. P. Couperus, A. Köhler, T. A. W. A. W. Wolterink, A. Jochmann, O. Zarini, H. M. J. M. J. Bastiaens, K. J. J. Boller, A. Irman, and U. Schramm, "Tomographic characterisation of gas-jet targets for laser wakefield acceleration", Nuclear Instruments and Methods in Physics Research, Section A: Accelerators, Spectrometers, Detectors and Associated Equipment **830**, 504-509, (2016).

138. ”Smart Shot Co, Ltd., Japan”, https://www.japanlaser.co.jp/wp-content/uploads/2020/04/smartshot_ja.pdf.
139. V. Tomkus, V. Girdauskas, J. Dudutis, P. Gečys, V. Stankevič, and G. Račiukaitis, “High-density gas capillary nozzles manufactured by hybrid 3D laser machining technique from fused silica”, Optics Express **26**(21), 27965, (2018).
140. V. Tomkus, V. Girdauskas, J. Dudutis, P. Gečys, V. Stankevič, G. Račiukaitis, I. Gallardo González, D. Guénot, J. B. Svensson, A. Persson, and O. Lundh, “Laser wakefield accelerated electron beams and betatron radiation from multijet gas targets”, Scientific Reports **10**(1), 16807, (2020).
141. N. M. Bulgakova, V. P. Zhukov, A. R. Collins, D. Rostohar, T. J.-Y. Derrien, and T. Mocek, “How to optimize ultrashort pulse laser interaction with glass surfaces in cutting regimes?”, Applied Surface Science **336**, 364-374, (2015).
142. Y. Li, K. Itoh, W. Watanabe, K. Yamada, D. Kuroda, J. Nishii, and Y. Jiang, “Three-dimensional hole drilling of silica glass from the rear surface with femtosecond laser pulses”, Optics Letters **26**(23), 1912, (2001).
143. D. J. Hwang, T. Y. Choi, and C. P. Grigoropoulos, “Liquid-assisted femtosecond laser drilling of straight and three-dimensional microchannels in glass”, Applied Physics A: Materials Science & Processing **79**(3), 605-612 (2004).
144. D. Ashkenasi, T. Kaszemeikat, N. Mueller, A. Lemke, and H. J. Eichler, “Machining of glass and quartz using nanosecond and picosecond laser pulses”, Laser Applications in Microelectronic and Optoelectronic Manufacturing (LAMOM) XVIII **8243**(February), 82430M (2012).
145. Z. K. Wang, W. L. Seow, X. C. Wang, and H. Y. Zheng, “Effect of laser beam scanning mode on material removal efficiency in laser ablation for micromachining of glass”, Journal of Laser Applications **27**(S2), S28004, (2015).
146. P. Gečys, J. Dudutis, and G. Račiukaitis, “Nanosecond Laser Processing of Soda-Lime Glass”, Journal of Laser Micro/Nanoengineering **10**(3), 254-258, (2015).
147. G. Lott, N. Falletto, P. Devilder, and R. Kling, “Optimizing the processing of sapphire with ultrashort laser pulses”, Journal of Laser Applications **28**(2), 022206, (2016).
148. L. Hof and J. Abou Ziki, “Micro-Hole Drilling on Glass Substrates—A Review”, Micromachines **8**(2), 53, (2017).

149. X. Zhao and Y. C. Shin, “Femtosecond laser drilling of high-aspect ratio microchannels in glass”, Applied Physics A **104**(2), 713-719, (2011).
150. Y. Cai, Z. Liu, and Z. Shi, “Effects of dimensional size and surface roughness on service performance for a micro Laval nozzle”, Journal of Micromechanics and Microengineering **27**(5), 055001, (2017).
151. Y. Cai, Z. Liu, Q. Song, Z. Shi, and Y. Wan, “Fluid mechanics of internal flow with friction and cutting strategies for micronozzles”, International Journal of Mechanical Sciences **100**, 41-49, (2015).
152. A. Marcinkevičius, S. Juodkazis, M. Watanabe, M. Miwa, S. Matsuo, H. Misawa, and J. Nishii, “Femtosecond laser-assisted three-dimensional microfabrication in silica”, Optics Letters **26**(5), 277-279, (2001).
153. S. lo Turco, R. Osellame, R. Ramponi, and K. C. Vishnubhatla, “Hybrid chemical etching of femtosecond irradiated 3D structures in fused silica glass”, MATEC Web of Conferences **8**, 05009, (2013).
154. V. Stankevič and G. Račiukaitis, “Free-shape 3D structure formation in bulk fused silica by irradiation with femtosecond laser pulses”, JLMN-Journal of Laser Micro/Nanoengineering **9**(3), 271-275, (2014).
155. M. Hermans, J. Gottmann, and F. Riedel, “Selective, laser-induced etching of fused silica at high scan-speeds using KOH”, Journal of Laser Micro Nanoengineering **9**(2), 126-131, (2014).
156. V. Tomkus, V. Girdauskas, J. Dudutis, P. Gečys, V. Stankevič, and G. Račiukaitis, “Impact of the wall roughness on the quality of micrometric nozzles manufactured from fused silica by different laser processing techniques”, Applied Surface Science **483**, 205-211, (2019).
157. R. Lehe, M. Kirchen, I. A. Andriyash, B. B. Godfrey, and J. L. Vay, “A spectral, quasi-cylindrical and dispersion-free Particle-In-Cell algorithm”, Computer Physics Communications **203**, 66-82, (2016).
158. OpenCFD Ltd., “The Open Source CFD Toolbox, Version v1906” (February), (2019).
159. F. Böhle, M. Kretschmar, A. Jullien, M. Kovacs, M. Miranda, R. Romero, H. Crespo, U. Morgner, P. Simon, R. Lopez-Martens, and T. Nagy, “Compression of CEP-stable multi-mJ laser pulses down to 4 fs in long hollow fibers”, Laser Physics Letters **11**(9), 095401, (2014).
160. M. Miranda, C. L. Arnold, T. Fordell, F. Silva, B. Alonso, R. Weigand, A. L’Huillier, and H. Crespo, “Characterization of

broadband few-cycle laser pulses with the d-scan technique", Optics Express **20**(17), 18732, (2012).

161. R. Azambuja, M. Eloy, G. Figueira, and D. Neely, "Three-dimensional characterization of high-density non-cylindrical pulsed gas jets", Journal of Physics D: Applied Physics **32**(8), L35-L43, (1999).
162. M. Hipp, J. Woisetschläger, P. Reiterer, and T. Neger, "Digital evaluation of interferograms", Measurement **36**(1), 53-66, (2004).
163. J. Gregor and T. Benson, "Computational analysis and improvement of SIRT.", IEEE transactions on medical imaging **27**(7), 918-24, (2008).
164. J. Primot and L. Sogno, *Achromatic Three-Wave (or More) Lateral Shearing Interferometer* (The Optical Society, 1995), **12**(12), p. 2679.
165. J. Primot and N. Guérineau, "Extended Hartmann test based on the pseudoguiding property of a Hartmann mask completed by a phase chessboard", Applied Optics **39**(31), 5715, (2000).
166. A. Buck, K. Zeil, A. Popp, K. Schmid, A. Jochmann, S. D. Kraft, B. Hidding, T. Kudyakov, C. M. S. S. Sears, L. Veisz, S. Karsch, J. Pawelke, R. Sauerbrey, T. Cowan, F. Krausz, and U. Schramm, "Absolute charge calibration of scintillating screens for relativistic electron detection", Review of Scientific Instruments **81**(3), 033301, (2010).
167. Y. Glinec, J. Faure, A. Guemnie-Tafo, V. Malka, H. Monard, J. P. Larbre, V. de Waele, J. L. Marignier, and M. Mostafavi, "Absolute calibration for a broad range single shot electron spectrometer", in *Review of Scientific Instruments* (American Institute of Physics AIP, 2006), **77**(10), p. 103301.
168. P. Kirkpatrick, "Theory and use of ross filters. II", Review of Scientific Instruments **15**(9), 223-229, (1944).
169. "X-Ray Transition Energies Database | NIST", https://www.nist.gov/pml/x-ray-transition-energies-database.
170. K. Svendsen, I. G. González, M. Hansson, J. B. Svensson, H. Ekerfelt, A. Persson, and O. Lundh, "Optimization of soft X-ray phase-contrast tomography using a laser wakefield accelerator", Optics Express **26**(26), 33930, (2018).
171. S. Kneip, C. McGuffey, J. L. Martins, S. F. Martins, C. Bellei, V. Chvykov, F. Dollar, R. Fonseca, C. Huntington, G. Kalintchenko, A. Maksimchuk, S. P. D. Mangles, T. Matsuoka, S. R. Nagel, C. A. J. Palmer, J. Schreiber, K. T. Phuoc, A. G. R. Thomas, V. Yanovsky, L. O. Silva, K. Krushelnick, and Z. Najmudin, "Bright spatially coherent

synchrotron X-rays from a table-top source", Nature Physics **6**(12), 980-983, (2010).

172. I. N. Tilikin, T. A. Shelkovenko, S. A. Pikuz, and D. A. Hammer, "Determination of the size of a radiation source by the method of calculation of diffraction patterns", Optics and Spectroscopy (English translation of Optika i Spektroskopiya) **115**(1), 128-136, (2013).
173. "Matplotlib: Python plotting – Matplotlib 3.3.1 documentation", https://matplotlib.org/.
174. https://www. engineeringtoolbox. com/material-properties-t_24. html Engineering toolbox, "Engineering ToolBox. Material Properties.", https://www.engineeringtoolbox.com/material-properties-t_24.html.
175. H. R. Murphy and D. R. Miller, "Effects of nozzle geometry on kinetics in free-jet expansions", Journal of Physical Chemistry **88**(20), 4474-4478, (1984).
176. M. Skoblin, A. Chudinov, I. Soulimenkov, V. Brusov, and V. Kozlovskiy, "Gas Flow in the Capillary of the Atmosphere-to-Vacuum Interface of Mass Spectrometers", Journal of the American Society for Mass Spectrometry **28**(10), 2132-2142, (2017).
177. L. Bernier, M. Taesch, S. Rauschenbach, and J. Reiss, "Transfer conditions and transmission bias in capillaries of vacuum interfaces", International Journal of Mass Spectrometry **447**, 116239, (2020).
178. T. Adams, C. Grant, and H. Watson, "A Simple Algorithm to Relate Measured Surface Roughness to Equivalent Sand-grain Roughness", **1**(1), (2012).
179. Y. Çengel and J. Cimbala, *Fluid Mechanics Fundamentals and Applications* (McGraw-Hill Higher Education, 2006).
180. G. Pretzier, "A New Method for Numerical Abel-Inversion", Zeitschrift für Naturforschung A (1991).
181. T. E. Gureyev, Y. I. Nesterets, A. W. Stevenson, P. R. Miller, A. Pogany, and S. W. Wilkins, "Some simple rules for contrast, signal-to-noise and resolution in in-line x-ray phase-contrast imaging", Optics Express **16**(5), 3223, (2008).
182. A. W. Stevenson, S. W. Wilkins, Ya. I. Nesterets, T. E. Gureyev, S. C. Mayo, A. Pogany, and A. W. Stevenson, "On the evolution and relative merits of hard X-ray phase-contrast imaging methods", Philosophical Transactions of the Royal Society A: Mathematical, Physical and Engineering Sciences **372**(2010), 1-19, (2014).
183. J. D. B. O'Sullivan, J. Behnsen, T. Starborg, A. S. MacDonald, A. T. Phythian-Adams, K. J. Else, S. M. Cruickshank, and P. J. Withers,

"X-ray micro-computed tomography (μCT): An emerging opportunity in parasite imaging", Parasitology **145**(7), 848-854, (2018).

184. J. M. Cole, J. C. Wood, N. C. Lopes, K. Poder, R. L. Abel, S. Alatabi, J. S. J. Bryant, A. Jin, S. Kneip, K. Mecseki, D. R. Symes, S. P. D. Mangles, and Z. Najmudin, "Laser-wakefield accelerators as hard x-ray sources for 3D medical imaging of human bone", Scientific Reports **5**, 1-7, 13244, (2015).

185. M. Saes, C. Bressler, R. Abela, D. Grolimund, S. L. Johnson, P. A. Heimann, and M. Chergui, "Observing Photochemical Transients by Ultrafast X-Ray Absorption Spectroscopy", Physical Review Letters **90**(4), 047403, (2003).

186. M. Z. Mo, Z. Chen, S. Fourmaux, A. Saraf, S. Kerr, K. Otani, R. Masoud, J. C. Kieffer, Y. Tsui, A. Ng, and R. Fedosejevs, "Measurements of ionization states in warm dense aluminum with betatron radiation", Physical Review. E **95**(5-1), 053208, (2017).

187. B. Mahieu, N. Jourdain, K. Ta Phuoc, F. Dorchies, J. P. Goddet, A. Lifschitz, P. Renaudin, and L. Lecherbourg, "Probing warm dense matter using femtosecond X-ray absorption spectroscopy with a laser-produced betatron source", Nature Communications **9**(1), 1-6, 32766, (2018).

188. A. Rousse, C. Rischel, and J. C. Gauthier, "Colloquium: Femtosecond x-ray crystallography", Reviews of Modern Physics **73**(1), 17-31, (2001).

189. P. Montay-Gruel, A. Bouchet, M. Jaccard, D. Patin, R. Serduc, W. Aim, K. Petersson, B. Petit, C. Bailat, J. Bourhis, E. Bräuer-Krisch, and M. C. Vozenin, "X-rays can trigger the FLASH effect: Ultra-high dose-rate synchrotron light source prevents normal brain injury after whole brain irradiation in mice", Radiotherapy and Oncology **129**(3), 582-588, (2018).

190. M. Bazalova-Carter, B. Qu, B. Palma, B. Hårdemark, E. Hynning, C. Jensen, P. G. Maxim, and B. W. Loo, "Treatment planning for radiotherapy with very high-energy electron beams and comparison of VHEE and VMAT plans", Medical Physics **42**(5), 2615-2625, (2015).

191. K. Kokurewicz, E. Brunetti, G. H. Welsh, S. M. Wiggins, M. Boyd, A. Sorensen, A. J. Chalmers, G. Schettino, A. Subiel, C. DesRosiers, and D. A. Jaroszynski, "Focused very high-energy electron beams as a novel radiotherapy modality for producing high-dose volumetric elements", Scientific Reports **9**(1), 10837, (2019).

192. V. Favaudon, L. Caplier, V. Monceau, F. Pouzoulet, M. Sayarath, C. Fouillade, M. F. Poupon, I. Brito, P. Hupé, J. Bourhis, J. Hall, J. J. Fontaine, and M. C. Vozenin, "Ultrahigh dose-rate FLASH irradiation increases the differential response between normal and tumor tissue in mice", Science Translational Medicine **6**(245), 245ra93-245ra93, (2014).
193. L. Labate, D. Palla, D. Panetta, F. Avella, F. Baffigi, F. Brandi, F. di Martino, L. Fulgentini, A. Giulietti, P. Köster, D. Terzani, P. Tomassini, C. Traino, and L. A. Gizzi, "Toward an effective use of laser-driven very high energy electrons for radiotherapy: Feasibility assessment of multi-field and intensity modulation irradiation schemes", Scientific Reports **10**(1), 17307, (2020).
194. V. Malka, J. Faure, and Y. A. Gauduel, "Ultra-short electron beams based spatio-temporal radiation biology and radiotherapy", Mutation Research - Reviews in Mutation Research **704**(1-3), 142-151, (2010).
195. Y. Glinec, J. Faure, V. Malka, T. Fuchs, H. Szymanowski, and U. Oelfke, "Radiotherapy with laser-plasma accelerators: Monte Carlo simulation of dose deposited by an experimental quasimonoenergetic electron beam", Medical Physics **33**(1), 155-162, (2006).

LIST OF SYMBOLS

A- – atomic mass number
A_p - pipe's cross-sectional area
A_s - Sutherland coefficient
a_0 - normalized laser vector potential (laser strength parameter)
B_{bend} - magnetic field of a bending magnet
$\vec{B}_L$ - magnetic field of laser radiation
B_{0L} - amplitude of laser radiation magnetic field
B_u - magnetic field of the undulator magnets
Br - brightness
c - speed of light in vacuum
C - counts per pixel
C_{ra} - non-dimensional roughness parameter
C_p - constant pressure specific heat capacity
C_v - constant volume-specific heat capacity
C_{bg} - background part of counts per pixel
C_{gd} - Gaussian part of counts per pixel
D_h - hydraulic diameter
d_p - skin depth
d_v - reconstruction length of cubic voxel
e - electron charge
$\vec{E}_L$ - electric field of laser radiation
E_{0L} - amplitude of laser radiation electric field
E_p - plasma electric field
E_{pmax} - maximal plasma electric field
E_{pz} - a ponderomotive electric field in the axial z-direction
E_{WB} - wave-breaking limit of plasma electric field
F_p - ponderomotive force
F_{pz} - ponderomotive force in the axial z-direction
h - Planck constant
$\hbar$ - reduced Planck constant
I_{L18} - laser radiation intensity in W/cm^2 relative to the 10^{18} W/cm^2
I_L - laser radiation intensity
I_{sfr} - radiation intensity of Fresnel diffraction
$K_{2/3}$ - modified Bessel function of the second kind
K_β - betatron undulator strength parameter
K_{ICS} - ICS undulator strength parameter
K_u - undulator strength parameter

k_a - adiabatic index
k_β - betatron oscillation wave vector
k_p - plasma wave number
k_{rf} - sand roughness parameter
k_t - turbulent kinetic energy
$L_{2\pi}$ - carrier-envelope phase (CEP) phase slippage length
L_d - laser pulse dephasing length
L_{disp} - laser pulse dispersion length
L_{etch}- laser pulse etching length
L_{lam} - hydrodynamic entry length of laminar flow
L_{turb} - hydrodynamic entry length of turbulent flow
L_{pd} - laser pulse depletion length
L_{dr}- length of plasma concentration down-ramp
l_t - target thickness
l_{px} - pixel size
l_{sd}- the distance between the source X-ray camera detector
m_e - electron rest mass
m_i - ion rest mass
m_p - proton rest mass
M - Mach number
M_g - geometric magnification of the imaging system
M_m - molar mass
M_{xx}, M_{yy} and M_{xy} - momenta of Gaussian distribution
N_A - Avogadro number
N_β - total number of oscillations of one electron in the betatron ion channel
N_c - number of counts of X-ray camera per shot
N_e - number of electrons
N_{phot} - number of photons per shot
N_{photC} - number of photons per count
N_{phot1} - number of photons radiated by one electron
$\mathrm{N_{poles}}$ - number of magnetic poles
n_{cL} - critical plasma concentration of the laser wavelength
n - number of measurements
n_g - gas concentration
n_p - plasma concentration
n_{p18} - is the plasma concentration in cm^{-3} relative to the 10^{18} cm^{-3}
n_{p20} - plasma concentration in cm^{-3} relative to the 10^{20} cm^{-3}
n_r - plasma refraction index
n_{r0} - initial plasma refraction index

$\vec{p}_e$ - electron momentum

p_z - electron momentum in axial z-direction

$p_\perp$ - electron momentum in perpendicular to the propagation of laser direction

P_L - power of laser radiation

P_{Lc} - critical power of laser radiation

P_0 - total gas pressure

P - static gas pressure

q_e - total charge of electrons

q_{e40} - total charge of electrons with energy >40 MeV

$q_{r\perp}$ - total charge of electrons having radius coordinate perpendicular to z

$q_{r\beta}$ - total charge of electrons having betatron radius r_β

$q_{c\beta}$ - total charge of electrons with critical betatron energy

Q_e - quantum yield of an X-ray camera

Q_p - volumetric flow rate

R_a - arithmetic average of absolute roughness values

R_b - blowout radius of plasma wave

Re - Reynolds number

R_{pi} - peak-to-valley largest distance of roughness above the mean line

R_{vi} - peak-to-valley largest distance of roughness below the mean line

R_{RMS} - mean squared average of roughness values

R_{zd} - average of peak-to-valley values of roughness values

R_{spec} - specific gas constant

R_w - radius of the cross-wires

r_β - betatron oscillation radius

$\vec{r}_{e0}$ - radius vector of the electron oscillation

r_{1sw} - distance between the source and cross wires

r_{2wd} - distance between the cross wires and detector

r_{sd} - distance between the source and detector

S_s - distribution of X-ray source radiation

S_1 - normalized synchrotron-like spectrum

S_{eff} - effective synchrotron-like spectrum

t - time

T - temperature

T_0 - reference ambient temperature

T_L - oscillation period of the electric field of laser radiation

T_s - Sutherland temperature

$Tr_{c\beta}$ - X-ray transmission coefficient at the critical wavelength of betatron radiation

Tr_{tot} - X-ray transmission factor of all attenuating materials
U - gas velocity
V - gas volume
V_i - ion velocity
x_d - coordinates of the X-ray detector plane
x_s - coordinates of the X-ray source plane
$W_{c\beta}$ - critical energy of synchrotron of betatron radiation
W_e - energy of accelerated electrons
W_{em} - mean energy of accelerated electrons
W_{ekin} - electron kinetic energy
W_i - accelerated ion energy
W_L - laser pulse energy
W_{LS} - energy of ions accelerated in Light sail regime
W_{LSopt} - energy of ions accelerated in optimal Light sail regime
$W_{r\beta}$ - photon energy of electron betatron radiation
$W_{r\beta tot}$ - total energy of electron betatron radiation
W_{ru} - photon energy of undulator radiation
z - coordinate along the laser the propagation axis
Z_R- Rayleigh length of Gaussian laser beam
Z - ion charge number

LIST OF GREEK SYMBOLS

α_0 - relativistic transparency parameter
α_c - X-ray detector sensitivity calibration constant
α_p - polarizability of the argon gas atoms
β_φ - dimensionless phase velocity of the plasma wake wave
γ - Lorentz factor of the electron
γ_p - Lorentz factor of the plasma wave
γ_z - Lorentz factor of an electron in the axial direction of laser propagation
$\gamma_\perp$ - Lorentz factor of an electron in perpendicular to the laser propagation direction
δ_a - target thickness parameter
ε_p - normalized surface density
ε_t - rate of dissipation of turbulent kinetic energy
ζ - normalized z coordinate along laser the propagation axis
θ_{gd} - tilting angle of Gaussian distribution
θ_{ey} - divergence of the electron beam in the y-direction
θ_u - undulator radiation angle relative to the electron beam axis

$\theta_{\perp\beta}$ - divergence of the betatron radiation in the oscillation plane

$\theta_{s\beta}$ - divergence of the betatron radiation in the perpendicular of the oscillation plane

λ_{cbend} - characteristic critical wavelength of bending magnet radiation

λ_{ICS} - fundamental wavelength of ICS radiation

$\lambda\!\!\!^{-}_{C}$ - reduced Compton wavelength

λ_{β} - wavelength of the electron betatron oscillation

$\lambda_{c\beta}$ - critical wavelength of electron betatron radiation

λ_{L} - laser radiation wavelength

λ_{p} - plasma wavelength

$\lambda_{r\beta}$ - fundamental wavelength of betatron radiation

λ_{ru} - fundamental wavelength of undulator radiation

λ_{u} - a spatial period of the undulator magnets

$\mu_{c\beta}$ - X-ray attenuation coefficient at the critical wavelength of betatron radiation

μ_{s} - dynamic fluid viscosity

μ_{s0} - initial dynamic fluid viscosity

ν - kinematic viscosity,

$\vec{v}_{e}$ - electron velocity

v_{ph} - laser radiation phase velocity

v_{g} - laser radiation group velocity

v_{etch} - laser pulse etching velocity

v_{φ} - plasma wake wave phase velocity

ρ - gas density

ρ_{0} - critical gas density at the point of transition from subsonic to supersonic flow

σ_{det} - standard deviation of the point distribution of the detector

σ_{src} - standard deviation of X-ray source intensity distribution

σ_{sys} - standard deviation of the point distribution of the imaging system

σ_{x} - standard deviation of Gaussian distribution in x-direction

σ_{y} - standard deviation of Gaussian distribution in y-direction

σ_{compt} - Compton scattering cross-section

τ_{L} - laser pulse duration

τ_{L0} - laser pulse Fourier transform-limited duration

φ_{int} - integral phase of the interferogram

ψ_{c} - gas compressibility parameter

ψ_{pond} - ponderomotive potential

$\omega_{c\beta}$ - cyclic critical frequency of betatron radiation

ω_L - cyclic frequency of electric field of laser radiation

ω_p - cyclic frequency of the plasma

ω_t - the specific rate of dissipation of the turbulence kinetic energy

ω_s - waist of Gaussian laser beam

ω_0 - waist of Gaussian laser beam at the focal point

Ω - solid angle

DAKTARO DISERTACIJOS SANTRAUKA

1. ĮVADAS

Didelio intensyvumo lazeriai suteikia galimybę kurti kompaktiškus dalelių greitintuvus ir antrinės spinduliuotės šaltinius. Antrinės Rentgeno ir γ-spinduliuotės šaltiniai plačiai taikomi medžiagotyroje, biochemijos ir branduolinės fotonikos tyrimuose. Didelės energijos jonizuojančioji spinduliuotė išplečia fundamentalias materijos pažinimo ribas ir leidžia analizuoti subatominius procesus atosekundžių tikslumu. Tradiciniai radijo dažnio dalelių greitintuvai užima didžiules teritorijas, o jų įrengimo kaštai siekia kelis šimtus milijonų eurų. Dėl to jų panaudojimas tyrimų laboratorijose ir pramonėje yra ribotas. Lazeriniai plazmos greitintuvai (LPG – LWFA, Laser Wakefield Accelerator) leidžia pasiekti daug didesnį greitinančio elektrinio lauko stiprumą ir šimtus kartų sutrumpina greitinimo atstumą.

Šiame darbe tiriami struktūriniai plazmos profiliai, taikomi greitinamų elektronų pluošto valdymui ir Rentgeno spinduliuotės žadinimui. Struktūrinių profilių plazmos koncentraciją apibrėžia viršgarsinių dujų čiurkšlių skirstinys ir susikertančių smūginių bangų interferencija. Dujų čiurkšles suformuoja mikrotūtos, pagamintos iš monolitinio lydyto kvarco bloko 3D lazerinio mikroapdirbimo būdu. Rentgeno spinduliuotę žadina skersine kryptimi lazerio pluošto suformuotame jonų kanale svyruojantys elektronai.

Šis darbas suskirstytas į septynis skyrius. Pirmuosius tris skyrius sudaro įvadas, ginamieji teiginiai, aprobacija, literatūros apžvalga ir metodai. 4 skyriuje aprašomas skaitmeninis LPG modeliavimas, panaudojant struktūrinius plazmos koncentracijos profilius. 5 skyriuje pateikiami skaitmeninio viršgarsinių dujų čiurkšlių dinamikos modeliavimo rezultatai. 6 skyriuje aprašomi tūtų lazerinio mikroapdirbimo būdai ir dujų čiurkšlių parametrų matavimas interferometriniais metodais. 7 skyriuje aptariami LPG ir antrinės spinduliuotės žadinimo eksperimentiniai rezultatai. Darbo pabaigoje pateikiama pagrindinių išvadų santrauka.

1.1. Disertacijos tikslas

Disertacijos darbo tikslas – ištirti antrinės Rentgeno spinduliuotės, žadinamos didelio intensyvumo lazerio laukais, savybes ir Rentgeno vaizdų taikymą medžiagotyroje. Šiam tikslui pasiekti buvo suformuluoti du uždaviniai:

1. LPG elektronų kiekio injekcijos ir antrinės Rentgeno spinduliuotės priklausomybės nuo struktūrinių plazmos koncentracijos profilių tyrimas;

2. Naujų adaptyvių plazmos koncentracijos profilių formavimo ir mikrotūtų struktūrų gamybos metodų tyrimas.

1.2. Darbo naujumas ir praktinė nauda

1.2.1. Darbo naujumas

1. Eksperimentiškai pademonstruotas naujas LPG elektronų injekcijos ir antrinės Rentgeno spinduliuotės valdymo metodas, panaudojant injektoriaus ir svyravimo struktūrų plazmos koncentracijos profilius. Atliktas elektronų greitinimo ir antrinės spinduliuotės skaitmeninis modeliavimas.
2. Pasiūlytas naujas struktūrinių plazmos koncentracijos profilių formavimo būdas naudojant susikertančių viršgarsinių dujų čiurkšlių smūginių bangų interferenciją. Dujų čiurkšlių koncentracijos skirstiniai apskaičiuoti skaitmeninio modeliavimo būdu ir išmatuoti eksperimentiškai.
3. Mikrotūtų gamybai panaudotas naujas hibridinis lydyto kvarco lazerinio apdirbimo metodas, pasižymintis didele apdorojimo sparta, tiksliu mikrometrinių struktūrų ir reikiamos kokybės paviršių formavimu.

1.2.2. Praktinė darbo nauda

1. Pasiūlytas elektronų injekcijos būdas padidina LPG pagreitintų elektronų pluošto krūvio kiekį ir sumažina energijos sklaidą. Injekcijos būdą galima naudoti elektronų pluošto parametrų valdymui ir antrinės betatrono, stabdymo ir inversinės Komptono sklaidos – spinduliuotės šaltinių optimizacijai.
2. Panaudojant svyravimo struktūros plazmos koncentracijos profilius, padidėja elektronų betatrono skersinių svyravimų amplitudė ir antrinės spinduliuotės ryškis. Antrinius betatrono Rentgeno spinduliuotės šaltinius galima panaudoti mikrometrinių objektų vaizdavimui biomedicinoje, medžiagotyroje ir femtosekundinių pereinamųjų procesų tyrimams.
3. Struktūrinius plazmos koncentracijos profilius galima panaudoti elektronų greitinimui įvairiais teravatinės ir petavatinės smailinės galios lazeriais. Profiliai suteikia ypač daug privalumų, greitinant ultratrumpais kelių ciklų trukmės impulsų kHz dažnio lazeriais. Mikrometrinius subkritinės plazmos koncentracijos plazmos profilius galima pritaikyti jonų greitinimui lazeriais, veikiančiais didelio pasikartojimo dažniu.

1.3. Ginamieji teiginiai

1. LPG pagreitintų elektronų pluošto krūvio kiekį galima padidinti ir energijos sklaidą galima sumažinti naudojant injektoriaus struktūros plazmos koncentracijos profilius bei derinant neigiamo plazmos koncentracijos gradiento ir jonizacijos injekciją.
2. Betatrono Rentgeno spinduliuotės lazerio impulso fotonų skaičių ir ryškį galima padidinti panaudojant svyravimo struktūros plazmos koncentracijos profilius, padidinančius skersinę elektronų svyravimo amplitudę.
3. Injektoriaus ir svyravimo struktūrų plazmos koncentracijos profilius galima suformuoti naudojant susikertančių siaurėjančių-platėjančių ir fiksuoto skersmens mikrotūtų viršgarsines čiurkšles.
4. Atsparias optiniams pažeidimams mikrometrinių matmenų tūtas iš skaidrių medžiagų, pvz., lydyto kvarco, galima pagaminti derinant didelės spartos nanosekundinį lazerinį apdirbimą iš apačios bei aukšto tikslumo femtosekundinio lazerio inicijavimo ir selektyvaus ėsdinimo (FLSE) metodą.

1.4. Aprobacija

Šioje disertacijoje pateikti rezultatai buvo publikuoti 4 recenzuotuose moksliniuose straipsniuose ir kartu su bendraautoriais pristatyti 8 tarptautinėse mokslinėse konferencijose. Pateiktos 2 nacionalinės patentinės paraiškos.

1.4.1. Publikacijų sąrašas

Publikacijos disertacijos tema žurnaluose, referuojamuose CA WoS duomenų bazėje:

A1. L. Rovige, I. Andriyash, J. Huijts, A. Vernier, V. Tomkus, V. Girdauskas, G. Raciukaitis, J. Dudutis, V. Stankevic, P. Gecys, M. Ouill, Z. Cheng, R. Lopez-Martens, and J. Faure, **Demonstration of stable long-term operation of a kilohertz laser-plasma accelerator**, Phys. Rev. Accel. Beams., 23, 093401(9), (2020), https://doi.org/10.1103/PhysRevAccelBeams.23.093401

A2. V. Tomkus, V. Girdauskas, J. Dudutis, V. Stankevic, P. Gecys, G. Raciukaitis, I. Gallardo González, D. Guénot, J. B. Svensson, A. Persson, O. Lundh, **Radiation from laser wakefield accelerated electron beams and**

betatron radiation using multijet gas targets, Sci. Rep. 10, 16807, (2020), https://doi.org/10.1038/s41598-020-73805-7

A3. V. Tomkus, V. Girdauskas, J. Dudutis, P. Gečys, V. Stankevič, G. Račiukaitis, **Impact of the wall roughness on the quality of micrometric nozzles manufactured from fused silica by hybrid different laser processing techniques**, Appl. Surf. Sc., 483, 205-211, (2019), https://doi.org/10.1016/j.apsusc.2019.03.007

A4. V. Tomkus, V. Girdauskas, J. Dudutis, P. Gečys, V. Stankevič, G. Račiukaitis, **High-density gas capillary nozzles manufactured by hybrid 3D laser machining technique from fused silica**, Opt. Express. 26, 27965, (2018), https://doi.org/10.1364/OE.26.027965

Kitos publikacijos disertacijos tema periodiniuose leidiniuose:

A5. V. Tomkus, L. Rimgaila, V. Stankevič G. Račiukaitis, **Three-dimensional Supersonic Sapphire Micronozzles for Laser-Plasma Wakefield Accelerators**, Chapter in: Kawachi T., Bulanov S., Daido H., Kato Y. (eds) X-Ray Lasers 2016. ICXRL 2016. Springer Proceedings in Physics, 202, 167–171, (2018), https://doi.org/10.1007/978-3-319-73025-7_26

A6. V. Tomkus, L. Rimgaila, V. Stankevič, G. Račiukaitis, **Characterisation of Tuneable Gas Target Profiles for Laser Wakefield Acceleration**, High-brightness Sources and Light-driven Interactions Congress 2018 High-Brightness Sources and Light-driven Interactions, OSA Technical Digest, EM3B.4, (2018), https://doi.org/10.1364/EUVXRAY.2018.EM3B.4

A7. V. Tomkus, L. Rimgaila, V. Stankevič, G. Račiukaitis, **Real-time characterization of profiles of laser wakefield and electrons accelerated by few-cycle 1 kHz OCPA system**, 2017 Conference on Lasers and Electro-Optics Europe & European Quantum Electronics Conference (CLEO/Europe-EQEC), CG_P_2, (2017), https://doi.org/10.1109/CLEOE-EQEC.2017.8086823

Publikacijos ne disertacijos tema:

A8. V. Tomkus, L. Rimgaila, V. Stankevič, G. Račiukaitis, **Plasma Guiding and Scattering Microstructures for Laser Driven Thomson Sources**, First International Conference on Nuclear Photonics, Proc. SPIE, 10419, 1041901, 198, (2017), https://doi.org/10.1117/12.2280421

1.4.2. Patentai

P1. V. Tomkus, V. Girdauskas, J. Dudutis, V. Stankevič, G. Račiukaitis, **Koherentinės spinduliuotės generavimo būdas ir įrenginys**, 2020-12-10 patentas Nr. 6785, 2019-05-03 patento paraiška Nr. LT2019513.

P2. V. Tomkus, V. Girdauskas, J. Dudutis, V. Stankevič, G. Račiukaitis, **Lazerinis jonizuojančios spinduliuotės didelės momentinės dozės generavimo įrenginys**, 2019-10-03 patento paraiška Nr. LT2019075.

1.4.3. Pranešimų konferencijose sąrašas

Publikacijos disertacijos tema:

Cl. V. Tomkus, V. Girdauskas, J. Dudutis, V. Stankevic, G. Raciukaitis, I. Gallardo González, D. Guénot, J. B. Svensson, A. Persson, O. Lundh, **Enhanced betatron radiation from multistage gas targets**, ELI User Workshop on Laser-Driven X-ray Sources and Applications, Prague, 24-25.10.2019

C2. V. Tomkus, V. Girdauskas, J. Dudutis, V. Stankevic, G. Raciukaitis, I. Gallardo González, D. Guénot, J. B. Svensson, A. Persson, O. Lundh, **Multistage gas targets from fused silica**, 4th Targetry for High Repetition Rate Laser-Driven Sources Workshop, Milan, Italy, 10-12.06.2019

C3. V. Tomkus, V. Girdauskas, J. Dudutis, V. Stankevic, G. Raciukaitis, I. Gallardo González, D. Guénot, J. B. Svensson, A. Persson, O. Lundh, **The control of laser wakefield accelerated electron beams and betatron X-ray radiation using arrays of multiple gas jets**, Laser-Plasma Accelerator Workshop, (LPAW2019), Split, Croatia, 05-10.05.2019

C4. V. Tomkus, V. Girdauskas, J. Dudutis, V. Stankevic, P. Gecys, G. Raciukaitis, **Impact of the Wall Roughness on the Quality of Micrometric Nozzles Manufactured from Fused Silica by Hybrid Laser Processing**, The International Conference on Photo-Excited Processes and Applications ICPEPA-2018“, Vilnius, Lithuania, 10-11.09.2018

C5. V. Tomkus, V. Girdauskas, J. Dudutis, V. Stankevic, G. Raciukaitis, **High Density Gas Capillaries for Betatron X-ray Sources of Laser Accelerated Electrons**, Nuclear Photonics NP-2018“, Bražov, Romania, 24-29.06.2018

C6. V. Tomkus, V. Girdauskas, J. Dudutis, V. Stankevic, G. Raciukaitis, **Characterisation of Tuneable Gas Target Profiles for Laser Wakefield Acceleration**, High- brightness Congress HB-2018“, Strasbourg, France, 25-29.03.2018

C7. V. Tomkus, L. Rimgaila, V. Stankevič, G. Račiukaitis, **Real-time Characterization of Profiles of Laser Wakefield and Electrons Accelerated by Few-Cycle 1 kHz OCPA system**, CLEO/Europe-EQEC, Munich, Germany, 25-27.06.2017

C8. V. Tomkus, L. Rimgaila, V. Stankevič, G. Račiukaitis. **Three-dimensional Supersonic Sapphire Micronozzles for Laser-Plasma Wakefield Accelerators**, 15th International Conference on X-Ray Lasers (ICXRL2016), Kansai, Japan, 22-27.05.2016

Publikacijos ne disertacijos tema:

C9. V. Tomkus, L. Rimgaila, V. Stankevič, G. Račiukaitis, **Plasma Guiding and Scattering Microstructures for Laser Driven Thomson Sources**, Nuclear Photonics 2016 Conference, Monterey, USA, 16-21.10.2016

1.5. Autoriaus ir bendraautorių indėlis

1.5.1. Autoriaus indėlis

Disertacijos autorius atliko šiuos teorinius ir eksperimentinius darbus:

- Tyrimo metodų kūrimas, eksperimento planavimas, techninis ir organizacinis vadovavimas tyrimų veikloms;
- Struktūrinių plazmos koncentracijų profilių parinkimas, LPG elektronų greitinimo ir antrinės Rentgeno spinduliuotės skaitmeninis modeliavimas;
- Mikrotūtų parametrų nustatymas ir viršgarsinių čiurkšlių dinamikos skaitmeninis modeliavimas;
- Lydyto kvarco mikrotūtų projektavimas ir dalyvavimas mikrotūtų čiurkšlių koncentracijos profilių matavimuose interferometriniais metodais;
- Dalyvavimas LPG elektronų greitinimo eksperimentuose, panaudojant mikrotūtų struktūras ir matuojant antrinę Rentgeno spinduliuotę;
- Antrinės Rentgeno spinduliuotės taikymas biologinių objektų ir polimerinių plėvelių vaizdams bei vaizdų parametrų nustatymas;
- Rezultatų analizė, interpretacija ir vizualizacija, mokslinių straipsnių rengimas ir pristatymas konferencijose.

1.5.2. Bendraautorių indėlis

- Juozas Dudutis, dr. Valdemar Stankevič ir dr. Paulius Gečys atliko lydyto kvarco mikrotūtų struktūrų 3D lazerinės gamybos darbus;
- dr. Valdas Girdauskas konsultavo dėl viršgarsinių dujų čiurkšlių skaitmeninio modeliavimo ir sukūrė interferometrinių tūtų matavimo metodą;
- dr. Isabel Gallardo González, dr. Diego Guénot, Jonas Björklund Svensson, Anders Persson, dr. Olle Lundh dalyvavo LPG elektronų greitinimo ir antrinės Rentgeno spinduliuotės matavimo eksperimentuose Lundo lazerių centre;
- Lucas Rovige, dr. Igor Andriyash sukūrė vienos pusės smūginių bangų mikrotūtas ir kartu su dr. Juliumi Huijts, dr. Aline Vernier, Marie Ouillé, Zhao Cheng, Rodrigo Lopez-Martens, prof. dr. Jérôme Faure dalyvavo LPG elektronų greitinimo eksperimentuose LOA, Palezo „Ecole Polytechnique ENSTA“;
- dr. Kęstutis Regelskis ir dr. Gediminas Račiukaitis dalyvavo diskusijose ir konsultavo rengiant disertacijos rankraštį.

1.6. Disertacijos sandara

Daktaro disertacija, kurios apimtis 240 puslapiai ir kurioje yra 9 lentelės, 51 paveikslas ir 195 literatūros šaltiniai, parašyta anglų kalba. Disertaciją sudaro 7 skyriai, padėka, sutrumpinimų ir naudotos literatūros sąrašai. Kiekvieno skyriaus, pradedant nuo ketvirto, pabaigoje pateikti apibendrinti rezultatai ir išvados. Pagrindinės išvados pateikiamos disertacijos pabaigoje.

2. LITERATŪROS APŽVALGA

Disertacinio darbo literatūros apžvalgoje aprašomi krūvininkų greitinimo didelio intensyvumo lazerio impulsų plazmos greitintuvais (LPG – LWFA, Laser Wakefield Accelerator) ir antrinės spinduliuotės žadinimo principai bei valdymo būdai. Apžvalgos pabaigoje pateikiama LPG Rentgeno šaltinių parametrų suvestinė ir trumpai apibūdinamos plazmos profilių formavimui naudojamų viršgarsinių dujų tūtų gamybos technologijos.

10^{18} W/cm^2 lazerio intensyvumo elektromagnetinis laukas elektronus pagreitina iki reliatyvistinių energijų. Petavatiniai lazeriai, kurių smailinis intensyvumas siekia 10^{22}–10^{23} W/cm^2, leidžia pagreitinti ne tik elektronus, bet ir protonus bei sunkesnius jonus [1]. Šiuolaikinių sinchrotronų Rentgeno spindulių vidutinis ryškis yra ~ 10^{22}, o smailinis laisvųjų elektronų lazerių (LEL – FEL, Free Electron Laser) ryškis yra apie 10^{33} fotonų/s/mm^2/mrad^2/0,1 % JP (0,1 % JP reiškia –10^{-3} juostos pločio nuo atitinkamo kvanto energijos). Tai daugeliu eilių viršija Rentgeno lempų ryškį, kuris yra maždaug 10^7. 10–20 keV sinchrotronų ir LEL Rentgeno spinduliuotės šaltiniams reikia 8–17 GeV energijos elektronų pluoštų, o kiekvienam GeV reikia apytiksliai 100 m radijo dažnio (RD) greitintuvo ilgio [13]. Didelių matmenų RD greitintuvų kaštai siekia šimtus milijonų eurų.

LPG sukuriamas 100 GV/m – 1 TV/m elektrinis laukas daugiau kaip 3 eilėmis viršija didžiausią RD greitintuvuose naudojamą 200–400 MV/m lauką. LPG pagreitina elektronų pluoštus iki šimtų MeV – kelių GeV energijos. Elektronų pluoštai naudojami betatrono, atvirkštinės Komptono sklaidos (AKS – ICS, Inversed Compton Scattering) ir stabdymo (Bremsstrahlung) antrinės spinduliuotės šaltiniuose. LPG leidžia žymiai sutrumpinti greitinimo atstumą, sumažinti įrengimo išlaidas ir suteikia universitetams, mokslinių tyrimų institucijoms bei pramonės įmonėms galimybę naudotis šiuolaikiniais jonizuojančiosios spinduliuotės šaltiniais [5].

LPG elektronai greitinami išilginiame plazmos elektriniame lauke, susidarančiame dėl lazerio Gauso pluošto netiesinės panderomotorinės jėgos. Nehomogeninio silpnesnio elektrinio lauko jėga neatsveria jėgos stipresnio lauko srityje ir lazerio lauke svyruojantys krūvininkai per svyravimo ciklą juda mažesnės jėgos link. Ponderomotorinė jėga atskiria krūvius išilgine z kryptimi ir sukuria plazmos bangą, greitinančią elektronus. LPG elektronai efektyviausiai greitinami nuskurdinto elektronais plazmos burbulo režimu, kai skersinė lazerio elektrinio lauko ponderomotorinė jėga kompensuoja atskirtų krūvininkų joninio kanalo traukos jėgą. Plazmos burbulo spindulys apytiksliai lygus ketvirčiui plazmos bangos ilgio, o šio režimo lazerio lauko stiprio

parametras $a_0 > 2$. a_0 aprašomas kaip normuotas lazerio vektorinio lauko $\vec{E}_L$ potencialas: $a_0 = e\vec{E}_L/m_e c^2$, kur e – elektrono krūvis, m_e – elektrono masė, o c – šviesos greitis vakuume. Elektronų LPG parametrų suvestinė pateikta 1 lentelėje.

1 lentelė. Lazerio plazmos burbulo greitintuvų parametrai, kai lazerio bangos ilgis λ_L=0,8 μm [29].

P_L	a_0	W_L, J	τ_L, fs	ω_0, μm	Z_R, mm	n_p, cm^{-3}	L_d, mm	W_e, MeV
0,5 PW	4,8	30	60	26	2,6	10^{17}	45	4200
30 TW	3,5	1	25	10	0,4	10^{18}	2,8	500
1 TW	2	0,004	5	2,1	0,018	10^{20}	0,025	10

P_L yra lazerio impulso smailinė galia, a_0 – lazerio lauko stiprio parametras, τ_L – lazerio impulso trukmė, ω_0 – lazerio Gauso pluošto sąsmaukos plotis, Z_R – Gauso pluošto Rayleigh ilgis, n_p – plazmos koncentracija, L_d – greitinimo išsifazavimo atstumas. Lazerio impulso energija W_L, reikalinga elektronams pagreitinti, proporcinga $W_L \sim \tau_L^3 \sim \lambda_p^3$, o pagreitintų elektronų energija proporcinga $W_e \sim \tau_L^2 \sim \lambda_p^2$. Greitinamų elektronų pluošto energiją ir skėstį galima keisti keičiant injektuojamo į plazmos bangą krūvį. Disertaciniame darbe nagrinėjamos betatrono spinduliuotės parametrai priklauso nuo elektronų energijos, svyravimo amplitudės ir plazmos koncentracijos.

3. TYRIMO METODAI

Eksperimentiniai disertacijos darbai buvo atlikti Lundo lazerių centre (LLC) ir CNRS - „Ecole Polytechnique“ (EP) ir „ENSTA-Paristech“ - „Laboratoire d’Optique Appliqué“ (LOA). Prieigą prie lazerių įrenginių rėmė Europos Sąjungos mokslinių tyrimų ir inovacijų programa „Horizontas 2020“ pagal ARIES dotacijos susitarimą Nr. 730871 ir „Laserlab-Europe“, H2020 projektas Nr. EC-GA 654148.

Pagrindiniai antrinės Rentgeno spinduliuotės tyrimai buvo atlikti su 40 TW 35 fs lazeriu Lundo lazerių centre. LLC eksperimento metu 800 mJ energijos lazerio impulsas buvo fokusuojamas į 8 μm dydžio FWHM (Full Width Half Maximum – visas plotis ties puse maksimumo) pluoštą, kuris atitinka $3{,}6 \times 10^{19}$ W/cm^2 smailinį intensyvumą ir lazerio lauko stiprio parametrą $a_0 = 4{,}0$. Po to disertacijoje pasiūlyta plazmos struktūrinių profilių formavimo ir tūtų apdirbimo technologija buvo pritaikyta LOA suprojektuotų vienos pusės smūginių bangų (OSS) tūtų gamybai. Šių tūtų sukurti plazmos koncentracijos profiliai buvo naudojami LPG elektronų greitinimui su 0,8 TW 4 fs 1 kHz lazeriu. LOA eksperimento metu 3,8 mJ lazerio impulsas buvo fokusuojamas į 6,2 μm × 5,5 μm dydžio FWHM pluoštą, kuris atitinka $2{,}0 \times 10^{18}$ W/cm^2 smailinį intensyvumą ir lauko stiprio parametrą $a_0 \simeq 1{,}0$.

LLC eksperimente plazmos profilių formavimui buvo naudotos viršgarsinių tūtų struktūros, nurodytos 2 lentelėje. Jos susideda iš dviejų sekcijų. Pirmoji sekcija, kurią sudaro 1,5 mm plyšinė arba 2,25 mm Lavalio tūta, buvo naudojama elektronų greitinimui. Antroji sekcija susideda iš vienos ar keturių mažesnių matmenų 200–300 μm tūtų struktūros, esančios 100 μm atstumu nuo pirmosios sekcijos. Sutrumpinimai (LxW) ir (L1xW1) nurodo atitinkamai pirmosios ir antrosios sekcijos žiočių ilgį ir plotį, o (L2xW2) ir (LxW) ir (L3xW3) nurodo pirmosios ir antrosios sekcijos tūtos kakliuko ilgį ir plotį. Priklausomai nuo tūtų orientacijos lazerio pluošto sklidimo atžvilgiu, šios tūtos sudarė elektronų injektoriaus arba svyravimo struktūrą (1 pav.). Atsižvelgiant į medžiagos atsparumą optiniams pažeidimams, gamybos tikslumą bei lankstumą, disertacijos darbe mikrotūtų gamybai buvo pasirinktas lydytas kvarcas, turintis reikšmingų privalumų plastikų ir metalų atžvilgiu [140].

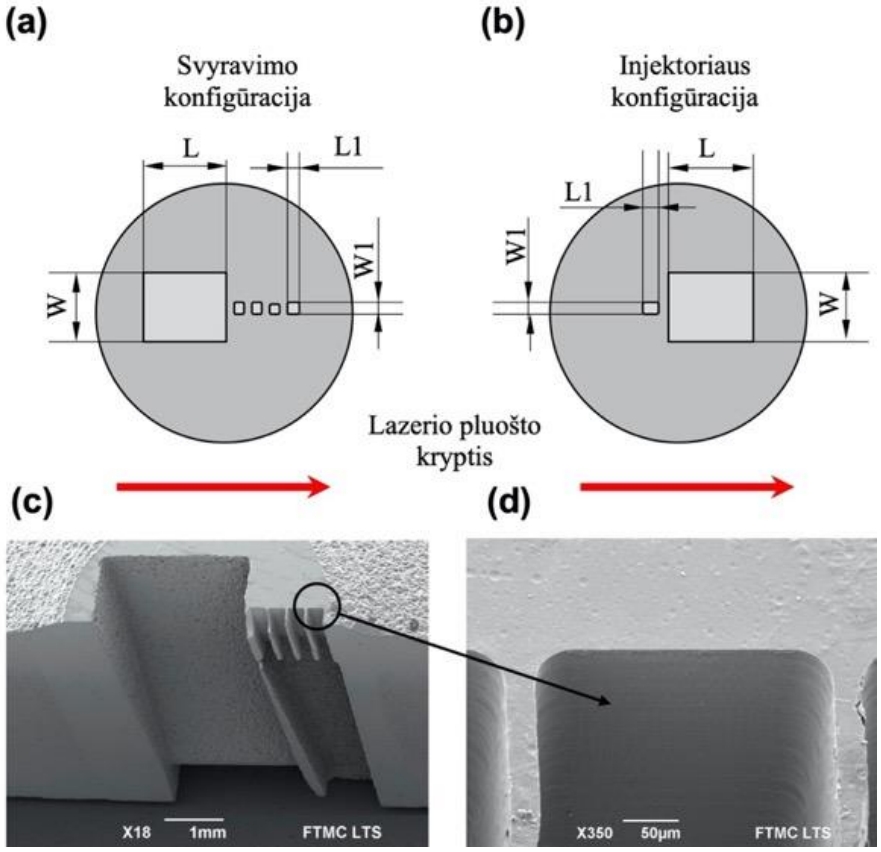

1 pav. Arr2 (a) ir **Arr4 (d)** tūtų struktūrų, naudotų LLC eksperimentuose, schema ir perpjautos pusiau **Arr2** struktūros **(c, d)** SEM vaizdas [140].

LLC eksperimento metu LPG pagreitintų elektronų energija ir erdvinis skirstinys, panaudojant struktūrinius plazmos koncentracijos profilius, buvo modeliuojami skaitmeniniu būdu naudojant FBPIC PIC (Particle-in-Cell) algoritmą [157]. Remiantis modeliavimo rezultatais ir naudojant analitines išraiškas [103], buvo apskaičiuoti lazerio impulso žadinamos betatrono Rentgeno spinduliuotės fotonų skaičius bei spinduliuotės ryškis. Dujų tūtų čiurkšlių koncentracija, greitis, slėgis ir temperatūra buvo modeliuojami skaitmeniniu būdu, naudojant OpenFOAM programinę įrangą [158].

2 lentelė. Tūtų struktūrų, naudotų LLC eksperimentuose, matmenys [140].

Nr.	Pirmoji sekcija			Antroji sekcija		
	Struktūra	Žiočių matmenys, mm, (LxW)	Kakliuko matmenys, mm, (L2xW2)	Struktūra	Žiočių matmenys, mm, (L1xW1)	Kakliuko matmenys, mm, (L3xW3)
#1	Plyšinė Lavalio tūta S1	1,5 x 1,2	1,5 x 0,12	–	–	–
#2	Plyšinė Lavalio tūta Arr2	1,5 x 1,2	1,5 x 0,12	Plyšinė 4 tūtų struk-tūra	0,2 x 0,2	0,2 x 0,2
#3	Cilindrinė Lavalio tūta Arr3	∅ 2,25	∅ 0,5	Plyšinė 4 tūtų struk-tūra	0,2 x 0,2	0,2 x 0,2
#4	Plyšinė Lavalio tūta Arr4	1,5 x 1,2	1,5 x 0,12	Plyšinė Lavalio tūta	0,3 x 0,27	0,3 x 0,18

Didelės plazmos koncentracijos profilių formavimui buvo naudojamos fiksuoto skersmens kapiliarinės tūtos. Tūtų čiurkšlių azoto dujų koncentracijos profiliai buvo matuojami Macho–Zehnderio interferometru su 632,8 nm He-Ne lazeriu. Po to interferogramos buvo filtruojamos naudojant Furjė transformaciją. Naudojant Abelio transformaciją ir IDEA algoritmą buvo apskaičiuojami 3D dujų koncentracijos skirstiniai [162]. LLC ir LOA eksperimentuose naudotų tūtų struktūrų dujų koncentracijos profiliai buvo išmatuoti naudojant bangos fronto jutiklio interferometrą (SID4-HR, Phasics). LLC atveju buvo naudotos argono, o LOA – azoto dujos. LOA eksperimento metu buvo papildomai matuota jonizuotų azoto dujų plazmos koncentracija. Nesimetrinių tūtų čiurkšlių dujų koncentracijos skirstinys buvo apskaičiuotas naudojant SIRT algoritmą [163].

Pagreitintų elektronų energija ir skėstis buvo matuojama 0,8 T magnetinio spektrometro, kalibruoto naudojant Kodak Lanex Regular scintiliacijos ekraną ir CCD kamerą. LOA eksperimento metu buvo naudotas kalibruotas CsI (Tl) fosforo ekranas. Betatrono spinduliuotė LLC eksperimente buvo registruojama „Andor iKon - L SO“ Rentgeno kamera, jautria Rentgeno spinduliuotei nuo 100 eV iki 20 keV. Rentgeno kameros langas buvo pagamintas iš 250 μm storio berilio. Siekiant apsaugoti kamerą nuo 800 nm lazerio ir didelės energijos ultravioletinės (XUV) spinduliuotės, generuojamos elektronų, atlenkiamų spektrometro magnetiniame lauke, vakuuminės

kameros langas buvo uždengtas papildoma 3 μm aliuminio folija ir 50 μm kaptonu. Rentgeno kamera buvo sumontuota vakuuminės kameros išorėje 73 cm atstumu nuo šaltinio, ir betatrono spinduliuotė praeidavo pro 12 cm oro tarpą. Betatrono šaltinio energijos spektras buvo matuotas naudojant Ross filtrus, turinčius skirtingus storius ir skirtingas K/L absorbcijos krašto energijas [168]. Betatrono šaltinio spindulys buvo apskaičiuotas matuojant Frenelio difrakciją nuo 50 μm volframo sukryžiuotų vielų, sumontuotų 28 mm atstumu nuo šaltinio [172]. Lazerio impulso Rentgeno fotonų skaičius, skėstis ir ryškis buvo apskaičiuoti apdorojant Rentgeno vaizdų duomenis ir taikant spinduliuotės erdvinio Gauso skirstinio aproksimaciją.

4. SKAITMENINIS LAZERINIO PLAZMOS GREITINTUVO MODELIAVIMAS

Šiame skyriuje pateikta medžiaga buvo publikuota moksliniuose straipsniuose [A2] ir konferencijų pranešimuose [C1, C2, C3].

4.1. Skaitmeninis lazerinio greitintuvo modeliavimas

LPG pagreitintų elektronų pluošto krūvio energija ir erdvinis skirstinys bei betatrono antrinė Rentgeno spinduliuotė, generuojama elektronų, svyruojančių jonų kanale, buvo modeliuojami skaitmeniniu būdu naudojant FBPIC PIC algoritmą [157]. Kvazicilindrinis FBPIC PIC algoritmas leidžia greičiau išspręsti lazerio ir elektronų pluoštų sklidimo uždavinius, palyginti su visos apimties 3D algoritmais. Injektoriaus ir svyravimo struktūrų modeliavimui buvo naudoti supaprastinti injektoriaus (2ab pav.) ir svyravimo (2cd pav.) plazmos koncentracijos profiliai. Pasirinktas injektoriaus struktūros plazmos koncentracijos profilis buvo sudarytas iš trumpos 200 μm plazmos sekcijos, 100 μm tarpo ir 1,5 mm plazmos greitinimo sekcijos.

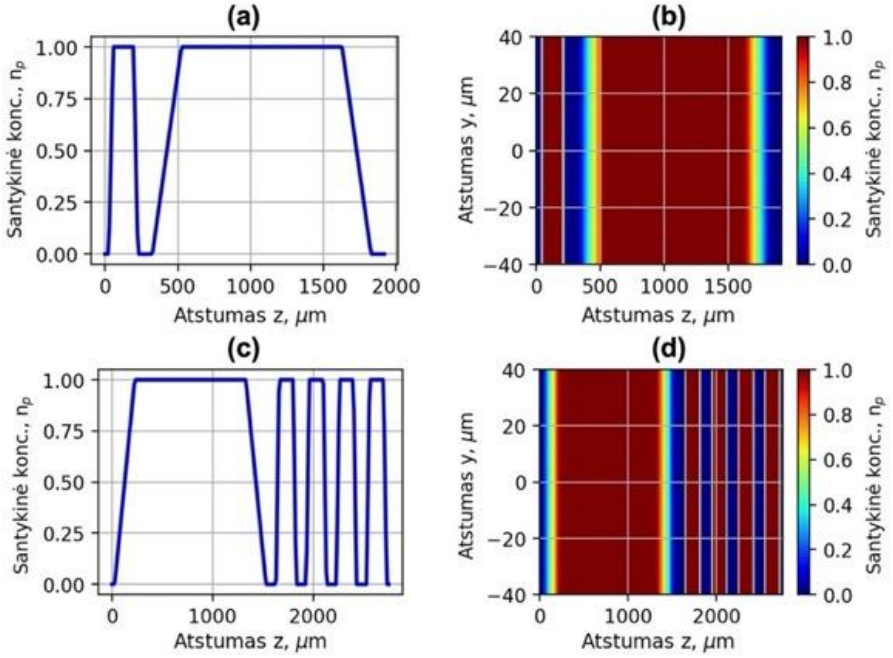

2 pav. Modeliavimui naudoti supaprastinti injektoriaus **(a, b)** ir svyravimo **(c, d)** struktūrų plazmos koncentracijos profiliai [140].

Svyravimo struktūra buvo sudaryta iš 1,5 mm ilgio plazmos greitinimo sekcijos ir svyravimo struktūros, susidedančios iš keturių 200 μm plazmos

sričių ir 100 μm ilgio tarpų. Injektoriaus struktūros modelis buvo panaudotas Arr4 tūtų struktūros projektavimui, o svyravimo modelis – Arr2 tūtų struktūros projektavimui. 1,5 mm plazmos greitinimo sekcijos modelis atitinka S1 pavienės tūtos suformuojamą dujų čiurkšlės koncentracijos profilį. Šie tūtų pavadinimai toliau vartojami aptariant teorinius ir eksperimentinius rezultatus.

Modeliavimo parametrai buvo parinkti atsižvelgiant į LLC eksperimento metu naudoto fokusuojančio veidrodžio 465 mm židinio nuotolį ir sufokusuoto lazerio pluošto 8,0 μm skersmenį FWHM. Tai atitiko lazerio lauko stiprio parametrą $a_0 = 4{,}0$. Norint įvertinti įvairias LPG sąlygas buvo atliktas modeliavimas su $a_0 = 2{,}3$ ir 10,9 μm lazerio pluošto skersmeniu. Modeliavimo zonos spindulys buvo 20 μm, o ilgis 0,5–2,5 mm. Skaitmeninio tinklelio skiriamoji geba buvo 0,05 μm, o laiko žingsnis – 0,17 fs. Pradinė $n_p = 3\times10^{18}$ cm^{-3} plazmos koncentracija, atitinkanti plazmos burbulo režimą, buvo apskaičiuota taikant analitines formules. Modeliuojant plazmos koncentracija buvo keičiama nuo 1×10^{18} iki $1{,}0 \times 10^{19}$ cm^{-3}. Modeliavimas buvo atliktas gryno He ir He + 1 % N_2 dujų mišinio atvejams. Modeliuojant buvo palyginti neigiamo plazmos koncentracijos gradiento, jonizacijos ir kombinuoto neigiamo plazmos koncentracijos gradiento ir jonizacijos injektavimo būdai. Esant $a_0 = 2{,}3$ ir $n_p = 3\times10^{18}$ cm^{-3}, tiek gryno helio, tiek He + 1 % N_2 dujų mišinio atveju bei naudojant neigiamą plazmos koncentracijos gradientą buvo pagreitinami nedidelio krūvio mažos energijos sklaidos elektronų pluoštai. Esant tiems patiems parametrams He + 1 % N_2 dujų mišinio atveju bei naudojant kombinuotą neigiamą plazmos koncentracijos gradientą ir jonizaciją buvo injektuojama daugiau elektronų, tačiau šis padidėjimas nebuvo žymus. Padidinus lazerio lauko stiprį iki $a_0 = 4{,}0$ ir sumažinus plazmos koncentraciją iki $n_p = 1 \times 10^{18}$ cm^{-3}, buvo jonizuojama daugiau elektronų, tačiau dėl mažesnės plazmos koncentracijos injektuotas krūvis išliko mažas.

Esant $a_0 = 4{,}0$ ir $n_p = 3 \times 10^{18}$ cm^{-3} optimalaus plazmos burbulo atveju (3a pav.) bei naudojant pavienę S1 tūtą buvo pasiekta didžiausia pagreitintų elektronų energija bei mažiausia elektronų pluošto skėstis. Šią koncentraciją atitinkantis plazmos bangos ilgis $\lambda_p = 19{,}3$ μm, sufokusuoto lazerio pluošto skersmuo FHWM 10,9 μm ir nuotolis, per kurį nusklinda $\tau_L = 32$ fs trukmės impulsas, atitiko plazmos burbulo režimą. Elektronų, pagreitintų pavienės 1,5 mm ilgio S1 tūtos čiurkšlės plazmoje, energija siekė 150–200 MeV, o skėstis – 2 – 3 mrad. Nuolat injektuojami jonizuoto azoto elektronai turėjo didelę pagreitintų elektronų energijos sklaidą. Esant tiems patiems parametrams bei naudojant Arr4 kombinuoto injektavimo struktūrą ir jonizacijos injektuotus elektronus (3b pav.) buvo pagreitintas didesnio krūvio kvazimonoenergetinis

elektronų pluoštas, kurio vidutinė energija 50 MeV. Lazerio pluoštas buvo fokusuojamas į plazmos koncentracijos gradiento profilio pradžią. Lazerio intensyvumas buvo pakankamas, kad pagreitintų didesnio krūvio elektronų kiekį, bet neviršytų nuolatinės jonizacijos intensyvumo vertės.

3cd pav. pavaizduoti pavienės tūtos S1 (3c pav.) ir plazmos koncentracijos svyravimo struktūrų (3d pav.) pagreitintų elektronų krūvio skirstiniai esant $n_p = 1 \times 10^{19}$ cm^{-3} ir $a_0 = 4{,}0$. Esant $n_p = 1 \times 10^{19}$ cm^{-3} trumpesnį plazmos bangos ilgį atitinka 7,9 μm FHWM optimalus lazerio pluošto skersmuo. Optimali lazerio impulsų trukmė $\tau_L = 18$ fs yra trumpesnė nei eksperimente naudojama $\tau_L = 35$ fs. Dėl to buvo sužadinamos kelios plazmos bangos ir elektronai buvo injektuojami ne tik į užpakalinę, bet ir į šonines plazmos burbulo dalis. Pagreitintų elektronų pluošto energija sumažėjo, o skėstis išaugo. Padidinus dujų koncentraciją nuo $n_p = 3 \times 10^{18}$ cm^{-3} iki $n_p = 1{,}0 \times 10^{19}$ cm^{-3}, pavienės 1,5 mm ilgio S1 tūtos pagreitintų elektronų energija siekė 30–100 MeV, o elektronų pluošto skėstis padidėjo iki 20 – 40 mrad (3c pav.).

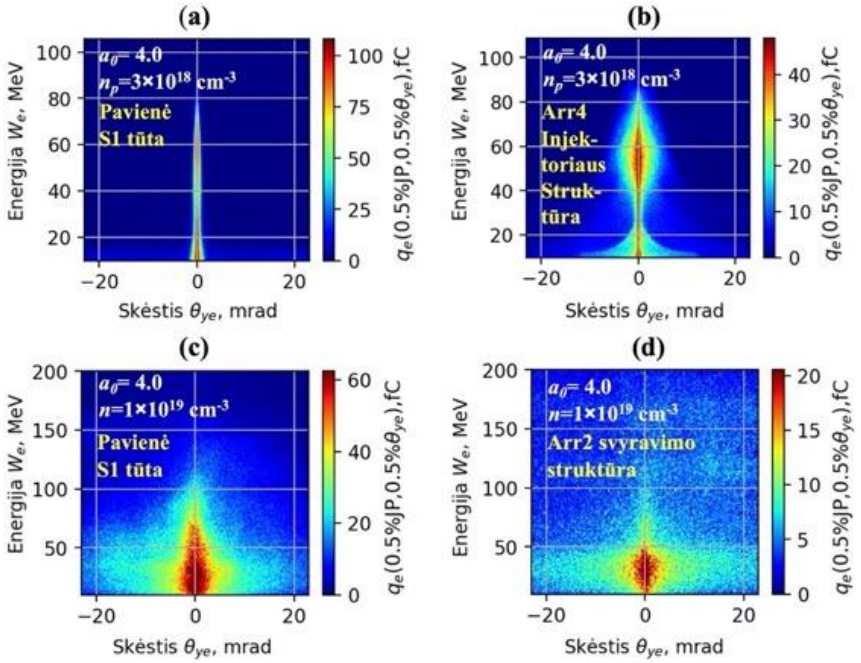

3 pav. S1 pavienės tūtos **(a)** ir **Arr4** injektoriaus struktūros **(b)** skaitmeninio modeliavimo būdu apskaičiuotas elektronų krūvio ir energijos erdvinis skirstinys jonizacijos **(a)** ir kombinuoto neigiamo plazmos koncentracijos gradiento ir jonizacijos injektavimo **(b)** atveju esant $n_p = 3 \times 10^{18}$ cm^{-3} bei pavienės tūtos **S1 (c)** bei **Arr2** svyravimo struktūros **(d)** elektronų krūvio ir energijos erdvinis skirstinys esant $n_p = 1 \times 10^{19}$ cm^{-3} [140].

Esant $n_p = 3 \times 10^{18}$ cm^{-3} bei naudojant Arr2 svyravimo struktūros plazmos koncentracijos profilį elektronų pluošto skėstis padidėjo iki 30–60 mrad. Pluošto skėstis buvo 2–3 kartus didesnė palyginti su pavienės tūtos elektronų pluošto skėstimi. Elektronų energija išliko panaši. Esant $n_p = 1 \times 10^{19}$ cm^{-3} (3d pav.) elektronų pluošto skėstis padidėjo iki 30–50 mrad ir buvo 30–50 % didesnė palyginti su pavienės tūtos elektronų pluošto skėstimi, parodyta 3c pav. Dėl mažesnės skėsties esant $n_p = 3 \times 10^{18}$ cm^{-3} svyravimo struktūra padidino skėstį daugiau nei esant $n_p = 1 \times 10^{19}$ cm^{-3}.

4.2. Skaitmeninis antrinės spinduliuotės modeliavimas

Lazerio impulso žadinamos betatrono antrinės Rentgeno spinduliuotės fotonų skaičius ir ryškis buvo apskaičiuoti, remiantis FBPIC PIC elektronų impulsų erdvinio skirstinio duomenimis.

Betatrono svyravimo spindulys r_β sklindančio lazerio impulso suformuotame jonų kanale buvo įvertintas taikant aproksimaciją $r_\beta^2/2\gamma_z \simeq p_{e\perp}^2/p_{ez}^2 \simeq p_{e\perp}^2/\gamma_z^2$ ir tariant, kad betatrono svyravimo spindulys yra proporcingas elektronų skersinio $p_{e\perp}$ ir išilginio p_{ez} impulsų santykiui [7]. 4a –c pav. pavaizduoti elektronų, atitinkančių skersinę elektronų pluošto skėstį $\theta_\perp$ (a), betatrono spindulį r_β (b) ir kritinę sinchrotrono energiją $W_{c\beta}$ (c), krūvio modeliavimo rezultatai. Skersinė elektronų pluošto skėstis $\theta_\perp$ (FWHM) buvo apskaičiuota kaip elektronų pluošto skėsties x ir y kryptimis vidurkis. Modeliavimo rezultatai parodė, kad Arr2 svyravimo struktūros plazmos koncentracijos skirstinys padidina elektronų, turinčių didesnę pluošto skėstį, skaičių (4a pav.) ir 15–20 % padidina betatrono spindulio ir kritinės energijos vidurkį (4bc pav.). Nors betatrono spindulys, apskaičiuotas remiantis elektronų skersinio $p_{e\perp}$ ir išilginio p_{ez} impulsų santykiu, padidėja palyginti nedaug, elektronų pluošto skėstį Arr2 svyravimo struktūra pavienės tūtos atžvilgiu S1 padidina 30–50 % (3 pav.). Apskaičiuotasis betatrono svyravimų spindulys siekia 1–2 μm, o elektronų pluošto skėstis 2,5 mm greitinimo atstumu atitinka 50 μm spindulio elektronų erdvinį skirstinį. Suminė betatrono spinduliuotė susideda iš atskirų elektronų, esančių skirtingose erdvinėse pozicijose, žadinamos spinduliuotės. 4d pav. pavaizduotas Arr2 struktūros ir S1 pavienės tūtos apskaičiuotas lazerio impulso Rentgeno fotonų spektro tankis $dN_{phot}/dW_{r\beta}$. Arr2 plazmos koncentracijos svyravimo struktūra padidino lazerio impulso Rentgeno fotonų skaičių 2–3 kartus (4d pav.).

Apskaičiuotų fotonų skaičius siekė 5×10^8. Padidinus plazmos koncentraciją nuo 3×10^{18} cm^{-3} iki 1×10^{19} cm^{-3}, betatrono sinchrotrono parametras K_β padidėjo nuo 5 iki 10. Arr2 svyravimo struktūros atveju,

palyginti su paviene S1 tūta, parametras K_β padidėjo nuo 10 iki 14–20. Esant šioms K_β parametro vertėms betatrono spinduliuotė turi ištisinį plačiajuostį spektrą. Vyraujanti spinduliuotė atitiko sinchrotrono spinduliuotę, kurios kritinė energija $W_{c\beta} \sim 2–3$ keV.

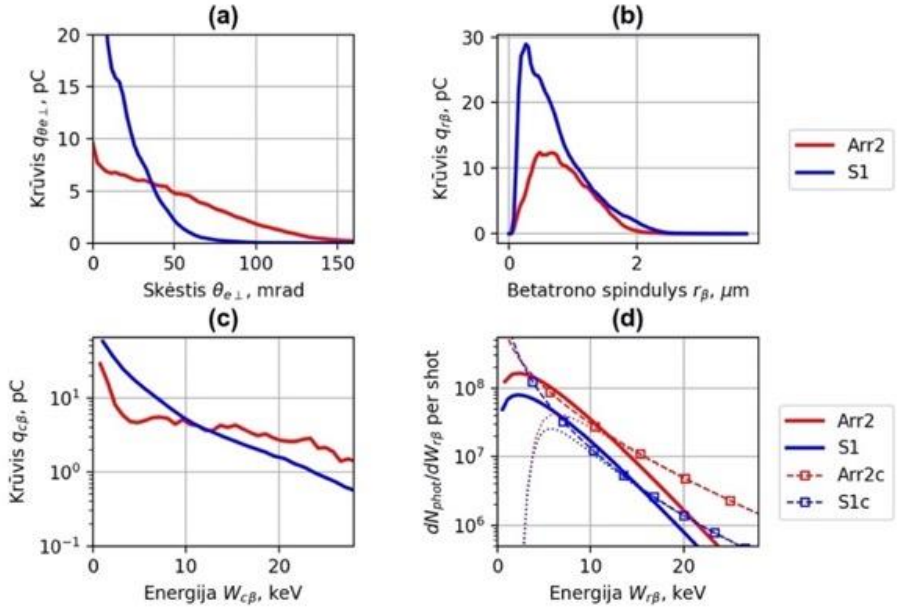

4 pav. Arr2 svyravimo struktūros ir pavienės tūtos **S1** skaitmeninio modeliavimo būdu apskaičiuotas elektronų krūvis, atitinkantis skersinę skėstį $\theta_\perp$ **(a)**, betatrono spindulį r_β **(b)** ir kritinę sinchrotrono energiją $W_{c\beta}$ **(c)**. **Arr2** svyravimo struktūros ir pavienės tūtos **S1** apskaičiuotas lazerio impulso Rentgeno fotonų tankis $dN_{phot}/dW_{r\beta}$ **(d)**. Punktyrinės linijos **Arr2c** ir **S1c** vaizduoja apskaičiuotą $dN_{phot}/dW_{r\beta}$ Rentgeno fotonų tankį, taškinės linijos – apskaičiuotą Rentgeno fotonų tankį, nuslopinto medžiagų, esančių tarp šaltinio ir fotokameros, o ištisinės linijos **Arr2** ir **S1** vaizduoja Rentgeno fotonų tankį, atitinkantį vidutinę sinchrotrono kritinę energiją $W_{c\beta}$, išmatuotą naudojant Ross filtrus [140].

4.3. Išvados

Pagreitintų elektronų krūvį, energiją, skėstį bei antrinės spinduliuotės parametrus galima valdyti naudojant struktūrinius plazmos koncentracijos profilius, sudarytus iš injektoriaus, greitinimo ir svyravimo sekcijų:

- LPG pagreitintų elektronų pluošto krūvio kiekį galima padidinti ir energijos sklaidą galima sumažinti naudojant injektoriaus struktūrinius plazmos profilius bei derinant neigiamo plazmos koncentracijos gradiento ir jonizacijos injekciją.
- Norint pasiekti didžiausią pagreitintų elektronų energiją ir mažiausią dispersiją, LPG sekcijos plazmos koncentracija turi atitikti nuskurdinto elektronais plazmos burbulo režimo reikalavimus.
- Lazerio pluošto intensyvumas tuir būti pakankamas, kad pagreitintų didesnio krūvio elektronų kiekį, bet neviršytų nuolatinės jonizacijos intensyvumo vertės plazmos burbulo srities viduje.
- Padidinus plazmos koncentraciją 2–3 kartus, 2–2,5 karto padidėjo pagreitinto krūvio kiekis ir elektronų pluošto skėstis. Tai padidino betatrono spinduliuotės efektyvumą.
- Naudojant svyravimo struktūros plazmos koncentracijos profilį betatrono svyravimo spindulys ir spinduliuotės kritinė energija padidėjo 15–20 %. Apskaičiuotasis betatrono svyravimų spindulys siekė 1–2 μm. 2,5 mm greitinimo atstumu antrinę spinduliuotę generuojantys elektronai buvo pasiskirstę ~50 μm spinduliu.
- Svyravimo struktūros plazmos koncentracijos skirstinys, palyginti su pavienės tūtos plazmos koncentracijos profiliu, elektronų skėstį esant $a_0 = 4{,}0$ ir $n_p = 1 \times 10^{19}$ cm^{-3} padidino 30–50 %, o lazerio impulso Rentgeno fotonų skaičius padidėjo 2–3 kartus.

5. SKAITMENINIS DUJŲ ČIURKŠLIŲ MODELIAVIMAS

Šiame skyriuje pateikta medžiaga buvo publikuota moksliniuose straipsniuose [A1, A2, A3, A4] ir konferencijų pranešimuose [C1, C2, C3, C4].

FBPIC supaprastintus plazmos koncentracijos profilius atitinkantys tūtų čiurkšlių dujų koncentracijos profiliai buvo modeliuojami pritaikius OpenFOAM programinį paketą [13], naudojant spūdžiųjų skysčių pastovaus srauto „rhoSimpleFoam“ algoritmą ir k_t-ω_t šlyties įtempių (SST – Shear Stress Turbulence) turbulencijos modelį. k_t aprašo turbulencijos kinetinę energiją, o ω_t – savitąją turbulencijos kinetinės energijos sklaidos spartą.

Įvertinant dujų koncentracijos n_g priklausomybę nuo paduodamų dujų slėgio, buvo taikoma idealiųjų dujų aproksimacija. Idealiųjų dujų molekulinė koncentracija n_g buvo apskaičiuota kaip $n_g = N_A\rho/M_m$, kur N_A yra Avogadro konstanta, ρ – dujų tankis, o M_m – molinė dujų masė. Esant standartinei temperatūrai T = 273,15 K ir slėgiui P = 101,325 kPa, idealiųjų dujų koncentracija $n_g = 2{,}687 \times 10^{25}$ m^{-3}. Lokaliai molekulinei dujų koncentracijai apskaičiuoti esant dviem skirtingiems slėgiams $P_{1,2}$, tūriams $V_{1,2}$ ir temperatūroms $T_{1,2}$, buvo naudojama formulė $p_1V_1/T_1 = p_2V_2/T_2$. Molekulinė dujų koncentracija didėja proporcingai esamo slėgio ir temperatūros santykiui. Modeliavimui naudotų medžiagų savybės pateiktos 3 lentelėje.

3 lentelė. Modeliavimui naudotų medžiagų savybės [139].

Savybės	Vienetai	Azotas	Helis
Molekulinė masė	g/mol	28,02	4,02
Tankis esant 1 baro slėgiui ir 273,15 K	kg/m^3	1,256	0,185
Savitoji šiluminė talpa C_p	J/(kg K)	1004	5193
C_p/C_v	–	1,4	1,67
Garso greitis esant 273,15 K	m/s	331,2	973
Sutherlando konstanta A_s	–	$1{,}458 \times 10^{-6}$	$1{,}633 \times 10^{-6}$
Sutherlando temperatūra T_s	K	110,8	147,0
Lūžio rodiklis esant 632nm, 1 baro slėgiui ir 273,15 K	–	1,000298	1,0000349

Skysčio klampumas buvo apskaičiuotas atsižvelgiant į Sutherlando klampos priklausomybę nuo temperatūros. Skaitmeninis modeliavimas buvo atliktas azoto ir helio dujų čiurkšlėms. Helis paprastai naudojamas kaip pagrindinė LPG elektronų greitinimo terpė. Azoto ir helio dujų koncentracijos

tūtų žiotyse skiriasi tik apie 7–10 %. Dėl didesnio lūžio rodiklio azotą patogu naudoti eksperimentiniuose tūtų čiurkšlių charakteristikų matavimuose.

Didelės plazmos koncentracijos profiliams formuoti buvo tiriamas kapiliarinių mikrotūtų dujų čiurkšlių išsiplėtimas į vakuumą. Fiksuoto skersmens kapiliarai turi mažesnį 1,2–1,4 dujų išsiplėtimo koeficientą, palyginti su tipiškomis siaurėjančiomis-platėjančiomis Lavalio tūtomis. Pagrindinėje kanalo dalyje srauto greitis yra mažesnis už garso greitį. Garso barjeras, ties kuriuo dujų greitis yra lygus garso greičiui (Macho skaičius M = 1), yra kapiliaro viduje netoli tūtos žiočių. Dėl didelio slėgio gradiento netoli tūtos žiočių dujų srautas, įveikdamas klampumo šlyties jėgas, šalia sienelių suformuoja skirtingo storio siaurėjantį-platėjantį pasienio sluoksnį. Tokiu būdu susiformuoja Lavalio tūta ir tūtos žiotyse dujų srautas pasiekia viršgarsinį M = 1,2–1,4 greitį [175].

5.1. Skaitmeninis dujų čiurkšlių ir paviršiaus šiurkštumo modeliavimas

5 pav. parodyti fiksuoto 300 μm skersmens apskaičiuotas cilindrinės tūtos azoto ir helio dujų koncentracijos bei Macho skaičiaus skirstinys esant 60 barų slėgiui. Dujų plėtimasis buvo modeliuotas 6 × 4 mm plote, tačiau dėl didelio kraštinių santykio 18:1 (2,8 mm ir 150 μm) parodyta tik 600 × 600 μm skirstinio dalis, esanti arti tūtos žiočių. Azoto ir helio koncentracijų skirstiniai yra panašūs, nes abiem atvejais dujų srautas iš ikigarsinio virsta į viršgarsinį arti tūtos žiočių. Nedidelius koncentracijos skirtumus nulemia monoatominių helio ir diatominių azoto dujų adiabatinio indekso skirtumas. Didesni azoto ir helio Macho skaičiaus skirtumai priklauso nuo dujų masės. Dujų temperatūra ir garso greitis yra atvirkščiai proporcingi kvadratinei šakniai iš molekulinės dujų masės. Mažesnės masės helio dujos plečiasi greičiau, o lokali temperatūra nukrinta iki žemesnių, palyginti su azotu, verčių.

Siekiant įvertinti tūtų vidinių paviršių apdorojimo kokybės įtaką, buvo ištirtas sienelių šiurkštumo poveikis fiksuoto 50 μm, 100 μm ir 200 μm skersmens cilindrinių lydyto kvarco mikrotūtų kokybei bei čiurkšlių dujų koncentracijai. Izoentropinio srauto teorija ir analitinės išraiškos, naudojamos didelio skersmens tūtų modeliavimui, neatsižvelgia į trinties nuostolius ir nėra tinkamos mažesnių nei 1 mm skersmens mikrotūtų dujų koncentracijos ir greičio skirstinių skaičiavimui. Sienelių šiurkštumas buvo modeliuojamas skaitmeniniu būdu, naudojant smiltelių šiurkštumo parametrą k_{rf}, apskaičiuojamą matuojant turbulentinio srauto slėgio kritimą vamzdžiuose, padengtuose vienodo skersmens smiltelėmis [156].

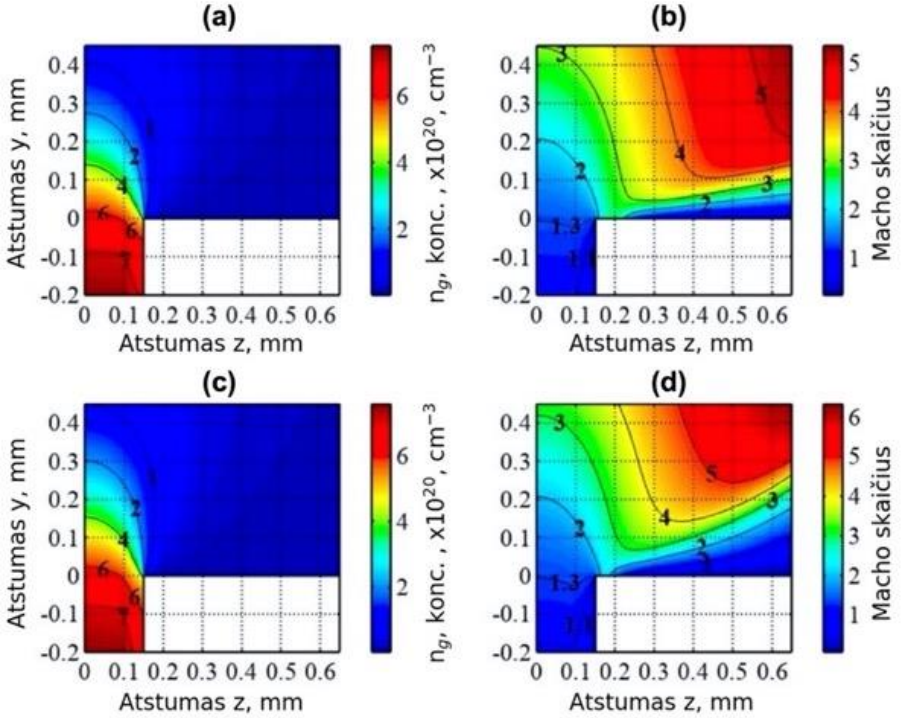

5 pav. 300 μm fiksuoto skersmens cilindrinės tūtos skaitmeninio modeliavimo būdu apskaičiuota azoto dujų koncentracija **(a)**, Macho skaičius **(b)** ir helio dujų koncentracija **(c)** bei Macho skaičius **(d)** esant 60 barų slėgiui [139].

Eksperimentiškai buvo matuojama keletas kitų parametrų, apibūdinančių paviršiaus šiurkštumą: šiurkštumo nuokrypio modulio aritmetinis vidurkis R_a, vidutinis kvadratinis šiurkštumo nuokrypis R_{RMS} ir penkių skirtumo tarp minimalaus ir maksimalaus paviršiaus aukščio matavimų aritmetinis vidurkis R_{zd}. Remiantis išmatuotais paviršiaus šiurkštumo parametrais, smiltelių šiurkštumo parametras k_{rf} buvo apskaičiuotas remiantis 4 lentelėje pateiktais sąryšiais.

4 lentelė. Smiltelių šiurkštumo parametro k_{rf} sąryšiai su išmatuotais paviršiaus šiurkštumo parametrais [178].

Išmatuotas šiurkštumo parametras	Apskaičiuotas smiltelių šiurkštumo parametras k_{rf}
R_a	$k_{rf} = 5{,}863\ R_a$
R_{RMS}	$k_{rf} = 3{,}100\ R_{RMS}$
R_{zd}	$k_{rf} = 0{,}978\ R_{zd}$

Laminaraus dujų srauto greičio profilis dėl sienelių trinties ir klampumo jėgų po tam tikro atstumo nuo vamzdelio įėjimo tampa parabolinis. Toks profilis vadinamas visiškai išsivysčiusiu, o atstumas, per kurį profilis tampa parabolinis, vadinamas hidrodinaminiu įėjimo ilgiu. Laminaraus srauto įėjimo ilgis gali viršyti vamzdelio skersmenį dviem eilėmis. Turbulentinio srauto atveju greičio profilis yra labiau plokščias dėl dujų maišymosi radialine kryptimi, o hidrodinaminis įėjimo ilgis apytiksliai 10 kartų didesnis už vamzdelio skersmenį. Srauto paviršiaus ploto ir tūrio santykis didėja, mažinant vamzdelio skersmenį ir didėjant sienelės šiurkštumui, kadangi dujų srauto ir sienelių sąlyčio plotas tampa didesnis. Dėl to padidėja trintis ir energijos nuostoliai. 50–200 μm skersmens kapiliaruose dujų srautas yra turbulentinis. Mažo skersmens šiurkščių sienelių kapiliaruose dujų srauto greitis ir bendrasis slėgis, palyginti su didesnio skersmens tūtomis, sumažėja. Skaitmeninio šiurkštumo modeliavimo rezultatai, pateikti 6a pav., rodo, kad sienelės nelygumai, kurių smiltelių šiurkštumo parametras k_{rf} = 2,5 μm, daro didelę įtaką 50 μm skersmens cilindrinių tūtų dujų koncentracijos skirstiniui.

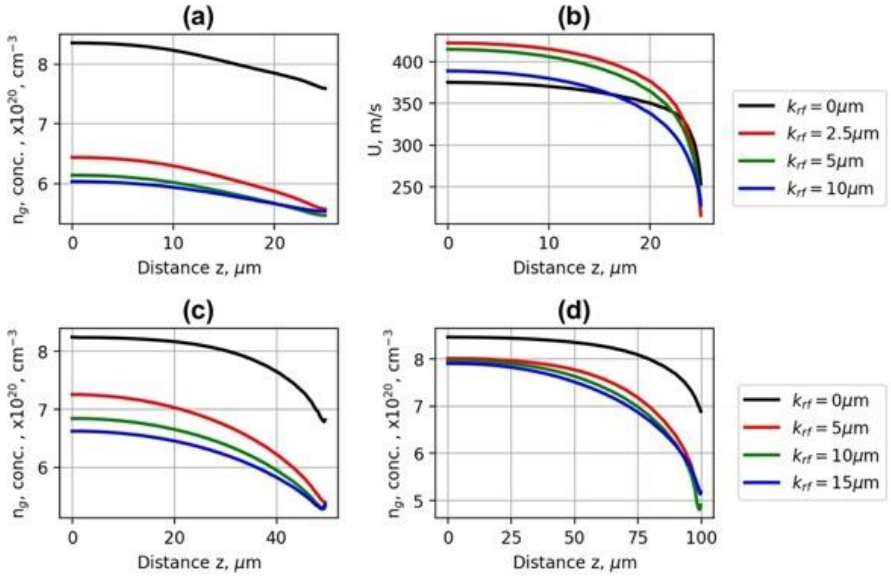

6 pav. Fiksuoto 50 μm **(a, b)**, 100 μm **(c)** ir 200 μm **(d)** skersmens tūtų skaitmeninio modeliavimo skersiniai N_2 dujų koncentracijos n_g **(a, c, d)** ir greičio **(b)** profiliai ties tūtų žiotimis esant 60 barų slėgiui ir skirtingoms smiltelių šiurkštumo parametro vertėms k_{rf} [156].

Esant k_{rf} = 0 μm 2,8 mm atstumu nuo kapiliaro įėjimo dujų srauto greičio profilis nėra išsivystęs ir yra gana plokščias (6b pav.). Esant k_{rf} = 2,5–15 dujų

srautas tampa labiau turbulentinis, o greičio profilis – daugiau išvystytas. Tačiau dujų srauto greitis, bendrasis ir statinis slėgis bei dujų koncentracija ties žiotimis krenta 23% palyginti su k_{rf} = 0 μm. Dėl dujų srauto trinties šalia sienelių padidėja pasienio sluoksnio temperatūra, slėgis ir dujų koncentracija (6c pav.). Tokio paties šiurkštumo sienelių įtaka 100 μm skersmens cilindrinės tūtos srautui yra santykinai mažesnė. Esant k_{rf} = 10 μm 100 μm skersmens cilindrinės tūtos (6c pav.) dujų koncentracija, palyginti su lygia sienele, sumažėja 17 %, o esant k_{rf} = 15 μm 200 μm skersmens cilindrinės tūtos (6d pav.) dujų koncentracija sumažėja 7 %. Modeliavimo rezultatai parodė, kad paviršiaus šiurkštumas turi įtakos tūtos kokybei ir čiurkšlės parametrams, kai smiltelių šiurkštumo parametras k_{rf} viršija 1–2 % nuo cilindrinės tūtos skersmens arba Lavalio tūtos kakliuko skersmens. Fiksuoto skersmens cilindrinės tūtos kraštų nuskilimo 30° kampu modeliavimas parodė, kad dujų koncentracija dėl nuskilimo ties tūtos žiotimis sumažėja 15–17 %.

5.2. Dujų čiurkšlių smūginių bangų modeliavimas

7 pav. pateikti Arr3 svyravimo struktūros helio čiurkšlių greičio, temperatūros ir koncentracijos modeliavimo rezultatai esant 30 barų slėgiui. Susikertančių čiurkšlių smūginės bangos suformuoja rombo formos slėgio (7c pav.) ir tankio (7d pav.) erdvinę gardelę. Smūginės bangos turi įtakos ir greitinimui naudojamos sekcijos dujų koncentracijai. Dėl smūginės bangos ši sritis susispaudžia ir sutrumpėja. Svyravimo struktūros sekcijoje smūginės bangos 2 kartus padidina vidurinių tūtų čiurkšlių dujų koncentraciją, palyginti su kraštinėmis tūtomis. Vidurinių tūtų čiurkšlių aukštis virš tūtos žiočių siekia 0,9–1,2 mm, o kraštinių čiurkšlių aukštis – 0,5–0,6 mm. Lazerio pluoštas, sklisdamas skirtingu aukščiu virš tūtos žiočių, praeina pro skirtingos plazmos koncentracijos sritis. 8 pav. pateikti LOA skaitmeninio modeliavimo būdu apskaičiuoti vienos pusės smūginės tūtos azoto dujų molekulinės koncentracijos profiliai. Smūginė banga susiformuoja dėl vienoje pusėje esančios 100 μm aukščio tiesios sienelės prie 300 μm skersmens Lavalio tūtos žiočių ir sukuria neigiamą dujų koncentracijos gradientą. 3D skaitmeninis modeliavimas buvo atliktas naudojant ANSYS Fluent programinę įrangą.

Skaitmeniniai dujų čiurkšlių modeliavimo rezultatai parodė, kad struktūrinius plazmos koncentracijos profilius galima suformuoti naudojant siaurėjančias-platėjančias ir fiksuoto skersmens tūtas bei jų sukuriamas smūgines bangas. Atsižvelgiant į tūtų išsiplėtimo santykį ir 20–60 barų slėgį ir naudojant Lavalio tūtas 400–800 μm atstumu nuo tūtos žiočių galima pasiekti $1 \times 10^{18} – 8 \times 10^{19}$ cm^{-3} čiurkšlių dujų koncentraciją. Lavalio tūtų čiurkšlių dujų koncentracija, tolstant nuo žiočių, krinta lėtai ir sumažėja 1,5–

2 kartus per atstumą, lygų tūtos skersmeniui. Fiksuoto skersmens cilindrinių mikrotūtų čiurkšlių dujų koncentracija ties žiotimis yra didesnė nei Lavalio tūtų ir siekia 2 – 6 × 10^{20} cm^{-3}.

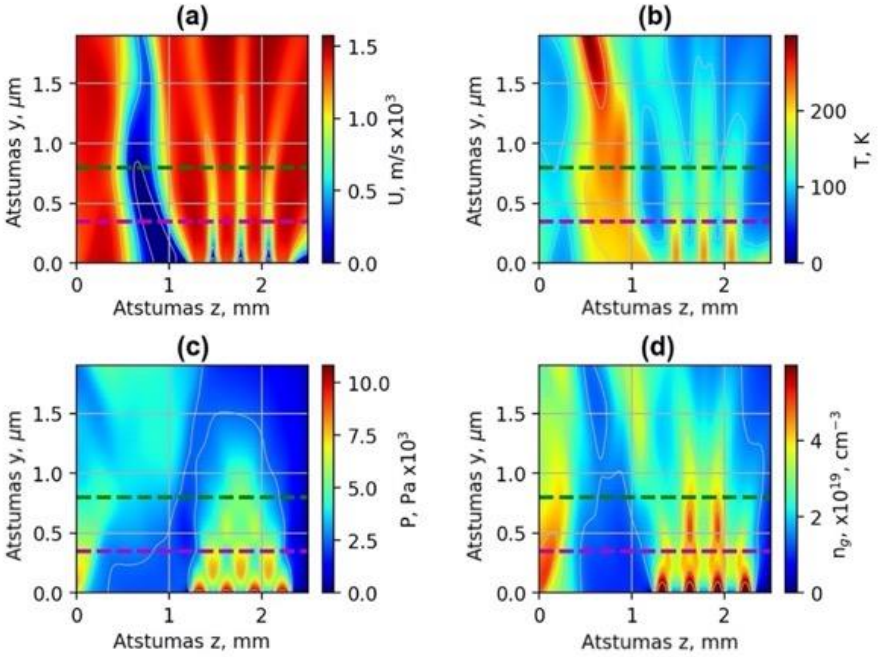

7 pav. Skaitmeninio modeliavimo būdu apskaičiuoti **Arr3** svyravimo struktūros He dujų čiurkšlių greičio **(a)**, temperatūros **(b)**, slėgio **(c)** ir He dujų koncentracijos n_g **(d)** erdviniai skirstiniai esant 30 barų slėgiui. Žalia punktyrinė linija vaizduoja 800 μm, o violetinė punktyrinė linija – 400 μm lazerio pluošto atstumą virš tūtos žiočių [140].

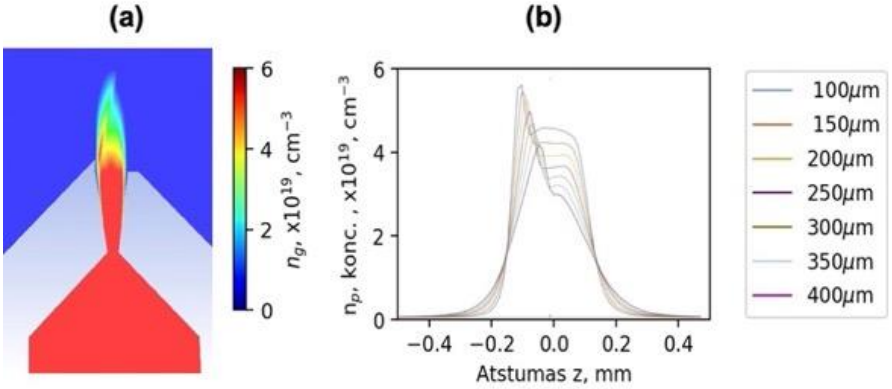

8 pav. 300 μm skersmens vienos pusės smūginės bangos tūtos 2D dujinė molekulinio azoto koncentracija, apskaičiuota naudojant Fluent 3D, esant 50 barų slėgiui **(a)**, ir 1D dujų koncentracijos profiliai esant skirtingiems aukščiams virš tūtos žiočių **(b)** [136].

Tačiau ši koncentracija greitai krinta ir sumažėja eile per atstumą, lygų 4–5 tūtų skersmenims. Ilgesni Lavalio tūtų formuojami mažesnės plazmos koncentracijos profiliai tinka LPG elektronų greitinimui. Fiksuoto skersmens cilindrinės tūtos padeda suformuoti mažų matmenų didelės koncentracijos dujų sritis, smūginių bangų frontus bei injektavimo ir svyravimo struktūrų plazmos koncentracijos profilius.

5.3. Išvados

Struktūrinius plazmos koncentracijos profilius galima suformuoti naudojant mikrotūtų viršgarsines dujų čiurkšles:

- Atsižvelgiant į išilginių ir skersinių plazmos koncentracijos profilių reikalavimus, dujų čiurkšlių koncentracijos skirstiniai gali būti formuojami naudojant siaurėjančias-platėjančias cilindrines, plyšines Lavalio bei fiksuoto skersmens tūtas.
- Injektoriaus ir svyravimo struktūrinius plazmos koncentracijos profilius galima suformuoti naudojant susikertančių viršgarsinių dujų čiurkšlių smūginių bangų arba dujų čiurkšlių smūginių bangų, atsispindėjusių nuo tūtos sienelės, interferenciją.
- Smūginės bangos fronto padėtis apibrėžia neigiamo plazmos koncentracijos gradiento vietą injektoriaus ir svyravimo struktūriniuose plazmos profiliuose.
- Paviršiaus šiurkštumas turi įtakos tūtos kokybei ir čiurkšlės parametrams, kai smiltelių šiurkštumo parametras viršija 1–2 % nuo cilindrinės tūtos skersmens arba Lavalio tūtos kakliuko skersmens.
- Fiksuoto skersmens cilindrinės tūtos kraštų nuskilimas 30° kampu sumažina tūtos žiočių dujų koncentraciją 15–17 %.

6. MIKROTŪTŲ GAMYBA IR CHARAKTERIZAVIMAS

Šiame skyriuje pateikta medžiaga buvo publikuota moksliniuose straipsniuose [A2, A3, A4, A5, A6, A7] ir konferencijų pranešimuose [C1, C2, C3, C4, C5, C6, C7].

6.1. Mikrotūtų gamyba

Lydyto kvarco mikrotūtų struktūrų gamybai buvo sukurtas naujas hibridinis 3D lazerinio apdirbimo technologijos metodas. Tūtos rėmo gamybai buvo naudojamas greitas nanosekundinis medžiagos apdirbimas iš apačios, o didelio tikslumo kanalų formavimui – femtosekundinis lazeriu inicijuoto selektyvaus cheminio ėsdinimo (FLSE – Femtosecond laser-assisted selective etching) būdas (9a pav.). 12–35 mm skersmens kūginis tūtų laikiklio rėmas buvo pagamintas iš ištisinės 6,3–12,7 mm lydyto kvarco plokštės (10 pav.). Po to išilgai kūgio ašies buvo suformuotos mikrometrinių matmenų tūtų struktūros (9a pav., 11 pav.). Nanosekundinio medžiagos apdirbimo iš apačios schema pateikta 9b pav.

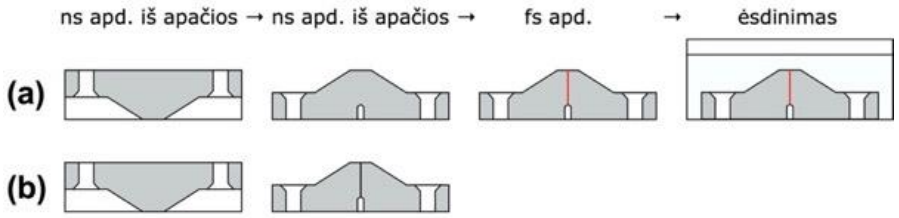

9 pav. Tūtų gamybos schema, naudojant hibridinį lazerinį apdirbimo metodą **(a)** ir nanosekundinį apdirbimą iš apačios **(b)**. Lazerio pluoštas nukreiptas iš viršaus į apačią [156].

Pirmojo hibridinės technologijos etapo metu (9a pav.) apdirbimui buvo naudojama DPSS (Diode-Pumped Solid-State) „Ekspla“ lazerio antroji (532 nm) harmonika. Impulsų FHWM trukmė buvo 4,5 ns. Lazeris veikė 18 W vidutine galia 200 kHz impulsų pasikartojimo dažniu. Lazerio spinduliui XY plokštumoje nukreipti buvo naudojamas „SCANLAB“ galvanometro skeneris intelliSCAN 14. 80 mm objektyvu lazerio spinduliuotė buvo fokusuojama $1/e^2$ lygyje į 10,5 μm skersmens pluoštą. Lazerio impulso energija ir energijos tankis buvo atitinkamai 90 μJ ir 210 J/cm^2. Medžiagos šalinimo greitis buvo didesnis nei 2 mm^3/s.

Antrojo etapo metu (9a pav.) ruošinys buvo apverstas ir suformuotas dujų tiekimo kanalas, paliekant 2 mm storio lydyto kvarco sritį mikrometrinių tūtų struktūrų modifikavimui FLSE būdu. Femtosekundinio „Light Conversion“ Yb: „KGW Pharos“ lazerio bangos ilgis buvo 515 nm, impulsų FHWM trukmė – 300 fs, o impulsų energija < 1 μJ. Pasikartojimo dažnis buvo 500 kHz. Skenuojama buvo 0,5 mm/s greičiu, kad būtų užtikrintas 1 000 impulsų/μm tankis. Lazerio spinduliuotė buvo fokusuojama 100x mikroskopu objektyvu (Mitutoyo, NA = 0,5) į ~ 2 μm skersmens lazerio pluoštą.

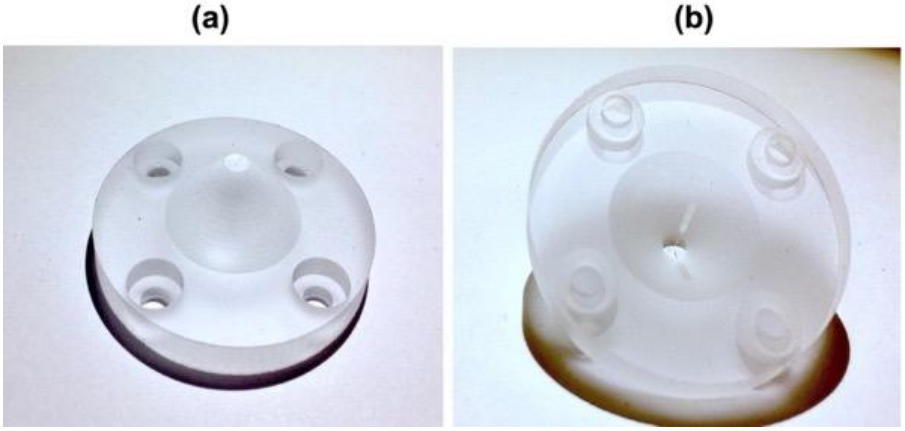

10 pav. 35 mm skersmens ir 12,7 mm aukščio tūtos rėmas **(a)** su 2 mm ilgio 100 μm skersmens cilindrine tūta **(b)**, pagaminta modifikuojant lazeriu lydytą kvarcą ir ėsdinant KOH [139].

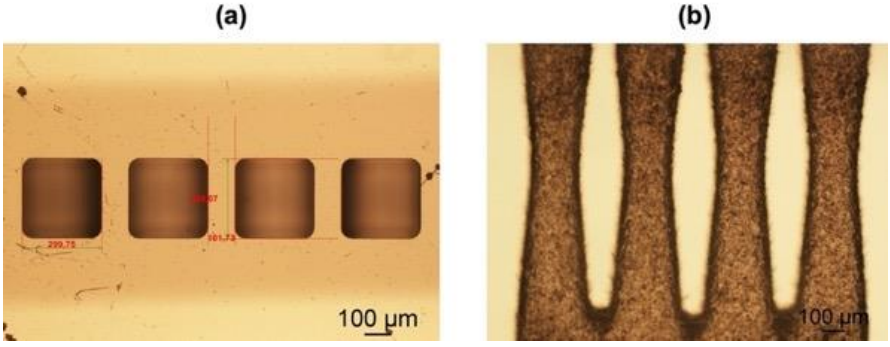

11 pav. 200 μm Lavalio mikrotūtų struktūros, pagamintos naudojant FLSE metodą, vaizdas iš viršaus **(a)** ir pjūvio vaizdas **(b)**, gauti optiniu mikroskopu.

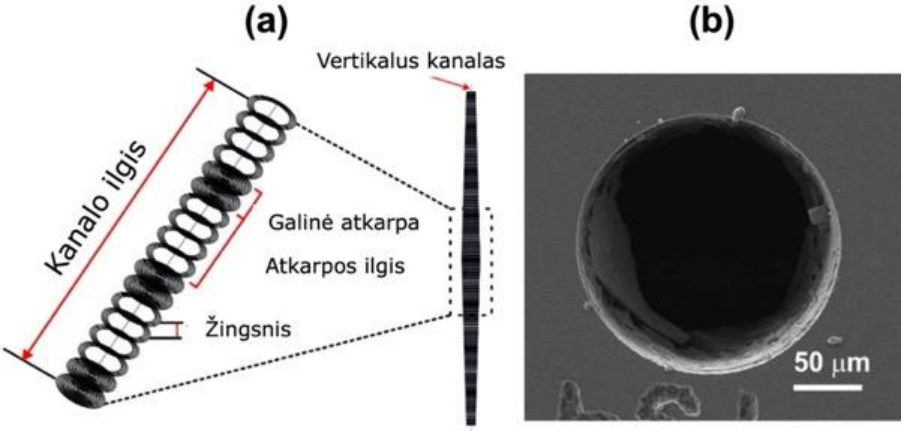

12 pav. FLSE lydyto kvarco modifikacijų struktūra, skirta cheminiam ėsdinimui **(a)**, ir cilindrinės tūtos kanalo SEM vaizdas po 22 h ėsdinimo 10M KOH **(b)** [139].

12a pav. parodyta vertikalaus kanalo lazerinio modifikavimo schema. Kanalas buvo padalintas į 9-ias 230 µm ilgio sekcijas. Kiekvienoje sekcijoje, naudojant XY padėties 300 nm tikslumo (Aerotech ANT150) nustatymo sistemą ir perstumiant bandinį sufokusuoto lazerio pluošto atžvilgiu, lydytame kvarce 4–5 µm žingsniu buvo modifikuojamai koncentriniai apskritimai. Siekiant kompensuoti kūginę vertikalaus kanalo formą, modifikacijos spindulys buvo keičiamas apdirbimo metu. 100 µm skersmens 2 mm ilgio kanalo modifikacija lazeriu užtruko ~ 21 min. 12b pav. parodytas cilindrinės tūtos kanalo SEM vaizdas po 22 h ėsdinimo 10M KOH. Kanalo skersmuo buvo pagamintas +/– 2 µm tikslumu. Ši technologija leido suformuoti 40–50 µm skersmens kanalus. Nanosekundinio medžiagos apdirbimo iš apačios atveju (9b pav.) mažiausio kanalo skersmuo buvo 100 µm.

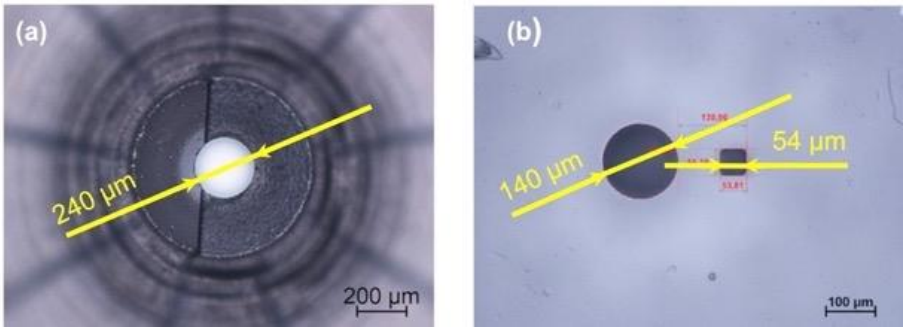

13 pav. LOA eksperimentuose naudotų vienos pusės smūginės bangos tūtos **(a)** ir dvigubos tūtos **(b)**, kurios žiočių skersmuo 140 µm ir 54 µm, pagamintų FLSE metodu, vaizdai, gauti optiniu mikroskopu.

FLSE metodu pagamintų LOA vienos pusės smūginės bangos tūtos ir dvigubos tūtos vaizdai parodyti atitinkamai 13a pav. ir 13b pav. Vienos pusės smūginės bangos tūtos rėmas buvo pagamintas naudojant nanosekundinį apdirbimą iš apačios, o vidinis kanalas buvo suformuotas FLSE metodu. Viršutinis paviršius buvo papildomai apdorotas naudojant femtosekundinę ir pikosekundinę abliaciją, leidžiančią pagerinti paviršiaus šiurkštumą iki 3–5 μm, palyginti su 5 -8 μm nanosekundiniu apdirbimo paviršiaus šiurkštumu.

6.2. Mikrotūtų charakterizavimas

14 pav. parodyti pagamintų tūtų perpjautų mikrotūtų SEM elektroninio mikroskopo paviršiaus vaizdai ir topologijos. Atlikus pradinius dujų tankio ir paviršiaus šiurkštumo matavimus, tūtų, pagamintų nanosekundiniu apdirbimu iš apačios, paviršius buvo papildomai ėsdintas KOH tirpale. Viršutinis nutrupėjęs sluoksnis buvo nupoliruotas ir buvo atkurtas status kampas tarp tūtos sienelių ir žiočių. Po to mikrotūtų profiliai buvo vėl išmatuoti „Veeco“ profilometru „Dektak 150“.

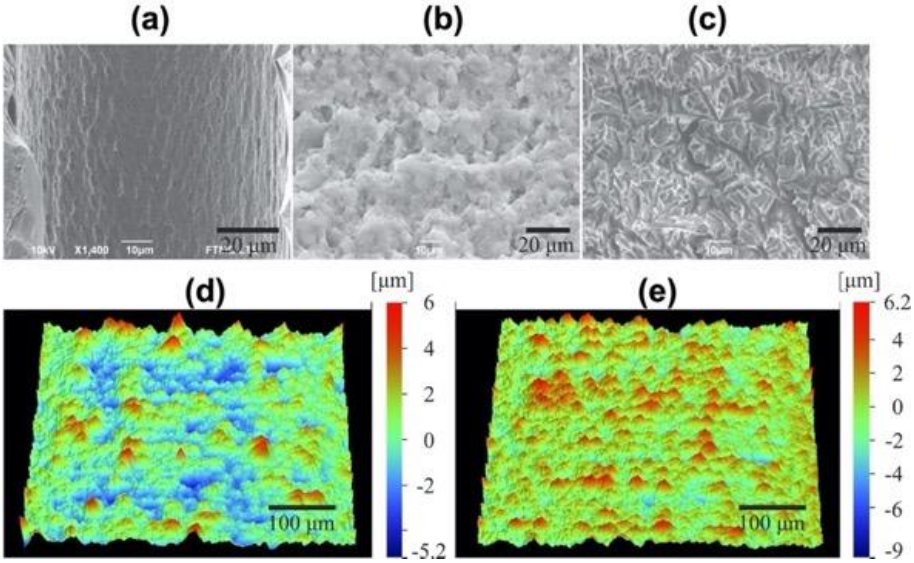

14 pav. Perpjautų mikrotūtų kanalų, pagamintų FLSE metodu **(a)**, nanosekundiniu apdirbimu iš apačios **(b)** ir nanosekundiniu apdirbimu iš apačios su vėlesniu ėsdinimu KOH **(c)**, SEM vaizdai. 0,5 × 0,4 mm^2 ploto tūtų, pagamintų nanosekundiniu apdirbimu iš apačios **(d)** ir nanosekundiniu apdirbimu iš apačios su vėlesniu ėsdinimu KOH **(e)**, paviršiaus topografijos [156].

Mikrotūtų, pagamintų nanosekundiniu apdirbimu iš apačios, šiurkštumo nuokrypio modulio aritmetinis vidurkis buvo R_a = 1,4 μm, o minimalaus ir

maksimalaus paviršiaus aukščio matavimų aritmetinis vidurkis R_{zd} = 8 μm. Po 4 valandų ėsdinimo KOH paviršiaus šiurkštumas padidėjo iki R_a = 1,7 μm ir R_{zd} = 10,4 μm. Smiltelių šiurkštumo parametras k_{rf} buvo lygus atitinkamai ~ 8 μm ir ~ 10 μm. FLSE atveju buvo pasiekti šiurkštumo parametrai R_a = 0,12 μm ir R_{zd} = 0,57 μm. Apskaičiuotas smiltelių šiurkštumo parametras k_{rf}, remiantis R_a ir R_{zd}, vertėmis buvo < 0,7 μm. Paviršiaus smiltelių šiurkštumo parametro k_{rf} vertės, apskaičiuotos naudojant 4 lentelės sąryšius, pateiktos 5 lentelėje.

Macho–Zehnderio interferometru išmatuoti dujų koncentracijos profiliai buvo rekonstruoti naudojant IDEA programinės įrangos paketą ir Abelio transformaciją. Dėl tūtos k_{rf} = 8 μm sienelių šiurkštumo ir tūtos žiočių kraštų nuskilimo 30 laipsnių kampu 100 μm fiksuoto skersmens cilindrinės tūtos, pagamintos naudojant nanosekundinį apdirbimą iš apačios, dujų koncentracija 50–80 μm atstumu nuo tūtos žiočių buvo 25–30 % mažesnė, palyginti su tūtos, pagamintos naudojant FLSE būdą. FLSE metodu pagamintų tūtų sienelės smiltelių šiurkštumas buvo k_{rf} = 0,56 μm. Išmatuota dujų čiurkšlių koncentracija atitinkamai siekė 1,4–2,2 × 10^{20} ir 1,8–3 × 10^{20} cm^{-3}. 200 μm cilindrinės tūtos, pagamintos naudojant nanosekundinį apdirbimą iš apačios, dujų čiurkšlių koncentracija 80–140 μm atstumu nuo tūtos žiočių buvo 15–25 % mažesnė nei naudojant FLSE metodą. Dujų koncentracijos buvo atitinkamai 2,3–4,5 × 10^{20} ir 2,9–5,1 × 10^{20} cm^{-3}.

5 lentelė. Išmatuoti ir apskaičiuoti kanalų paviršiaus šiurkštumo parametrai, remiantis sąryšiais, pateiktais 4 lentelėje [156].

	FLSE	Nanosekundinis apdirbimas iš apačios	Nanosekundinis apdirbimas iš apačios ir ėsdinimas KOH
R_a [μm]	0,12	1,4	1,7
R_{RMS} [μm]		1,7	2,1
R_{zd} [μm]	0,57	8	10,4
k_{rf} @ R_a [μm]	0,70	8,	10,0
k_{rf} @ R_{RMS} [μm]		5,3	6,5
k_{rf} @ R_{zd} [μm]	0,56	7,8	10,2

15ab pav. pavaizduoti Lundo lazerio centre naudotų pavienių 2,25 mm skersmens ir 1,5 mm ilgio plyšinės S1 tūtos rekonstruoti koncentracijos profiliai esant 30 barų argono slėgiui. 2,25 mm skersmens cilindrinė Lavalio tūta suformuoja plokščią 1,5 mm ilgio dujų koncentracijos profilį ir 0,6 mm ilgio koncentracijos didėjimo ir mažėjimo sritis tūtos kraštuose. 1,5 mm ilgio

S1 plyšinė Lavalio tūta turi 0,9 mm ilgio plokščią dujų koncentracijos profilį ir 0,8 mm ilgio koncentracijos didėjimo ir mažėjimo sritis tūtos kraštuose.

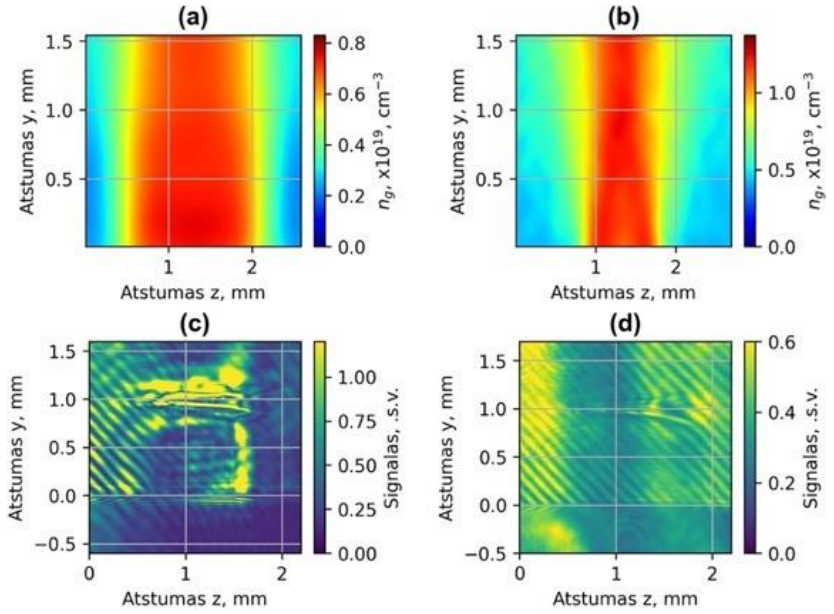

15 pav. Rekonstruoti 2,25 mm skersmens cilindrinės Lavalio tūtos **(a)** ir 1,5 mm ilgio plyšinės Lavalio tūtos **S1 (b)** dujų koncentracijos skirstiniai esant 30 barų slėgiui, išmatuoti naudojant bangos fronto jutiklio fazių diagramas. Pavienės tūtos **S1 (c)** ir **Arr4** injektoriaus struktūros šlynogramos **(d)** [140].

Išmatuota 2,25 mm skersmens cilindrinės Lavalio tūtos ir S1 plyšinės tūtos dujų koncentracija $n_g = 5 \times 10^{18}$ cm^{-3} buvo pasiekta atitinkamai esant 26 ir 18 barų paduodamų dujų slėgiui ir 10 % tikslumu atitiko skaitmeninio modeliavimo rezultatus, pateiktus 5-ame skyriuje. Eksperimento metu helis buvo jonizuotas iki He^{+2}, ir plazmos koncentracija $n_p = 1 \times 10^{19}$ cm^{-3} du kartus viršijo molekulinę dujų koncentraciją. Pavienės tūtos S1 ir Arr4 injektoriaus struktūros šlynogramos esant atitinkamai $n_p = 1 \times 10^{19}$ cm^{-3} ir $n_p = 2 \times 10^{18}$ cm^{-3} parodytos 15c ir 15d pav. 16 pav. parodyti interferenciniai vaizdai, gauti naudojant Wollastono prizmę lazerio pluošto sukurtos plazmos šlynogramų diagnostikai. Arr2 struktūros atveju smūginės bangos buvo stebimos lazerio pluoštui sklindant 800 μm atstumu nuo tūtos žiočių (16a pav.). Arr3 svyravimo struktūros šlynogramos ženkliai skyrėsi priklausomai nuo lazerio pluošto atstumo virš tūtos žiočių. 800 μm atstumu (16b pav.) lazerio pluošto jonizuota sritis buvo siauresnė – 150–200 μm pločio, o smūginės bangos buvo matomos tik Arr3 struktūros centrinėje dalyje. 400 μm atstumu virš tūtos

žiočių (16c pav.) jonizuotos srities plotis padidėjo iki 200–250 μm, ir buvo aiškiai matomi visų struktūros tūtų susikertančių smūginių bangų frontai.

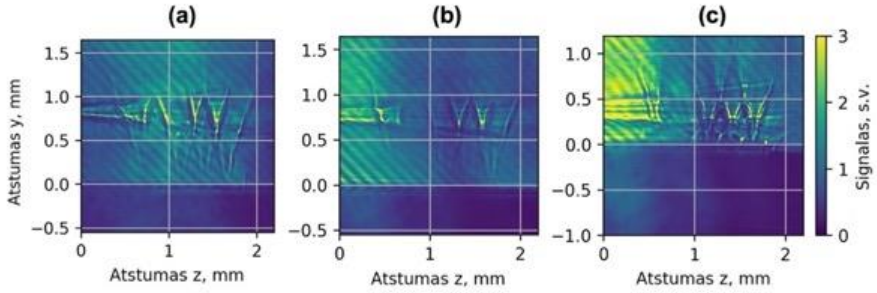

16 pav. Arr2 (a) ir **Arr3** svyravimo struktūrų interferogramos esant n_p=1 × 10^{19} cm^{-3}, lazerio pluoštui sklindant 800 μm **(b)** ir 400 μm **(c)** atstumu virš tūtos žiočių [140].

17a pav. parodytas 300 μm vienos pusės smūginės bangos tūtos, naudotos LOA eksperimentuose, Abelio transformacijos būdu rekonstruotas azoto plazmos koncentracijos profilis.

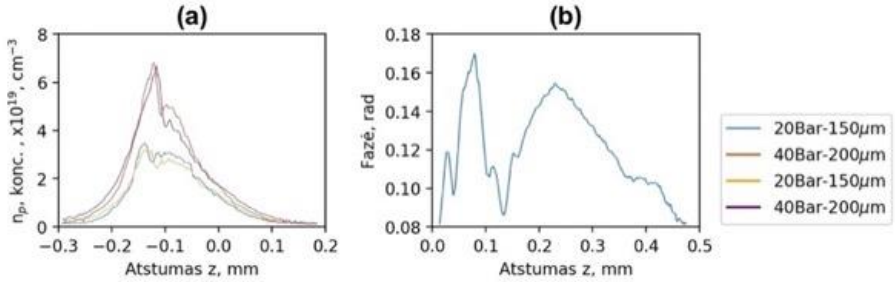

17 pav. LOA eksperimentuose naudotos vienos pusės smūginės bangos 300 μm tūtos čiurkšlių eksperimentiniai N_2 plazmos koncentracijos n_p profiliai esant 20 ir 40 barų slėgiui **(a)**. Išmatuotas dvigubos 54/140 μm tūtos N_2 integralinis fazės profilis esant 30 barų slėgiui **(b)** [136].

Rekonstruoti profiliai patvirtino neigiamo plazmos koncentracijos gradiento susiformavimą. 17b pav. pavaizduotas dvigubos 54/140 μm tūtos N_2 integralinės fazės profilis. Profiliai atitinka tikrąją plazmos koncentraciją, naudotą eksperimentuose, kurių metu azoto L elektronų sluoksnis yra visiškai jonizuotas iki N^{+5} ir apytiksliai 10 kartų viršija molekulinę dujų koncentraciją.

6.3. Išvados

Atsparias optiniams pažeidimams mikrometrinių matmenų tūtų struktūras galima pagaminti iš skaidrių medžiagų, pvz., lydyto kvarco, derinant kelis lazerinio apdirbimo būdus:

- Nanosekundinis lazerinis apdirbimas iš apačios, kurio apdorojimo sparta ~ 2–2,5 mm^3/s, greitai pašalina didelius medžiagos kiekius ir naudoja 18 W vidutinę lazerio galią.
- Nanosekundinio lazerinio apdirbimo iš apačios 5–8 μm paviršiaus šiurkštumo nuokrypis R_{zd} ir tūtos žiočių kraštų nuskilimas riboja šio metodo taikymą mažesnių nei 200–300 μm struktūrų formavimui.
- Nanosekundinio lazerinio apdirbimo iš apačios atveju 100 μm skersmens tūtos žiotyse dujų koncentracija sumažėja 20–30 %, o 200 μm skersmens tūtos žiotyse – 15–25 %, palyginti su FLSE metodu.
- Sienelių šiurkštumas daro reikšmingą įtaką dujų čiurkšlių koncentracijai, kai paviršiaus šiurkštumo nuokrypis R_{zd} viršija 1–2 % nuo tūtos skersmens.
- Femtosekundinė ir pikosekundinė paviršiaus abliacija, palyginti su nanosekundiniu lazeriniu apdirbimu iš apačios, pagerina paviršiaus šiurkštumo nuokrypį R_{zd} iki 3–5 μm.
- Naudojant FLSE metodą, galima suformuoti tūtų kanalus, kurių matmenys yra mažesni nei 40 μm, o paviršiaus šiurkštumo nuokrypis $R_{zd} < 0,7$ μm. Didelių medžiagos kiekių apdirbimui FLSE būdas mažiau efektyvus nei nanosekundinio apdirbimo iš apačios metodas.

7. EKSPERIMENTINIS ELEKTRONŲ GREITINIMAS IR ANTRINĖS SPINDULIUOTĖS ŽADINIMAS

Šiame skyriuje pateikta medžiaga buvo publikuota moksliniuose straipsniuose [A1, A2] ir konferencijų pranešimuose [C1, C2 ir C3].

7.1. Elektronų greitinimas ir spinduliuotės žadinimas

Eksperimentiniai LPG elektronų greitinimo ir betatrono spinduliuotės žadinimo darbai buvo atlikti Lundo lazerių centre. Sufokusuoto lazerio pluošto intensyvumas atitiko lazerio lauko stiprio parametrą $a_0 \simeq 4{,}0$. Pagreitintų elektronų krūvio energijos ir skėsties erdviniai skirstiniai pateikti 18 pav. Elektronų energijos spektras, greitinimo elektronų skėstis ir krūvis buvo matuojami naudojant magnetinį spektrometrą ir „Lanex“ scintiliacijos ekraną.

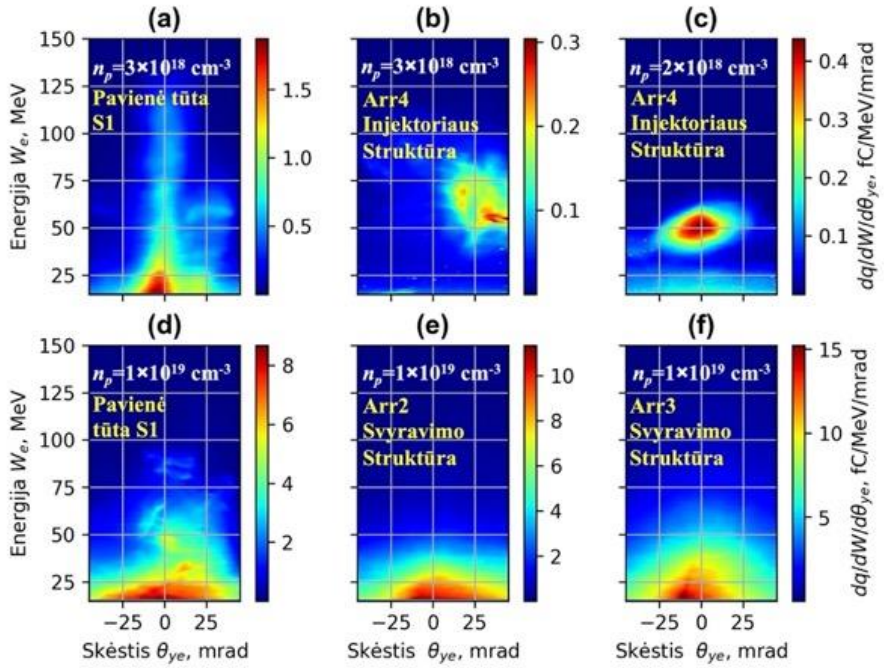

18 pav. Pavienės **S1** tūtos $n_p = 3 \times 10^{18}$cm^{-3} He + 1 % N_2 mišinio **(a)** ir **Ar4** injektoriaus struktūros gryno He **(b)** bei $n_p = 2 \times 10^{18}$ cm^{-3} He + 1 % N_2 mišinio **(c)** elektronų krūvio ir energijos suvidurkinti erdviniai skirstiniai. Pavienės **S1** tūtos $n_p = 1 \times 10^{19}$ cm^{-3} He + 1 % N_2 mišinio **(d)** ir **Arr2 (e)** bei **Arr3**, lazerio pluoštui sklindant 400 μm atstumu virš tūtos žiočių, **(f)** svyravimo struktūrų elektronų krūvio ir energijos suvidurkinti erdviniai skirstiniai [140].

18 pav. pateikti suvidurkintų 10-ies lazerio impulsų S1 tūtos ir Arr2, Arr3, Arr4 struktūrų elektronų energijos ir krūvio erdvinių skirstinių eksperimentiniai duomenys. Didžiausia pagreitintų elektronų energija ir mažiausia skėstis buvo gautos esant nedideliam 5–12 barų He + 1 % N_2 dujų slėgiui bei naudojant pavienę S1 tūtą (18a pav.). Naudojant Arr4 injektoriaus struktūrą bei esant 5–7 barų gryno He slėgiui buvo stebimi 50–80 MeV elektronų pluoštai (18b pav.), susiformuojantys dėl neigiamo plazmos koncentracijos gradiento elektronų injekcijos. Šis dujų slėgis apytiksliai atitinka plazmos koncentraciją $n_p = 3\times 10^{18}\text{cm}^{-3}$. Atskirų elektronų pluoštų energijos dispersija buvo nedidelė – 5–10 MeV, tačiau pagreitinto krūvio dydis ir erdvinis skirstinys keitėsi nuo impulso prie impulso ir tai padidino suvidurkinto 10-ies impulsų energijos skirstinio dispersiją. (18a,c–f pav.) eksperimentų metu vieno impulso erdvinis krūvio skirstinys ir elektronų pluošto skėstis iš esmės nesiskyrė nuo 10-ies impulsų vidurkio. Naudojant Arr4 injektoriaus struktūrą ir 1,5 karto mažesnį nei gryno helio He + 1 % N_2 mišinio paduodamų dujų slėgį, krūvio injekcija buvo stabilesnė. Šiuo atveju buvo išmatuoti 4–5 pC ir 50 ± 10 MeV kvazimonoenergetiniai elektronų pluoštai (18c pav.). Esant didesniam 21–26 barų slėgiui bei greitinimui naudojant S1 tūtą ir Arr2–Arr3 svyravimo struktūras, buvo injektuojamas didesnis elektronų kiekis ir pluošto skėstis padidėjo (18d–f pav.). 18 barų slėgis S1 tūtos, Arr2, Arr4 struktūrų atveju ir 26 barų slėgis Arr3 struktūros atveju apytiksliai atitinka plazmos koncentraciją $n_p = 1\times 10^{19}\,\text{cm}^{-3}$. Svyravimo struktūra padidino vidutinę elektronų pluošto skėstį ir betatrono spinduliuotės žadinimo efektyvumą (18ef pav.).

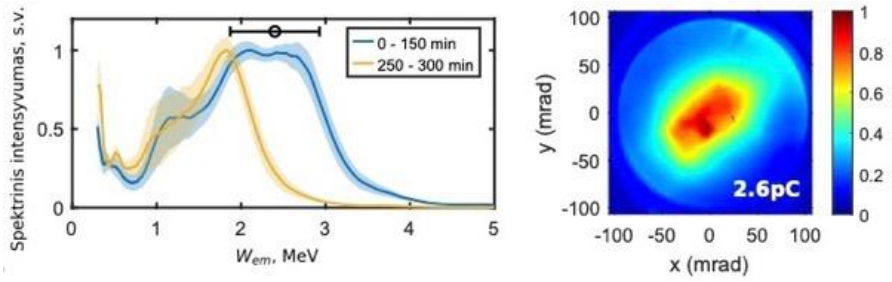

19 pav. 300 μm vienos pusės smūginės tūtos LOA 3,8 mJ 4 fs 1 kHz lazerio pagreitintų elektronų energijos spektrinio intensyvumo **(a)** ir krūvio **(b)** skirstinio profiliai [136]. Šešėlio zona parodo standartinį nuokrypį, o paklaidų juosta rodo spektrometro rezoliuciją **(a)**.

19 pav. pavaizduotas LOA 0,8 TW 4 fs 1 kHz lazeriu pagreitintų elektronų energijos spektrinio intensyvumo ir krūvio skirstinys, kurio stabilumą 5 valandas trunkančio eksperimento metu užtikrino 300 μm vienos pusės

smūginės tūtos (OSS) neigiamo plazmos koncentracijos gradiento elektronų injekcija. Elektronų energija buvo 2–3 MeV, o suvidurkintas 200 lazerio impulsų pagreitintų elektronų krūvis apie 2,6 pC. Lydyto kvarco tūtos pasižymėjo dideliu atsparumu pažeidimams ir patikimai veikė po 3–5 × 10^7 lazerio impulsų eksploatacijos.

Eksperimentinė Rentgeno spinduliuotės priklausomybė nuo paduodamų dujų slėgio pateikta 20–21 pav. Lazerio impulso Rentgeno fotonų skaičius didėjo kartu su elektronų vidutinės energijos, pagreitintų elektronų krūvio ir elektronų pluošto skėsties didėjimu. Injektuotas elektronų krūvis modifikuoja elektrinį lauką plazmos burbulo viduje, ir vidutinė elektronų energija pradeda kristi. 1,5 mm pavienės tūtos S1 atveju, esant mažam 9–11 barų paduodamų dujų slėgiui, vidutinė elektronų energija buvo didžiausia ir siekė 46 MeV. Pagreitintų elektronų krūvis buvo mažas, apie 30 pC, o skėstis siekė 30 mrad. Rentgeno spinduliavimo intensyvumas buvo mažas. Efektyviausiai Rentgeno spinduliuotė buvo žadinama esant 16–18 barų paduodamų dujų slėgiui (20ab pav.), kai 60–80 pC pagreitintų elektronų krūvis buvo artimas maksimaliam, elektronų pluošto skėstis padidėjo iki 75–85 mrad, o 35–40 MeV vidutinė elektronų energija buvo artima maksimaliai šio injektuoto krūvio pasiekiamai energijai.

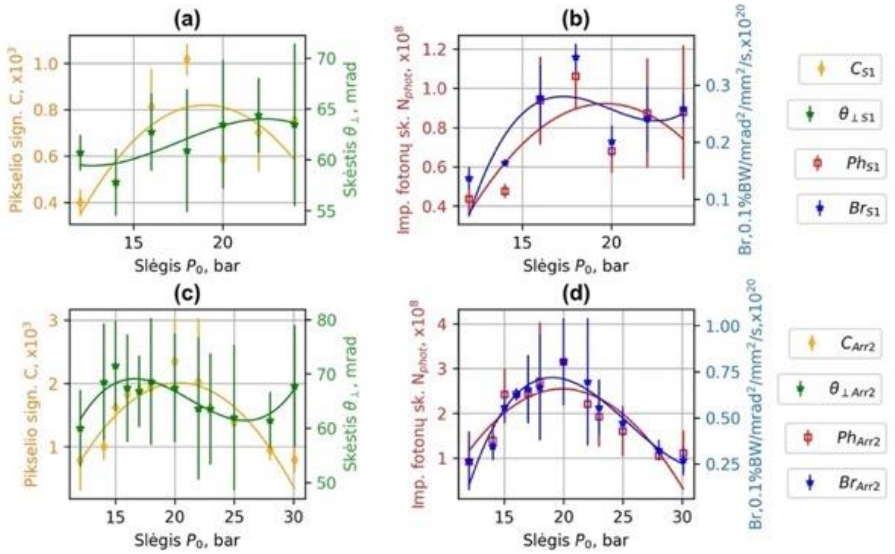

20 pav. Eksperimentinė Rentgeno spinduliuotės pikselio signalo C, skėsties $\theta_{\perp}$ (FHWM) (**a, c**), impulso fotonų skaičiaus N_{phot} ir ryškio Br (**b, d**) priklausomybė nuo paduodamų dujų slėgio. $\boldsymbol{C_{S1}}$, $\boldsymbol{\theta_{\perp S1}}$, $\boldsymbol{Ph_{S1}}$, $\boldsymbol{Br_{S1}}$ atitinka pavienės tūtos **S1**, o $\boldsymbol{C_{Arr2}}$, $\boldsymbol{\theta_{\perp Arr2}}$, $\boldsymbol{Ph_{Arr2}}$, $\boldsymbol{Br_{Arr2}}$ – **Arr2** svyravimo struktūros parametrus. Ištisinės linijos vaizduoja matavimo rezultatų interpoliacines kreives [140].

Toliau didinant dujų slėgį, elektronų skėstis irgi didėjo. Nukritus elektronų energijai ir sumažėjus pagreitintų elektronų krūviui, sumažėjo Rentgeno spinduliuotės intensyvumas. Esant mažesniam 15 barų slėgiui Arr2 svyravimo struktūra elektronų pluošto skėstį pavienės S1 tūtos atžvilgiu padidino 40 % nuo 40 mrad iki 60 mrad. Esant 20 barų slėgiui vidutinė S1 ir Arr2 elektronų skėstis buvo panaši, tačiau Arr2 atveju buvo stebimas 20 % elektronų krūvio (W_e > 40 MeV) padidėjimas ir vidutinės energijos sumažėjimas. Esant 18–22 barų slėgiui svyravimo struktūra pavienės S1 tūtos atžvilgiu lazerio impulso Rentgeno fotonų skaičių N_{ph} bei ryškį padidino 2–3 kartus (20cd pav.). Impulso fotonų skaičius (FWHM) lygyje padidėjo nuo 1,1 × 10^8 iki 2,9 × 10^8, o šaltinio ryškis nuo 0,3 × 10^{20} iki 0,7 × 10^{20} fotonų/s/mrad^2/mm^2/0,1 % JP.

2,25 mm cilindrinės tūtos Arr3 svyravimo struktūros atveju (21 pav.) elektronų greitinimo atstumas buvo 1,5 karto ilgesnis nei S1 ir Arr2 atveju. Dėl to buvo pasiekta didesnė pagreitintų elektronų energija. Arr3 dujų čiurkšlės išsiplėtimo koeficientas, palyginti su S1 ir Arr2, buvo didesnis. Didžiausia Rentgeno spinduliuotės vertė buvo pasiekta esant 24–26 barų paduodamų dujų slėgiui.

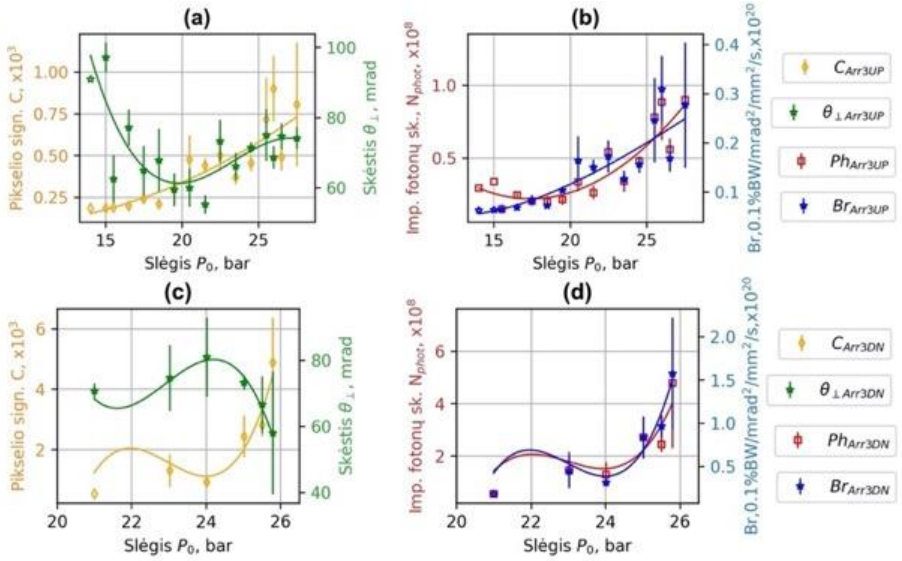

21 pav. Eksperimentinė Rentgeno spinduliuotės pikselio signalo C, skėsties $\theta_\perp$ (FHWM) (**a, c**), impulso fotonų skaičiaus N_{phot} ir ryškio Br (**b, d**) priklausomybė nuo paduodamų dujų slėgio. $\boldsymbol{C_{Arr3UP}}$, $\boldsymbol{\theta_{\perp Arr3UP}}$, $\boldsymbol{Ph_{Arr3UP}}$, $\boldsymbol{Br_{Arr3UP}}$ atitinka svyravimo struktūros **Arr3** parametrus, lazerio pluoštui sklindant 800 μm, o $\boldsymbol{C_{Arr3DN}}$, $\boldsymbol{\theta_{\perp Arr3DN}}$, $\boldsymbol{Ph_{Arr3DN}}$, $\boldsymbol{Br_{Arr3DN}}$ – 400 μm virš tūtos žiočių. Ištisinės linijos vaizduoja matavimo rezultatų interpoliacines kreives [140].

Didinant slėgį nuo 15 iki 28 barų ir lazerio pluoštui sklindant 800 μm virš Arr3 struktūros žiočių, elektronų krūvis ($W_e > 40$ MeV) nuolat didėjo, tačiau neviršijo 30 pC. Vidutinė elektronų energija sumažėjo nuo 50 MeV iki 32 MeV, o skėstis padidėjo nuo 20 iki 80 mrad. Didinant paduodamų dujų slėgį nuo 20 iki 28 barų, didėjo ir lazerio impulso Rentgeno fotonų skaičius N_{ph}, Rentgeno spinduliuotės skėstis bei ryškis (21ab pav.). Lazerio pluoštui sklindant 400 μm virš Arr3 struktūros žiočių, buvo užfiksuotas žymus elektronų krūvio padidėjimas iki 100 pC, o vidutinė energija išaugo nuo 36 MeV iki 43 MeV. Elektronų pluošto skėstis išliko to paties 80 mrad lygio kaip ir 800 μm atstumo atveju. Sumažinus atstumą tarp struktūros žiočių ir lazerio pluošto iki 400 μm, esant 25–26 barų dujų slėgiui pagreitintų elektronų krūvis padidėjo 4 kartus, o lazerio impulso Rentgeno fotonų skaičius N_{ph} ir ryškis padidėjo 5 kartus (21cd pav.). Fotonų skaičius padidėjo nuo $1{,}0 \times 10^8$ iki $5, \times 10^8$, o šaltinio ryškis nuo $0{,}3 \times 10^{20}$ fotonų/s/mrad^2/mm^2/0,1 % JP iki $1{,}6 \times 10^{20}$ fotonų/s/mrad^2/mm^2/0,1 % JP.

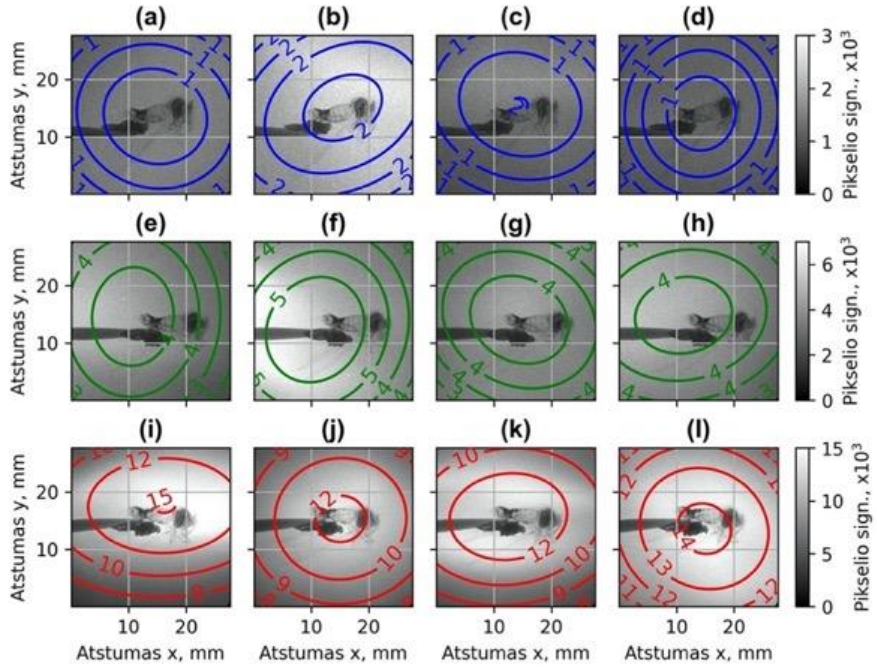

22 pav. Būdingų Rentgeno spinduliuotės Gauso skirstinių vaizdai, elektronų greitinimui naudojant pavienę tūtą **S1** (**a–d**) ir svyravimo struktūras **Arr2** (**e–h**) bei **Arr3** (**i–l**), lazerio pluoštui sklindant 400 μm atstumu virš tūtos žiočių [140].

Dujų tiekimo sistemos apribojimai neleido toliau didinti paduodamų dujų slėgio, todėl duomenų apie galimą Rentgeno spinduliuotės sumažėjimą toliau didinant paduodamų dujų slėgį negauta. Arr2 ir Arr3 (400 μm virš tūtos

žiočių) struktūrų atveju, esant paduodamų dujų slėgiui, atitinkančiam didžiausią Rentgeno spinduliuotės žadinimo intensyvumą, buvo pastebėtas Rentgeno spinduliuotės 15–30 % (FHWM) skėsties sumažėjimas (20c pav., 21c pav.).

S1 tūtos, Arr2 ir Arr3 struktūrų būdingi Rentgeno spinduliuotės erdviniai skirstiniai parodyti 22 pav. Eksperimento metu erdvinis Rentgeno spinduliuotės intensyvumo skirstinys x ir y kryptimis keitėsi nuo simetrinio apskritimo iki elipsės, kurios orientacijos kampas keitėsi nuo impulso prie impulso. Arr3 struktūros Rentgeno spinduliuotės skirstinys, lazerio pluoštui sklindant 400 μm atstumu virš tūtos žiočių, vidutiniškai buvo ilgesnis x koordinatės kryptimi, atitinkančia lazerio poliarizaciją.

Betatrono Rentgeno šaltinio spindulio dydis keitėsi nuo 3,5 ± 1 μm esant 11 barų dujų slėgiui S1 pavienės tūtos atveju iki 7,5 ± 1 μm esant 29 barų dujų slėgiui Arr2 struktūros atveju. Esant 15–26 barų slėgiui, atitinkančiam didžiausią Rentgeno spinduliuotės žadinimo efektyvumą, betatrono šaltinio spindulys buvo vidutiniškai 5 ± 1 μm horizontalia ir vertikalia kryptimis. Ši fiksuota betatrono šaltinio spindulio vertė buvo panaudota Rentgeno šaltinio ryškiui apskaičiuoti. Pavienės tūtos S1 ir Arr2 struktūros betatrono spinduliuotės sinchrotrono kritinė energija buvo 2,3–2,5 ± 0,1 keV, o Arr3, lazerio pluoštui sklindant 800 μm ir 400 μm atstumu nuo tūtos žiočių, struktūros – atitinkamai 2,2 keV ± 0,2 keV ir 2,6 keV ± 0,1 keV.

7.2. Antrinės spinduliuotės taikymas medžiagotyroje

Antriniai LPG elektronų betatrono šaltiniai buvo panaudoti biologinių objektų ir polimerinės folijos vaizdinimui praeinančia Rentgeno spinduliuote. 23b–d pav. pateikti pavienės tūtos S1 (23b pav.) ir svyravimo struktūrų Arr2 (23c pav.) bei Arr3 (23d pav.) naktinio drugelio vaizdai, gauti praeinančia Rentgeno spinduliuote. 24b pav. parodyti polimerinės folijos vaizdai, gauti praeinančia Rentgeno spinduliuote, naudojant svyravimo struktūrą Arr2.

Iš 23b–d pav. vaizdų matyti, kad, didėjant lazerio impulso Rentgeno fotonų skaičiui ir šaltinio ryškiui, vaizdo kokybė pagerėja. Dėl didesnio Rentgeno spindulių srauto, kurį sukuria didesnės energijos elektronai, Arr3 struktūros sukuriamas vaizdas turi mažiau triukšmo nei Arr2 struktūros vaizdas. 25a–c pav. parodyti vaizdai, naudoti Rentgeno šaltinio sukuriamo vaizdo skiriamajai gebai įvertinti. 25bc pav. matomos mažo, apytiksliai 20 μm skersmens, drugelio kojos kontūrai ir plaukai. Drugelis buvo padėtas už vakuumo kameros lango 6 cm atstumu prieš Rentgeno detektorių. Vaizdas buvo didinamas 1,08 karto, o vaizdo skiriamąją gebą ribojo 13,5 μm detektoriaus pikselio dydis.

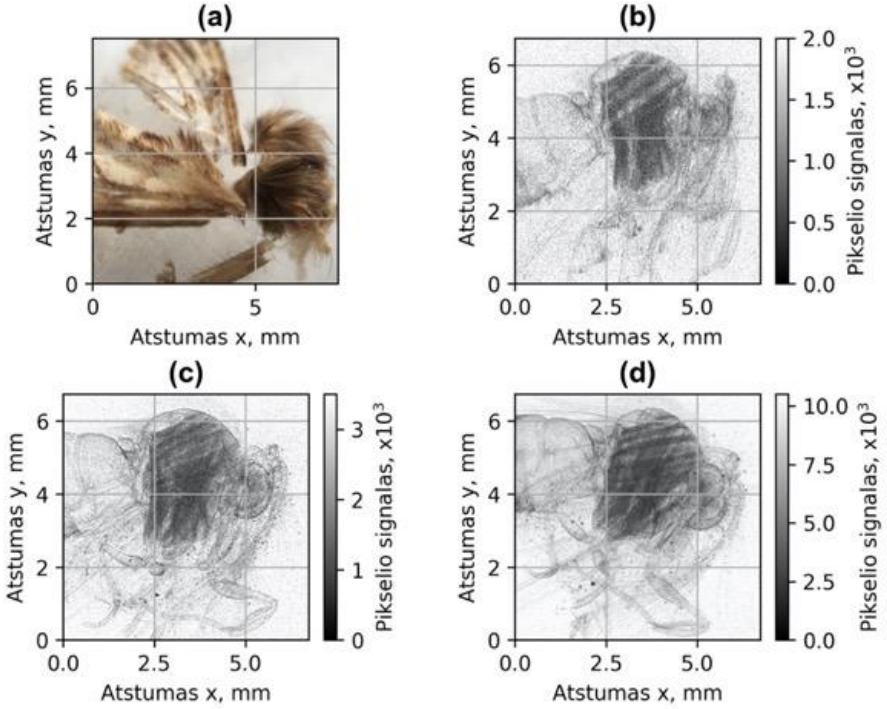

23 pav. Naktinio drugelio vaizdai, gauti optiniu mikroskopu **(a)** ir praeinančia Rentgeno spinduliuote **(b–d)**, suvidurkinus 10 lazerio impulsų esant $a_0 = 4{,}0$ ir $n_p = 1 \times 10^{19}$ cm^{-3}, naudojant pavienę tūtą **S1 (b)** ir **Arr2 (c)** bei **Arr3** svyravimo struktūras, lazerio pluoštui sklindant 400 μm atstumu virš tūtos žiočių **(d)** [140].

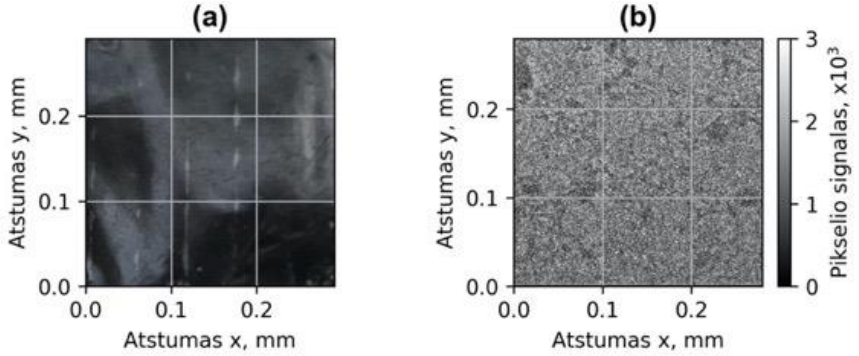

24 pav. 40 μm storio polimerinės folijos vaizdai, gauti optiniu mikroskopu **(a)** ir praeinančia Rentgeno spinduliuote **(b)**, suvidurkinus 10 lazerio impulsų, naudojant **Arr2** svyravimo struktūrą.

25d pav. parodytas sukryžiuotų volframo vielų, išdėstytų 70 cm atstumu nuo detektoriaus, vaizdas. Vaizdo didinimas buvo 26 kartai. Gauso skirstinio aproksimacijos atveju 10 μm šaltinio skersmens (FWHM) apskaičiuota

vaizdo skiriamoji geba buvo 9 μm. Šie antrinės LPG elektronų betatrono Rentgeno spinduliuotės šaltiniai gali būti naudojami minkštųjų audinių fazinio kontrasto vaizdavimui ir tomografijai.

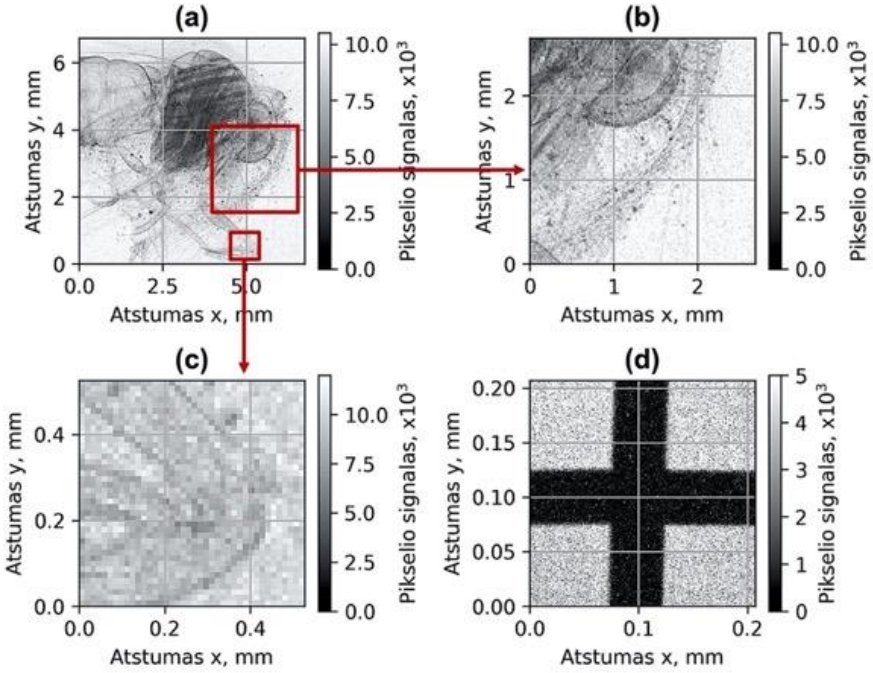

25 pav. Drugelio **(a–c)** ir 50 μm sukryžiuotų volframo vielų **(d)** vaizdai, gauti praeinančia Rentgeno spinduliuote, suvidurkinus 10 lazerio impulsų. Vaizdai buvo panaudoti **Arr3** svyravimo struktūros Rentgeno šaltinio sukuriamo vaizdo skiriamajai gebai įvertinti, lazerio pluoštui sklindant 400 μm atstumu virš tūtos žiočių [140].

LPG eksperimentai patvirtino skaitmeninio modeliavimo rezultatus. Suderinus lazerio impulso ir plazmos koncentracijos parametrus, nuskurdinto elektronais plazmos burbulo režimu pasiekiama didžiausia pagreitintų elektronų energija. Dėl mažos elektronų pluošto skėsties Rentgeno spinduliuotės išeiga buvo maža. Didinant plazmos koncentraciją, pagreitintų elektronų energija sumažėjo, tačiau dėl padidėjusios skėsties padidėjo betatrono spinduliuotės srautas.

Naudojant injektoriaus struktūros plazmos koncentracijos profilį Arr4 ir jonizacijos injektuotus elektronus buvo pagreitinti kvazimonoenergetiniai 4–5 pC krūvio 50 ± 10 MeV energijos elektronų pluoštai (18c pav.). Didinant plazmos koncentraciją ir naudojant svyravimo struktūras Arr2, Arr3, padidėjo pagreitintų elektronų krūvis ir skėstis (18d–f pav.). Arr2, Arr3 struktūrų (16 pav.) plazmos šlynogramos ir Arr2 dujų čiurkšlių modeliavimo rezultatai (7cd pav.) parodė, kad elektronų injekciją ir skėsties didėjimą lėmė smūginių

bangų suformuota dujų koncentracijos profilio struktūra. Skaitmeninio LPG modeliavimo rezultatai parodė, kad svyravimo struktūros panaudojimas esant $n_p = 1 \times 10^{19}$ cm^{-3} padidina pagreitintų elektronų skėstį (3cd pav., 4a pav.) 30–50 %. Daugiau elektronų turi didesnę kritinę sinchrotrono spinduliuotės energiją ir jų indėlis į bendrą Rentgeno spinduliuotę yra didesnis (4cd pav.). Skaitmeninio modeliavimo metu apskaičiuotas 1–2 μm betatrono šaltinio spindulys buvo mažesnis (4b pav.) nei eksperimentiškai išmatuoto 5 ± 1 μm betatrono šaltinio spindulys. Skirtumą tarp apskaičiuoto ir eksperimentiškai išmatuoto betatrono Rentgeno šaltinio spindulio galima paaiškinti daug didesne elektronų pluošto skėstimi, atitinkančia platesnį > 50 μm elektronų skirstinio spindulį 2,5 mm greitinimo atstumu. Suminis Rentgeno spinduliuotės spektras ir šaltinio dydis susideda iš skirtingų energijų elektronų, esančių skirtingose erdvinėse padėtyse, spinduliuočių. Išmatuotą Rentgeno spinduliuotės maksimumą nulemia didesnės energijos elektronai, išsidėstę apytiksliai 5 μm spinduliu. Intensyvesnė Rentgeno spinduliuotė iš centrinės 5 μm spindulio srities taip pat galėtų paaiškinti spinduliuotės skėsties sumažėjimą esant dujų slėgiui, atitinkančiam didžiausią spinduliuotės intensyvumą. Elektronai, pasiskirstę 50 μm spinduliu, turi mažesnę energiją ir jų indėlis į kelių keV fotonų energijos Rentgeno spinduliuotę yra mažesnis.

Mažas betatrono Rentgeno spinduliuotės šaltinio dydis ir femtosekundinė impulso trukmė suteikia naujų diagnostikos galimybių. Klinikinės kompiuterinės tomografijos erdvinė skiriamoji geba paprastai siekia apie milimetrą. Rentgeno mikrokompiuterinės tomografijos (μCT) skiriamoji geba yra mažesnė, apie 100 μm. Tačiau μCT spinduliuotės intensyvumas yra ribotas dėl mažos milimetrinio dydžio Rentgeno lempos anodo išsilydymo srovės. LPG žadinamos Rentgeno spinduliuotės šaltinių erdvinė skiriamoji geba – keletas mikronų. Betatrono spinduliuotė leidžia tirti dinaminius fizinius procesus femtosekundžių tikslumu. Didelio intensyvumo lazerio spinduliuotė sužadina dominantį mėginį, o antrinė spinduliuotė naudojama pereinamųjų procesų tyrimui taikant Rentgeno absorbcijos spektroskopiją (XAS), Rentgeno absorbcijos krašto struktūrą (XANES) ar išplėstinės Rentgeno absorbcijos smulkiąją struktūrą (EXAFS) [185]. Femtosekundinė Rentgeno kristalografija leidžia tirti biologinių ir cheminių struktūrų virpesių momentines atomų padėtis, fazinius virsmus tarp amorfinės, kristalinės ar skystosios būsenos ir ekstremalius šiltosios tankios materijos (WDM) procesus [186].

LPG pagreitinti elektronų pluoštai gali būti naudojami didelės energijos MeV spinduliuotei žadinti naudojant Komptono sklaidą ar stabdymą tankiose medžiagose. Subkritinės koncentracijos mikrometrinės plazmos struktūros

gali būti taikomos jonų greitinimui lazerių sistemose, veikiančiose dideliu pasikartojimo dažniu.

Labai didelės energijos 50–200 MeV elektronų (VHEE) pluoštus galima panaudoti didelės momentinės dozės spartos blyksnio (FLASH) radioterapijai. Sinchrotronų ir tiesinių LINAC pagreitinti VHEE elektronų pluoštai leidžia pasiekti 10–20 Gy vienkartines radiacijos dozes, kurių vidutinė sparta 30–100 Gy/s. Medicininiai linijiniai greitintuvai pagreitina elektronų pluoštus nuo 5 iki 20 MeV, o jų dozės sparta siekia 0,03–0,05 Gy/s. Didelę jų energijos dalį sugeria oda. Tokios energijos elektronai naudojami tik paviršinių navikų gydymui. Dėl reliatyvistinio poveikio padidėjusi VHEE inercija sumažina elektronų sklaidą ir suteikia galimybę apšvitinti 15 cm gylyje esančias vėžines ląsteles. Keletas ikiklinikinių tyrimų rodo, kad didelės spartos (~ 40 Gy/s) VHEE dozė turi efektyvų terapinį poveikį navikams ir apsaugo sveikus plaučių ir smegenų audinius [189]. Praktinį FLASH gydymo metodo taikymą riboja didelės energijos greitintuvų trūkumas. LPG galėtų būti ekonomiška VHEE radioterapijos alternatyva. 200 TW lazerio 50–250 MeV vieno impulso elektronų pluošto dozė yra cGy dydžio, o momentinė dozės sparta ~ 10^{13} Gy/s [196]. 40 Gy/s FLASH dozės spartai pasiekti reikia lazerinių sistemų, veikiančių kHz pasikartojimo dažniu ir stabiliai greitinančių vienodos energijos elektronų pluoštus. Stabilaus elektronų greitinimo LOA 4 TW 1 kHz lazerine sistema rezultatus [136] galima panaudoti kuriant kompaktiškas LPG FLASH radioterapijos sistemas.

7.3. Išvados

Eksperimentinių bandymų metu buvo patvirtinta, kad, naudojant struktūrinius plazmos koncentracijos profilius, galima valdyti elektronų injekciją ir padidinti lazerio generuojamų Rentgeno fotonų skaičių, betatrono spinduliuotės kritinę energiją ir ryškį.

- Naudojant injektoriaus mikrotūtų struktūrą ir derinant neigiamo plazmos koncentracijos gradiento bei jonizacijos elektronų injekciją, buvo pagreitinti 4–5 pC krūvio 50 ± 10 MeV energijos kvazimonoenergetiniai elektronų pluoštai.
- Naudojant 40 TW 35 fs lazerį Lundo lazerio centre elektronai buvo pagreitinti iki 30–150 MeV energijos, o vienas lazerio impulsas sužadino $1{,}0 \times 10^8$–$5{,}5 \times 10^8$ betatrono Rentgeno spinduliuotės fotonų.
- Naudojant svyravimo struktūros plazmos koncentracijos profilius, palyginti su pavienės tūtos formuojamu plazmos profiliu, lazerio impulso Rentgeno fotonų skaičius ir ryškis padidėjo 2–3 kartus,
- Išmatuotas betatrono Rentgeno šaltinio dydis vidutiniškai siekė 3–7 μm.
- Šaltinio dydžio apribota Rentgeno spinduliuotės vaizdo skiriamoji geba buvo 9 μm.
- Naudojant 0,8 TW 4 fs 1 kHz lazerį 1–2,6 pC krūvio elektronų pluoštai buvo pagreitinti iki ~ 2–3 MeV. Lazerio sistema stabiliai veikė nepertraukiamu režimu 5 valandas.
- Lydyto kvarco mikrotūtos pasižymėjo dideliu atsparumu optiniams pažeidimams ir patikimai veikė po $3–5 \times 10^7$ lazerio impulsų eksploatacijos.

PAGRINDINĖS IŠVADOS

1. Skaitmeninis modeliavimas ir eksperimentiniai rezultatai patvirtino, kad LPG pagreitintų elektronų pluošto krūvio kiekį galima padidinti ir energijos sklaidą galima sumažinti naudojant injektoriaus struktūros plazmos koncentracijos profilį bei derinant neigiamo plazmos koncentracijos gradiento ir jonizacijos injekciją.
2. Naudojant svyravimo struktūros plazmos koncentracijos profilius, skersinė elektronų skėstis, palyginti su pavienės tūtos formuojamu plazmos profiliu, esant $a_0 = 4{,}0$ ir $n_p = 1 \times 10^{19}$ cm^{-3} padidėjo 30–50 %, o lazerio impulso betatrono Rentgeno spinduliuotės fotonų skaičius padidėjo 2–3 kartus.
3. Dujų dinamikos skaitmeninis modeliavimas ir interferometriniai matavimai patvirtino, kad struktūrinius plazmos koncentracijos profilius galima suformuoti naudojant siaurėjančių-platėjančių ir fiksuoto skersmens mikrotūtų viršgarsinių čiurkšlių susikertančių smūginių bangų interferenciją.
4. Atsparias optiniams pažeidimams mikrometrinių matmenų tūtų struktūras galima pagaminti iš skaidrių medžiagų, pvz., lydyto kvarco, derinant kelis lazerinio apdirbimo būdus: nanosekundinį medžiagos apdirbimą iš apačios, pikosekundinę ir femtosekundinę abliaciją bei aukšto tikslumo femtosekundinio lazerio inicijavimo ir selektyvaus ėsdinimo (FLSE) metodą.

PUBLICATIONS

Paper I

Demonstration of stable long-term operation of a kilohertz laser-plasma accelerator

L. Rovige, I. Andriyash, J. Huijts, A. Vernier, **V. Tomkus**, V. Girdauskas, G. Račiukaitis, J. Dudutis, V. Stankevič, P. Gečys, M. Ouill, Z. Cheng, R. Lopez-Martens, and J. Faure.

Phys.Rev.Accel.Beams. **23,** 093401(9), (2020)

DOI: 10.1103/PhysRevAccelBeams.23.093401

Demonstration of stable long-term operation of a kilohertz laser-plasma accelerator

L. Rovige,[1] J. Huijts,[1] A. Vernier,[1] V. Tomkus,[2] V. Girdauskas,[2,3] G. Raciukaitis,[2] J. Dudutis,[2] V. Stankevic,[2] P. Gecys,[2] M. Ouill,[1] Z. Cheng,[1] R. Lopez-Martens,[1] and J. Faure[1]

[1] *LOA, CNRS, École Polytechnique, ENSTA Paris, Institut Polytechnique de Paris, Palaiseau, France*

[2] *Center for Physical Sciences and Technology, Savanoriu Ave. 231, LT-02300, Vilnius, Lithuania*

[3] *Vytautas Magnus University, K.Donelaicio St. 58. LT-44248, Kaunas, Lithuania*

We report on the stable and continuous operation of a kilohertz laser-plasma accelerator. Electron bunches with 2.6 pC charge and 2.5 MeV peak energy were generated via injection and trapping in a downward plasma density ramp. This density transition was produced in a newly designed asymmetrically shocked gas nozzle. The reproducibility of the electron source was also assessed over a period of a week and found to be satisfactory with similar values of the beam charge and energy. These results show that the reproducibility and stability of the laser-plasma accelerator are greatly enhanced on the long-term scale when using a robust scheme for density gradient injection.

I. INTRODUCTION

Laser-plasma wakefield acceleration [1] enables the generation and acceleration of electrons beams over very short distances due to their extreme longitudinal accelerating fields, orders of magnitude higher than in conventional accelerators. When driven by 100 TW to PW scale laser systems, Laser-Plasma Accelerators (LPA) can produce electron beams in the 100 MeV-GeV energy range and are being considered as drivers for femtosecond X-ray beams, either via betatron radiation [2] , Compton scattering [3, 4] , undulator radiation [5] or free electron laser radiation. Such femtosecond X-ray beams could enable time-resolved (pump-probe) experiments based on e.g. X-ray diffraction or spectroscopy. A more recent line of research is currently focusing on the development of high-repetition rate (100 Hz-kHz) LPAs producing lower energy beams and requiring more modest laser parameters. TW-scale and kilohertz lasers with few-mJ pulse energy are capable of generating few MeV, pC range electrons beams [6–9] with femtosecond durations. Such beams could be used for low-energy applications such as ultrafast electron diffraction [10, 11] or irradiation of biological samples [12, 13].

In general, applications of LPAs require highly stable accelerator performances and the capacity to operate continuously and reliably over long periods of time, while providing consistent beam parameters from one day to the next. While numerous articles report on LPA stability on short time scales (as in a short series of shots over minutes) [14–16], there is a lack of consistent data in the literature addressing the issue of long-term stability and reproducibility. This is presumably because most published studies have focused on proof-of-principle experiments and on studying the physics of various regimes of plasma acceleration. This is now changing with initiatives such as the LUX beamline at DESY, aiming at turning a LPA into an actual machine [17]. In Ref. [17], day-long operation at a few Hz repetition rate is reported. However, to the best of our knowledge, no data has actually been published.

Concerning kHz laser-plasma accelerators, results obtained in the resonant condition for the bubble regime [6, 7] yielded electron beams with pC charge in the MeV range. These experiments have reported on short term stability of the electron beam distribution but long-term stability has remained a challenge so far. This is because the kHz laser systems currently used to drive high-repetition LPAs have parameters that are at the limit of what is necessary to efficiently inject and accelerate electrons in the wakefield. In previous experiments, electron beam generation relied on ionization injection [6, 18, 19] and self-injection [7]. Both mechanisms being rather sensitive to the laser intensity, this made electron injection in the wakefield difficult to control and stabilize, resulting in a high sensitivity to experimental parameters such as laser intensity, pulse duration and small laser misalignments. Therefore, long-term stability has been difficult to achieve in this regime.

On the other hand, controlled injection techniques are known to increase the reliability of electron injection and, consequently, beam stability [14]. In particular, injection in a plasma density-transition [20–24] is relatively straightforward to implement experimentally. While the laser pulse goes through the density transition, the plasma wavelength increases so that the bubble is rapidly elongated, causing an effective slowing down of its back that facilitates the trapping of electrons. The concept of downward density ramp injection was validated in proof-of-principle experiments [25, 26]. Other experiments relying on shock-front injection have also been successful [27–29]. In these experiments, a sharp density transition is obtained by inserting a knife-edge into the supersonic flow of the gas jet. These results indicate that density transition injection consistently triggers localized injection, and could provide the necessary stability for long-term and reproducible operation of a kilohertz laser-plasma accelerator.

In this paper, we report on the continuous and autonomous operation over 5 hours of a kilohertz LPA, generating MeV-pC range electron beams thanks to the use of a newly designed asymmetrically shocked supersonic

gas jet allowing injection in a sharp downward density gradient. The paper is organized as follows: in section II, we first describe the experimental apparatus and in particular the gas jet design for generating a density transition. In part III we show the result of 5h operation and day-to-day reproducibility. Finally, we conclude in part III.

II. EXPERIMENTAL METHODS

A. One-sided shock nozzle

Previous implementation of the density transition injection scheme relied on the lateral insertion of a knife-edge after the exit of the jet in order to induce a shock-front in the gas flow [16, 27]. We propose a similar method, but the formation of the shock-front is directly incorporated in the design of the nozzle, which consists of a 100 µm throat and 300 µm exit diameter "De Laval" nozzle to which a 100 µm long flat section has been added at the end of one side of the nozzle (see Fig. 1.a). These nozzles will thereafter be referred to as "One-Sided Shock" (OSS) nozzles. The flat section induces an abrupt change of direction in the gas flow which, due to the flow being supersonic, translates into a shock-front formation and therefore leads to a sharp density gradient downstream [30]. Compared to inserting a knife edge into the jet, incorporating the shock-front generation directly in the nozzle design offers a solution that is more robust and easier to install, for such a small nozzle. However, machining such a complicated nozzle geometry, including micrometer scale features, is technologically demanding. In practice, the nozzle was made using nanosecond laser rear-side processing and the Femtosecond Laser-assisted Selective Etching technique (FLSE,[31, 32]) which consists of chemical etching of previously selectively laser-irradiated fused silica. 3D computational fluid dynamics (CFD) simulations were realized with the software Fluent to validate and optimize the design. Figure 1.b shows a map of the molecular density obtained by simulating a nitrogen flow through the OSS nozzle, with a backing pressure of 20 bar. The shock-front in gas density originating from the final straight section is clearly visible.

The plasma density profile was characterized experimentally by sending the laser pulse into a nitrogen gas jet produced from the OSS nozzle. The plasma column produced by the main beam was illuminated from the side by a probe beam, and imaged on a quadriwave lateral shearing interferometer (SID4-HR, Phasics, [33, 34]). The plasma density line outs can be derived from the phase maps (see Fig. 1.d) via Abel inversion, assuming radial symmetry around the horizontal axis. Figure 1.e shows the measured electron density line out at 150 µm from the nozzle exit, with a backing pressure of 22 bar. The peak density is $9.7 \times 10^{19}\,\mathrm{cm}^{-2}$ and the density after the shock is $7.3 \times 10^{19}\,\mathrm{cm}^{-2}$, corresponding to a 25% density drop with a transition width of 15 µm. Note that

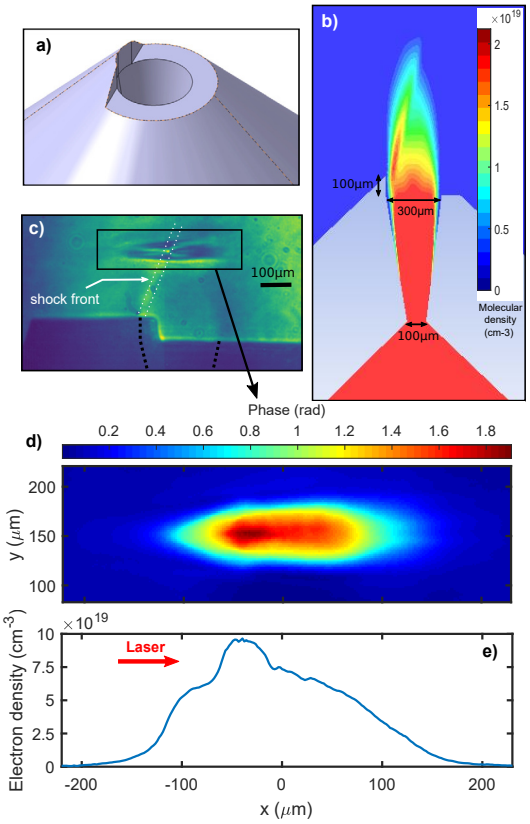

FIG. 1. a) 3D model of the One-Sided Shock Nozzle. b) Molecular density map from a 3D CFD simulation of an OSS jet performed with Fluent. Gas is N_2 and backing pressure P = 20 Bar. Colormap is capped at $2.1 \times 10^{19}\,\mathrm{cm}^{-2}$ for viewing purpose. c) Shadowgraphic side view image of the plasma. Black dotted line suggests the inner walls of the nozzle, white dotted lines follow the shock front. d) Experimental phase from the plasma column measured with the wave-front sensor. The y-axis represents the distance from the OSS nozzle's exit, the x-axis is the laser propagation axis. e) Electronic density profile at 150 µm from the OSS nozzle's exit, retrieved by Abel inversion of the phase map. Laser propagation direction is from left to right (red arrow).

with nitrogen, a single molecule of N_2 produces 10 electrons once ionized by the laser to N^{5+}, which provides the high plasma density required to resonantly drive the plasma wakefield, while keeping the background pressure in the vacuum chamber to a reasonable level and therefore making continuous kilohertz operation possible.

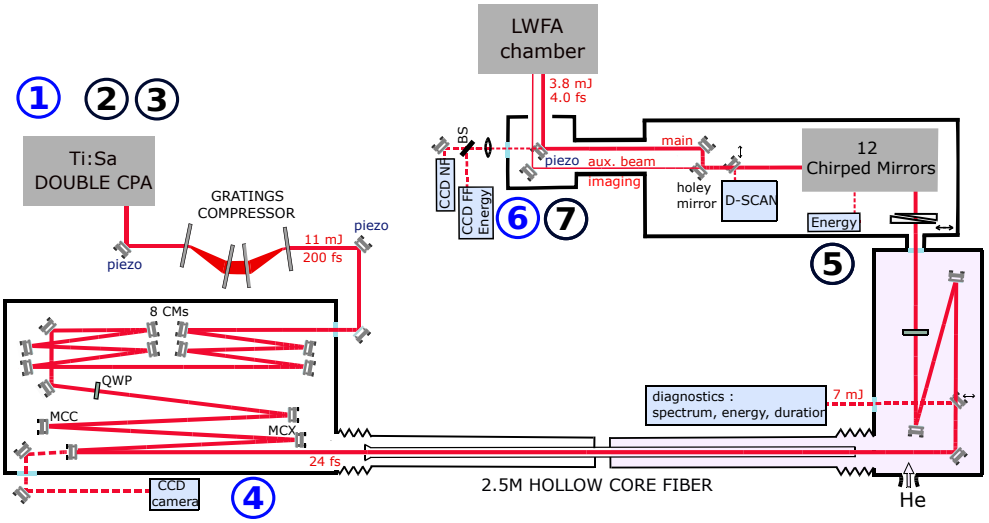

FIG. 2. Schematic of the laser system. Numbers ①,④,⑥ show the position of the beam pointing stabilization devices, numbers ②,③,⑤,⑦ correspond to the position of energy diagnostics for the booster amplifier, the power amplifier, the Hollow Core Fiber (HCF) compressor and the turning box, respectively.

B. Experimental set-up

The experiment was conducted using the Salle Noire laser system at LOA [35, 36], which provides 10 mJ, 25 fs FWHM laser pulses at kilohertz repetition rate, with a central wavelength $\lambda_0 = 800$ nm. The pulse is then post-compressed in a helium-filled Hollow Core Fiber (HCF). Through a pair of motorized fused silica wedges we can control the amount of dispersion to fine-tune pulse compression or add chirp to the pulse, and measure the pulse temporal intensity profile using the d-scan technique [37]. The energy on target was 3.8 mJ and the pulses are focused by a f/4 off-axis parabola, resulting in a 6.2 µm × 5.5 µm FWHM focal spot, which corresponds to a Rayleigh range of $z_R \sim 100$ µm. These laser parameters yield a measured peak intensity in vacuum of $I = 2.0 \times 10^{18}$ W cm^{-2} and a normalized vector potential $a_0 \simeq 1.0$. The charge as well as the electron beam distribution were measured with a calibrated CsI(Tl) phosphor screen imaged onto a high dynamic range CCD camera. The laser beam was blocked by a thin aluminum foil in front of the phosphor screen, so as to block electrons with energies below 100 keV. The energy of the electrons was measured with a retractable spectrometer made of a 500 µm pinhole and two permanent cylindrical magnets.

It is important to note that the laser-plasma accelerator truly runs at a repetition rate of 1 kHz: the gas jet flows continuously while the pumping system is able to maintain a vacuum of a few 10^{-3} mbar; the data was continuously collected during the experimental run, often by acquiring data accumulated over several shots. In order to perform a long run it was necessary to implement numerous diagnostics and feedback loops in the laser system to make sure that the laser parameters remained stable over a long time. Figure 2 shows a schematic of the laser system with indicated positions where laser energy monitoring was performed. In order to maximize the stability of the energy, the spectrum, and the spatial mode output of the HCF, a fast beam pointing system is essential. In our case, it ensured an energy stability within one percent over the course of a full day. Considering the long optical path from the exit of the fiber to the experiment itself, compensation for long-term thermal drifts proved crucial to the long-term stability of the LPA. We thus set up a slow beam pointing device operating at < 1 Hz just before the experiment, using the leakage through of mirror in the turning box just before the final focusing parabola– point ⑦ in Fig. 2. This ensured that the laser beam alignment on the gas jet stayed rigorously the same and that the focal spot quality was kept consistent throughout the long acquisition run.

III. EXPERIMENTAL RESULTS

A. Stability over several hours of continuous operation

The beam profile and charge were measured right before the start of the electron spectrum monitoring. Statistics were performed from 20 acquisitions, each consisting of an accumulation over 10 shots, thus accounting

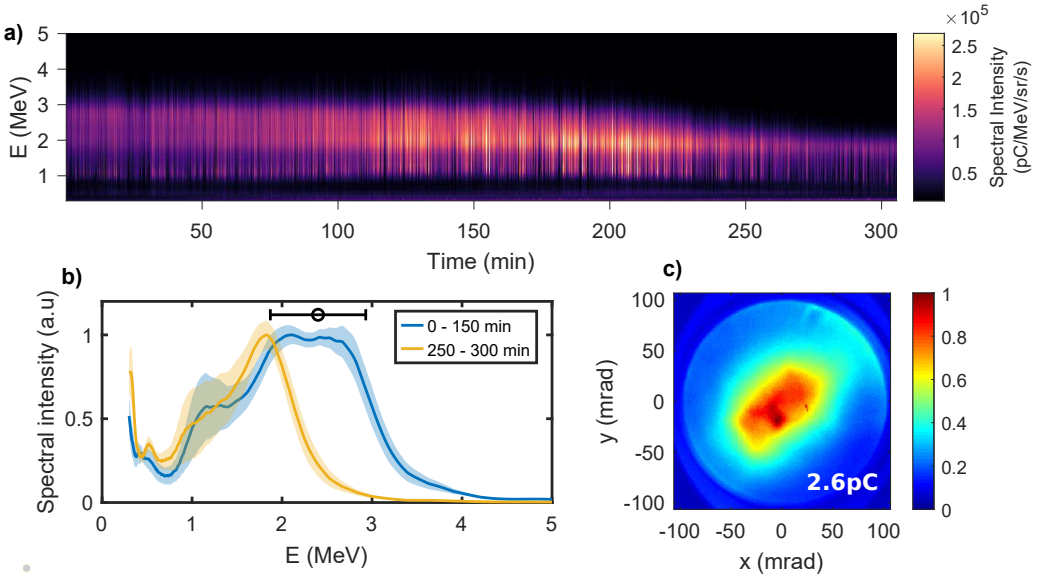

FIG. 3. a) Electron spectra measured continuously for 306 min. Each spectrum is averaged over 100 shots. b) Blue line: mean spectrum over the 0-150 min period. Yellow line: mean spectrum over the 250-300 min period. Shaded areas show standard deviation. The black error bar indicates the spectrometer resolution at 2.4 MeV. c) Electron beam measured just before the start of the 5h spectrum monitoring. The total charge per shot is 2.6 pC ± 0.6 pC (std). The beam divergence is approximately 80 mrad FWHM.

for 200 shots in total. This initial measurement yielded a mean charge of 2.6 pC per shot with a 0.6 pC standard deviation, and a beam divergence of 80×75 mrad FWHM (see Fig. 3.c). The electron spectrum was then monitored during 5 hours of complete hands-off operation of the kilohertz laser-plasma accelerator, i.e. with no other intervention than the beam pointing stabilization feedback loops at the three above-mentioned locations in the laser chain, see Fig. 2. Results of this measurement are displayed in Fig. 3.a. Beams with peaked spectra and a large majority of electrons of energy greater than 1 MeV were reliably produced throughout the whole 306 min of monitoring. Moreover, during the first 150 min, the spectrum remained very stable, with a peak energy of 2.5 MeV. After that, the high-energy part noticeably eroded with time, lowering the peak energy to 1.9 MeV. Possible reasons for this energy loss will be addressed later in this article. A comparison of the spectra during the first 150 min and the last 50 min is represented in Fig. 3.b.

To complete these data and assess more thoroughly the question of stability, we plot the temporal evolution of the total charge per solid angle $dQ/d\Omega$ collected through the pinhole of the spectrometer (Fig. 4.a), the mean energy of the electrons $\langle E \rangle$ (Fig. 4.b), as well as the relative laser energy at different points of the laser chain (Fig. 4.c). All curves are averaged over a 1 min moving window. The data show an increase in $dQ/d\Omega$ (Fig. 4.a) during the first 130 min. This is likely due to a small angular drift of the electron beam on a long time scale, resulting in a higher electron signal through the electron spectrometer pinhole. Therefore, only the short term variation of the charge can be estimated from this measurement, giving typical fluctuation of about 50 pC/sr/shot corresponding to 20% RMS.

Figure 4.b confirms the observations made previously regarding the stability of the spectrum, and indeed, shows that the mean energy of the electrons is quite stable at $\langle E \rangle \simeq 2.1$ MeV during the first 150 min of monitoring, with short-term RMS variations of only 2-4% (shaded area in Fig. 4.b). The decrease of the mean beam energy to $\langle E \rangle \simeq 1.5$ MeV toward the end of the run can also be clearly observed. Note that during the run, the laser system was extremely stable, see Fig. 4.c, except for the energy measured using the turning box diagnostic (red curve in Fig. 4.c), which is the last measurement point before the focusing parabola and is, therefore, the most representative of the evolution of the laser energy on target. The energy measured at this point decreased steadily during the experiment and reached a 11% relative loss after 306 min. It is likely that this progressive energy loss was due to the slow damage of a few chirped mirrors at the end of the compressor. The damage on the mirrors was found during the inspection which we

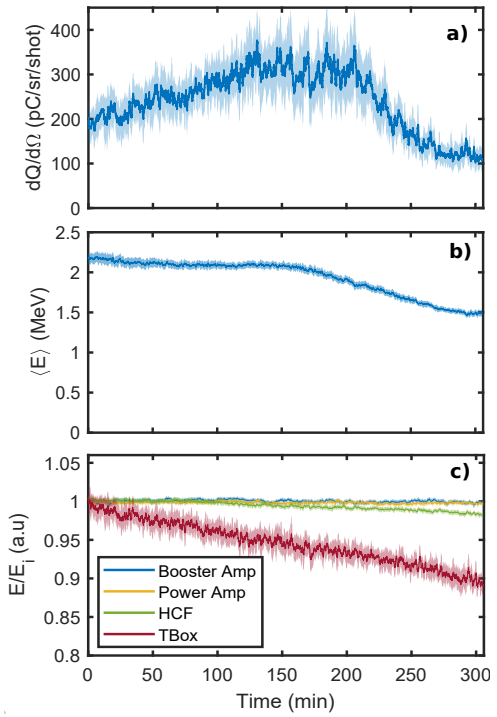

FIG. 4. a) Total charge per solid angle collected through the electron spectrometer pinhole. b) Mean electron beam energy versus time. c) Monitoring of the laser energy at four points in the laser chain. Each curve in this figure is averaged over a one minute moving window and shaded areas represent the corresponding standard deviation.

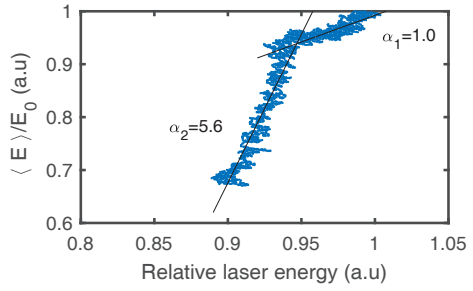

FIG. 5. Correlation between the electron mean energy and the relative laser energy at the turning box measurement point (right before the off-axis focusing parabola), and linear fits of the two different parts of the curve, with slopes α_1 and α_2.

performed the day after the experiment. Interestingly, the evolution of the electron energy can be correlated to the evolution of the laser energy at this last measurement point. To display these correlations, Fig. 5 shows the normalized mean energy of the electrons plotted against the laser relative energy. Two different correlation regimes are clearly distinguishable: (i) the first 5% of laser energy loss leads to a $\sim 5\%$ energy loss of the electrons suggesting a linear correlation. We then observe a threshold effect, (ii) as the next 5% drop of laser energy correlates with a $\sim$30% electron mean energy loss. Assuming a linear dependence in both regimes, the two parts of the correlation plot are linearly fitted, yielding a slope $\alpha_1 = 1.0$ in the first five percents of energy loss, and a slope $\alpha_2 = 5.6$ in the following five percents. This highlights the importance of laser energy stability: in our case, energy variations larger than 5% can cause significant modifications of the electron spectrum due to what seems like a threshold effect. Nevertheless, decent stability of the electron beam was achieved over the 300 min of continuous operation, with the first 150 min period displaying a remarkable stability correlated to the highest laser performance. Stability over multiple hours of operation with pC-MeV range electron beams at kilohertz repetition rate, corresponding to more than 18×10^6 consecutive shots, represents significant progress toward scientific applications of laser-plasma accelerators.

	Day 1	Day 2	Day 3
I (W.cm^{-2})	1.8×10^{18}	2.0×10^{18}	1.6×10^{18}
$n_{e,peak}$ (cm^{-3})	8.8×10^{19}	9.7×10^{19}	9.7×10^{19}
Q (pC/shot)	1.6±0.2	2.6±0.6	1.4±0.2
div. fwhm (mrad)	42±10	77±7	57±11
⟨E⟩ (MeV)	2.29±0.13	2.11±0.06	2.19±0.04

TABLE I. Various experimental parameters and electron beam performance showing slight variations from day to day but overall fair reproducibility of the experiment. The values after the ± sign are RMS deviation.

B. Day to day reproducibility

In order to determine the reproducibility of the electron beam and to assess the sensitivity of the accelerator to small day-to-day variations of the laser parameters, the measurements were repeated on three different days, each separated by about a week. The same actual OSS nozzle was used for the three experimental runs and showed no degradation over time. Table I summarizes experimental conditions for each day, as well as the charge and mean electron energy corresponding to the electrons spectra displayed in Fig. 6. These results show that the downward gradient injection method with one-sided shock nozzles increased significantly the reliability of the accelerator. Indeed, electrons beams with similar charge and 2-3 MeV peaked spectrum were easily

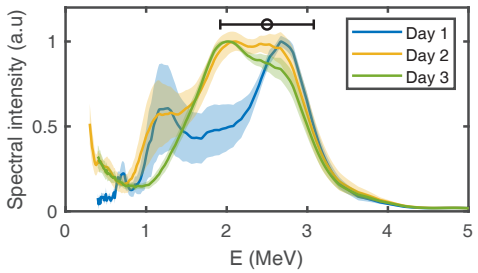

FIG. 6. Electron spectra obtained on three different days with the same one-sided shock nozzle. Spectra are the results of averaging over 2000 shots for day 1 and day 2, and 5000 shots for day 3. Day 1 and day 2 are 7 days apart, day 2 and day 3 are 6 days apart.

obtained even though the experimental parameters varied slightly from day to day. In particular, we see that experiments from day 2 and day 3, performed at the same plasma density, yield very similar electron spectra. This level of reproducibility was not observed in our previous experiments relying on ionization injection and self-injection. Such level of reproducibility is also decisive for a reliable use of the accelerator for applications. Moreover, these fused-silica nozzles showed a great resilience to damage, as the one used for this experiment provided reliable and reproducible results even after using it for about $30\text{-}50 \times 10^6$ shots.

IV. CONCLUSION

In conclusion, by using an asymmetrically shocked fused-silica nozzle, we were able to produce the sharp density transition and the high plasma density necessary for downward density gradient injection in a LPA driven by few-cycle laser pulses. We managed to stabilize the injection and obtained electron beams with picocoulomb charge and MeV peaked spectrum for 5 hours of continuous operation. In addition, the electron energy was correlated to the laser energy stability, showing that energy fluctuations should remain at the percent level in order to ensure stable accelerator performance. Finally, we demonstrated good day-to-day reproducibility over a period of two weeks thus making our accelerator ready for first application experiments.

ACKNOWLEDGMENTS

This work was funded by the European Research Council (ERC Starting Grant FEMTOELEC) under Contract No. 306708. Financial support from the Région Île-de-France (under contract SESAME-2012-ATTOLITE) and the Extreme Light Infrastructure-Hungary Non-Profit Ltd (under contract NLO3.6LOA) is gratefully acknowledged. We also acknowledge Laserlab-Europe, H2020 EC-GA 654148 and the Lithuanian Research Council under grant agreement No. S-MIP-17-79.

[1] T. Tajima and J. M. Dawson, Phys. Rev. Lett. **43**, 267 (1979).
[2] A. Rousse, K. T. Phuoc, R. Shah, A. Pukhov, E. Lefebvre, V. Malka, S. Kiselev, F. Burgy, J.-P. Rousseau, D. Umstadter, and D. Hulin, Phys. Rev. Lett. **93**, 135005 (2004).
[3] K. Ta Phuoc, S. Corde, C. Thaury, V. Malka, A. Tafzi, J. P. Goddet, R. C. Shah, S. Sebban, and A. Rousse, Nature Photonics **6**, 308 (2012).
[4] S. Chen, N. D. Powers, I. Ghebregziabher, C. M. Maharjan, C. Liu, G. Golovin, S. Banerjee, J. Zhang, N. Cunningham, A. Moorti, S. Clarke, S. Pozzi, and D. P. Umstadter, Phys. Rev. Lett. **110**, 155003 (2013).
[5] M. Fuchs, R. Weingartner, A. Popp, Z. Major, S. Becker, J. Osterhoff, I. Cortrie, B. Zeitler, R. Hörlein, G. D. Tsakiris, U. Schramm, T. P. Rowlands-Rees, S. M. Hooker, D. Habs, F. Krausz, S. Karsch, and F. Grüner, Nature Physics **5**, 826 (2009).
[6] D. Guénot, D. Gustas, A. Vernier, B. Beaurepaire, F. Böhle, M. Bocoum, M. Lozano, A. Jullien, R. Lopez-Martens, A. Lifschitz, and J. Faure, Nature Photonics **11**, 293 (2017).
[7] D. Gustas, D. Guénot, A. Vernier, S. Dutt, F. Böhle, R. Lopez-Martens, A. Lifschitz, and J. Faure, Phys. Rev. Accel. Beams **21**, 013401 (2018).
[8] F. Salehi, A. J. Goers, G. A. Hine, L. Feder, D. Kuk, B. Miao, D. Woodbury, K. Y. Kim, and H. M. Milchberg, Opt. Lett. **42**, 215 (2017).
[9] J. Faure, D. Gustas, D. Guénot, A. Vernier, F. Bhle, M. Ouillé, S. Haessler, R. Lopez-Martens, and A. Lifschitz, Plasma Physics and Controlled Fusion **61**, 014012 (2018).
[10] Z.-H. He, A. G. R. Thomas, B. Beaurepaire, J. A. Nees, B. Hou, V. Malka, K. Krushelnick, and J. Faure, Applied Physics Letters **102**, 064104 (2013).
[11] J. Faure, B. van der Geer, B. Beaurepaire, G. Gallé, A. Vernier, and A. Lifschitz, Phys. Rev. Accel. Beams **19**, 021302 (2016).
[12] O. Rigaud, N. O. Fortunel, P. Vaigot, E. Cadio, M. T. Martin, O. Lundh, J. Faure, C. Rechatin, V. Malka, and Y. A. Gauduel, Cell Death & Disease **1**, e73 (2010).
[13] O. Lundh, C. Rechatin, J. Faure, A. Ben-Ismal, J. Lim, C. De Wagter, W. De Neve, and V. Malka, Medical Physics **39**, 3501 (2012).
[14] J. Faure, C. Rechatin, A. Norlin, A. Lifschitz, Y. Glinec, and V. Malka, Nature **444**, 737 (2006).
[15] J. Osterhoff, A. Popp, Z. Major, B. Marx, T. P. RowlandsRees, M. Fuchs, R. Hrlein, F. Grner, D. Habs, F. Krausz, S. M. Hooker, and S. Karsch, AIP Conference Proceedings **1086**, 125 (2009).

[16] A. Buck, J. Wenz, J. Xu, K. Khrennikov, K. Schmid, M. Heigoldt, J. M. Mikhailova, M. Geissler, B. Shen, F. Krausz, S. Karsch, and L. Veisz, Phys. Rev. Lett. **110**, 185006 (2013).

[17] N. Delbos, C. Werle, I. Dornmair, T. Eichner, L. Hbner, S. Jalas, S. Jolly, M. Kirchen, V. Leroux, P. Messner, M. Schnepp, M. Trunk, P. Walker, P. Winkler, and A. Maier, Nuclear Instruments and Methods in Physics Research Section A: Accelerators, Spectrometers, Detectors and Associated Equipment **909**, 318 (2018), 3rd European Advanced Accelerator Concepts workshop (EAAC2017).

[18] A. Pak, K. A. Marsh, S. F. Martins, W. Lu, W. B. Mori, and C. Joshi, Phys. Rev. Lett. **104**, 025003 (2010).

[19] C. McGuffey, A. G. R. Thomas, W. Schumaker, T. Matsuoka, V. Chvykov, F. J. Dollar, G. Kalintchenko, V. Yanovsky, A. Maksimchuk, K. Krushelnick, V. Y. Bychenkov, I. V. Glazyrin, and A. V. Karpeev, Phys. Rev. Lett. **104**, 025004 (2010).

[20] S. Bulanov, N. Naumova, F. Pegoraro, and J. Sakai, Phys. Rev. E **58**, R5257 (1998).

[21] P. Tomassini, M. Galimberti, A. Giulietti, D. Giulietti, L. A. Gizzi, L. Labate, and F. Pegoraro, Phys. Rev. ST Accel. Beams **6**, 121301 (2003).

[22] J. U. Kim, N. Hafz, and H. Suk, Phys. Rev. E **69**, 026409 (2004).

[23] H. Suk, H. J. Lee, and I. S. Ko, J. Opt. Soc. Am. B **21**, 1391 (2004).

[24] A. V. Brantov, T. Z. Esirkepov, M. Kando, H. Kotaki, V. Y. Bychenkov, and S. V. Bulanov, Physics of Plasmas **15**, 073111 (2008).

[25] C. G. R. Geddes, K. Nakamura, G. R. Plateau, C. Toth, E. Cormier-Michel, E. Esarey, C. B. Schroeder, J. R. Cary, and W. P. Leemans, Phys. Rev. Lett. **100**, 215004 (2008).

[26] J. Faure, C. Rechatin, O. Lundh, L. Ammoura, and V. Malka, Physics of Plasmas **17**, 083107 (2010).

[27] K. Schmid, A. Buck, C. M. S. Sears, J. M. Mikhailova, R. Tautz, D. Herrmann, M. Geissler, F. Krausz, and L. Veisz, Phys. Rev. ST Accel. Beams **13**, 091301 (2010).

[28] C. Thaury, E. Guillaume, A. Lifschitz, K. Ta Phuoc, M. Hansson, G. Grittani, J. Gautier, J.-P. Goddet, A. Tafzi, O. Lundh, and V. Malka, Scientific Reports **5**, 16310 (2015).

[29] K. K. Swanson, H.-E. Tsai, S. K. Barber, R. Lehe, H.-S. Mao, S. Steinke, J. van Tilborg, K. Nakamura, C. G. R. Geddes, C. B. Schroeder, E. Esarey, and W. P. Leemans, Phys. Rev. Accel. Beams **20**, 051301 (2017).

[30] R. D. Zucker and O. Biblarz, *Fundamentals of Gas Dynamics* (John Wiley & Sons, 2002).

[31] A. Marcinkevičius, S. Juodkazis, M. Watanabe, M. Miwa, S. Matsuo, H. Misawa, and J. Nishii, Opt. Lett. **26**, 277 (2001).

[32] V. Tomkus, V. Girdauskas, J. Dudutis, P. Gečys, V. Stankevič, and G. Račiukaitis, Opt. Express **26**, 27965 (2018).

[33] J. Primot and L. Sogno, J. Opt. Soc. Am. A **12**, 2679 (1995).

[34] J. Primot and N. Guérineau, Appl. Opt. **39**, 5715 (2000).

[35] F. Bhle, M. Kretschmar, A. Jullien, M. Kovacs, M. Miranda, R. Romero, H. Crespo, U. Morgner, P. Simon, R. Lopez-Martens, and T. Nagy, Laser Physics Letters **11**, 095401 (2014).

[36] M. Ouillé, A. Vernier, F. Böhle, M. Bocoum, A. Jullien, M. Lozano, J.-P. Rousseau, Z. Cheng, D. Gustas, A. Blumenstein, P. Simon, S. Haessler, J. Faure, T. Nagy, and R. Lopez-Martens, Light: Science & Applications **9**, 47 (2020).

[37] M. Miranda, C. L. Arnold, T. Fordell, F. Silva, B. Alonso, R. Weigand, A. L'Huillier, and H. Crespo, Opt. Express **20**, 18732 (2012).

Paper II

Radiation from laser wakefield accelerated electron beams and betatron radiation using multijet gas targets

V. Tomkus, V. Girdauskas, J. Dudutis, V. Stankevič, P. Gečys, G. Račiukaitis, I. Gallardo González, D. Guénot, J. B. Svensson, A. Persson, O. Lundh.

Sci. Rep. **10**, 16807, (2020)

DOI: 10.1038/s41598-020-73805-7

SCIENTIFIC REPORTS
nature research

Check for updates

OPEN

Laser wakefield accelerated electron beams and betatron radiation from multijet gas targets

Vidmantas Tomkus[1]✉, Valdas Girdauskas[1,2], Juozas Dudutis[1], Paulius Gečys[1], Valdemar Stankevič[1], Gediminas Račiukaitis[1], Isabel Gallardo González[3], Diego Guénot[3], Jonas Björklund Svensson[3], Anders Persson[3] & Olle Lundh[3]

Laser Plasma Wakefield Accelerated (LWFA) electron beams and efficiency of betatron X-ray sources is studied using laser micromachined supersonic gas jet nozzle arrays. Separate sections of the target are used for the injection, acceleration and enhancement of electron oscillation. In this report, we present the results of LWFA and X-ray generation using dynamic gas density grid built by shock-waves of colliding jets. The experiment was done with the 40 TW, 35 fs laser at the Lund Laser Centre. Electron energies of 30–150 MeV and 1.0×10^8–5.5×10^8 photons per shot of betatron radiation have been measured. The implementation of the betatron source with separate regions of LWFA and plasma density grid raised the efficiency of X-ray generation and increased the number of photons per shot by a factor of 2–3 relative to a single-jet gas target source.

Laser Plasma Wakefield Accelerators (LWFA) are attractive alternatives to radio-frequency accelerators for a number of applications. LWFA enable the development of compact, next-generation X-ray and γ-ray sources for use in biomedical applications, physics, materials science, and significantly facilitate their access to universities and smaller research centres[1–3]. In LWFA an intense ultrashort laser is focused down to 10 μm into a gas jet. If the laser pulse reaches so called relativistic intensities around 10^{18} W/cm^2, it will excite a non-linear plasma wave which accelerates electrons up to relativistic velocities. During their acceleration, the electrons oscillate transversally inside the plasma wave, which leads to the emission of X-ray radiation in the keV range defined as betatron emission. Additional work is, however, required to increase the energy and charge of accelerated electrons, and to reduce the energy dispersion of the electron beams. The charge and energy dispersion of accelerated electrons is controlled by tapered plasma channels using capillary discharge[4], by ionization-assisted[5,6] or self-truncated electron injection[7,8], by injection utilising colliding beams[9,10] or the density down-ramp triggered injection[11–13]. Density down-ramp injection is implemented by the formation of tailored plasma profiles using two or more stages of nozzles[14,15] by insertion of a wire[16], a razor blade[17] or a capillary jet[18] into the nozzle jet causing shock waves. Implementation of separate nozzles and insertion of external objects into the gas jet increases mechanical complexity, lowers the stability and is hard to realise in the case of laser pulses with duration < 10 fs where a dephasing length is less than 100 μm[19]. Tailored plasma channels are also interesting for optimisation of betatron radiation aiming to increase the critical energy, the number of photons per shot and brightness of X-ray and γ-ray sources. The efficiency of betatron radiation is raised by increasing the energy of electrons, plasma concentration and betatron radius. Tuning of the betatron radiation is implemented using two-stage nozzles: one with a lower plasma concentration, optimised for the acceleration of electrons, and the second one with a higher concentration – acting as a plasma radiator[20,21].

In this report, we present the experimental results of LWFA and X-ray generation using the 40 TW, 35 fs laser at the Lund Laser Centre using novel multi-stage micronozzles manufactured from a single block of fused silica. The charge, energy and divergence of accelerated electrons and efficiency of betatron X-ray radiation were defined by the formation of gas density grid using shock wave interference. Fused silica nozzles are more resistant to optical damage than polymeric or metallic nozzles. Fused silica has by order of magnitude higher optical damage threshold[22] comparing to polymeric structures[23]. The ablation threshold of fused silica[24] is several times larger than for metals[25]. Furthermore, the softening temperature of the fused silica is larger than that of plastics

[1]Center for Physical Sciences and Technology, 02300 Vilnius, Lithuania. [2]Vytautas Magnus University, 44248 Kaunas, Lithuania. [3]Department of Physics, Lund University, 221 00 Lund, Sweden. ✉email: vidmantas.tomkus@ftmc.lt

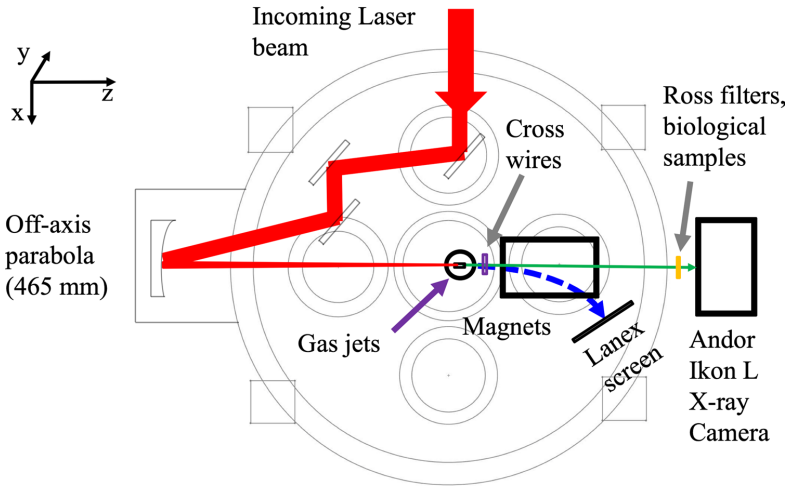

Figure 1. Experimental setup of the laser wakefield acceleration of electrons and measurement of betatron radiation.

and the melting point of metals, such as aluminium, copper or iron[26]. By repetitive use, the nozzles get damaged due to the plasma produced in the laser–gas interaction. For example, the gas flux of stainless-steel nozzles starts to show turbulence for less than 10^4 shots due to nozzle damage[27]. The fused-silica nozzles demonstrated high resilience to damage and provided reliable and reproducible results after operation at kilohertz repetition rate for about $3–5 \times 10^7$ shots[28]. Comparing to gas capillaries or gas cells, the supersonic nozzles targets are more easily to setup and can be combined to multijet longitudinal plasma profiles. The implementation of metallic nozzles can be more favourable in the conditions when the backing pressure exceeding 100 bar is required. The nozzles manufactured from fused silica are fragile and have to be handled with care. At the modest pressure of 20–60 bar fused silica nozzles ensure significantly longer operation times than metallic or polymeric nozzles. Laser-assisted hybrid microfabrication technique[29,30] of fused silica allows the formation of centimetre-size frame and channels of the diameter less than 40 μm with the surface roughness < 1 μm from a single block. The formation quality exceeds the precision of 3D printing[31] and electro-erosion technique[32].

The experiment has been done using the experimental setup shown in Fig. 1 and LWFA parameters described in Table 2 in "Methods". For the laser wakefield acceleration and X-ray generation, laser beam focused to the spot of 8 μm at FWHM, and plasma concentration $2 \times 10^{18}–1 \times 10^{19}$ cm^{-3} were implemented. The peak laser intensity was 3.6×10^{19} W/cm^2 and the corresponding laser strength parameter $a_0 = 4.0$. The geometries and dimensions of the nozzle arrays used in the experiments are presented in Fig. 2a,b and in Table 3 (see "Methods"). The nozzle arrays were made from two sections. The first section comprises a main supersonic converging–diverging nozzle of 1.5 mm length (S1, Arr2, Arr4) or 2.25 mm (Arr3) length commonly used for laser-plasma acceleration. The second section consists of 1 or 4 smaller nozzles of 200–300 μm length located 100 μm away from the main nozzle (Arr2, Arr3, Arr4). The nozzles are oriented in wiggler or injector geometry. In wiggler geometry, the array is placed after the main nozzle, and in injector geometry, the array is placed before the main nozzle relative to the incoming laser beam. The SEM image of a cross-section of a nozzle array cut in half is shown in Fig. 2c,d.

The microarrays of gas-jet nozzles were designed by iterative numerical simulation of FBPIC PIC (Particle in Cell) and OpenFOAM algorithms. The energy and spatial distribution of the LWFA accelerated electrons were modelled using the FBPIC PIC simulation[33]. The obtained results were post-processed to evaluate the number of X-ray photons per shot and the brightness of electron-generated betatron radiation using the analytical expressions[34–36] (see Supplementary information S1). The concentrations, velocities, pressures and temperatures of the gas jets were calculated using the OpenFOAM software[37].

Experimental results. The electron energy spectrum, divergence and charge of accelerated electrons were measured using a magnetic spectrometer and Lanex scintillation screen. The spectrum data and spatial distribution of charge of electrons averaged over 10 shots for a single S1 nozzle and Arr2, Arr3, Arr4 arrays are shown in Fig. 3. Highest energy and lowest divergence (FWHM) of accelerated electrons were obtained with a single nozzle and moderate focusing at a lower backing pressure of 5–12 bar of He + 1%N gas (Fig. 3a). Quasi-monoenergetic electron bunches were observed at a low backing pressure of 5–7 bar of pure He using an injector geometry of Arr4 with a density-triggered injection of electrons (Fig. 3b). The corresponding plasma concentration was approximately $n_p = 3 \times 10^{18}$ cm^{-3}. The energy of separate electron bunches had low energy dispersion of 5–10 MeV. However, the amount of accelerated charge and spatial distribution fluctuated from shot to shot, which increased the averaged distribution. Using the mixture of He + 1%N and lowering the backing pressure by

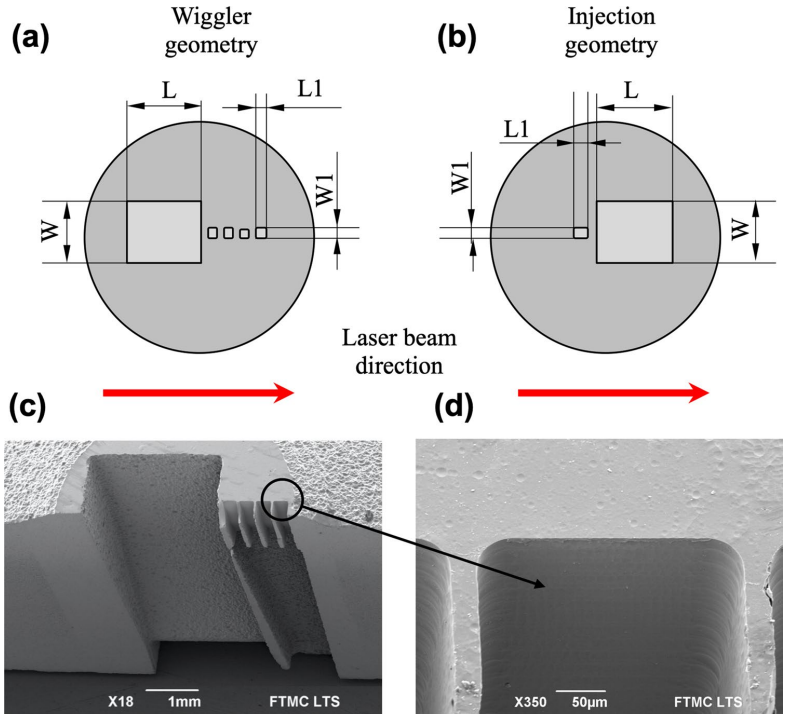

Figure 2. The geometry of the nozzle array **Arr2** in wiggler geometry (**a**) and **Arr4** in injector geometry (**b**). The red arrows indicate the orientation of the nozzle arrays relative to the incoming laser beam. SEM images of the cross-section of the array **Arr2** cut-in-half manufactured using the nanosecond rear side machining (**c**) and an element of the slit array with the length of 200 μm manufactured using the Femtosecond Laser-Induced Chemical Etching (FLICE) technique (**d**). **Arr2** consists of a converging–diverging 1.5 mm slit nozzle **S1** and four capillary nozzles with the fixed channel dimensions of 200 μm × 200 μm.

a factor of 1.5 the injector array enabled to get more stable quasi-monoenergetic electron bunches with a mean energy of 50 MeV and dispersion ± 10 MeV (Fig. 3c). Adding a wiggler array (Fig. 3e,f) as well increasing of the backing pressure up to 18–26 bar led to a massive injection of electrons and broadening of the beam. Note that, the wiggler geometry increased the efficiency of betatron radiation. In the case of (Fig. 3a,c–f), the spatial distribution of the charge and divergence of the electron beam of a single shot did not differ substantially from the average of 10 shots. The backing pressure of 18 bar for S1, Arr2 and 26 bar for Arr3 corresponded approximately to the plasma concentration of $n_p = 1 \times 10^{19}$ cm^{-3}.

In Figs. 4 and 5, the dependence of mean energy, charge and divergence of accelerated electrons on gas backing pressure are presented. The arrows and the ellipses indicate the regions of the highest X- ray yield. For the 1.5 mm single nozzle S1, the maximum of X-ray radiation was reached at the backing pressure of 18–21 bar. (Fig. 4a,b). The maximum of X-ray counts was registered at the highest divergence values when the mean energy started to drop. At the lower backing pressure of 15 bar, adding the wiggler array to S1, increased the average divergence (FWHM) of accelerated electrons by 50% from 40 to 60 mrad. At the backing pressure of 20 bar, the average divergence of accelerated electrons for S1 and Arr2 was similar in the range of 70–90 mrad. However, for Arr2, the increase of the charge of accelerated electrons ($W_{mean} > 40$ MeV) and a drop of mean energy by 20% relative to S1 nozzle was observed.

The same trend of the increase of X-ray yield with the increase of divergence and charge was also observed for the array Arr3. The 2.25 mm cylindrical nozzle array Arr3 had longer acceleration distance by a factor 1.5 times relative to the nozzle S1 and array Arr2. The energy of accelerated electrons using this nozzle was higher. Arr3 nozzle had a higher expansion ratio than S1 and Arr2 nozzles. For the array Arr3, the maximum of X-ray radiation was reached at the backing pressure of 24–26 bar. At the distance of 800 μm of laser beam above the array Arr3 (Fig. 5a,b), when increasing the backing pressure from 15 until 28 bar, the charge grew continuously even though it remained low (in the range of 25–30 pC). In addition, the mean energy dropped from 50 to 32 MeV, and the divergence increased from 20 to 80 mrad. At the distance of 400 μm of laser beam above the array Arr3 (Fig. 5c,d), the substantial increase of charge ($W_{mean} > 40$ MeV) up to 100 pC and mean energy to 43 eV was registered. The divergence of the electron beam remained at the same level of 80 mrad. Decrease of

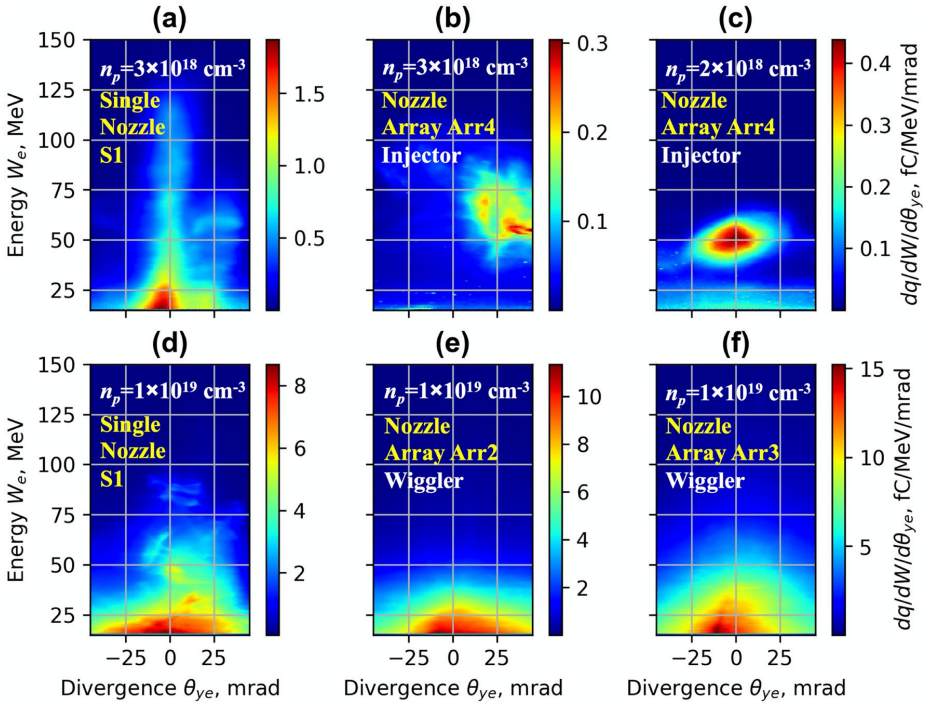

Figure 3. Experimental profiles of energy and spatial distribution of electrons for $n_p = 3 \times 10^{18}$ cm^{-3} for the single **S1** nozzle for the mixture He + 1% N_2 (**a**) and the array **Arr4** in injector geometry for pure He (**b**) and $n_p = 2 \times 10^{18}$ cm^{-3} for the mixture He + 1%N_2 (**c**). Experimental profiles of energy and spatial distribution of the charge of electrons for $n_p = 1 \times 10^{19}$ cm^{-3} for the single **S1** nozzle (**d**) and for the array **Arr2** (**e**) and **Arr3** (**f**) for the mixture He + 1%N_2 in wiggler geometry.

the distance between the array output and laser beam resulted in the growth of the charge by a factor of 4 and the enhancement of X-ray radiation by a factor of 5.

The experimental data of betatron X-ray radiation are presented in Figs. 6, 7, 8 and Table 1. The number of X-ray photons per shot and brightness increased proportionally to the amount of accelerated charge and the divergence of electron beam increasing the amplitude of betatron oscillation of electrons. The average energy of electrons with higher divergence is lower, however, and the maximum of X-ray radiation does not correspond to the maximum of the average energy of electrons. With increasing the pressure > 22 bar for S1 and Arr2 with the divergence of the electron beam increased further. The declining mean energy of electrons caused the drop in the number of photons of X-ray radiation. For the array Arr3, having a higher expansion rate of the gas jet, just the increase of X-ray radiation with the increase of pressure was observed. The highest number of photons and brightness of X-ray radiation was reached at 26 bar when the laser beam was propagating 400 μm above the nozzle. For the single S1 nozzle, and Arr3 at a laser-nozzle distance of 800 μm, the divergence of X-ray radiation (FHWM) increased proportionally to the divergence of the electron beam (Figs. 6a, 7a). For the array Arr2, and Arr3 at the laser-nozzle distance of 400 μm, the drop of the divergence of X-ray radiation (FHWM) by 15–30% was observed in the region of the backing pressure corresponding to the highest X-ray yield (Figs. 6c, 7c).

The critical energy of the betatron sources was measured using Ross filters. The spatial profiles of the betatron radiation were estimated using the relations[38–41] of Gaussian approximation of intensity of X- ray radiation. The critical energy of betatron radiation was evaluated by calculating the squared difference between the measured transmission and the theoretical one for each critical energy of synchrotron radiation. The number of photons per shot was calculated by postprocessing the images at FWHM level of counts per pixel and corresponding critical energy E_c.

The typical examples of X-rays radiation spatial distribution for the single nozzle S1 and arrays Arr2, Arr3 are shown in Fig. 8. The measurement of the divergence θ (FHWM) of X-ray radiation has demonstrated that the intensity distribution in the x–y direction changes from circular to elliptical from shot to shot. In average, the X-ray distribution for Arr3 was more elongated in x-direction parallel to laser polarisation relative to the X-ray distribution for S1 and Arr2 nozzles.

The radius size of betatron source was measured by imaging tungsten wires placed close to the betatron source, and comparison of diffraction intensity signals in the horizontal and vertical directions with the calculated Fresnel diffraction integrals for different X-ray source sizes[42–44]. The evaluation of Fresnel diffraction has shown

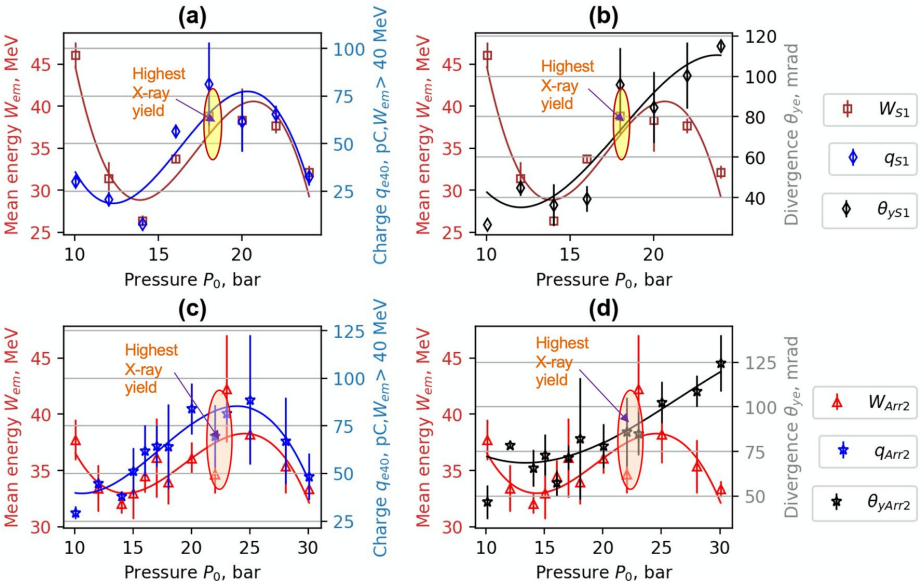

Figure 4. Experimental dependence of mean energy W_{mean}, charge q_{40} for $W_{mean} > 40$ MeV (**a**,**c**) and mean divergence θ_{ye} (FWHM) (**b**,**d**) of accelerated electrons on gas backing pressure. $\boldsymbol{W_{S1}}$, $\boldsymbol{q_{S1}}$, $\boldsymbol{\theta_{S1}}$ correspond to the single nozzle **S1,** and $\boldsymbol{W_{Arr2}}$, $\boldsymbol{q_{Arr2}}$, $\boldsymbol{\theta_{Arr2}}$ correspond to the array **Arr2** in wiggler geometry. Interpolated solid lines provide a guide to the eye.

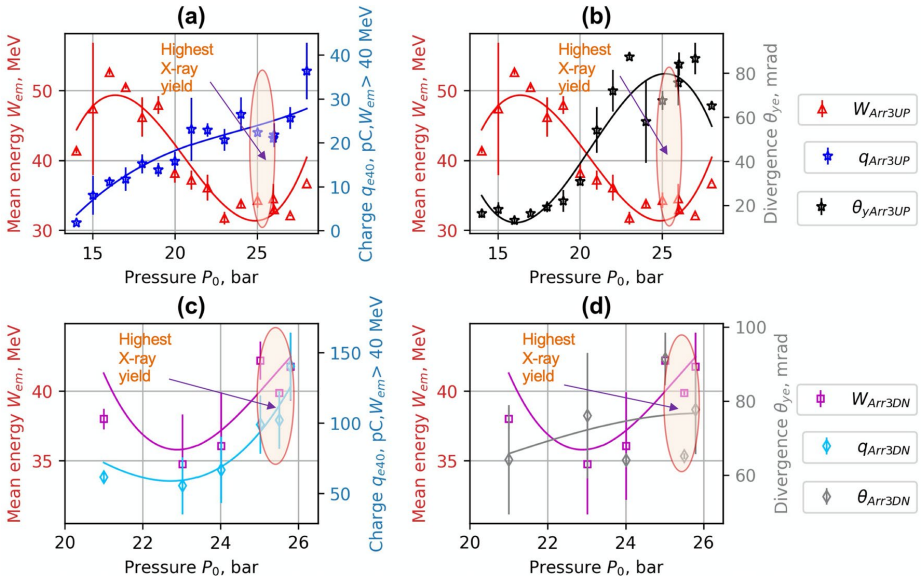

Figure 5. Experimental dependence of mean energy W_{mean}, charge q_{40} for $W_{mean} > 40$ MeV (**a**,**c**) and mean divergence θ_{ye} (FWHM) (**b**,**d**) of accelerated electrons on gas backing pressure for the array **Arr3** in wiggler geometry. $\boldsymbol{E_{Arr3UP}}$, $\boldsymbol{q_{Arr3UP}}$, $\boldsymbol{\theta_{Arr3UP}}$ were measured at the distance of 800 μm, and—$\boldsymbol{E_{Arr3DN}}$, $\boldsymbol{q_{Arr3DN}}$, $\boldsymbol{\theta_{Arr3DN}}$—at the distance of the laser beam above the nozzle of 400 μm. Interpolated solid lines provide a guide to the eye.

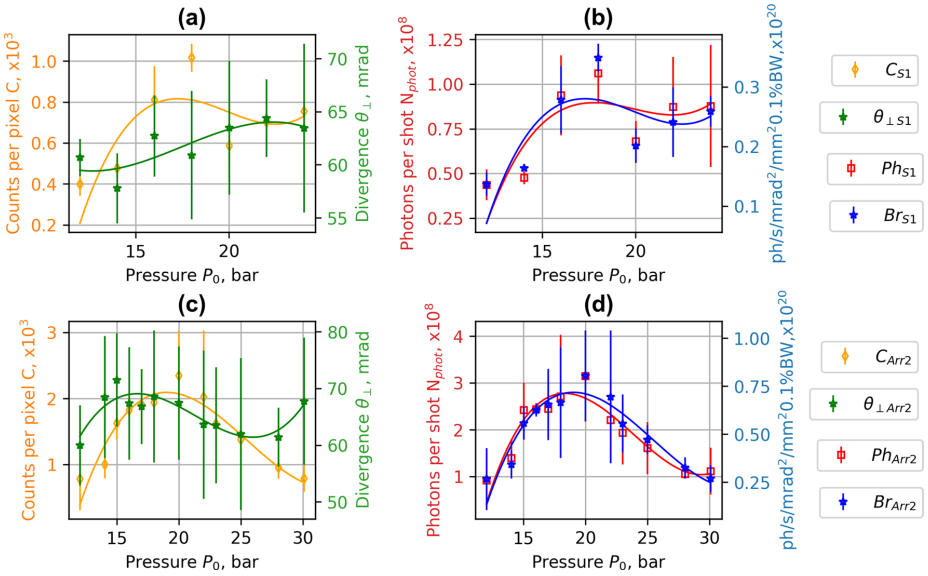

Figure 6. Experimental dependence of counts per pixel C, divergence θ (FHWM) (**a**,**c**), photons per shot N_{phot} and brightness Br (**b**,**d**) of X-ray radiation on gas backing pressure. $\boldsymbol{C_{S1}}$, θ_{S1}, Ph_{S1}, $\boldsymbol{Br_{S1}}$ correspond to the single nozzle **S1** and $\boldsymbol{C_{Arr2}}$, θ_{Arr2}, $\boldsymbol{Ph_{Arr2}}$, $\boldsymbol{Br_{Arr2}}$ correspond to the array **Arr2** in wiggler geometry. Interpolated solid lines provide a guide to the eye.

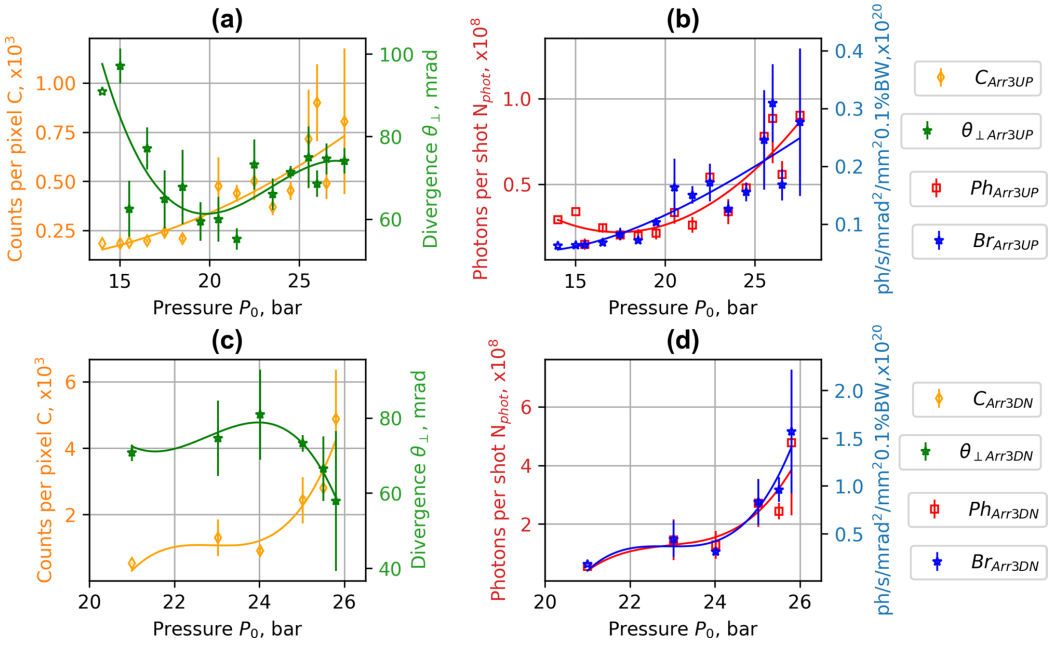

Figure 7. Experimental dependence of counts per pixel C, divergence θ (FHWM) (**a**,**c**), photons per shot N_{phot} and brightness Br (**b**,**d**) of X-ray radiation on gas backing pressure for the array **Arr3** in wiggler geometry. $\boldsymbol{C_{Arr3UP}}$, θ_{Arr3UP}, $\boldsymbol{Ph_{Arr3UP}}$, $\boldsymbol{Br_{Arr3UP}}$ were measured at the distance of 800 μm, and—$\boldsymbol{C_{Arr3DN}}$, θ_{Arr3DN}, $\boldsymbol{Ph_{Arr3DN}}$, $\boldsymbol{Br_{Arr3DN}}$ at the distance of laser beam above the nozzle of 400 μm. Interpolated solid lines provide a guide to the eye.

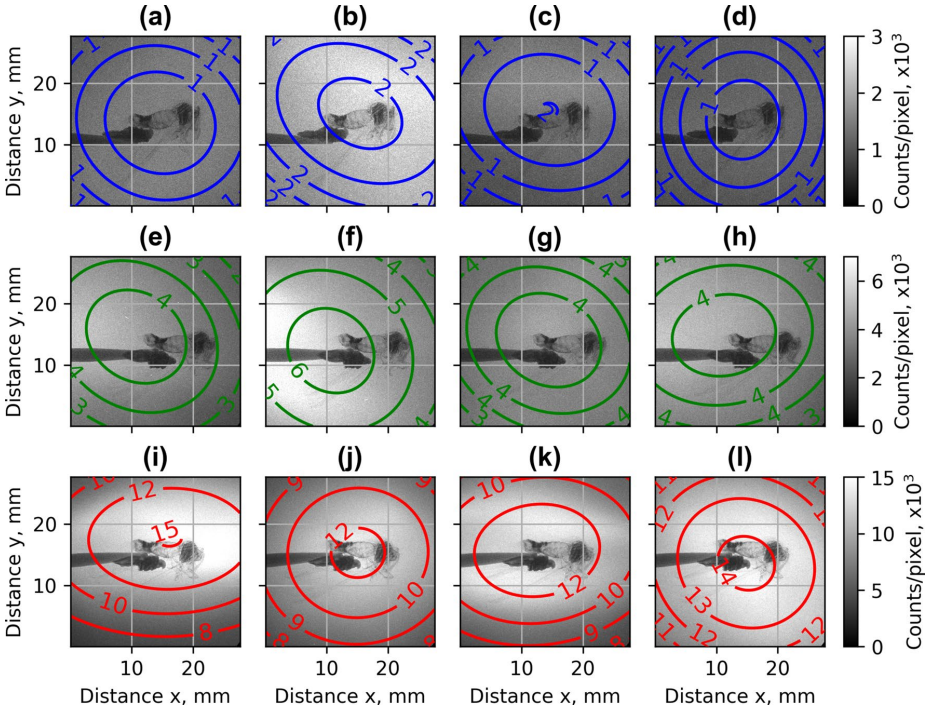

Figure 8. Examples of X-rays images, the colored ellipses represent regions with a number of counts per pixel higher than indicated (in thousands): single nozzle **S1** (**a**–**d**), array **Arr2** (**e**–**h**), and array **Arr3** (**i**–**l**) at the distance of laser beam above the nozzle of 400 μm.

No.	Description	Charge > 40 MeV, pC	Counts per pixel, FHWM	Critical energy, keV	Diver-gence θ (θ_{ey}), mrad, FHWM	Photons per shot, FHWM	Brightness, ph/s/mrad^2/ mm^2/0.1%BW, FHWM
#1	1.5 mm single slit converging–diverging nozzle **S1**	70 ± 10	900 ± 300	2.3 ± 0.2	75 ± 10 (80 ± 20)	$1.1 \pm 0.5 \times 10^8$	$0.3 \pm 0.1 \times 10^{20}$
#2	1.5 mm slit converg-ing–diverging nozzle with an array of 4 nozzles **Arr2**	85 ± 20	1800 ± 500	2.5 ± 0.2	80 ± 10 (80 ± 20)	$2.9 \pm 0.7 \times 10^8$	$0.7 \pm 0.1 \times 10^{20}$
#3	2.25 mm cylindrical converging–diverging nozzle with an array of 4 nozzles **Arr3** (distance 800 μm)	30 ± 10	900 ± 200	2.2 ± 0.2	50 ± 15 (80 ± 10)	$1.0 \pm 0.2 \times 10^8$	$0.3 \pm 0.1 \times 10^{20}$
#4	2.25 mm cylindrical converging–diverging nozzle with an array of 4 nozzles **Arr3** (distance 400 μm)	130 ± 25	4900 ± 1500	2.6 ± 0.1	70 ± 30 (90 ± 20)	$5.5 \pm 4.8 \times 10^8$	$1.6 \pm 0.5 \times 10^{20}$

Table 1. The data of accelerated electrons and betatron radiation of a single nozzle and arrays in wiggler geometry for $n_p = 1 \times 10^{19}$ cm^{-3} and $a_0 = 4.0$. In the #1–#3 cases, the laser beam was propagating 800 μm, in the #4 case—400 μm above the nozzle. The field of view of the camera was only 35 mrad; the divergence values of X-ray radiation are extrapolated from the evaluated Gaussian distribution.

that the radius of X-ray source changes from 3.5 ± 1 μm for single slit nozzle S1 and 11 bar of gas backing pressure to 7.5 ± 1 μm for array Arr2 and 29 bar of gas backing pressure. In the region of interest of measuring the brightness of X-ray corresponding to 15–26 bar of backing pressure, the source size was defined as 5 ± 1 μm in

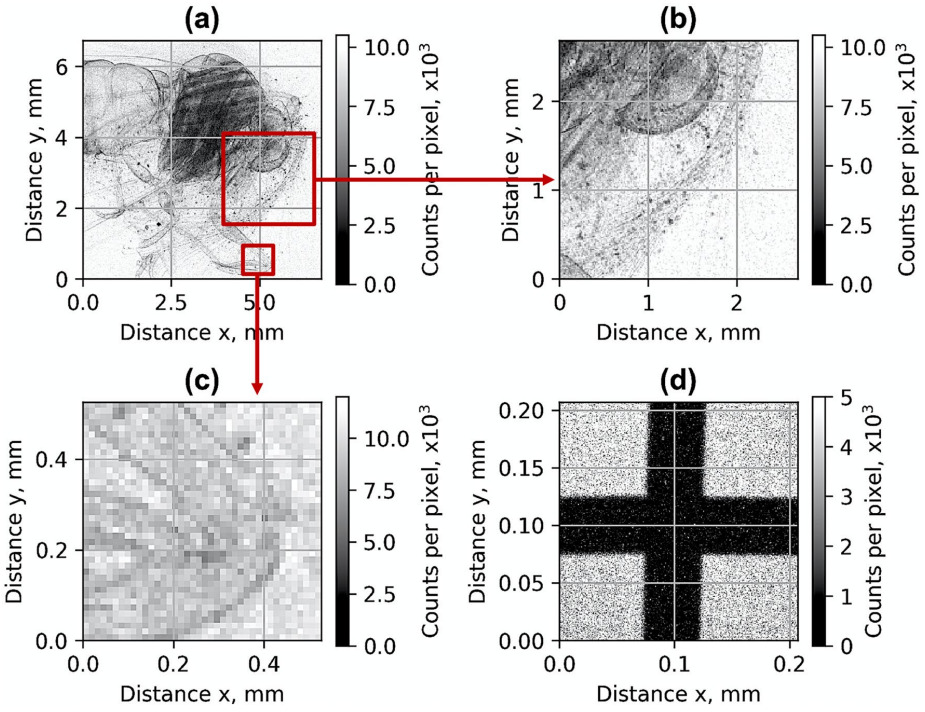

Figure 9. The X-ray transmission image (**a–c**) of a moth averaged over 10 shots and 50 μm tungsten cross-wires (**d**) for plasma concentration $n_p = 1 \times 10^{19}$ cm^{-3} using X-ray source of array **Arr3** for the laser beam propagating 400 μm above the nozzle.

average in both horizontal and vertical direction. The fixed value of 5 μm was used for the brightness calculation of the source for all nozzles indicated in Table 1.

The spectra of betatron radiation of the single nozzle S1 and array Arr2 had the best match to the synchrotron radiation with the critical energy of 2.3 ± 0.2 keV and 2.5 ± 0.2 keV correspondingly. The spectrum of the array Arr3 for laser-nozzle distance of 400 μm had the best matching to the synchrotron radiation with the critical energy of 2.6 ± 0.1 keV. The divergence values θ (FWHM), presented in Table 1, were calculated by measuring separately and averaging of the ellipse radii afterwards. The numbers in parentheses in Table 1 indicate the mean divergence θ_{ye} of electrons in the y-direction. The implementation of the nozzle array Arr2 increased the critical betatron energy by 8–10% relative to the single nozzle S1. For the Arr2, the number of X-ray photons per shot relative to the single S3 nozzle increased from 1.1×10^8 to 2.9×10^8 and the brightness of the source from 0.3×10^{20} to 0.7×10^{20} ph/s/mrad^2/mm^2/0.1%BW. For the array Arr3, the changing of the laser-nozzle distance from 800 μm to 400 μm increased the number of X-ray photons per shot from 1.0×10^8 to 5.5×10^8 and the brightness of the source—from 0.3×10^{20} to 1.6×10^{20} ph/s/mrad^2/mm^2/0.1%BW.

The X-ray source was used for the transmission imaging of biological objects. In Fig. 9a–c, the X-ray images of a moth averaged over ten shots are shown. Small details as leg edges and hairs of the moth of approximatively 20 μm diameter can be seen (Fig. 9b,c). The moth was placed outside of the vacuum chamber at the distance of 6 cm before the X-ray detector. The magnification was 1.08, and the imaging resolution was limited by the pixel size of 13.5 μm of the detector. The X-ray source can be further implemented for phase-contrast imaging (PCI) and tomography[44] allowing non-invasive analysis in low-absorbing materials, such as soft tissue. In-line, or propagation based, phase-contrast imaging (PB–PCI) requires no optical components. With appropriate propagation distances, the phase-shift evolves by itself into measurable intensity modulation. The PB-PCI imaging resolution was defined using the relations in reference[45,46]. In the case of Fig. 9d, the cross wires were located at 70 cm from the source. Assuming the Gaussian distribution, 10 μm diameter (FWHM) of the source, and magnification of 26, the imaging resolution was estimated to be 9 μm (defined as double the standard deviation of the source intensity distribution).

The propagation of the laser beam and the formation of the plasma channel was monitored using a probe beam split from the driving laser and crossing the gas jet perpendicularly. The interferograms of Wollaston prism was used for shadowgraphy diagnostics. The interferogram images of array Arr2 and Arr3 (Fig. 10) showed the formation of shock waves of gas jets. For Arr2, the shock waves were observed at the laser-nozzle distance of 800 μm (Fig. 10a). For Arr3, the substantial difference in the distribution of plasma density depending on the

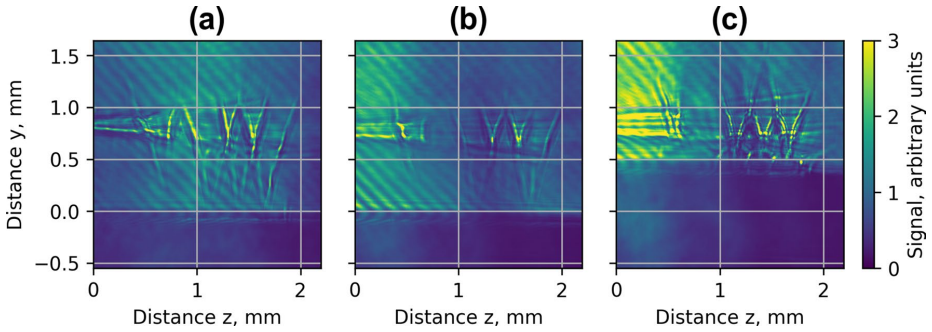

Figure 10. The interferograms of the array **Arr2** (**a**) and the array **Arr3** for the laser beam at the distance of 800 μm (**b**) and 400 μm (**c**) above the array for the $n_p = 1 \times 10^{19}$ cm^{-3}.

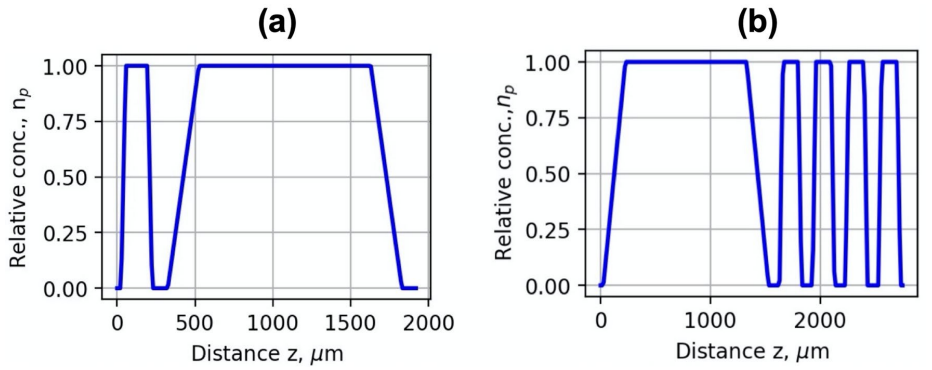

Figure 11. Simplified relative plasma density profiles of the injector (**a**) and wiggler (**b**) geometries used in the simulation.

distance of the laser beam above the nozzle is visible (Fig. 10b,c). At the distance of 800 μm (Fig. 10b), the width of the laser wakefield of the ionised region was narrower, in the range of 150–200 μm, and the shock waves only in the centre part of array Arr3 were visible. At the distance of 400 μm (Fig. 10c), the width of the ionised region increased to 200–250 μm, and the intersecting shock-wave fronts of all array nozzles were clearly visible.

Numerical simulation. To evaluate the impact of the plasma density grid on LWFA and X-ray radiation the iterative simulation process using the FBPIC PIC (Particle in Cell), and OpenFOAM algorithms was run. First, the simplified plasma concentration profiles were used in the FBIC simulation. The injector geometry was simulated by a 200 μm long plasma region, 100 μm gap and 1.5 mm plasma section for electron acceleration (Fig. 11a). A 1.5 mm long plasma acceleration section and wiggler comprising four 200 μm plasma regions and 100 μm gaps were used for the simulation of wiggler geometry (Fig. 11b).

Based on the FBIC LWFA results, several geometries of converging–diverging nozzles with different expansion rates were designed using OpenFOAM simulation, allowing to reach approximate plasma concentration profiles used in FBPIC simulation. The simulation parameters were chosen according to the experimental setup of Lund Ti:Sa laser. The laser strength parameter a_0 was calculated, taking into account the focal length of the focusing mirror of 465 mm and the laser beam diameter at the FWHM level of 8 μm. It corresponded to the $a_0 = 4.0$. The resolution of the mesh grid was 0.05 μm, and the time step was 0.17 fs. The simulation was performed for various acceleration distances, and the plasma concentration was changed within the range of 3×10^{18}–1×10^{19} cm^{-3}. Calculations were made for the gas mixture of He + 1%N_2.

In Fig. 12a, the LWFA simulation results of the spatial distribution of energy and charge of ionization injected electrons for the single nozzle is presented. The matched plasma wavelength of $n_p = 3 \times 10^{18}$ cm^{-3} allows achieving high energy and the lowest divergence of accelerated electrons. The electrons are injected continuously, however, causing a broad energy spectrum of accelerated electrons. In Fig. 12b, the simulation results of the injection scheme using combined density-triggered and nitrogen ionization for Arr4 in injector geometry are presented. Adjusting the laser strength parameter and matching the plasma wavelength for $a_0 = 4.0$ and $n_p = 3 \times 10^{18}$ cm^{-3} the formation of a quasi-monoenergetic bunch of higher charge was achieved.

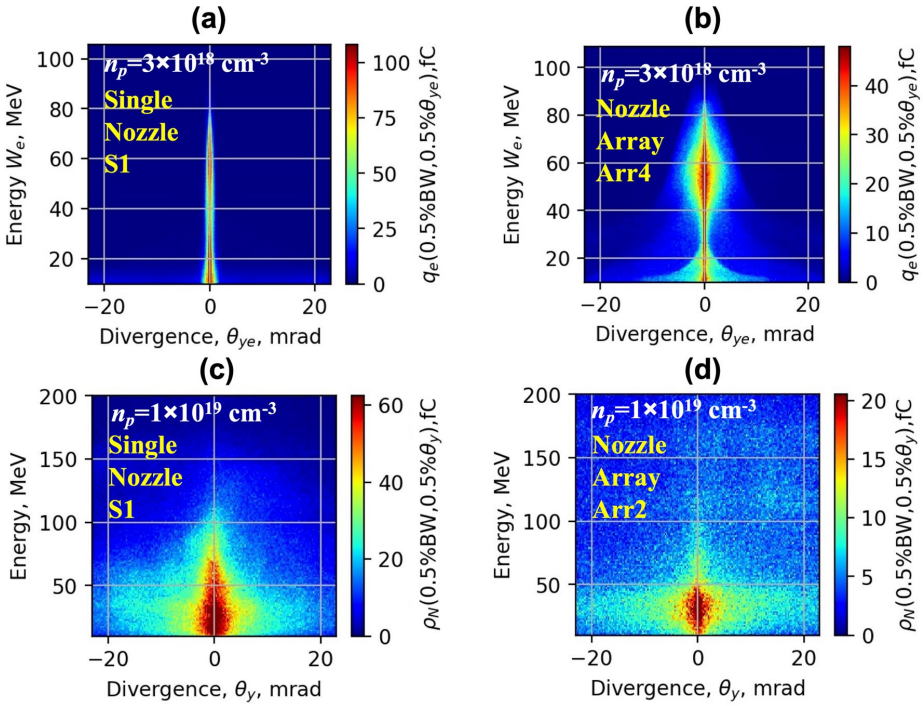

Figure 12. Simulated profiles of the transversal spatial distribution of the electron energy and charge for the single nozzle **S1** (**a**), array **Arr4** (**b**) in injector geometry for the mixture He + 1%N_2, a_0 = 4.0 and $n_p = 3\times10^{18}$ cm^{-3} at the acceleration distance z = 0.5 mm, and for $n_p = 1\times10^{19}$ cm^{-3} for the single nozzle **S1** (**c**) and array **Arr2** (**d**) at the acceleration distance z = 2.5 mm.

In Fig. 12c,d, the simulation results of single nozzle S1 and array Arr2 in wiggler geometry at the plasma concentration $n_p = 1\times10^{19}$ cm^{-3} are shown. The energy of accelerated electron for a single S1 nozzle and $n_p = 3\times10^{18}$ cm^{-3} reaches 150–200 MeV, the divergence is 4–6 mrad. With the increase of the gas concentration from $n_p = 3\times10^{18}$ cm^{-3} to $n_p = 1\times10^{19}$ cm^{-3}, the plasma wavelength becomes shorter and, several plasma waves are formed. The electrons are injected into the multiple plasma waves and the lateral plasma wake. The charge of the injected electrons increases, but the energy of accelerated electrons drops to 30–80 MeV, and the divergence of the electron beam increases to 20–40 mrad (Fig. 12c). In Fig. 12d, the simulation results of electron acceleration using the nozzle array Arr2 is presented. First, the electrons are accelerated in the gas jet of a longer section of array Arr2. Then, the electrons pass the second section, where the divergence of the electron beam increases up to 30–50 mrad.

To estimate the parameters of X-ray betatron radiation, the data of momenta and spatial distribution of electrons simulation were post-processed using analytical relations (see Supplementary information S1 for details). In Fig. 13a–c, the amount of charge of electrons corresponding the divergence in the transversal direction θe (a), betatron radius r_β (b), and critical synchrotron energy E_c (c) are presented. The divergence in transversal direction θe (FWHM) was calculated as an average of the divergence of electrons in the x- and in y-direction. The betatron radius was defined as the transverse amplitude of electron motion in the ion channel produced in the wake of the laser pulse[47].

The calculations have shown that the implementation of nozzle array Arr2 increased the number of electrons having a higher transversal divergence and slightly extended the average of betatron radius and critical energy. In Fig. 13d, the calculated spectral density dN_{phot}/dE_r of radiated photon number per shot for the array Arr2 and single nozzle S1 is presented, where E_r is the energy of emitted photons.

The calculation demonstrated the increase of the number of photons per shot caused by the plasma density array by a factor of 2 and the total number of photon number reached 5×10^8. The simulation results of critical energy E_c and the number of photons per shot were in good correspondence with experimental results. However, the calculated average radius of betatron r_β was in the range of 1–2 μm and differed from the size of 5 μm got by cross-wire diffraction measurements. It also resulted in mismatched values of the brightness of X-ray radiation.

To interpret the experimental results of the spatial distribution of gas jets, the fluid simulation using the rhoSimpleFoam compressible stationary OpenFOAM solver was performed. In Fig. 14a,b, the simulation results of gas pressure and concentration at the backing pressure of 30 bar are presented. The simulation has shown the

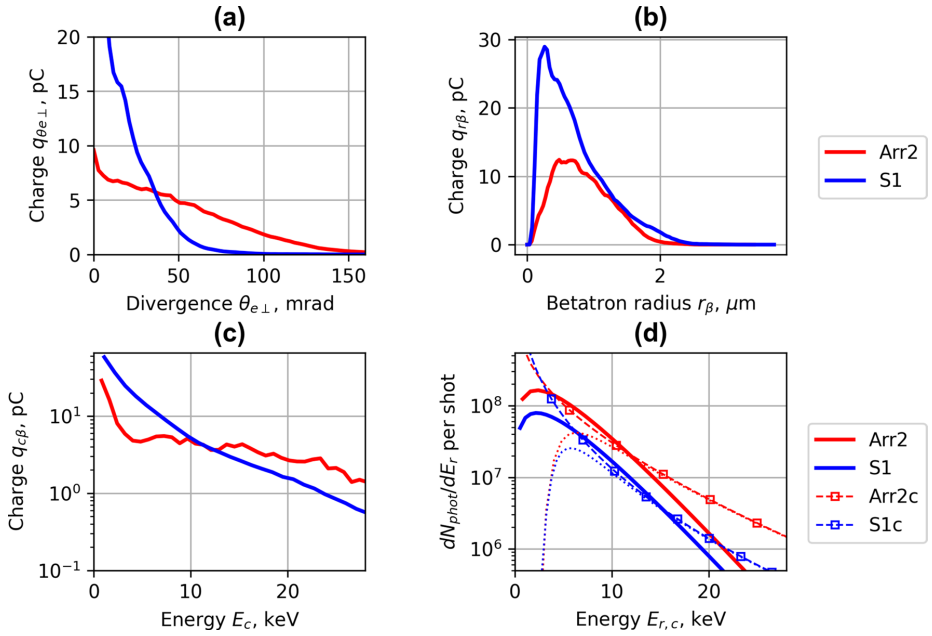

Figure 13. The simulated charge of electrons accelerated by array **Arr2** and single nozzle **S1** having divergence θ_e (FWHM) (**a**), betatron radius r_β (**b**), and critical synchrotron energy E_c (**c**). Calculated spectral density dN_{phot}/dE_r of photon number per shot of electrons accelerated by array **Arr2** and single nozzle **S1** (**d**) for $a_0 = 4.0$ and $n_p = 1 \times 10^{19}$ cm^{-3}. The dashed lines **Arr2c** and **S1c** show the calculated density of dN_{phot}/dE_r, the dotted lines—the dN_{phot}/dE_r attenuated by the materials placed between the X-ray source and camera, and the bold lines **Arr2** and **S1** show the best match of the synchrotron-like spectra with the mean critical energy E_c measured using Ross filters.

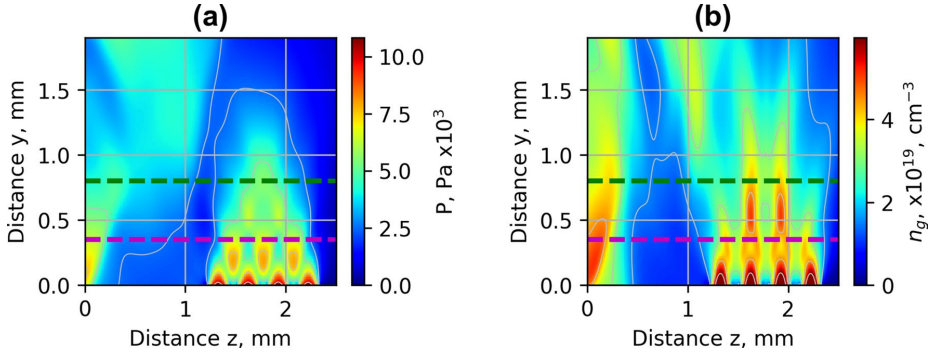

Figure 14. Simulated spatial distribution of pressure (**a**) and gas concentration (**b**) of He jet of **Arr3** at the backing pressure of 30 bar. The green dotted line indicates the distance of the laser beam of 800 μm, and the magenta dotted line shows the distance of 400 μm above the nozzle.

formation of diamond-shaped pressure (Fig. 14a) and density (Fig. 14b) grid is caused by the interference of shock waves of colliding jets. The shock waves also affected the region of the nozzle array used for LWFA. Thus, the region was compressed, and a shock wavefront between the first and second part of the array was built. The shock waves increased the gas density of the middle jets by a factor of 2 relatively to the edge jets without the neighbouring jet streams. The middle jets reached the height of 0.9–1.2 mm while the height of outside jets was 0.5–0.6 mm.

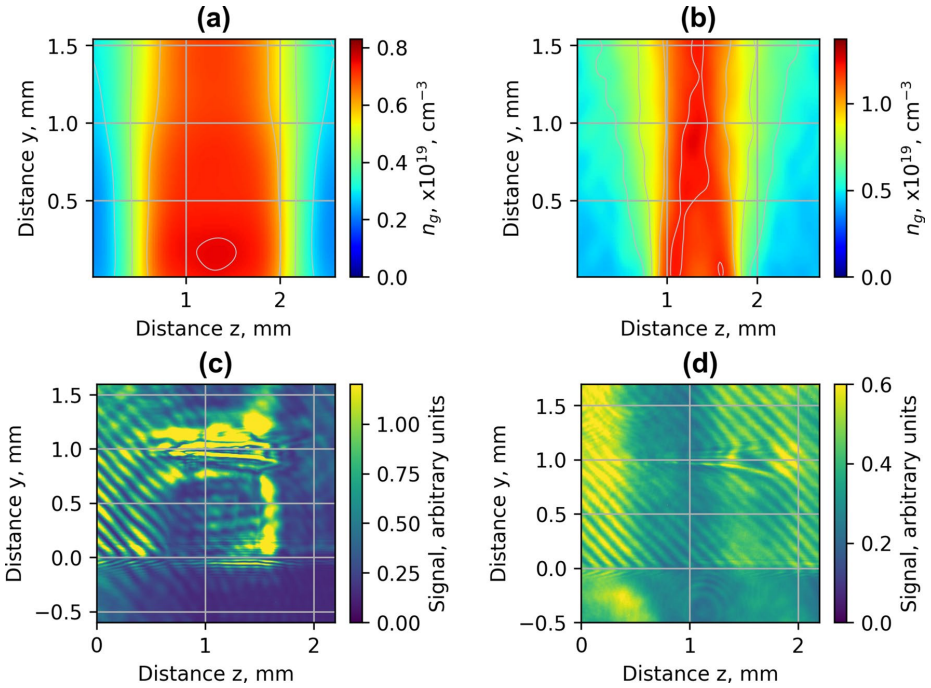

Figure 15. Gas concentration profiles reconstructed using measured wavefront sensor phase diagrams for the cylindrical converging–diverging nozzle with the diameter of 2.25 mm (**a**), slit converging–diverging nozzle with the length of 1.5 mm **S1** (**b**) at the backing pressure of 30 bar. Shadowgrams of the nozzle **S1** (**c**), and **Arr4** in injector geometry (**d**).

Discussion

The data analysis of backing pressure scan has shown that the maximum of X-ray radiation corresponds to the maximum divergence of the electron beam while maintaining a high accelerated charge. For the single nozzle S1 and array Arr2 (Fig. 4), the maximum energy of accelerated electrons was reached at the backing pressure of 5–12 bar. At this backing pressure, the gas density matches the plasma bubble condition and is optimal for the acceleration of electrons. However, the divergence of the electron beam is small, and the yield of X-ray radiation is low. When increasing the gas density, even though the energy starts to drop, the accelerated charge grows, and the divergence increases a lot leading to an increase in X-ray flux. The maximal number of X-ray photons per shot was reached at a maximum of divergence and minimum of mean energy at the backing pressure of 18–21 bar for the single nozzle S1 and 24–26 bar for the array Arr2. The nozzle S1, Arr2 and Arr3 arrays have different gas expansion rates resulting in different gas concentration at the output of the nozzle. The corresponding gas concentration for S1 nozzle and Arr2 was reached at lower backing pressure relative to Arr3 nozzle. The distance of LWFA acceleration for Arr3 nozzle was longer than for S1 nozzle. Therefore, the energy of accelerated electrons and X-ray yield relative to S1 nozzle was higher. In wiggler geometry, the presented results of S1 and Arr2, Arr3 correspond to the highest photons per shot and brightness observed. In the injector geometry, the presented results of Arr4 correspond to the best results of the formation of quasi-monoenergetic electron bunches.

Implementation of nozzle arrays in wiggler geometry resulted in the increase of divergence of electron beam and growth of accelerated charge (Figs. 4, 5). The comparison of shadowgrams of plasma diagnostics of the S1, Arr2, Arr3 nozzles (Figs. 10, 15c) and the OpenFOAM simulation results (Fig. 14) confirmed the formation of the grid of maximums and minimums of gas concentration in the propagation path of laser beam approximately corresponding to the plasma density profiles simulated using FBPIC algorithm. The modelled accelerator and wiggler plasma sections indicated the growth of divergence of accelerated electrons and photon number of X-ray radiation relative to a single plasma section profile. For the array Arr2, the shock waves were present at the laser-nozzle distance of 800 μm. For the Arr3 having higher gas jet expansion rate, the laser beam did not cross all the intersecting jets of smaller nozzles of the diameter of 200 μm at the height of 800 from the output of nozzles. Hence, only by changing the distance between the laser beam and nozzle output from 800 to 400 μm, the laser beam propagated through the whole region of varying gas density. The gas density grid increased the transversal motion of electrons and increased the efficiency of X-ray radiation. The spatial distribution of X-ray radiation varied from circular to elliptical one as well as the orientation of elliptical distribution altered from shot to shot. It indicated that the divergence and orientation of X-ray radiation depend on the spatial distribution of

	Geometry	Laser strength parameter a_0	Plasma concentration, cm^{-3}	Laser spot FWHM, μm	Gas
1	Injector	4.0	3×10^{18}	8	He
2	Injector	4.0	2×10^{18}	8	$He+1\%N_2$
3	Wiggler	4.0	1×10^{19}	8	$He+1\%N_2$

Table 2. The experimental LWFA parameters.

plasma rather than on laser polarization. In average, the X-ray distribution was more elongated in x-direction parallel to laser polarisation, however. The interference of shock waves is defined by the period of nozzle array as well as by the pressure, temperature, and expansion rate of colliding jets. The numerical plasma simulation has shown that using array in wiggler geometry increases the divergence of accelerated electrons (Figs. 12c,d, 13a) by 30–50%. More electrons have higher critical energy of synchrotron radiation, and their contribution to the total X-ray emission is more extensive (Fig. 13c,d). The ratio of transversal and longitudinal momenta of electrons and betatron radius changes at a smaller extent in the range of 1–2 μm (Fig. 13b). The radius of the betatron source measured experimentally was 5 ± 1 μm on average. The difference between the calculated and experimentally measured radius of X-ray source could be explained by a much broader divergence of electrons corresponding to the transversal distribution radius > 50 μm at the acceleration distance of 2.5 mm. The resulting spectrum and source size of X-ray radiation is defined by the superposition of radiation of electrons with diverse momenta radiating at different spatial positions. We assume the main contribution to the X-ray radiation is from electrons of higher energy concentrated in the radius of 5 μm approximately. The X-ray radiation from the central 5 μm radius region can also explain the decrease of X-ray divergence (FWHM) observed at the backing pressure corresponding to the highest X-ray radiation yield. The electrons located in the broad halo of 50 μm have lower energy and do not contribute substantially to the X-ray radiation with the photon energy of several keV.

Conclusion

In conclusion, the implementation of the nozzle array with separate regions of LWFA and gas density grid raised the efficiency of X-ray generation and increased the number of photons per shot by a factor of 2–3 relative to a single-jet gas target source. The critical energy of synchrotron radiation measured using Ross filters was in the range of 2.2–2.6 keV. The radius of the X-ray source in the region of the best X- ray yield was defined as 5 μm on average. The number of photons per shot was in the range of 1.0×10^8–5.5×10^8, and the brightness was 0.3×10^{20}–1.6×10^{20} ph/s/mrad^2/mm^2/0.1%BW. The analysis of experimental data and numerical simulation has shown that the increased efficiency of X-ray radiation was caused by the formation of a gas density grid created by colliding jets. The experimental results of the energy and number of photons per shot were in good correspondence with the results of FBPIC simplified model. The calculated betatron radius of 1–2 μm differed from the measured X-ray source size of 5 μm however. The difference in sizes can be explained by the spatial distribution of radiating electrons in the radius of 50 μm on average. Also, the fixed betatron radius used in the definition of brightness has added the uncertainty in the calculations. The imaging tests of the biological samples in the transmission X-rays demonstrated the resolution higher than 20 μm. The resolution was limited by the pixel size of the detector of 13.5 μm. The X-ray source can be implemented for phase-contrast imaging and tomography. The estimated PB-PCI source size-limited resolution was 9 μm. In future work, it would be advantageous to test the nozzle arrays with independent adjustment of backing pressure of gas supply of accelerating and wiggler section. It would allow maximizing the energy of accelerated electrons and divergence of the electron beam. The collected data will be used for the optimisation of micronozzle geometry and efficiency of the X-ray source. The laser-assisted fabrication technology of the micronozzles from single fused silica block ensures higher precision, resistance to optical damage, and the formation of tailored plasma profiles with the dimensions of less than 40 μm with surface roughness < 1 μm.

Methods

Experimental setup. The diagram of the experimental setup for LWFA of electrons and betatron radiation measurement is presented in Fig. 1. In Table 2, the LWFA parameters in the wiggler and injector geometry are shown. For the LWFA experiments, the 800 nm 1.8 J Ti:Sa laser at the repetition rate < 1 Hz with a pulse duration of 35 fs, and pulse energy on the target of 700–880 mJ was used. The laser beam was focused on the gas jet in a vacuum chamber using a 4-inch offset parabolic mirror with the focal length of 465 mm, leading to a focal spot of 8 μm at FWHM. The laser strength parameter a_0 was defined as the maximum amplitude of the normalized vector potential of the laser field A: $a_0 = eA/m_e c^2$, where A is the maximum amplitude of the laser electric field, e—electron charge, m_e—electron mass, and c is the speed of light in vacuum[1]. In practical units, the a_0 parameter for the linearly polarized laser field with a Gaussian radial profile was calculated as $a_0^2 = 7.3\times10^{-19}[\lambda_L(\mu m)]^2 I_0(W/cm^2)$, where λ_L – is the laser wavelength and I_0 – is the laser intensity. The aberration correction of the laser beam has been controlled by a deformable mirror, which ensured the high quality of the focused beam. The laser polarisation was horizontal along the x-axis. The energy of the accelerated electrons was measured using a Kodak Lanex Regular scintillation screen with a dipolar 0.8 T magnet of the total length of 20 cm located at the distance of 50 mm from the source. The width of the magnetic spectrometer was 5 cm, and the gap of the dipole gap was 15 mm. The measuring range of the spectrometer was 20–300 MeV. The relation between electron energy and position on the scintillating screen were determined by simulation using COMSOL Mul-

No.	First section			Second section		
	Description	Output dimensions, mm (L × W)	Throat dimensions, mm, (L2 × W2)	Description	Output dimensions, mm, (L1 × W1)	Throat dimensions, mm, (L3 × W3)
#1	Single slit converging–diverging nozzle **S1**	1.5 × 1.2	1.5 × 0.12	–	–	–
#2	Single slit converging–diverging nozzle **Arr2**	1.5 × 1.2	1.5 × 0.12	Slit array of 4 nozzles	0.2 × 0.2	0.2 × 0.2
#3	Single cylindrical converging–diverging nozzle **Arr3**	Φ2.25	Φ0.5	Slit array of 4 nozzles	0.2 × 0.2	0.2 × 0.2
#4	Single slit converging–diverging nozzle **Arr4**	1.5 × 1.2	1.5 × 0.12	Single slit converging–diverging nozzle	0.3 × 0.27	0.3 × 0.18

Table 3. The list of nozzles used in the experiment.

tiphysics and the measured map of the magnetic field. The energy resolution at 300 MeV was 1.3%/mrad. The uncertainty introduced by the ± 10 mrad divergence of the 125 MeV electron beam was 7.5 MeV, corresponding to the accuracy of ± 6%.

Scintillation screen images were captured using the Andor Zyla 4.2 Plus CMOS 16-bit camera. The camera was of 2048 × 2048 pixels with a pixel size of 6.5 µm. The energy and divergence of the electron beam were calculated using the images of Lanex scintillation screen. The response of the full imaging system was calibrated using previously published calibration factors of 6.95×10^{-8} pC/count for the scintillating screens measured at linear accelerator[48,49]. The betatron radiation was registered using the Andor iKon-L SO X-ray camera, sensitive to X-rays up to 20 keV. The X-ray CCD was of 2048 × 2048 square pixels with a pixel size of 13.5 µm. The camera window was made of 250 µm-thick beryllium. A 50 µm Kapton window with an additional shield of 3 µm aluminium foil was installed at the outlet of the vacuum chamber. The X-ray camera was installed at a distance of 73 cm from the source, and the betatron radiation passed through the air gap of 12 cm. To characterize the flux distribution and energy distribution of the X-ray pulse, a Ross-filter array[50] was inserted into the X-ray beam at the distance of 6 cm from the exit of the experimental chamber. The filter array used was composed of intersecting strips of the elements Ni, Cu, Zn, Al, Ti, Zr, Cu of thickness 5 µm, 25 µm, 5 µm, 6 µm, 6 µm, 3 µm, 3 µm respectively. The transmission of the betatron X-rays through the filters was measured using Andor iKon-L Xray camera and compared to the transmission of synchrotron-like spectra with critical energy E_c using least-squares fitting method[51]. The radius of the betatron source was determined by measuring the Fresnel diffraction from the 50 µm tungsten cross-wires, placed 28 mm from the source, magnifying the image 26 times and comparing the intensities of X-ray signals in the horizontal and vertical directions. The intensity distribution of the Fresnel diffraction was calculated using the relations given in[42–44].

Nozzle manufacturing. The geometry and dimensions of nozzle arrays are presented in Fig. 2 and Table 3. The designed micronozzles were manufactured from fused silica with a thickness of 6.3 mm, using the second harmonic radiation (532 nm) of the DPSS nanosecond laser (from Ekspla) and the second harmonic radiation (515 nm) of the femtosecond Yb:KGW Pharos laser (from Light Conversion).

All nozzle frames were fabricated using the nanosecond laser and a rear-side or bottom-up machining approach alone, which allowed a high material removal rate[29,52]. However, depending on the design, some of the inner channels were fabricated in combination with the front-side laser ablation. This step was required due to the incapability of the rear-side machining technique to fabricate high negative taper angles, which are unavoidable in the configuration of converging–diverging Laval nozzles. Additionally, the output surface of nozzles with small channels was mechanically polished to reduce the gas concentration drop due to the chamfered edges[30]. For the formation of structures smaller than 200 µm, the femtosecond laser-induced selective chemical etching FLICE technique was implemented. The FLICE technique ensured the formation of microchannels with the surface roughness less than 1 µm[31,52,53].

Nozzle characterisation. Characterisation of gas density profiles of the nozzle used in the LWFA experiments was performed using an optical wavefront sensor, the collimated light beam of a HeNe laser, and the Python library of the open-source 3D tomographic image reconstruction algorithms "Astra Toolbox"[54]. The integral phase change was recorded by the wavefront sensor in two orthogonal planes perpendicular to the nozzle symmetry axis. The wavefront sensor resolution was 157 × 117 pixels with a pixel size of 17 µm. Using the integral phase distribution $\varphi(x,y,z)$, the gas concentration n was calculated by the relation $n = \varepsilon_0 \lambda \varphi / \pi \alpha d$, where ε_0 is the vacuum permittivity, $\lambda = 632$ nm is the laser wavelength, $\alpha = 18.52 \times 10^{-41}$ Fm^2 is the polarizability of the argon gas atoms, and $d = 17$ µm is the reconstruction length of cubic voxels. The tomographic reconstruction of the phase volume profile was calculated using Simultaneous Iterative Reconstruction Technique (SIRT) algorithm[55]. The reconstructed concentration profiles of the nozzles S1 and 2.25 mm nozzle of Arr3 at the backing pressure of 30 bar argon are presented in Fig. 15a,b, respectively. The characterisation has shown that the gas target of the single slit converging–diverging 1.5 mm nozzle S1 has the 0.9 mm-long gas concentration plateau and the ramps with the length of 0.8 mm at each side of the nozzle. The single cylindrical Laval nozzle with the diameter of 2.25 mm has the 1.5 mm-long gas concentration plateau and the ramps with the length of 0.6 mm at each side of the nozzle. The shadowgrams of the single nozzle S1 (c), and array Arr4 in injector geometry (d) are shown in Fig. 15c,d, respectively.

Estimating the dependence of plasma concentration n_p on backing pressure, the approach of ideal gases was used. The molecular concentration of ideal gases n_g was calculated as $n_g = N_A \rho / M$, where N_A is the Avogadro constant, ρ is the gas density, and M is the molar mass of the gas[56]. At the standard temperature and pressure of $T = 273.15$ K, and $P = 101.325$ kPa, n_g corresponds to 2.687×10^{25} m^{-3}. For the calculation of the molecular gas concentration of the same gas under two different sets of the pressure $P_{1,2}$, volume $V_{1,2}$ and temperature $T_{1,2}$, the relation $p_1 V_1 / T_1 = p_2 V_2 / T_2$ was used. The molecular gas concentration increases proportionally to the ratio of actual pressure and temperature. The molecular concentration in the central part of the Arr2 cylindrical nozzle at the backing pressure of 26 bar and n_g was estimated as 5×10^{18} cm^{-3}. The same concentration for the S1 nozzle was reached at the backing pressure of 18 bar. Calculating the plasma concentration n_p, it was assumed that helium is fully ionized to the level of He^{+2}, and helium plasma concentration n_p corresponding to the $n_g = 5 \times 10^{18}$ cm^{-3} was estimated as $n_p = 1 \times 10^{19}$ cm^{-3}.

The Figs. 3, 4, 5, 6, 7, 8, 9, 10, 11, 12, 13, 14 and 15 and the Fig. S1 in the Supplementary information were visualized using Matplotlib plotting library for the Python programming language[57].

Data availability

The authors confirm that all of the data used in this study are available from the corresponding author on reasonable request.

Received: 3 June 2020; Accepted: 17 September 2020
Published online: 08 October 2020

References

1. Esarey, E., Schroeder, C. B. & Leemans, W. P. Physics of laser-driven plasma-based electron accelerators. *Rev. Mod. Phys.* **81**, 1229–1285 (2009).
2. Corde, S. *et al.* Femtosecond x rays from laser-plasma accelerators. *Rev. Mod. Phys.* **85**, 1–48 (2013).
3. Albert, F. & Thomas, A. G. R. Applications of laser wakefield accelerator-based light sources. *Plasma Phys. Controlled Fusion* **58**, 103001 (2016).
4. Sprangle, P. *et al.* Wakefield generation and GeV acceleration in tapered plasma channels. *Phys. Rev. E Stat. Nonlinear Soft Matter Phys.* **63**, 564051–5640511 (2001).
5. Matlis, N. H. *et al.* Transient behavior of a supersonic three-dimensional micronozzle with an intersecting capillary. *J. Appl. Phys.* **119**, 074501 (2016).
6. Gallardo González, I. *et al.* Effects of the dopant concentration in laser wakefield and direct laser acceleration of electrons. *New J. Phys.* **20**, 053011 (2018).
7. Zeng, M., Chen, M., Sheng, Z. M., Mori, W. B. & Zhang, J. Self-truncated ionization injection and consequent monoenergetic electron bunches in laser wakefield acceleration. *Phys. Plasmas* **21**, 030701 (2014).
8. Koehler, A. *et al.* Minimizing betatron coupling of energy spread and divergence in laser-wakefield accelerated electron beams. https://arxiv.org/abs/1905.02240 (2019).
9. Fubiani, G., Esarey, E., Schroeder, C. B. & Leemans, W. P. Beat wave injection of electrons into plasma waves using two interfering laser pulses. *Phys. Rev. E Stat. Phys. Plasmas Fluids Relat. Interdiscip. Topics* **70**, 12 (2004).
10. Hansson, M., Aurand, B., Ekerfelt, H., Persson, A. & Lundh, O. Injection of electrons by colliding laser pulses in a laser wakefield accelerator. *Nucl. Instrum. Methods Phys. Res. Sect. A* **829**, 99–103 (2016).
11. Ta Phuoc, K. *et al.* Betatron radiation from density tailored plasmas. *Phys. Plasmas* **15**, 063102 (2008).
12. Schmid, K. *et al.* Density-transition based electron injector for laser driven wakefield accelerators. *Phys. Rev. Spec. Topics Acceler. Beams* **13**, 91301–91302 (2010).
13. Gonsalves, A. J. *et al.* Tunable laser plasma accelerator based on longitudinal density tailoring. *Nat. Phys.* **7**, 862–866 (2011).
14. Vargas, M. *et al.* Improvements to laser wakefield accelerated electron beam stability, divergence, and energy spread using three-dimensional printed two-stage gas cell targets. *Appl. Phys. Lett.* **104**, 174103 (2014).
15. Zhang, Z. *et al.* Generation of high quality electron beams from a quasi-phase-stable cascaded laser wakefield accelerator with density-tailored plasma segments. *New J. Phys.* **17**, 103011 (2015).
16. Hansson, M. *et al.* Localization of ionization-induced trapping in a laser wakefield accelerator using a density down-ramp. *Plasma Phys. Controlled Fusion* **58**, 055009 (2016).
17. Swanson, K. K. *et al.* Control of tunable, monoenergetic laser-plasma-accelerated electron beams using a shock-induced density downramp injector. *Phys. Rev. Acceler. Beams* **20**, 051301 (2017).
18. Hansson, M. *et al.* Down-ramp injection and independently controlled acceleration of electrons in a tailored laser wakefield accelerator. *Phys. Rev. Spec. Top. Acceler. Beams* **18**, 71303 (2015).
19. Faure, J. *et al.* A review of recent progress on laser-plasma acceleration at kHz repetition rate. *Plasma Phys. Controlled Fusion* **61**, 014012 (2019).
20. Ferri, J. *et al.* High-Brilliance Betatron γ -Ray Source Powered by Laser-Accelerated Electrons. *Phys. Rev. Lett.* **120**, 254802 (2018).
21. Zhu, X.-L. *et al.* Extremely brilliant GeV γ-rays from a two-stage laser-plasma accelerator. *Sci. Adv.***6**, eaaz7240 (2020).
22. Stuart, B. C., Feit, M. D., Rubenchik, A. M., Shore, B. W. & Perry, M. D. Laser-induced damage in dielectrics with nanosecond to subpicosecond pulses. *Phys. Rev. Lett.* **74**, 2248–2251 (1995).
23. Butkutė, A. *et al.* Optical damage thresholds of microstructures made by laser three-dimensional nanolithography. *Opt. Lett.* **45**, 13 (2020).
24. Xu, S. Z. *et al.* Experimental study on 800 nm femtosecond laser ablation of fused silica in air and vacuum. *Nucl. Instrum. Methods Phys. Res., Sect. B* **385**, 46–50 (2016).
25. Mannion, P. T., Magee, J., Coyne, E., O'Connor, G. M. & Glynn, T. J. The effect of damage accumulation behaviour on ablation thresholds and damage morphology in ultrafast laser micro-machining of common metals in air. *Appl. Surf. Sci.* **233**, 275–287 (2004).
26. Weber, M. J. *Handbook of Optical Materials*. *Handbook of Optical Materials* (CRC Press, 2018). https://doi.org/10.1201/9781315219615.
27. Prencipe, I. *et al.* Targets for high repetition rate laser facilities: Needs, challenges and perspectives. *High Power Laser Sci. Eng.* **5**, 17 (2017).
28. Rovige, L. *et al.* Demonstration of stable long-term operation of a kilohertz laser-plasma accelerator. *Phys. Rev. Acceler. Beams* **23**, 093401 (2020).
29. Tomkus, V. *et al.* High-density gas capillary nozzles manufactured by hybrid 3D laser machining technique from fused silica. *Opt. Express* **26**, 27965 (2018).

30. Tomkus, V. *et al.* Impact of the wall roughness on the quality of micrometric nozzles manufactured from fused silica by different laser processing techniques. *Appl. Surf. Sci.* **483**, 205–211 (2019).
31. Döpp, A. *et al.* 3D printing of gas jet nozzles for laser-plasma accelerators. *Rev. Sci. Instrum.* **87**, 073505 (2016).
32. Schmid, K. & Veisz, L. Supersonic gas jets for laser-plasma experiments. *Rev. Sci. Instrum.* **83**, 053304 (2012).
33. Lehe, R., Kirchen, M., Andriyash, I. A., Godfrey, B. B. & Vay, J. L. A spectral, quasi-cylindrical and dispersion-free Particle-In-Cell algorithm. *Comput. Phys. Commun.* **203**, 66–82 (2016).
34. Kostyukov, I., Kiselev, S. & Pukhov, A. X-ray generation in an ion channel. *Phys. Plasmas* **10**, 4818–4828 (2003).
35. Schnell, M. *et al.* Characterization and application of hard X-ray betatron radiation generated by relativistic electrons from a laser-wakefield accelerator. *J. Plasma Phys.* **81**, 1–38 (2015).
36. Köhler, A. *et al.* Single-shot betatron source size measurement from a laser-wakefield accelerator. *Nucl. Instrum. Methods Phys. Res., Sect. A* **829**, 265–269 (2016).
37. OpenCFD Ltd. The Open Source CFD Toolbox, Version v1906. (2019).
38. Maddox, B. R., Park, H. S., Remington, B. A. & McKernan, M. Calibration and characterization of single photon counting cameras for short-pulse laser experiments. *Rev. Sci. Instrum.* **79**, 10E924 (2008).
39. Fourment, C. *et al.* Broadband, high dynamics and high resolution charge coupled device-based spectrometer in dynamic mode for multi-keV repetitive x-ray sources. *Rev. Sci. Instrum.* **80**, 083505 (2009).
40. Fourmaux, S. *et al.* Demonstration of the synchrotron-type spectrum of laser-produced Betatron radiation. *New J. Phys.* **13**, 033017 (2011).
41. Hussein, A. E. *et al.* Laser-wakefield accelerators for high-resolution X-ray imaging of complex microstructures. *Sci. Rep.* **9**, 3249 (2019).
42. Kneip, S. *et al.* Bright spatially coherent synchrotron X-rays from a table-top source. *Nat. Phys.* **6**, 980–983 (2010).
43. Tilikin, I. N., Shelkovenko, T. A., Pikuz, S. A. & Hammer, D. A. Determination of the size of a radiation source by the method of calculation of diffraction patterns. *Opt. Spectrosc. (English translation of Optika i Spektroskopiya)* **115**, 128–136 (2013).
44. Svendsen, K. *et al.* Optimization of soft X-ray phase-contrast tomography using a laser wakefield accelerator. *Opt. Express* **26**, 33930 (2018).
45. Gureyev, T. E. *et al.* Some simple rules for contrast, signal-to-noise and resolution in in-line x-ray phase-contrast imaging. *Opt. Express* **16**, 3223 (2008).
46. Wilkins, S. W. *et al.* On the evolution and relative merits of hard X-ray phase-contrast imaging methods. *Philos. Trans. R. Soc. A Math. Phys. Eng. Sci.* **372**, 20130021 (2014).
47. Rousse, A. *et al.* Production of a keV X-ray beam from synchrotron radiation in relativistic laser-plasma interaction. *Phys. Rev. Lett.* **93**, 135005 (2004).
48. Hansson, M. *et al.* Localization of ionization-induced trapping in a laser wakefield accelerator using a density down-ramp. *Plasma Phys. Controll. Fusion* **58**, 055009 (2016).
49. Buck, A. *et al.* Absolute charge calibration of scintillating screens for relativistic electron detection. *Rev. Sci. Instrum.* **81**, 033301 (2010).
50. Kirkpatrick, P. Theory and use of ross filters II. *Rev. Sci. Instrum.* **15**, 223–229 (1944).
51. Gallardo González, I. *Development and Applications of a Laser-Wakefield X-ray Source* (Department of Physics, Faculty of Engineering, LTH, Lund University, Division of Atomic Physics, 2018).
52. Gečys, P., Dudutis, J. & Račiukaitis, G. Nanosecond laser processing of soda-lime glass. *J. Laser Micro/Nanoeng.* **10**, 254–258 (2015).
53. Marcinkevičius, A. *et al.* Femtosecond laser-assisted three-dimensional microfabrication in silica. *Opt. Lett.* **26**, 277–279 (2001).
54. van Aarle, W. *et al.* Fast and flexible X-ray tomography using the ASTRA toolbox. *Opt. Express* **24**, 25129 (2016).
55. Gregor, J. & Benson, T. Computational analysis and improvement of SIRT. *IEEE Trans. Med. Imaging* **27**, 918–924 (2008).
56. Engineering toolbox, https://www.engineeringtoolbox.com/material-properties-t_24.html. (2009).
57. Matplotlib: Python plotting—Matplotlib 3.3.1 documentation. https://matplotlib.org/.

Acknowledgements

This work has been supported by European Union's Horizon 2020 Research and Innovation program under ARIES Grant Agreement 730871, by Research Council of Lithuania under the grant agreement S-MIP-17-79, by the Knut and Alice Wallenberg Foundation, the Swedish Research Council, and The Crafoord Foundation.

Author contributions

The experiment was conceived by V.T., V.G., J.D., V.G., I.G.G., D.G., J.B.S and was conducted by P.G., R.G. and O.L. A.P. supported the laser maintenance. The data were analysed by V.T., V.G., J.D., I.G.G., D.G., J.B.S, with assistance from P.G., R.G. and O.L. The manuscript was written by V.T., V.G., J.D. and D.G. All authors reviewed the manuscript.

Competing interests

The authors declare no competing interests.

Additional information

Supplementary information is available for this paper at https://doi.org/10.1038/s41598-020-73805-7.

Correspondence and requests for materials should be addressed to V.T.

Reprints and permissions information is available at www.nature.com/reprints.

Publisher's note Springer Nature remains neutral with regard to jurisdictional claims in published maps and institutional affiliations.

Paper III

Impact of the wall roughness on the quality of micrometric nozzles manufactured from fused silica by hybrid different laser processing techniques

V. Tomkus, V. Girdauskas, J. Dudutis, P. Gečys, V. Stankevič, G. Račiukaitis.

Appl. Surf. Sc. **483**, 205-211, (2019)

DOI: 10.1016/j.apsusc.2019.03.007

Applied Surface Science 483 (2019) 205–211

Contents lists available at ScienceDirect

Applied Surface Science

journal homepage: www.elsevier.com/locate/apsusc

Full length article

Impact of the wall roughness on the quality of micrometric nozzles manufactured from fused silica by different laser processing techniques

Vidmantas Tomkus[a,*], Valdas Girdauskas[a,b], Juozas Dudutis[a], Paulius Gečys[a], Valdemar Stankevič[a], Gediminas Račiukaitis[a]

[a] Center for Physical Sciences and Technology, Savanoriu Ave. 231, LT-02300 Vilnius, Lithuania
[b] Vytautas Magnus University, Vileikos St. 8, LT-44404 Kaunas, Lithuania

ARTICLE INFO

Keywords:
Laser processing
Micrometric nozzles
Wall roughness

ABSTRACT

In this report, the impact of the wall roughness of the cylindrical micronozzles with the diameter of 50 µm, 100 µm and 200 µm on the concentration profiles of the gas targets for laser plasma wakefield acceleration was investigated. Micronozzles were manufactured using three different laser processing techniques – nanosecond laser rear-side (RS) machining with and without the subsequent etching in the potassium hydroxide (KOH) solution and hybrid laser machining technique – the combination of nanosecond laser rear-side machining and femtosecond laser-assisted selective etching (FLSE). Processing efficiency, accuracy and the wall roughness of micronozzles, fabricated by these techniques, are compared, and the best application areas are defined. Finally, the numerical simulation results of the gas concentration profiles are compared with experimental data with the satisfactory agreement.

1. Introduction

Gas nozzles are used in many laser plasma experiments for Laser Wakefield Acceleration (LWFA), secondary X-ray and γ-light generation [1]. With the development of ultrashort few-cycle femtosecond lasers [2,3], dimensions of the plasma target and concentration have to be controlled at the micrometric level being proportional to the propagation distance $c\tau$ of the laser pulse, where c is the speed of light and τ is the duration of the laser pulse. Gas density modulation, obtained by utilising several stages of gas targets, is implemented to increase the energy of accelerated electrons and X-ray radiation [4].

Jet nozzles for gas injection into the interaction area could be fabricated from different materials using various mechanical machining, etching and stereolithography-based technologies [5–8]. Independently of the design, the most challenging and critical part of a nozzle is its intrinsic channel for gas flow. Stereolithography-based methods or 3D printing enable fast prototyping of gas nozzles at low cost and complexity. However, this technology is incapable of fabricating of microchannels on a sub-millimeter scale. Also, the fabricated nozzles are usually made from plastics, therefore, may not be resistant to harsh operational conditions - high pressures, temperatures, etc. Although the mechanical machining is a relatively cheap technology, which could be applied for processing of different materials, it has limitations regarding the achievable aspect ratio of a channel, the minimum hole diameter and quality. Chemical processing of glasses allows fabricating micrometric channels with a very low surface roughness (down to tens of nanometers of average surface roughness R_a). However, it is an expensive, slow and complicated technique [9]. Laser-based methods may be an alternative, which gives relatively high processing quality and speed.

The performance of a gas jet nozzle depends on its dimensions and the wall roughness. Up to now, most of the research is dedicated for the investigation of micro de Laval or other types of converging-diverging nozzles [10–13] and the improvement of their manufacturing in order to reduce the wall roughness [5,12,13]. The surface roughness and waviness reduce the performance of these nozzles. Tailored plasma targets require implementation of the different types of nozzles both converging-diverging and cylindrical to get the modulation of gas concentration on a wide scale. Due to the expansion of the gas flow, de Laval nozzles are optimal where lower concentrations and longer interaction zone of gas for LWFA are required. Cylindrical nozzles containing cluster-jets can be efficient targets for high harmonics [14], secondary X-ray and γ-light generation [4], where higher concentrations and smaller gas density distribution zones of the size of 1–2

* Corresponding author.
E-mail addresses: vidmantas.tomkus@ftmc.lt (V. Tomkus), v.girdauskas@gmf.vdu.lt (V. Girdauskas), juozas.dudutis@ftmc.lt (J. Dudutis), p.gecys@ftmc.lt (P. Gečys), valdemar.stankevic@ftmc.lt (V. Stankevič), gediminas.raciukaitis@ftmc.lt (G. Račiukaitis).

https://doi.org/10.1016/j.apsusc.2019.03.007
Received 14 October 2018; Received in revised form 2 February 2019; Accepted 1 March 2019
Available online 20 March 2019
0169-4332/

diameters of the cylindrical nozzle, are required. However, there is a lack of research data on the influence of the wall quality to cylindrically-shaped nozzles with micrometric dimensions. Moreover, there is a need for developing a mature technique to fabricate these nozzles.

In this report, the impact of the wall roughness on the quality and jet concentration of cylindrical micronozzles, manufactured from fused silica, with diameters of 50 µm, 100 µm and 200 µm, was investigated. The simulation of the impact of the wall roughness on the gas flow in Laval nozzles of the diameter of millimeter dimensions can be performed using analytical methods of isentropic gas flow. However, the simulation results of the isentropic gas flow of the nozzles of the size of tens and hundreds of micrometers differ significantly from the experimental results [12,13]. In this report, the methods of computational fluid dynamics are implemented to evaluate the impact of the wall roughness on the gas flow in micronozzles and jet profiles. The laser processing technology of fused silica is limited by the specific surface roughness typical for the fabrication regime used and it is hard to measure the height of the surface roughness of internal walls inside of the nozzle channel. The simulation results were compared to the interferometric measurements of gas concentration profiles for the nozzles, manufactured by three laser-based processing techniques, resulting in various wall roughness. The validation of simulation results is essential for the definition the acceptable wall roughness and design of the gas jet profile at the output of the nozzle.

2. Simulations

A two-dimensional model of longitudinal and radial dimension was used for the analysis of the impact of the wall roughness on the supersonic gas flow inside of the cylindrical nozzle. Triangle mesh was created in the simulation area except for the region close to the wall. For the modelling of the boundary layer, a quadrilateral cell mesh with increasing thickness was implemented. Subsonic and supersonic gas flow was simulated using Reynolds-averaged Navier-Stokes (RANS) formulation and the two-equation k-ε turbulence model. Gas flow and heat exchange in the boundary layer were evaluated using a wall functions method. Boundary conditions at the input were defined by the total pressure P_{tot} (comprising static and dynamic pressure), uniform input velocity v_{in} and fluid temperature T_{in}. On the wall, the no-slip boundary condition, and at the output, a boundary condition of fixed static pressure P_{out_stat} = 0.1 mbar was applied. Nitrogen gas was implemented as a modelling media. The viscosity of the fluid μ was calculated according to the three coefficient Sutherland viscosity model as a function of the temperature T, reference value of viscosity $\mu_0 = 1.7894 \times 10^{-5}$ Pa/s, a reference temperature T_0 = 273.11 K and Sutherland temperature T_s = 110.56 K:

$$\mu = \mu_0 \left(\frac{T}{T_0}\right)^{\frac{3}{2}} \frac{(T_0 + T_s)}{(T + T_s)}. \quad (1)$$

Wall roughness was modelled using two parameters: k_{rf}, which is equivalent to the sand roughness height, defined as roughness on turbulent flows by measuring the pressure drop in pipes coated with uniform sand grain [15] and non-dimensional roughness parameter C_{ra}, which can take into account other types of roughness [16,17]. Experimentally, a number of different parameters was defined to characterise the surface roughness. An arithmetic average of absolute values R_a was calculated as [18]:

$$R_a = \frac{1}{n} \sum_{i=1}^{n} |y_i|, \quad (2)$$

where y_i is the distance from the average height of a profile for measurement i, and n is the number of measurements. R_{RMS} and R_{zd} roughness parameters are calculated correspondingly as a mean squared and the peak-to-valley values of from the average height of a profile. The peak-to-valley parameter R_{pi} and R_{vi} refer to the largest distances above and below the mean line for one of five measurements with equal scanning length in the longitudinal direction.

Table 1
Estimated sand-grain roughness based on measured surface roughness parameters [18].

Measured surface roughness parameter	Estimated sand-grain roughness, k_{rf}
R_a	$k_{rf} = 5.863R_a$
R_{RMS}	$k_{rf} = 3.100R_{RMS}$
R_{zd}	$k_{rf} = 0.978R_{zd}$

$$R_{RMS} = \sqrt{\frac{1}{n} \sum_{i=1}^{n} y_i^2} \quad (3)$$

$$R_{zd} = \frac{1}{5} \sum_{i=1}^{n} (R_{pi} - R_{vi}) \quad (4)$$

The estimation of sand-grain roughness parameter k_{rf} based on the relations with measured surface roughness values is presented in Table 1.

The simulation results, presented in Fig. 1(a), indicate that wall roughness with sand-grain roughness parameter k_{rf} = 2.5 µm (line 2) has a considerable impact on the gas concentration values at the output of the 50 µm-diameter cylindrical nozzle. The gas concentration at the axis of the nozzle drops by 23% relative to the smooth wall with k_{rf} = 0 µm. The velocity of the gas at the output of 50 µm-diameter nozzle with sand-grain roughness parameter k_{rf} = 2.5 µm, presented in Fig. 1(b), increases in the center because of the turbulent boundary where gas flow is slowed down. The impact of wall roughness on the nozzle with a diameter of 100 µm is relatively smaller. The gas concentration, as shown in Fig. 1(c), indicates that on the axis of the nozzle with sand-grain roughness parameter k_{rf} = 10 µm (line 2) concentration drops by 17% relative to the smooth wall. The simulation results of the nozzle with a 200 µm diameter, presented in Fig. 1(d), show that the impact on the concentration at the output of the nozzle does not exceed 7% for sand-grain roughness parameter k_{rf} up to 15 µm.

Additionally, the impact of edge chipping at the output of the nozzle channel, fabricated by the nanosecond rear-side machining technique, was simulated. Chipping resulted in the formation of the chamfered edge, which was approximated by the section with the angle of 30° at 40 µm depth below the output of the nozzle (Fig. 4). The section of the nozzle edge at the angle of 30° decreased the gas concentration at the output of the nozzle by 15–17%. The total reduction of the concentration, comprising the impact of wall roughness with the parameter k_{rf} = 10 µm and edge section with the angle of 30°, was 30% for the nozzle with the diameter of 100 µm, and 20% for the nozzle with the diameter of 200 µm. The simulation results of the channels with k_{rf} = 0 µm and regular cylindrical nozzles are presented on the left side of Fig. 7(a, b, e) and the simulation results of the channels with k_{rf} = 10 µm and edge section with the angle of 30° - on the left side of Fig. 7(c, d, f).

3. Experimental data

Wall roughness was investigated of cylindrical nozzles, manufactured from fused silica using three different laser processing techniques: the hybrid nanosecond rear-side processing and femtosecond laser-assisted selective etching (FLSE) technique [19], the nanosecond laser rear-side (RS) processing alone [20], and nanosecond laser rear-side processing technique with the subsequent etching in KOH solution for 4 h. The nozzles with the diameter of 50 µm, 100 µm and 200 µm were fabricated and characterised using Mach-Zehnder interferometer and gas jet concentration reconstruction.

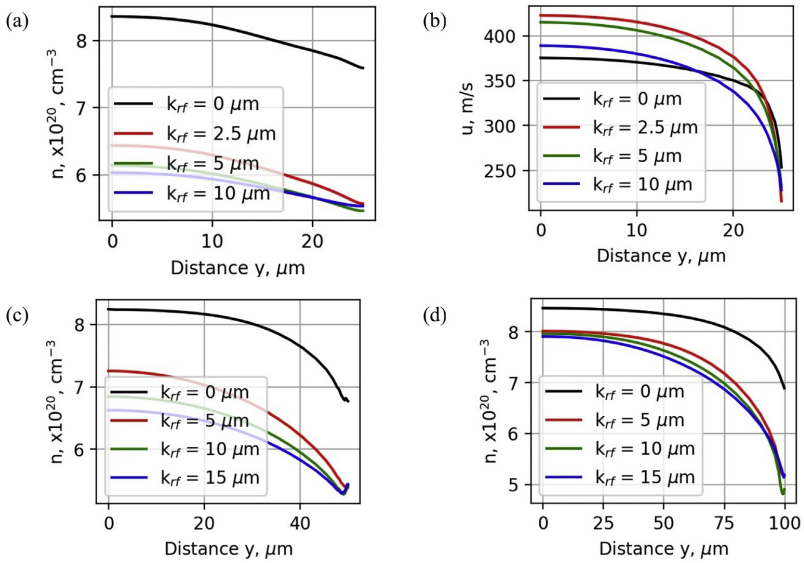

Fig. 1. Simulated transversal N_2 concentration (a, c-d) and velocity (b) profiles at 60 bar backing pressure at the valve of the nozzles with the diameter of 50 μm (a, b), 100 μm (c) and 200 μm (d) and different values of the sand-grain roughness parameter k_{rf}.

3.1. Manufacturing of nozzles

The 6.3 mm-thick fused silica plates were used as a raw material for nozzle manufacturing. The flowchart of different laser processing techniques is presented in Fig. 2. In the case of hybrid laser machining technique (Fig. 2(a)), in the first step, the large volume of the material was removed by nanosecond laser pulses via highly-efficient rear-side machining technique and the preform for a nozzle was fabricated. The material removal rate was over 2 mm^3/s. In the second step, the sample was turned upside down, and the adapter was fabricated via rear-side machining to connect the micronozzle to the valve and to reduce the thickness of glass to 2 mm for processing using FLSE. In the third step, the material was modified using a femtosecond laser and then etched in a KOH solution of 10 M concentration to form a microchannel. This technique allowed to fabricate 50 μm-diameter channels, while for the nanosecond rear-side machining alone (Fig. 2(b)), the minimum diameter was 100 μm. The wavelength, pulse duration at full-width at half-maximum, and pulse energy were 532 nm, 4.5 ns and 90 μJ, respectively, for the nanosecond laser system and 515 nm, 300 fs, < 1 μJ for the femtosecond laser system (Pharos laser from Light Conversion). The details about nozzle fabrication using hybrid and nanosecond rear-side machining techniques could be found in the reference [19]. Finally, the third technique was implemented: the nozzles, fabricated by the rear-side machining technique, were immersed in the KOH solution of 10 M concentration for 4 h (Fig. 2(c)).

The optical microscope images of fabricated nozzles are presented in Fig. 3. FLSE allowed fabricating 100 μm and 200 μm-diameter nozzles with excellent geometry and chip-free edges. However, slight chipping (~10 μm) appeared for 50 μm-diameter holes. It should be noted that the real diameter of 50 μm nozzle was 56 μm. In the case of nanosecond laser rear-side machining technique, the surface chipping was about 100 μm. The real diameters of nozzles, discussed below, were 92 μm, manufactured using FLSE technique, 105 μm, drilled using nanosecond laser rear-side processing and 108 μm, produced by nanosecond laser rear-side processing technique and etched additionally in KOH solution for 4 h. For simplicity, these are referred to 100 μm-diameter nozzles. The real diameters of 200 μm nozzles were 204 μm, 204 μm and 210 μm, respectively.

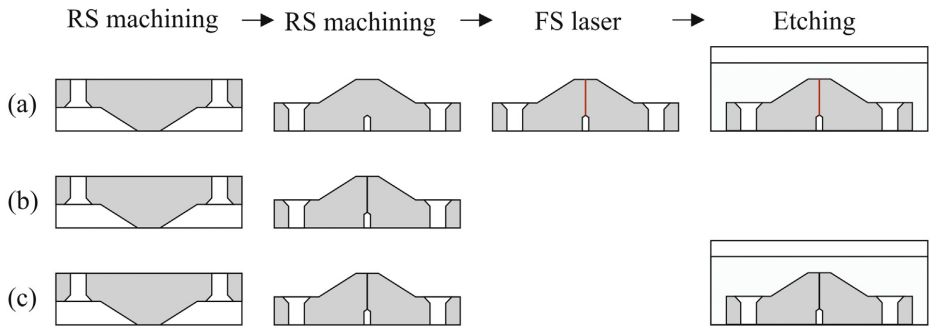

Fig. 2. The flowchart of nozzle fabrication by hybrid laser machining technique (a), nanosecond rear-side machining (b) and nanosecond rear-side machining with the subsequent etching in KOH solution (c). In the processing steps, laser beam propagates from top to bottom.

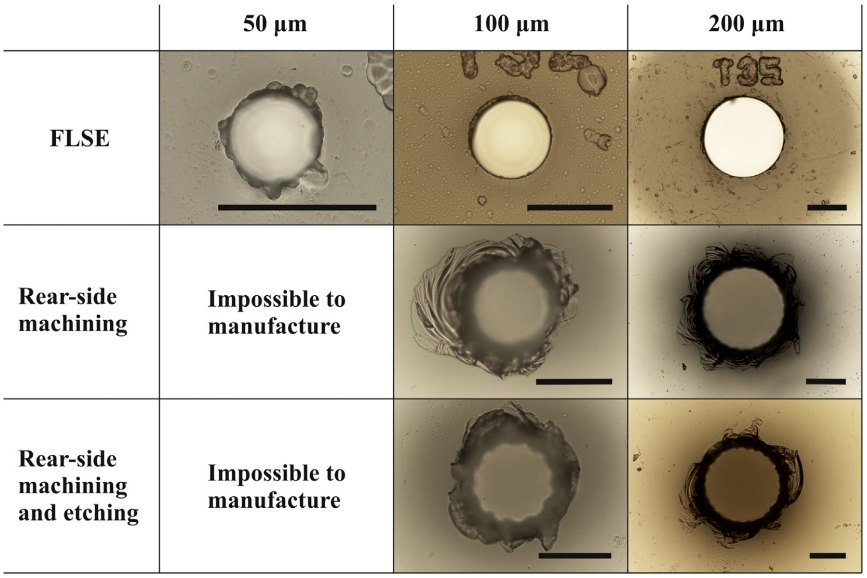

Fig. 3. Optical microscope images of nozzles, manufactured via different techniques. Scale bar is 100 µm-length.

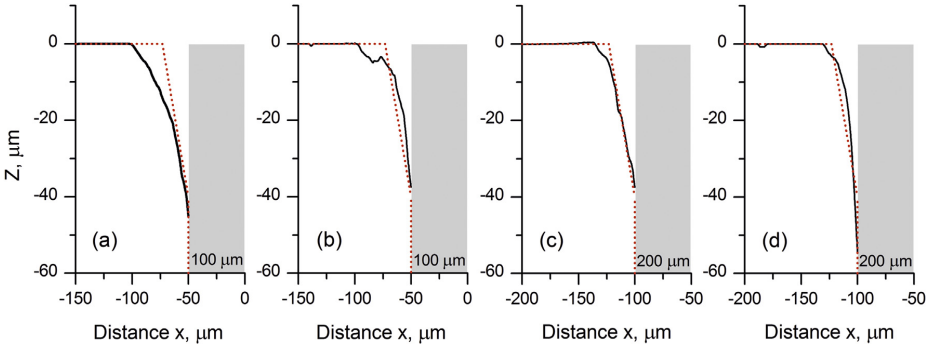

Fig. 4. Measured profiles (solid black lines) at the output of nozzles with the diameter of 100 µm (a, b) and 200 µm (c, d), fabricated by nanosecond rear-side machining technique alone (a, c) and by nanosecond rear-side machining technique with the subsequent etching in KOH (b, d). A grey area represents the ideal cylindrical nozzle, while the distance x = 0 µm is the axis of a nozzle. Red dashed contours show the geometry of the chamfered edge, used for simulations.

The blurred grey and black area around the holes, which were fabricated using nanosecond laser, indicates that the output edge of nozzles is chamfered. Therefore, the profiles of microchannels were investigated using stylus profiler Dektak 150 (from Veeco). The typical profiles at the output of nozzles with the diameter of 100 µm (a, b) and 200 µm (c, d), fabricated by nanosecond rear-side machining technique alone (a, c) and with the subsequent etching in KOH solution (b, d), are presented in Fig. 4. A grey area represents the ideal cylindrical nozzle, while the distance x = 0 µm is the axis of a nozzle. Red dotted contours show the geometry of the chamfered edge, used for simulations. After the initial interferometric measurements, the surface of the nozzles, drilled using nanosecond laser rear-side processing and produced by nanosecond laser rear-side processing technique and etched additionally in KOH solution, were polished and the upper layer, containing the chamfered edge, was removed. The right angle of the output edge was nearly restored and the concentration profiles were measured again.

The scanning electron microscope (SEM) images of the opened microchannels are presented in Fig. 5(a–c). The topologies of surfaces, fabricated by nanosecond laser rear-side machining alone and with the subsequent etching in KOH for 4 h, were measured using stylus profiler and are presented in Fig. 5(d) and (e), respectively. The measured surface roughness and estimated sand-grain roughness parameter k_{rf}, according to the relations, are presented in Table 2. The average roughness and average peak-to-valley distance of a nozzle, fabricated by rear-side machining technique, were R_a = 1.4 µm and R_{zd} = 8 µm. The subsequent etching in KOH for 4 h resulted in a rougher surface with the average roughness of 1.7 µm (R_{zd} = 10.4 µm). In comparison, the FLSE technique allowed to achieve the significantly smoother surface. In this case, the average roughness and average peak-to-valley distance were R_a = 0.12 µm and R_{zd} = 0.57 µm. The estimated sand-grain roughness parameter k_{rf}, based on the average roughness and average peak-to-valley distance, was in the submicron range for FLSE technique, while for the rear-side machining alone and with subsequent etching in KOH it was equal to ~8 µm and ~10 µm, respectively. The values of sand-grain roughness, estimated according to the root-mean-

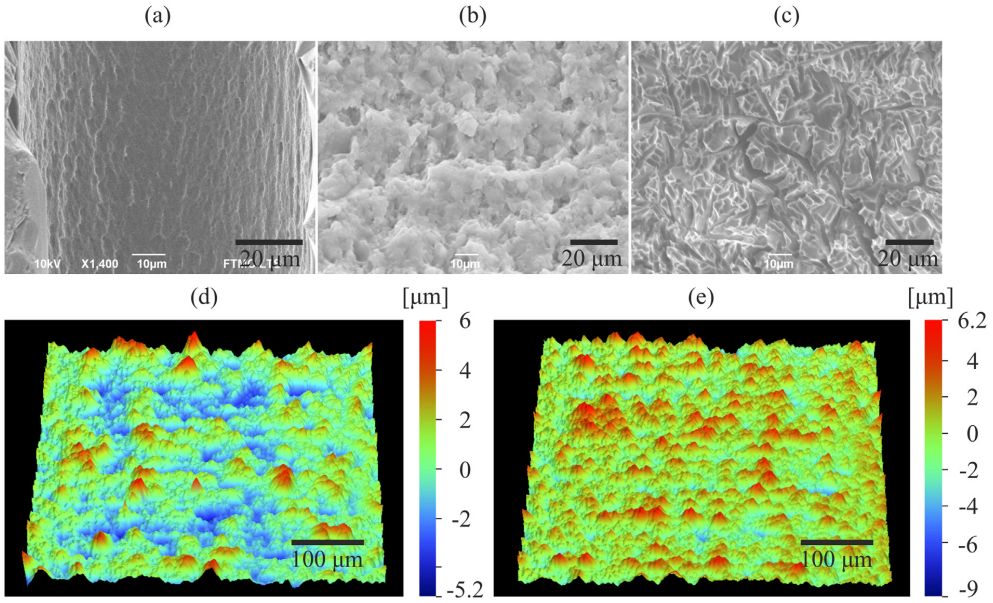

Fig. 5. SEM images of the opened microchannels, fabricated by FLSE technique (a), nanosecond rear-side machining (b) and rear-side machining with the subsequent etching in KOH (c). Scale bars are 20 μm-length. 0.5 x 0.4 mm^2 topographies of the flat surface, fabricated by rear-side machining (d) and rear-side machining with the subsequent etching in KOH (e).

Table 2
The measured surface roughness of the fabricated channels and estimated sand-grain roughness parameter, according to the relations, given in Table 1.

	FLSE	RS machining	RS machining and etching
R_a [μm]	0.12	1.4	1.7
R_{RMS} [μm]		1.7	2.1
R_{zd} [μm]	0.57	8	10.4
k_{rf} @ R_a [μm]	0.70	8.2	10.0
k_{rf} @ R_{RMS} [μm]		5.3	6.5
k_{rf} @ R_{zd} [μm]	0.56	7.8	10.2

square roughness R_{RMS}, were slightly lower.

3.2. Interferometric measurements

The transversal gas density profile was determined using nitrogen gas, a Mach–Zehnder interferometer [21], continuous wave 632.8 nm He—Ne laser and CCD camera. The density profiles were reconstructed using the Interferometric Data Evaluation Algorithms (IDEA) [22]. The nozzles were driven by the Parker 9 series microvalve. The nozzles were tested in a vacuum chamber at the vacuum level of 10^{-5} mbar. The images of measured and Fourier-filtered phase interferograms of the gas jets at the backing pressure of 60 bar of the cylindrical nozzles are presented in Fig. 6. The diameters of nozzles are 50 μm (Fig. 6(a)), 100 μm (Fig. 6(b–d)) and 200 μm (Fig. 6(e)). Nozzles were fabricated by the FLSE technique (Fig. 6(a, b)), nanosecond rear-side machining technique (Fig. 6(c, e)) and nanosecond rear-side machining technique with the subsequent etching in KOH (Fig. 6(d)).

The results of simulated (left side) and reconstructed (right side) transversal nitrogen concentration profiles using Abel transformation [23] of nozzles with the diameter of 50 μm, 100 μm, and 200 μm are given in Fig. 7. The concentration profiles of nozzles, manufactured by FLSE technology, are presented in Fig. 7(a, b, e), and the concentration profiles of nozzles, fabricated by nanosecond rear-side machining technique, are given in Fig. 7(c, f). The concentration profile of a 100 μm-diameter nozzle, fabricated by nanosecond rear-side machining technique with the subsequent etching in KOH, is shown in Fig. 7(d).

4. Results and discussion

The FLSE technique allowed to fabricate nozzles with the smallest sand-grain roughness k_{rf} = 0.56 of the wall, estimated according to the measured peak-to-valley distance. In the case of nanosecond rear-side processing technique, the material was removed due to the local cracking and consequent disintegration of material into smaller debris,

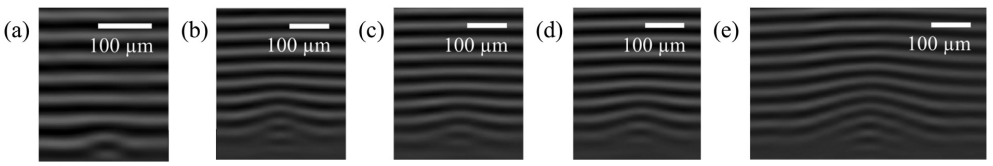

Fig. 6. Interferograms of Mach-Zehnder interferometer of transversal N_2 concentration profiles of nozzles with the diameter of 50 μm (a), 100 μm (b-d) and 200 μm (e) at 60 bar of backing pressure at the valve. Nozzles were fabricated by FLSE technique (a, b), nanosecond rear-side machining technique alone (c, e) and with the subsequent etching in KOH (d). Scale bar is 100 μm-length.

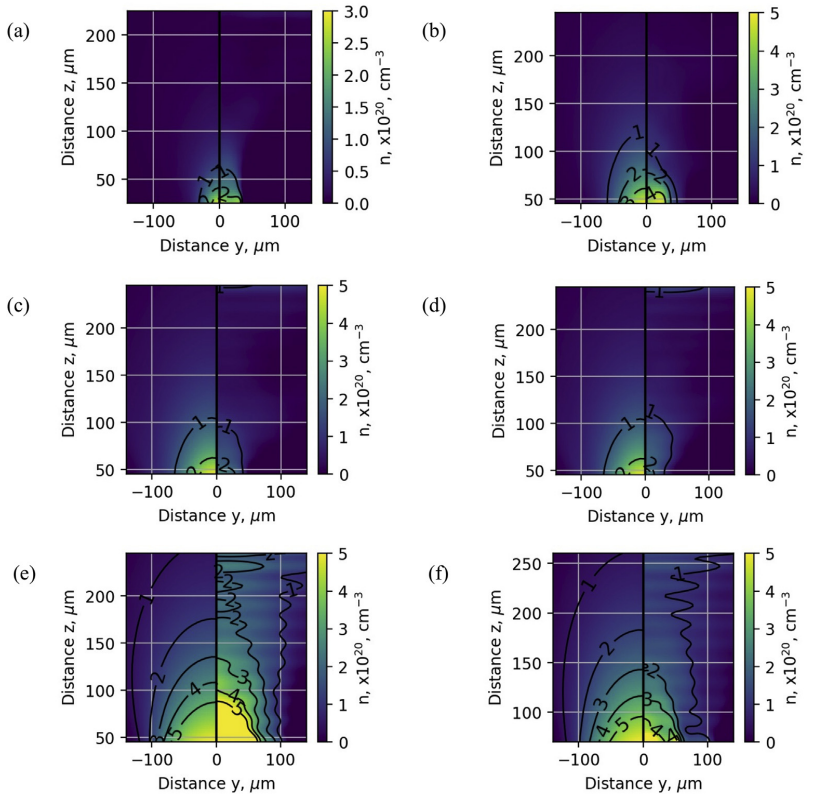

Fig. 7. Simulated (left side) and reconstructed (right side) transversal N_2 concentration profiles of nozzles with the diameter of 50 μm (a), 100 μm (b), 200 μm (e), manufactured by FLSE technology, 100 μm (c) and 200 μm (f), fabricated by the nanosecond rear-side machining technique, and 100 μm (d), made by the nanosecond rear-side machining technique with the subsequent etching in KOH, at 60 bar of backing pressure at the valve.

which then can be removed through the opposite direction. Therefore, the impact of ablation process was highly suppressed in this case. In addition to that, the removed debris takes away some heat from the interaction area. Therefore, the residual wall surface is considerably rougher with almost no sign of remelting. The sand-grain roughness of the wall equalled to 8 μm, which was by order of magnitude larger compared to FLSE technique. Another feature of nanosecond rear-side processing technique is the significant chipping of glass edges at the output of a nozzle, which occurs when a thin layer of glass fractures in the final stage of drilling. Chipping results in the chamfered nozzle output with the edge section of 30° at 40 μm depth below the output of the nozzle.

The gas concentration, measured at 60 bar backing pressure at the output of 50 μm cylindrical channel, manufactured by FLSE technique, at the distance of 40–60 μm from the output of the nozzle was $1–2 \times 10^{20}$ cm^{-3}. The gas concentration, measured at the output of 100 μm cylindrical channel, fabricated by nanosecond rear-side processing technique, at the distance of 50–80 μm from the output of the nozzle was 25–30% lower relative to the channel with the sand roughness of the wall $k_{rf} = 0.56$ μm, achieved by FLSE technique. The measured gas concentrations were $1.4–2.2 \times 10^{20}$ and $1.8–3 \times 10^{20}$ cm^{-3}, correspondingly. The gas concentration, measured at the output of 200 μm cylindrical channel at the distance of 80–140 μm from the output of the nozzle, was 15–25% lower in the channel, fabricated by nanosecond rear-side processing technique relative to the channel, made by FLSE technique. The measured gas concentrations were $2.3–4.5 \times 10^{20}$ and $2.9–5.1 \times 10^{20}$ cm^{-3} correspondingly.

The subsequent etching of channels, fabricated with nanosecond rear-side machining technique, in KOH solution for 4 h resulted in the quite different surface morphology, as seen in Fig. 5(c), and higher sand-grain roughness parameter equalled to 10 μm. The wet etching revealed the randomly-distributed intra-volume cracks close to the microchannel, which were induced due to nanosecond laser processing [24]. It is worth to note that longer etching durations lead to even higher values of surface roughness ($k_{rf} = 18$ μm for 22 h) and a worm-like surface structure [19]. At the beginning of the wet etching, the individual cracks are opened, which can intersect and coalesce during longer etching durations [24]. Also, the wet etching did not affect the angle of the edge section. Despite the different surface morphology and roughness, the results of the measured concentration of 100 μm and 200 μm nozzles, fabricated by nanosecond rear-side machining alone and nanosecond rear-side machining with the subsequent etching in KOH, did not show substantial differences within the accuracy of 10%.

The simulation results of the regular cylindrical nozzles with roughness parameter $k_{rf} = 0$ μm, presented in Fig. 7(a, b, e), are in good correspondence with experimental results of the nozzles with diameters of 50 μm, 100 μm and 200 μm, manufactured by FLSE technique. The simulation results of the channels with $k_{rf} = 10$ μm and edge section with the angle of 30°, presented at the Fig. 7(c, d, f), correspond with the experimental results of the nozzles fabricated by nanosecond rear-side processing technique within 10–15%. Additionally, the chipping of

the channel edges results in the more stochastic behaviour of the concentration of the gas jet and deviations of the concentration not described by the symmetrical model of cylindrical nozzles. After the polishing of the front surface with chamfered edges, the quality of nozzles, fabricated by a nanosecond laser, was improved by 10%. The gas concentration reduction decreased below 15% for 100 μm-diameter nozzles. Within the accuracy of 10% it corresponds to the simulations, presented in Section 2.

5. Summary and conclusions

Three different laser-based techniques were applied for the fabrication of cylindrical micronozzles, which resulted in different surface morphology and roughness. Femtosecond laser-assisted selective etching technology provided non-chamfered channels down to 50 μm diameter with sand-grain roughness parameter in the sub-micron range. At backing pressure of 60 bar the gas concentration at the distance of 40–60 μm from the output of cylindrical micronozzles in the range of $1–5 \times 10^{20}\,cm^{-3}$ was achieved. Therefore, it allows designing gas target profiles of high concentration and micrometric dimensions. The operation of nozzles is in good correspondence with simulation results with the wall roughness $k_{rf} = 0$ μm. However, due to the long fabrication time, this technology is less competitive for processing of high-volume parts.

Nanosecond laser rear-side processing technique provides excellent material processing rate and can be implemented for the removal of high volumes of fused silica and fabrication of channels down to 100 μm diameter. Technology has limitation for processing of structures with dimensions below 200 μm because chipping is in the range of 50–100 μm and the sand-grain roughness parameter of the wall is 8 μm. It results in the decrease of the nozzle quality and drop of concentration rates by 20–30% for a nozzle with the diameter of 100 μm. The influence of the absolute roughness value to the nozzle performance reduces with increase of a nozzle diameter. The reduction of gas concentration is 15–25%, compared to FLSE technique, for a nozzle with the diameter of 200 μm.

The subsequent etching in KOH alters the surface morphology of nozzles, fabricated by nanosecond laser rear-side machining technique. The wet etching opens intra-volume channels, which may coalesce, and the sand-grain roughness parameter of the wall is equal to 10 μm after 4 h etching. However, there was no significant difference in performance between additionally-etched and non-etched nozzles.

Simulations revealed that the section of the nozzle edge at the angle of 30° decreased the gas concentration at the output of the nozzle by 15–17%. The quality of nozzles, fabricated by nanosecond laser machining, was improved by 10% by mechanical polishing of the surface of a nozzle.

The FSLE technology is preferred where low surface roughness and < 200 μm diameter microchannels are required. It is less effective than nanosecond rear-side processing, where machining of high-volume parts is necessary. However, larger nozzles should be fabricated with nanosecond laser rear-side processing only, which is cheaper and less complicated.

The wall roughness has an effect on subsonic and ultrasonic gas flow when the height of the roughness structure exceeds 1–2% of the diameter of the cylindrical nozzle or the diameter of the throat of de Laval nozzle [10–12]. The 1–2% of the diameter of 50–100 μm corresponds to the roughness height of 0.5–1 μm. No degradation of the gas flow compared to the simulation results of an ideal wall with $k_{rf} = 0$ μm was observed. The sand-grain roughness parameter of nanosecond laser rear-side machining technique, equalled to $k_{rf} = 8–10$ μm, comprise 8–10% of the nozzle diameter of 100 μm and 4–5% of the nozzle diameter of 200 μm. The right angle of the channel of the cylindrical nozzle has to be maintained at the output of the nozzle. The gas concentration reduction was below 15% for 100 μm-diameter nozzles with polished output surface and nearly right edge angles. The subsequent etching in KOH alters the surface morphology of nozzles. However, it does not affect the performance of the nozzles. The roughness height has a substantial impact on the gas flow profile rather than the fractal dimension of the surface structure.

Acknowledgements

The research leading to these results was funded by The Research Council of Lithuania under grant agreement No. S-MIP-17-79.

References

[1] F. Albert, A.G.R. Thomas, Applications of laser wakefield accelerator-based light sources, Plasma Phys. Controlled Fusion 58 (2016) 103001.
[2] D. Guénot, D. Gustas, A. Vernier, B. Beaurepaire, F. Böhle, M. Bocoum, M. Lozano, A. Jullien, R. Lopez-Martens, A. Lifschitz, J. Faure, Relativistic electron beams driven by kHz single-cycle light pulses, Nat. Photonics 11 (5) (2017) 293–296.
[3] A.J. Goers, G.A. Hine, L. Feder, B. Miao, F. Salehi, J.K. Wahlstrand, H.M. Milchberg, Multi-MeV electron acceleration by subterawatt laser pulses, Phys. Rev. Lett. 115 (19) (2015) 194802.
[4] J. Ferri, S. Corde, A. Döpp, A. Lifschitz, A. Doche, C. Thaury, K. Ta Phuoc, B. Mahieu, I.A. Andriyash, V. Malka, X. Davoine, High-brilliance betatron γ-ray source powered by laser-accelerated electrons, Phys. Rev. Lett. 120 (2018) 254802.
[5] Y. Cai, Z. Liu, Z. Shi, Q. Song, Y. Wan, Optimization of machining parameters for micro-machining nozzle based on characteristics of surface roughness, Int. J. Adv. Manuf. Technol. 80 (5–8) (2015) 1403–1410.
[6] M.C. Louwerse, H.V. Jansen, M.N.W. Groenendijk, M.C. Elwenspoek, Nozzle fabrication for micropropulsion of a microsatellite, J. Micromech. Microeng. 19 (4) (2009) 045008.
[7] S.W. Jolly, Z. He, C. McGuffey, W. Schumaker, K. Krushelnick, A.G.R. Thomas, Stereolithography based method of creating custom gas density profile targets for high-intensity laser-plasma experiments, Rev. Sci. Instrum. 83 (7) (2012).
[8] A. Döpp, E. Guillaume, C. Thaury, J. Gautier, K. Ta Phuoc, V. Malka, 3D printing of gas jet nozzles for laser-plasma accelerators, Rev. Sci. Instrum. 87 (7) (2016).
[9] L. Hof, J. Abou Ziki, Micro-hole drilling on glass substrates—a review, Micromachines 8 (2) (2017) 53.
[10] F. La Torre, S. Kenjeres, C.R. Kleijn, J.-L.P.A. Moerel, Effects of wavy surface roughness on the performance of micronozzles, J. Propuls. Power 26 (4) (2010) 655–662.
[11] H. Yan, W.-M. Zhang, Z.-K. Peng, G. Meng, Effect of three-dimensional surface topography on gas flow in rough micronozzles, J. Fluids Eng. 137 (5) (2015) 051202.
[12] Y. Cai, Z. Liu, Z. Shi, Effects of dimensional size and surface roughness on service performance for a micro Laval nozzle, J. Micromech. Microeng. 27 (5) (2017) 055001.
[13] Y. Cai, Z. Liu, Q. Song, Z. Shi, Y. Wan, Fluid mechanics of internal flow with friction and cutting strategies for micronozzles, Int. J. Mech. Sci. 100 (2015) 41–49.
[14] M. Aladi, R. Bolla, D.E. Cardenas, L. Veisz, I.B. Földes, Cluster size distributions in gas jets for different nozzle geometries, J. Instrum. 12 (06) (2017) C06020.
[15] F. Albert, A.G.R. Thomas, S.P.D. Mangles, S. Banerjee, S. Corde, A. Flacco, M. Litos, D. Neely, J. Vieira, Z. Najmudin, R. Bingham, C. Joshi, T. Katsouleas, Laser wakefield accelerator-based light sources: potential applications and requirements, Plasma Phys. Controlled Fusion 56 (8) (2014) 084015.
[16] K.A. Flack, M.P. Schultz, Review of hydraulic roughness scales in the fully rough regime, J. Fluids Eng. 132 (4) (2010) 041203.
[17] B. Blocken, T. Stathopoulos, J. Carmeliet, CFD simulation of the atmospheric boundary layer: wall function problems, Atmos. Environ. 41 (2) (2007) 238–252.
[18] T. Adams, C. Grant, H. Watson, A simple algorithm to relate measured surface roughness to equivalent sand-grain roughness, Int. J. Mech. Eng. Mechatronics J. 1 (1) (2012).
[19] V. Tomkus, V. Girdauskas, J. Dudutis, P. Gečys, V. Stankevič, G. Račiukaitis, High-density gas capillary nozzles manufactured by hybrid 3D laser machining technique from fused silica, Opt. Express 26 (21) (2018) 27965.
[20] P. Gečys, J. Dudutis, G. Račiukaitis, Nanosecond laser processing of soda-lime glass, J. Laser Micro/Nanoeng. 10 (3) (2015) 254–258.
[21] R. Azambuja, M. Eloy, G. Figueira, D. Neely, Three-dimensional characterization of high-density non-cylindrical pulsed gas jets, J. Phys. D. Appl. Phys. 32 (8) (1999) L35–L43.
[22] M. Hipp, J. Woisetschläger, P. Reiterer, T. Neger, Digital evaluation of interferograms, Measurement 36 (1) (2004) 53–66.
[23] G. Pretzier, A new method for numerical Abel-inversion, Zeitschrift für Naturforsch. A 46 (7) (1991) 639–641.
[24] L. Wong, T. Suratwala, M.D. Feit, P.E. Miller, R. Steele, The effect of HF/NH4F etching on the morphology of surface fractures on fused silica, J. Non-Cryst. Solids 355 (13) (2009) 797–810.

Paper IV

High-density gas capillary nozzles manufactured by hybrid 3D laser machining technique from fused silica

V. Tomkus, V. Girdauskas, J. Dudutis, P. Gečys, V. Stankevič, G. Račiukaitis.

Opt. Express. **26**, 27965, (2018)

DOI: 10.1364/OE.26.027965

Research Article | Vol. 26, No. 21 | 15 Oct 2018 | OPTICS EXPRESS 27965
Optics EXPRESS

High-density gas capillary nozzles manufactured by hybrid 3D laser machining technique from fused silica

VIDMANTAS TOMKUS,[1,*] VALDAS GIRDAUSKAS,[2] JUOZAS DUDUTIS,[1] PAULIUS GEČYS,[1] VALDEMAR STANKEVIČ,[1] AND GEDIMINAS RAČIUKAITIS[1]

[1]*Center for Physical Sciences and Technology, Savanoriu Ave. 231, LT-02300, Vilnius, Lithuania*
[2]*Vytautas Magnus University, Vileikos St. 8, LT-44404, Kaunas, Lithuania*
[*]*vidmantas.tomkus@ftmc.lt*

Abstract: In this report, an efficient hybrid laser technique, nanosecond laser rear-side processing and femtosecond laser-assisted selective etching (FLSE) for the manufacturing of high-density gas capillary targets, is demonstrated. Cylindrical capillary nozzles for laser betatron X-ray sources were numerically simulated, manufactured from fused silica by 3D laser inscription and characterized using interferometry and gas density reconstruction. The dependence of gas concentration profiles on the wall roughness of cylindrical channels is presented.

1. Introduction

The need of modest scale research facilities, and the demand of higher X-ray energy for the investigation of warm dense matter [1] increase the interest in advanced X-ray sources, driven by laser-accelerated electrons. Such sources require manufacturing and characterization of tailored gas targets with micrometric dimensions. Confining the laser field inside the plasma bubble can act as an effective wiggler to produce betatron X-ray radiation with harmonics peaking in the range of tens and hundreds of keV [2]. The betatron critical frequency ω_c can be calculated from the relation (1), where γ is the relativistic factor of the accelerated electrons, n is the plasma concentration and r_β - the amplitude of the betatron orbit [3]:

$$\hbar\omega_c\left[\mathrm{keV}\right] \simeq 1.1\times10^{-23}\gamma^2 n\left[\mathrm{cm}^{-3}\right] r_\beta\left[\mu\mathrm{m}\right]. \quad (1)$$

The increase of the critical frequency ω_c and photon energy of betatron radiation cannot be done straightforwardly via increasing all three parameters γ, n, and r_β simultaneously. The relativistic factor of electrons is limited by the maximal energy of the laser. While shortening the laser pulse length, the gas target dimensions and corresponding plasma wavelength has to be decreased to maintain the optical path for the laser beam in the gas target within a half of the plasma wavelength [4]. The operation at near critical plasma densities and sharp focusing to the smaller target dimensions decrease the dephasing length of the laser wakefield acceleration (LWFA). It is difficult to maintain the optimal LWFA conditions to get the maximum energy of accelerated electrons and increase the energy of betatron radiation and r_β via transverse laser direct acceleration. Tailored concentration profiles [3,5,6], gas nozzles with different ionization energies [7], colliding laser pulses [8], two LWFA stages with lower plasma density for electron acceleration and higher density for optimized betatron radiation [9] are used to control the injection of the electrons, increase the energy of the accelerated electrons and raise the efficiency of betatron radiation. Implementation of short pulses and high plasma densities decreases the LWFA intensity threshold and opens the way of design of femtosecond table top medical grade ultrashort X-ray sources with lower laser energy of tens of millijoules and pulse duration of 7-20 fs at 1 kHz repetition rate [10–12].

#335978 https://doi.org/10.1364/OE.26.027965
Journal © 2018 Received 25 Jun 2018; revised 14 Sep 2018; accepted 16 Sep 2018; published 10 Oct 2018

Optics EXPRESS

In this report, we demonstrate a new method of 3D laser formation of tailored gas targets using micrometric nozzle arrays manufactured in fused silica. Depending on required plasma density profile, focus length and laser power, several stages of the accelerator with different nozzle geometry can be implemented to ensure the electron injection, acceleration and increased efficiency of betatron radiation on a single chip.

Gas jet nozzles for laser wakefield acceleration may be fabricated from various materials using various subtractive and additive technologies. The nozzle materials should be resistant to the harsh operational conditions. The conventional method of CNC machining from metals is time-consuming and is not suitable for fabricating complex structures with a high aspect ratio (structure depth to width ratio). Stereolithography-based methods allow rapid manufacturing from plastics of custom-shaped nozzles down to 100 μm size at a low cost [13]. However, additional post-processing is required to open the blocked nozzle, and the materials are of moderate resistance. Also, in the sub-millimeter scale, the printed holes fail in maintaining the circular shape, and the achievable aspect ratio is close to one [14]. Taking into account the hardness of material and manufacturing flexibility, glassy materials seems to be an appealing alternative.

Conventional mechanical drilling of glass suffers from limitations in hole aspect ratio (typically up to 10:1), achievable minimum hole diameter (on the order of 100 μm), relatively slow processing speed and low machining quality [15]. The performance of direct laser ablation is limited in the case of thick samples. Plasma shielding, scattering from kerf sidewalls, debris accumulation are serious challenges, preventing fabrication of deep and taper-less structures [16]. One of the solutions is to remove the material from the rear side of a sample, which is usually referred to as the rear-side processing, back-side ablation or bottom-up technique [17–23]. The overview and comparison of various micro-hole drilling techniques in glass could be found in [15].

Liquid-assisted femtosecond laser drilling of high aspect ratio holes (50:1) at the speed of several of μm/s from the rear side of the glass was already demonstrated more than a decade ago [18]. The drilling depth was mainly limited by the accumulation and redeposition of the processing debris [24]. The redeposition and accumulation effects can be reduced by tightly focusing nanosecond laser pulses, which induce micro-cracks in the glass. By choosing a proper pulse overlap, the material can be removed as large particles with the size up to hundreds of microns [19,21]. This technique is energy-efficient and could be applied for large-scale applications. However, it has limitations regarding the minimum hole diameter and surface quality. Nevertheless, in this paper, we demonstrate the hybrid 3D fabrication technique, in which the large volume of glass is removed by nanosecond pulses and the final micro-holes are manufactured by the femtosecond laser-assisted selective chemical etching technique (FLSE) [25–28].

In this report, we present results on the simulation, fabrication and characterization of cylindrical micronozzles with the diameter of 100-500 μm and length of several millimeters to produce high-density gas targets for laser wakefield acceleration. Nozzles were fabricated using the nanosecond laser rear-side processing approach alone and the hybrid 3D fabrication technique.

2. Numerical simulation

The concentration, velocity, pressure and temperature of gas jets, ejected by micronozzles, were simulated using OpenFOAM [29] compressible steady-flow solver rhoSimpleFoam. The Reynolds-averaged Navier–Stokes (RANS) k-ω Shear Stress Transport (SST) turbulence model describing turbulence using two transport equations and 2 transported variables - turbulent kinetic energy k and ω - the specific rate of dissipation of the turbulence kinetic energy k into internal thermal energy was applied. A general thermo-physical model of calculation was based on internal energy and compressibility parameter $\psi = 1/R_{spec}T$, where R_{spec} is the specific gas constant and T is the temperature. The viscosity of the fluid μ was calculated according to

Optics EXPRESS

the Sutherland viscosity model as a function of the temperature T from the Sutherland coefficient A_s and Sutherland temperature T_s, according to:

$$\mu = \frac{A_s\sqrt{T}}{\left(1+T_s/T\right)}. \tag{2}$$

Inlet and outlet boundary conditions were defined as the total pressure p_0 calculated by the static pressure p, velocity vector U and density ρ:

$$p_0 = p + \frac{1}{2}\rho\vec{U}^2, \tag{3}$$

fixed velocity and temperature at the inlet boundary and the static pressure at the outlet boundary. For the wall type boundaries, the no-slip condition was used, and the two-dimensional geometry of wedge symmetry was implemented.

Table 1. Material properties used in simulation [30]

Properties	Units	Nitrogen	Helium
Molecular mass	g/mol	28.02	4.02
Density at 1 bar and 273.15 K	kg/m^3	1.256	0.185
Specific heat capacity C_p	J/kg K	1004	5193
C_p/C_v	-	1.4	1.67
The speed of the sound at 273.15 K	m/s	331.2	973
Sutherland constant A_s	-	1.458 × 10^{-6}	1.633 × 10^{-6}
Sutherland temperature T_s	K	110.8	147.0
Refractive index n at 632 nm, 1 bar and 273.15 K	-	1.000298	1.0000349

Material properties used in the simulation are given in Table 1. The actual values of the density, the speed of sound and refraction index were recalculated in the simulation based on the local values of pressure and temperature.

Nitrogen gas was implemented as the main modelling media to define optimal geometries of the nozzles during their manufacturing. The results are applicable also to helium frequently used as a laser wakefield acceleration media. The concentration differences at the nozzle output for nitrogen and helium are in the range of 7-10% only. The refractive index of nitrogen is higher by order of magnitude compared to helium and allows much easier and precise interferometric measurements of the gas target distribution. The simulation area comprises the length of microcapillary of 2.8 mm and 6 x 4 mm simulation area of expansion of the gases. Because of the high aspect ratio 1:18 (150 µm and 2.8 mm) only the part of simulation – 600 x 600 µm close to the output of the nozzle is shown. Simulated images of gas concentration and Mach number of nitrogen and helium at the backing pressure of 60 bar of a cylindrical nozzle with the output diameter of 300 µm are presented in Fig. 1. The concentrations at the output of the nozzle for nitrogen and helium are similar because the gas density ρ depends on the Mach number M being close to critical to both of gases [31]:

$$\frac{\rho}{\rho_0} = \left(1+\frac{k-1}{2}M^2\right)^{\left(\frac{1}{k-1}\right)}, \tag{4}$$

where ρ_0 is the critical density at the point where gas flow turns from subsonic to supersonic flow. Slight differences of concentration are caused mainly by the difference of the adiabatic

Optics EXPRESS

index k of monoatomic gas of helium (5/3 = 1.67) and adiabatic index of diatomic nitrogen gas (7/5 = 1.4).

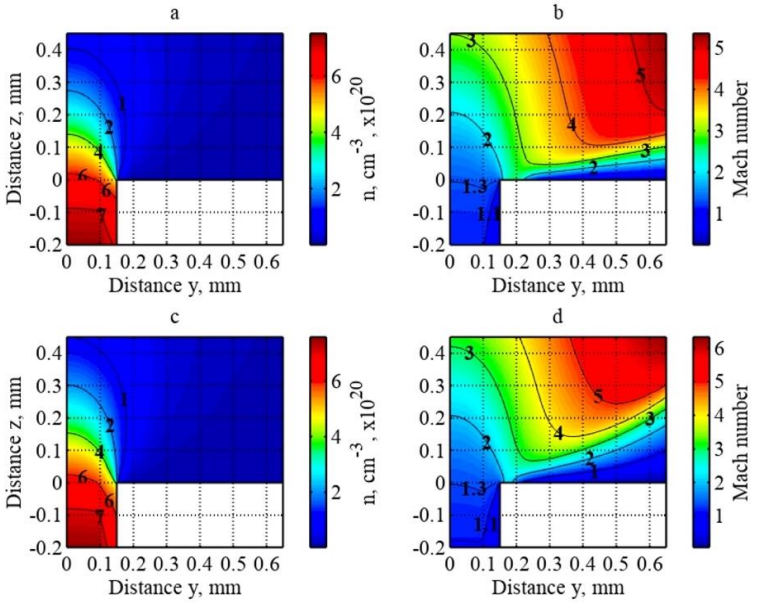

Fig. 1. Simulated gas concentration (a), Mach number (b) of nitrogen and concentration (c) and Mach number (d) of helium at the backing pressure of 60 bar of a cylindrical nozzle with the output diameter of 300 μm.

The higher deviations of Mach number between nitrogen and helium at larger distances depend on the gas temperature and speed of sound being inverse proportional to the square root of the mass of gases. Helium having lower molecular mass expands quicker, and the local temperature drops to the lower values compared to nitrogen. It results in higher Mach numbers of helium defined as a ratio of gas flow velocity and local speed of sound.

3. Manufacturing

The capillary nozzles were manufactured from fused silica using the nanosecond rear-side processing approach alone and the hybrid 3D laser machining technique. The sketch of the nozzle is presented in Fig. 2(a). The nozzle consisted of the 35 mm-diameter holder with a frustum of a cone and microcapillaries, fabricated along the element axis. The commercially-available 150 x 150 mm^2 and 76 mm-diameter fused silica plates with the thicknesses of 6.3 mm and 12.7 mm, respectively, were used as raw material.

3.1 Nanosecond laser processing

The processing setup with a nanosecond laser is presented in Fig. 2(b). Gas jet nozzles were fabricated using the second harmonics (532 nm) of a diode-pumped solid-state (DPSS) laser (from Ekspla). The pulse duration, measured at full-width at half-maximum, was 4.5 ns. The laser system provided the maximum average laser power of 18 W at the 200 kHz pulse repetition rate. The galvanometer scanner intelli*SCAN* 14 (from SCANLAB) was used to guide the laser beam in the XY plane, focused by the telecentric f-theta lens with the focal length of 80 mm. The diameter of the focused beam at the 1/e^2 level equalled to 10.5 μm. Typical pulse energy and laser fluence was 90 μJ and 210 J/cm^2, respectively. Samples were mounted on the

Optics EXPRESS

translational stage with a stepper motor 8MT167-100 (from Standa) for vertical positioning. The drilling and milling of fused silica were conducted using the spiral-mode cutting technique, presented in [21], with variable inner and outer diameters, depending on the desired structure. Initially, the laser beam was focused below the rear surface, and then the positioning stage was moved down at a fixed vertical speed, which depended on the area of the milled surface. The removed volume of glass was divided by the processing time to calculate the material removal rate (mm^3/s). The material removal rate was divided by the average laser power to obtain the energetic efficiency of processing (mm^3/J).

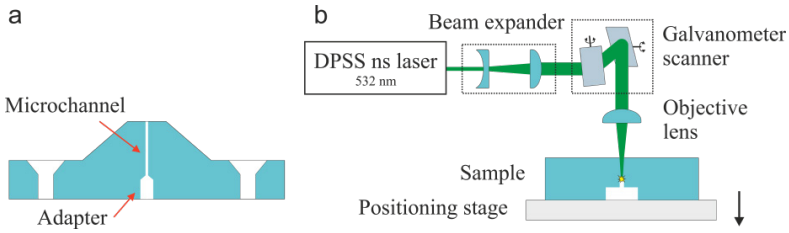

Fig. 2. The sketch of the nozzle (a). The nanosecond laser processing setup (b), which consisted of the galvanometer scanner to guide the beam in the XY plane and f-theta lens for focusing. The process was initiated from the rear side of a sample, and the positioning stage was continuously moved down.

The nozzle was fabricated by two stages. In the first stage, the frustum of a cone and screw holes were fabricated. The material removal rate for such high-volume milling reached 2.34 mm^3/s with the 18 W average laser power.

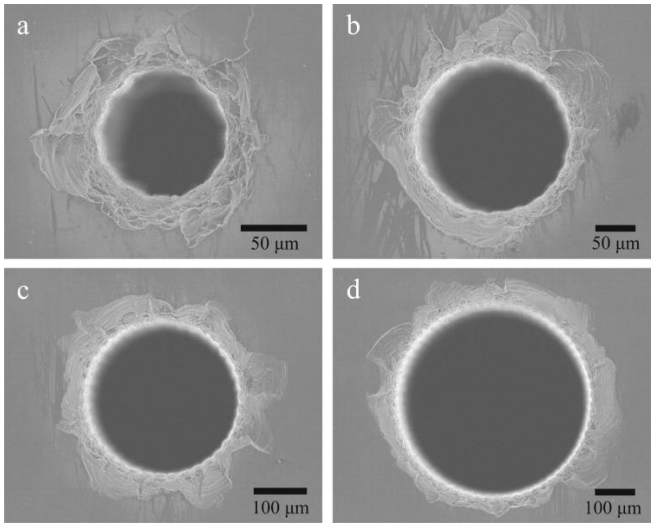

Fig. 3. Images of 6 mm-length capillaries with output diameters of 100 µm (a), 200 µm (b), 300 µm (c) and 500 µm (d), manufactured in fused silica using the nanosecond laser.

The energetic efficiency at such conditions was 0.13 mm^3/J. Therefore, it took a few dozen minutes to manufacture a 35 mm-diameter nozzle holder with the 2 mm height of the frustum of a cone. The average roughness R_a of the milled surface, measured in the horizontal direction by the stylus profiler Dektak 150 (from Veeco), was in the range of 4-6 µm.

In the second stage, the nozzle holder was turned upside down and the intrinsic structure, consisting of a microchannel and an adapter, was fabricated with reduced average laser power

Optics EXPRESS

and pulse repetition rate to achieve high-quality drilling and milling. The minimum diameter of the hole was 100 µm in the 6.3 mm-thick glass plate. For smaller diameters, processing debris was trapped inside a hole, and the process stopped. The achieved aspect ratio of 63:1 was comparable with the liquid-assisted femtosecond drilling technique [18]. However, the processing speed was significantly enlarged. It took only 15 s, 30 s, 60 s, 160 s to drill 100 µm, 200 µm, 300 µm and 500 µm-diameter holes, respectively, in the 6.3 mm-thick glass sheet with the 0.48 W average laser power. Therefore, the material removal rate and processing energetic efficiency where 3.3×10^{-3} mm^3/s and 6.9×10^{-3} mm^3/J, respectively, calculated for the 100 µm-diameter hole and approximately 15×10^{-3} mm^3/J for other holes. The front-side scanning electron microscope (SEM) images of drilled holes are presented in the Fig. 3. The maximum surface chipping, which is typical for nanosecond laser processing of glass, was around 100 µm. For examination of the surface roughness, the sample was cut through an array of holes and polished to open a channel. An SEM image of opened channels is given in Fig. 4(a). It is clearly seen that the fabricated channels are taper-less and maintain their cylindrical shape for the entire thickness of the glass. The rough surface, visible in Fig. 4(b), occurs due to the nature of the process. The surface topography of 500 µm-diameter channel, measured by the stylus profiler, is presented in Fig. 4(c). The measured average surface roughness R_a of a channel in the vertical direction was 1.4 µm, the average peak-to-valley distance R_z was 8 µm.

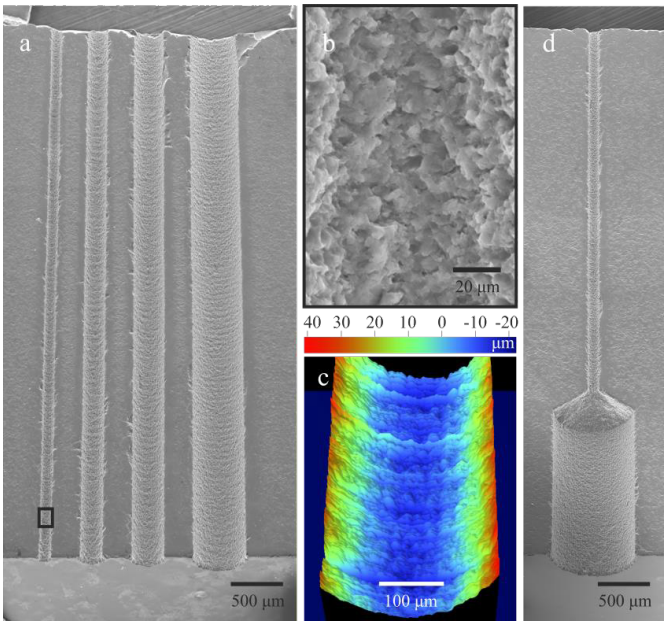

Fig. 4. Tilted SEM images of an opened drilled holes array with diameters of 100 µm, 200 µm, 300 µm and 500 µm (a). The magnified image of the 100 mm-diameter channel surface (b). The surface topography of 500 µm-diameter channel (c), 100 µm-diameter capillary, connected with a 0.8 mm-diameter adapter (d).

The nanosecond laser rear-side processing approach is a flexible technique, which allows us to fabricate the 2.5D structures in the bulk of glass. For instance, capillaries with variable diameters, as shown in the Fig. 4(d).

3.2 Hybrid 3D machining technique

Initially, samples were shaped using the DPSS nanosecond laser with a high material removal rate. In this step, a nozzle holder and an adapter without a microchannel, similar to the one

Optics EXPRESS

presented in Fig. 4(d), were fabricated. The 0.8 mm-diameter adapter with a conical tip was required to reduce the thickness of laser-untreated volume to 2 mm for the further processing step.

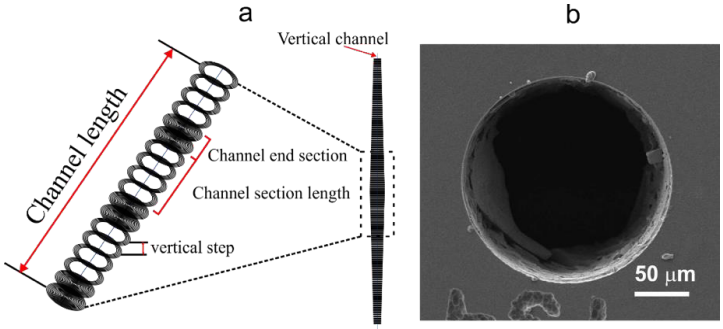

Fig. 5. Fabrication geometry of the modifications for the chemical etching (a) and the SEM picture of the channel entrance after 22 h etching in 10M KOH (b).

Then, micro-capillaries were inscribed using the femtosecond laser direct writing technique and etched in the potassium hydroxide (KOH) of 10M concentration for 22 hours. In such way, the manufacturing showed no chipping on the microchannel entrance surface, shown in Fig. 5(b), and the diameter accuracy control has been improved up to +/– 2 µm, depending on the channel size precompensation. For the channel fabrication, the femtosecond Yb:KGW Pharos laser (from Light Conversion) operating at the 515 nm wavelength and ~300 fs pulse duration was used. The repetition rate was set to 500 kHz, and the processing speed was 0.5 mm/s to ensure the 1000 pulses/µm density. The laser beam was focused with a 100x microscope objective (from Mitutoyo, NA = 0.5) to achieve ~2 µm spot size.

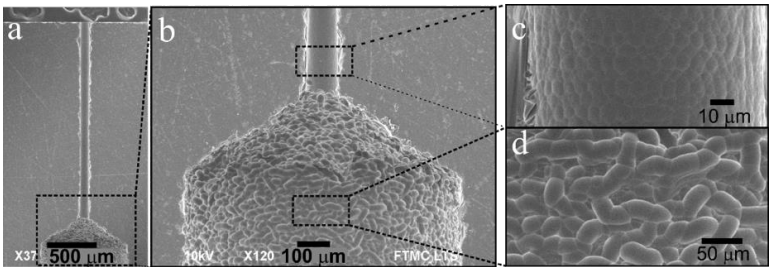

Fig. 6. SEM images of an opened channel with a diameter of ~100 µm after 22 h etching in 10 M KOH (a). The magnified image of the transition from the drilled adapter to the etched channel surface (b). Magnified surface morphology of the etched channel (c). Drilled and etched adapter (d).

The vertical channel was formed according to the fabrication geometry, demonstrated in the Fig. 5(a). The whole channel length was divided into the 9 sections with a single section length of ~230 µm. The section was composed of the layers consisting of a set of concentric circles, which increased the etched cavity size. The concentric circles were manufactured by translating the sample relative to the laser focus with the XY positioning system that allows the accuracy of ~300 nm (Aerotech ANT150). The single layer was not entirely filled by the circles to minimise the fabrication time. The z step between the layers in the single section was defined experimentally and was 4-5 µm. Each section was terminated by the end sections, composed of the few layers, fabricated by the same processing parameters. However, in this case, the whole area of the layer was filled entirely by concentric circles. The circle's radius in the layer

Optics EXPRESS

was changed by the 1.5 µm step. This sectional fabrication minimised the saturation during the etching as the etched section was separated and fall out. Therefore the clear etchant could achieve deeper and deeper sections. Due to the aberrations [32], for the deeper focusing the pulse energy dissipated, and higher energy was needed to induce the required modifications. In this way, ~300 nJ pulse energy was used for the first section and ~800 nJ pulse energy for the last section. The vertical channel shape was precompensated by changing the maximum section radius to achieve the taper-less microchannel. The total laser fabrication time of 100 µm diameter channel was ~21 min. SEM images of an opened channel are shown in Fig. 6. The magnified etched microchannel and adapter images demonstrate a significant difference in the surface morphology. The adapter, drilled using the nanosecond laser and etched for 22 h, shows the rough worm-like surface. The surface profile, measured with a stylus profiler, is given in Figs. 7(a) and 7(b).

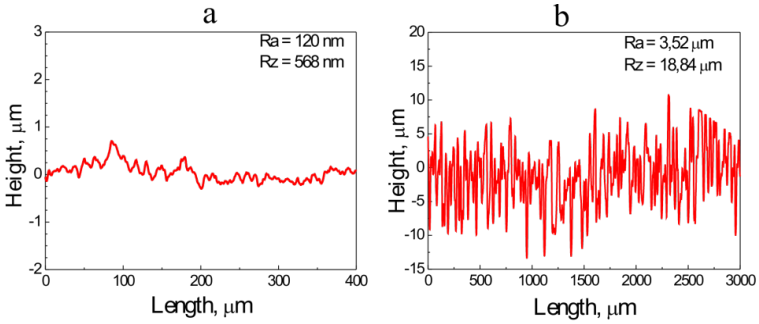

Fig. 7. Surface roughness measurement of the channel, fabricated by the FLSE technology (a), and of the adapter, drilled using nanosecond laser and 22 h-etched in 10 M KOH (b).

The surface roughness of the microchannel, fabricated with the FLSE technology, was R_a = 120 nm (R_z = 568 nm). For comparison, the surface roughness of the adapter, drilled with the nanosecond laser and etched for 22 hours, was R_a = 3.5 µm (R_z = 18.8 µm). Note that etching further increased the roughness of channels, fabricated using nanosecond laser.

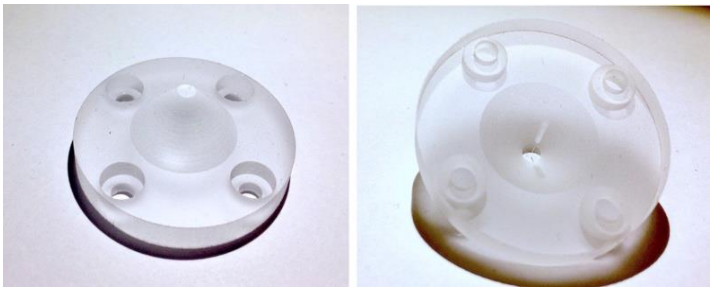

Fig. 8. The nozzle (diameter 35 mm, height 12.7 mm) of 2 mm-length capillaries with the output diameter of 100 µm, laser-machined in fused silica with the following etching in KOH.

The FLSE technology significantly improves the average surface roughness R_a (~12 times) and average peak-to-valley distance R_z (~14 times) of the microchannel; however, due to the long fabrication time, it is less competitive in the processing of high-volume parts. The minimum diameter that can be achieved in the 2 mm thick fused silica was ~30 µm, which is ~3 times smaller compared to the nanosecond laser drilling. Therefore, the FSLE technology can be preferred where the low surface roughness and small < 100 µm diameter microchannels are required. Images of the fabricated nozzle with the 2 mm-length capillaries are given in Fig. 8.

Optics EXPRESS

4. Characterization of nozzles

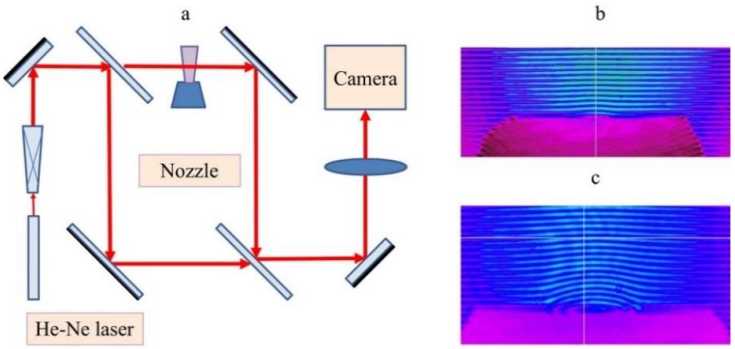

Fig. 9. Diagram of Mach-Zehnder interferometer (a), and measured phase interferogram of helium (b) and nitrogen (c) gas jet at the backing pressure of 60 bar of the cylindrical nozzle with the output diameter of 300 μm.

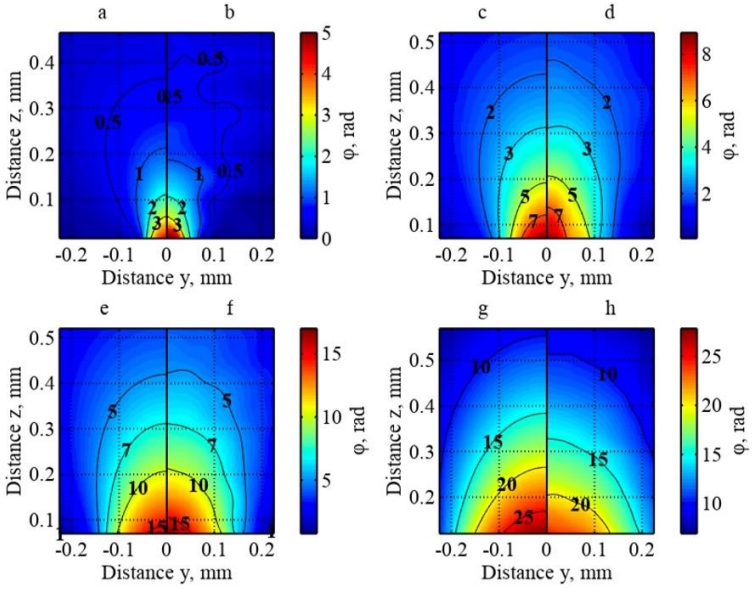

Fig. 10. Simulated (a, c, e, g) and reconstructed (b, d, f, h) integral phase profiles of Mach-Zehnder interferometer of nitrogen gas at 60 bar of cylindrical nozzles with the output diameter of 100 μm (a, b), 200 μm (c, d), 300 μm (e, f) and 500 μm (g, h).

The gas density profiles were measured using nitrogen, Mach-Zehnder interferometer, continuous wave 632.8 nm He-Ne laser and subsequently filtered using Fourier transformation [33]. The gas nozzles were tested in a vacuum chamber at the vacuum level of 10^{-5} mbar. The laser was operated, and the interferometer was installed outside of the vacuum chamber with one of the interferometer arms crossing the vacuum chamber through the windows of the optical quality of λ/10. The diagram of the Mach-Zehnder interferometer is presented in Fig. 9(a) and the images of measured phase interferograms of the gas jet at the backing pressure of 60 bar of the cylindrical nozzle with an output diameter of 300 μm for helium are given in Fig. 9(b) and for nitrogen in Fig. 9(c). The nozzles were driven by the Parker 9 series microvalve with the

Optics EXPRESS

0.8 mm orifice, actuated by a specialised pulse driver enabling millisecond operation. The operation of the microvalves and CCD cameras were synchronised and triggered by the master oscillator.

Nitrogen was used for the determination of the gas density profiles because of the sufficiently higher refractive index relative to the helium. The Abel transformation was performed to get the 3D map of the nozzle gas density. The phase was retrieved, and the density profiles were reconstructed using the interferometric data evaluation algorithms (IDEA) [34]. The simulated integral phase profiles of nitrogen gas at 60 bar of cylindrical nozzles with the output diameter of 100 μm, 200 μm, 300 μm and 500 μm are presented in Figs. 10(a), 10(c), 10(e) and 10(g), respectively.

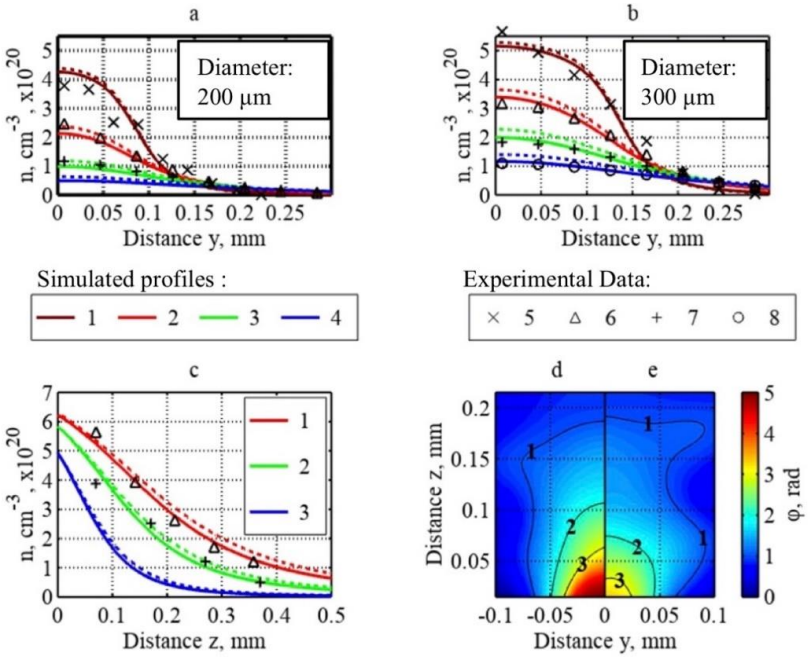

Fig. 11. Simulated and reconstructed transversal concentration profiles (a,b) of gas at 60 bar of cylindrical nozzles at the distance of 70 μm (line 1, marker 5), 170 μm (line 2, marker 6), 270 μm (line 3, marker 7) and 370 μm (line 4, marker 8). Solid lines correspond to the concentration simulations of nitrogen and dashed of helium. Markers represent the experimental data. Simulated and reconstructed longitudinal concentration profiles (c) of gas at 60 bar of cylindrical nozzles with output diameter of 300 μm (line 1, marker 6), 200 μm (line 2, marker 7) and 100 μm (line 3). Reconstructed integral phase profiles (d, e) of Mach-Zehnder interferometer of nitrogen gas at 60 bars of cylindrical nozzles with the output diameter of 100 μm and R_z = 568 nm (d), and R_z = 8 μm (e).

The reconstructed integral phase profiles are presented in Figs. 10(b), 10(d), 10(f) and 10(h). Integral phase φ was calculated from the OpenFOAM concentration simulations with following integration of the phase change while the interferometer beam was crossing the nozzle gas jet. The measured profiles of integral phase were reconstructed from measured interferograms using IDEA software package. In Figs. 11(a) and 11(b), the simulated and reconstructed transversal concentration profiles of gas at 60 bar of cylindrical nozzles with the output diameter of 200 μm and 300 μm, respectively, are presented. Solid lines correspond to the concentration simulations of nitrogen and dashed of helium. Markers represent the experimental data. In Fig. 11(c), the simulated and reconstructed longitudinal concentration

Optics EXPRESS

profiles of gas at 60 bar of cylindrical nozzles with output diameter 300 μm (line 1, marker 6), 200 μm (line 2, marker 7) and 100 μm (line 3) are given. In Figs. 11(d) and 11(e), the reconstructed integral phase profiles of Mach-Zehnder interferometer of nitrogen gas at 60 bar of cylindrical nozzles with the output diameter of 100 μm and R_z = 568 nm and R_z = 8 μm, respectively, are shown.

5. Results and discussion

The calculated and measured integral phase φ, presented in Fig. 10, and gas concentration profiles, presented in Fig. 11, are in good correspondence for the nozzles with the diameter of 100, 200 and 300 μm. The measured phase profiles of the nozzle with the output diameter of 500 μm were 15% lower relative to the predicted by numerical simulation because of the low removal rate of the residual gas by the vacuum pump system. Depending on the valve backing pressure of 20 to 60 bar, the achieved concentration of the gas density at the exit of micronozzles was in the range of 2-6 × 10^{20} cm^{-3}. The concentration profiles were parabolic, and the concentration dropped by orders of magnitude at the distance of 4-5 diameters from the output. At these distances, the concentration depends linearly on the backing pressure of the valve. The density at the output of the nozzle is close to the critical density of subsonic flow inside of the capillary, and the Mach number of the gas jet is in the range of 1.3-1.4. Leaving the capillary, the gas expands quickly, and at the distance of the diameter of the nozzle, reaches the velocity of 2-3 Mach. At a distance, being equal of 0.5-0.7 diameters of the nozzles from the output, the concentration profile is relatively flat, and the concentration changes 20-30% within the focused beam of 10-20 μm at FWHM of accelerating laser. The gas concentration of cylindrical nozzles with the diameter of 200-300 μm at 60 bar of backing pressure is 1.8-2.2 × 10^{20} cm^{-3}. This value is higher relative to Laval nozzles with the throat of the same size as cylindrical nozzle because the output area of Laval nozzles is typically several times greater than the critical area. The concentration can be raised by increasing the backing pressure several times. The maximal pressure is limited by the mechanical characteristics of the valve and strength of the material. Cylindrical nozzles have advantages where high-density and short gas target are required, and the laser beam is focused close to the nozzle output area. The supersonic Laval nozzles have advantages where more extended flat profiles with modest gas concentration and long focusing length of the laser beam are implemented.

The gas concentration of cylindrical nozzles with the diameter of 100 μm, measured at the distance of 50 μm from the output of the nozzle was 25% lower in the channel with the higher wall roughness of R_z = 8 μm relatively to the channel with the wall roughness of R_z = 568 nm. The corresponding gas concentrations were 2.2 × 10^{20} and 3 × 10^{20} cm^{-3}, respectively. The difference of the gas concentration of the channels decreased with the distance from the nozzle output and reached similar values of 0.8-1 × 10^{20} cm^{-3} at the distance of 150 μm from the nozzle output. The SEM images of wall roughness and integral phase of FLSE and rear-side technique are presented correspondingly in Fig. 6(c), Figs. 4(c) and 4(d), Figs. 11(d) and 11(e).

6. Conclusions and outlook

The combination of the 7-12 fs laser pulses and plasma targets of the size of 100-200 μm and the gas density of 1-3 × 10^{20} cm^{-3} allows to reach the laser strength parameter a_0 >2 and accelerate the electrons with lasers having several terawatt of power. It opens the opportunity to benefit from the generation of ultrashort X-ray pulses with a high repetition rate of 1 kHz. At the distance of the diameter of the channel, the concentration profile is relatively flat and changes 20-30% within the focused beam of 10-20 μm at FWHM of accelerating laser. Higher gas density will result in shorter dephasing length and lower the energy of accelerated electrons. The decreased energy will be partially compensated by higher plasma field. Additionally, to increase the dephasing length, a periodical nozzle array with modulation of the density with high and low concentrations regions can be implemented. The described manufacturing

Optics EXPRESS

technique can be used for manufacturing of Laval nozzles and combinations of cylindrical, slit and Laval nozzle arrays on a single chip to produce tailored gas concentration profiles.

The nanosecond laser rear-side processing approach allows rapid fabrication of gas jet nozzles with the minimum 100 µm-diameter capillaries in a 6.3 mm-thick fused silica. The maximum material removal rate for high-volume parts is 2.34 mm^3/s with the 18 W average laser power. However, due to the nature of the process, the channel roughness is on the order of several micrometers. The FLSE technology significantly improves the average surface roughness (~12 times) and average peak-to-valley distance (~14 times) of the microchannel; however, due to the low fabrication time, it is less competitive for processing of high-volume parts. The limitations above can be eliminated by the hybrid 3D machining technique, when high-volume parts, which do not require high quality, are removed by nanosecond pulses, and high-quality capillaries are fabricated by the laser-assisted chemical etching. Such a technique allows achieving both - high processing speed and quality.

Funding

Research Council of Lithuania (S-MIP-17-79).

References

1. M. Šmíd, I. Gallardo González, H. Ekerfelt, J. Björklund Svensson, M. Hansson, J. C. Wood, A. Persson, S. P. D. Mangles, O. Lundh, and K. Falk, "Highly efficient angularly resolving x-ray spectrometer optimized for absorption measurements with collimated sources," Rev. Sci. Instrum. **88**(6), 063102 (2017).
2. S. Cipiccia, M. R. Islam, B. Ersfeld, R. P. Shanks, E. Brunetti, G. Vieux, X. Yang, R. C. Issac, S. M. Wiggins, G. H. Welsh, M. P. Anania, D. Maneuski, R. Montgomery, G. Smith, M. Hoek, D. J. Hamilton, N. R. C. Lemos, D. Symes, P. P. Rajeev, V. O. Shea, J. M. Dias, and D. A. Jaroszynski, "Gamma-rays from harmonically resonant betatron oscillations in a plasma wake," Nat. Phys. **7**(11), 867–871 (2011).
3. K. Ta Phuoc, E. Esarey, V. Leurent, E. Cormier-Michel, C. G. R. Geddes, C. B. Schroeder, A. Rousse, and W. P. Leemans, "Betatron radiation from density tailored plasmas," Phys. Plasmas **15**(6), 063102 (2008).
4. E. Esarey, C. B. Schroeder, and W. P. Leemans, "Physics of laser-driven plasma-based electron accelerators," Rev. Mod. Phys. **81**(3), 1229–1285 (2009).
5. C. Thaury, E. Guillaume, A. Lifschitz, K. Ta Phuoc, M. Hansson, G. Grittani, J. Gautier, J. P. Goddet, A. Tafzi, O. Lundh, and V. Malka, "Shock assisted ionization injection in laser-plasma accelerators," Sci. Rep. **5**(1), 16310 (2015).
6. M. Hansson, B. Aurand, X. Davoine, H. Ekerfelt, K. Svensson, A. Persson, C. G. Wahlström, and O. Lundh, "Down-ramp injection and independently controlled acceleration of electrons in a tailored laser wakefield accelerator," Phys. Rev. Spec. Top. Accel. Beams **18**(7), 071303 (2015).
7. G. Golovin, S. Banerjee, S. Chen, N. Powers, C. Liu, W. Yan, J. Zhang, P. Zhang, B. Zhao, and D. Umstadter, ""Control and optimization of a staged laser-wakefield accelerator," Nucl. Instruments Methods Phys. Res. Sect. A Accel. Spectrometers," Detect. Assoc. Equip. **830**, 375–380 (2016).
8. M. Hansson, B. Aurand, H. Ekerfelt, A. Persson, and O. Lundh, ""Injection of electrons by colliding laser pulses in a laser wakefield accelerator," Nucl. Instruments Methods Phys. Res. Sect. A Accel. Spectrometers," Detect. Assoc. Equip. **829**, 99–103 (2016).
9. J. Ferri, S. Corde, A. Döpp, A. Lifschitz, A. Doche, C. Thaury, K. Ta Phuoc, B. Mahieu, I. A. Andriyash, V. Malka, and X. Davoine, "High-Brilliance Betatron γ-Ray Source Powered by Laser-Accelerated Electrons," Phys. Rev. Lett. **120**(25), 254802 (2018).
10. R. Budriūnas, T. Stanislauskas, J. Adamonis, A. Aleknavičius, G. Veitas, D. Gadonas, S. Balickas, A. Michailovas, and A. Varanavičius, "53 W average power CEP-stabilized OPCPA system delivering 5.5 TW few cycle pulses at 1 kHz repetition rate," Opt. Express **25**(5), 5797–5806 (2017).
11. A. J. Goers, G. A. Hine, L. Feder, B. Miao, F. Salehi, J. K. Wahlstrand, and H. M. Milchberg, "Multi-MeV Electron Acceleration by Subterawatt Laser Pulses," Phys. Rev. Lett. **115**(19), 194802 (2015).
12. D. Guénot, D. Gustas, A. Vernier, B. Beaurepaire, F. Böhle, M. Bocoum, M. Lozano, A. Jullien, R. Lopez-Martens, A. Lifschitz, and J. Faure, "Relativistic electron beams driven by kHz single-cycle light pulses," Nat. Photonics **11**(5), 293–296 (2017).
13. S. W. Jolly, Z. He, C. McGuffey, W. Schumaker, K. Krushelnick, and A. G. R. Thomas, "Stereolithography based method of creating custom gas density profile targets for high intensity laser-plasma experiments," Rev. Sci. Instrum. **83**(7), 073503 (2012).
14. A. Döpp, E. Guillaume, C. Thaury, J. Gautier, K. Ta Phuoc, and V. Malka, "3D printing of gas jet nozzles for laser-plasma accelerators," Rev. Sci. Instrum. **87**(7), 073505 (2016).
15. L. Hof and J. Abou Ziki, "Micro-Hole Drilling on Glass Substrates—A Review," Micromachines (Basel) **8**(2), 53 (2017).
16. N. M. Bulgakova, V. P. Zhukov, A. R. Collins, D. Rostohar, T. J.-Y. Derrien, and T. Mocek, "How to optimize ultrashort pulse laser interaction with glass surfaces in cutting regimes?" Appl. Surf. Sci. **336**, 364–374 (2015).

Optics EXPRESS

17. Y. Li, K. Itoh, W. Watanabe, K. Yamada, D. Kuroda, J. Nishii, and Y. Jiang, "Three-dimensional hole drilling of silica glass from the rear surface with femtosecond laser pulses," Opt. Lett. **26**(23), 1912–1914 (2001).
18. D. J. Hwang, T. Y. Choi, and C. P. Grigoropoulos, "Liquid-assisted femtosecond laser drilling of straight and three-dimensional microchannels in glass," Appl. Phys., A Mater. Sci. Process. **79**(3), 605–612 (2004).
19. D. Ashkenasi, T. Kaszemeikat, N. Mueller, A. Lemke, and H. J. Eichler, "Machining of glass and quartz using nanosecond and picosecond laser pulses," Proc. SPIE **8243**, 82430M (2012).
20. Z. K. Wang, W. L. Seow, X. C. Wang, and H. Y. Zheng, "Effect of laser beam scanning mode on material removal efficiency in laser ablation for micromachining of glass," J. Laser Appl. **27**(S2), S28004 (2015).
21. P. Gečys, J. Dudutis, and G. Račiukaitis, "Nanosecond Laser Processing of Soda-Lime Glass," J. Laser Micro Nanoeng. **10**(3), 254–258 (2015).
22. G. Lott, N. Falletto, P. Devilder, and R. Kling, "Optimizing the processing of sapphire with ultrashort laser pulses," J. Laser Appl. **28**(2), 022206 (2016).
23. K. Mishchik, K. Gaudfrin, and J. Lopez, "Drilling of through holes in sapphire using femto-second laser pulses," J. Laser Micro Nanoeng. **12**(3), 321–324 (2017).
24. X. Zhao and Y. C. Shin, "Femtosecond laser drilling of high-aspect ratio microchannels in glass," Appl. Phys., A Mater. Sci. Process. **104**(2), 713–719 (2011).
25. A. Marcinkevi Ius, S. Juodkazis, M. Watanabe, M. Miwa, S. Matsuo, H. Misawa, and J. Nishii, "Femtosecond laser-assisted three-dimensional microfabrication in silica," Opt. Lett. **26**(5), 277–279 (2001).
26. S. Lo Turco, R. Osellame, R. Ramponi, and K. C. Vishnubhatla, "Hybrid chemical etching of femtosecond irradiated 3D structures in fused silica glass," MATEC Web Conf. **8**, 05009 (2013).
27. V. Stankevič and G. Račiukaitis, ""Free-shape 3D structure formation in bulk fused silica by irradiation with femtosecond laser pulses," JLMN-," J. Laser Micro Nanoeng. **9**(3), 271–275 (2014).
28. M. Hermans, J. Gottmann, and F. Riedel, "Selective, laser-induced etching of fused silica at high scan-speeds using KOH," J. Laser Micro Nanoeng. **9**(2), 126–131 (2014).
29. L. Open CFD
30. "Engineering ToolBox. Material Properties.," https://www.engineeringtoolbox.com/material-properties-t_24.html.
31. M. J. Zucrow and J. D. Hoffman, *Gas Dynamics* (Krieger Pub. Co, 1985).
32. C. Hnatovsky, R. S. Taylor, E. Simova, V. R. Bhardwaj, D. M. Rayner, and P. B. Corkum, "High-resolution study of photoinduced modification in fused silica produced by a tightly focused femtosecond laser beam in the presence of aberrations," J. Appl. Phys. **98**(1), 013517 (2005).
33. R. Azambuja, M. Eloy, G. Figueira, and D. Neely, "Three-dimensional characterization of high-density non-cylindrical pulsed gas jets," J. Phys. D Appl. Phys. **32**(8), L35–L43 (1999).
34. M. Hipp, J. Woisetschläger, P. Reiterer, and T. Neger, "Digital evaluation of interferograms," Measurement **36**(1), 53–66 (2004).

NOTES

NOTES

Vilnius University Press
9 Saulėtekio Ave., Building III, LT-10222 Vilnius
Email: info@leidykla.vu.lt, www.leidykla.vu.lt
Print run 25